Université de Montréal

Spectroscopie optique de complexes aquo et chloro des éléments de transition de la première série: effets vibroniques, électroniques et propriétés des états excités de solides inorganiques.

Par

Guillaume Bussière

Département de Chimie

Faculté des Arts et des Sciences

Thèse présentée à la Faculté des études supérieures

en vue de l'obtention du grade de

Philosophiæ Doctor (Ph.D.)

Juin 2001

Université de Montréal

Faculté des études supérieures

Cette thèse intitulée :

Spectroscopie optique de complexes aquo et chloro des éléments de transition de la première série: effets vibroniques, électroniques et propriétés des états excités de solides inorganiques.

présentée par:

Guillaume Bussière

a été évaluée par un jury composé des personnes suivantes:

André Beauchamp.....…….....Président rapporteur

Christian Reber.....…….....Directeur de recherche

Gilles Durocher.....…….....Membre du jury

James K. McCusker.....…….....Examinateur externe

Manu Paranjape.....…….....Représentant du doyen

Thèse acceptée le: 28/09/2001

Sommaire

Les spectres d'absorption, de luminescence et Raman de monocristaux nous ont permis de caractériser un nombre d'états électroniques de façon quantitative. Les effets d'interaction entre deux états centrés sur le métal et entre les états du métal et du ligand ont été étudiés. L'influence de la dimension d'agrégats inorganiques sur la séparation énergétique entre l'état fondamental et l'état émissif a aussi été brièvement explorée.

Des complexes simples de métaux de transition ont été préparés (Ni^{2+}, V^{3+}, Co^{2+} et Cr^{3+}). Les complexes de métaux de transition sont idéaux pour l'étude du comportement des états électroniques qu'on peut varier facilement par substitution de ligands. Des mesures spectroscopiques ont été effectuées avec des échantillons sous forme solide, cristalline et à basse température dans le but de caractériser les énergies, fréquences de vibration et structure de leurs états électroniques. Les cas qui ont retenu notre attention sont ceux qui impliquent plusieurs états électroniques dans des situations où la dynamique des noyaux n'est plus séparable de celle des électrons. On peut aussi parler de comportement non-adiabatique ou de cas qui sortent du cadre de l'approximation de Born-Oppenheimer.

Pour les métaux de transition de la première série, le comportement non-adiabatique est surtout causé par le couplage spin-orbite. Pour les complexes $[Ni(H_2O)_6]^{2+}$, $[NiCl_2(H_2O)_4]$, $[CrCl_2(H_2O)_4]^{+}$ et $[VCl_2(H_2O)_4]^{+}$, les paramètres spectroscopiques sont bien connus, ce qui nous permet d'effectuer une analyse quantitative de l'interaction entre les états électroniques en utilisant la théorie dépendante du temps et la théorie du champ des ligands. Les spectres d'absorption

polarisés à basse température de $[Ni(H_2O)_6]^{2+}$ et de $[NiCl_2(H_2O)_4]$ montrent suffisamment de détails résolus pour mettre au point un modèle qui explique de façon quantitative les observations faites pour cette série de complexes. Les principales manifestations spectrales reproduites par le modèle sont: une forte intensité des transitions interdites, un changement des fréquences de vibration aux états excités et une chute de l'absorption (ou antirésonance) située entre les deux maxima. Dans tous les cas, l'intensité relative d'une transition interdite par rapport à une transition permise et la distribution des intensités dans les progressions vibroniques sont reproduites.

Une équation analytique dont la forme s'apparente à celle des antirésonances de Fano a été appliquée. Cette équation est une alternative simple à l'utilisation de la théorie dépendante du temps pour caractériser l'interaction entre deux états excités dans une molécule. Il s'est avéré que l'équation donne de bons résultats pour des systèmes dont les spectres sont peu résolus tels que des solutions gelées et des verres dopés contenant des complexes octaédriques du nickel(II) et du chrome(III).

Des calculs *ab-initio* ont été effectués pour caractériser les états triplets des complexes aquo du nickel(II) ($[Ar]3d^8$) et du vanadium(III) ($[Ar]3d^2$). Les états électroniques de ces complexes sont identiques, mais leur ordre énergétique est inversé, une conséquence de l'analogie électrons-trous qui existe entre les métaux de transitions de configuration électronique d^n et d^{10-n}. Les résultats obtenus ont été comparés avec la théorie du champ des ligands notamment pour les deux états électroniques $^3T_{1g}$ pour lesquels une forte interaction de configuration existe. Des spectres d'absorption ont été calculés à partir des surfaces d'énergie potentielle *ab-initio* et les résultats concordent avec les expériences. Ces résultats nous ont permis

de mettre en évidence un couplage entre états électroniques de même multiplicité de spin. Les spectres ont été calculés dans ce cas-ci suivant l'approximation de Born-Oppenheimer, c'est-à-dire en utilisant seulement les potentiels adiabatiques des états $^3T_1$ générés par les calculs *ab-initio*.

Des ligands radicalaires de type nitronyl-nitroxyde ont aussi été synthétisés et des complexes ont été formés avec des métaux de transition et des terres rares (Eu^{3+}, La^{3+}, Gd^{3+}). Ces composés sont très particuliers car le ligand possède un électron non pairé et des transitions d'absorption dans la région du visible. Les spectres d'absorption et de luminescence de ces matériaux ont été mesurés. Une luminescence à été observée pour les ligands seuls et pour les complexes avec des terres rares. L'émission de ces complexes est centrée sur le nitronyl-nitroxyde dans certains cas. Cette observation est surprenante puisque les transitions f-f centrées sur ces métaux sont en général dominantes, peu importe le ligand. Un but à long terme de ce projet est d'établir un lien entre les propriétés optiques et le magnétisme de ces matériaux.

Des mesures de luminescence ont été faites sur des agrégats de silicium de taille nanométrique. La longueur d'onde d'émission est reliée à la taille des particules. Les petits agrégats émettent à plus haute énergie tandis que les plus gros émettent à plus basse énergie.

Table des matières

Liste des tableaux

Liste des figures

Chapitre 1: Introduction

1.1. Contexte et domaine de recherche

Les propriétés physiques et chimiques des complexes métalliques sont déterminées à la fois par leur structure et par la nature de leur densité électronique, souvent décrit par le terme 'structure électronique'. La couleur est un exemple particulièrement simple d'une propriété physique déterminée par la structure électronique. Un changement de structure électronique est généralement accompagné d'un changement de couleur, souvent visible à l'oeil nu. La spectroscopie d'absorption nous permet de mesurer ces couleurs et leurs variations de façon très précise et aussi d'avoir accès à des domaines d'énergie supérieurs et inférieurs à celui correspondant à la lumière visible. Dans cette thèse, c'est surtout la région à basse énergie, le proche infrarouge et le rouge, qui est d'intérêt.

Il est possible de contrôler la structure électronique des complexes par des substitutions de ligands[1], en variant la température[2, 3], en variant la pression[4-6] ou en irradiant l'échantillon[3]. On retrouve des exemples touchant à tous ces aspects pour certains complexes du fer(II) qui présentent des transitions de spin contrôlables par irradiation et par des changements de température[3, 7]. Ces molécules aux propriétés magnétiques et optiques contrôlables sont d'intérêt pour applications dans les domaines d'affichage et d'enregistrement de données. Un exemple pertinent de l'utilisation des techniques spectroscopiques pour l'étude des propriétés chimiques

est la chimie bio-inorganique. Les méthodes spectroscopiques appliquées aux biomolécules inorganiques sont le sujet d'un livre de référence récent[8]. L'analyse des centres métalliques de certaines enzymes, résumé récemment pour quelques exemples de fine pointe[9], démontre encore la puissance de la spectroscopie électronique.

Cette thèse examine des situations où les modèles bien établis sont insuffisants pour expliquer les observations expérimentales. Nous avons développé une approche performante pour l'analyse d'une gamme de phénomènes spectroscopiques. Notre but est d'obtenir le maximum d'information à partir d'expériences spectroscopiques et d'effectuer des analyses à l'aide du modèle développé. Nous avons utilisé des complexes simples pour les analyses approfondies. Ensuite nous analysons de façon qualitative des matériaux modernes où des effets qui dépassent les modèles établis jouent aussi un rôle important.

L'approche standard pour l'analyse des spectres consiste à attribuer un seul état excité, ou pire encore une seule configuration électronique, à chaque bande d'absorption. Nous démontrons qu'il faut souvent considérer plusieurs états électroniques couplés pour analyser une bande d'absorption. La forme de la bande est définie par la position et la forme d'une seule surface d'énergie potentielle dans l'approche standard. Ici, nous démontrons qu'il faut souvent considérer plusieurs surfaces couplées, même si des bandes d'absorption sont bien séparées en énergie.

Dans cette introduction, nous présentons des exemples expérimentaux et leur analyse par les approches traditionnelles, puis nous illustrons leurs limites. Pour déterminer la structure électronique des molécules d'intérêt, l'utilisation des méthodes spectroscopiques telles le Raman, la luminescence et l'absorption polarisée

est essentielle. En général, les observations sont faites à basse température pour augmenter la résolution spectrale et donc la quantité d'informations que fournissent les spectres[10]. Il est aussi possible d'étudier ces mêmes molécules et matériaux par des méthodes magnétiques, comme il est montré à la fin de cette introduction. Dans ce cas on peut caractériser la structure électronique de l'état fondamental uniquement, ce qui n'est pas suffisant pour notre but. L'avantage de la spectroscopie optique réside dans le fait que l'on peut, en principe, s'en servir pour observer tous les états électroniques d'une molécule ou d'un matériau.

1.2. Approche traditionnelle à l'analyse de spectres électroniques: exemples et limitations

La Figure 1.1 montre un exemple simple illustrant que la spectroscopie d'absorption peut servir à déterminer les caractéristiques des états électroniques et le nombre de coordination de l'ion métallique dans un complexe. Il est essentiel de réaliser que certaines caractéristiques spectroscopiques telles que l'intensité et l'énergie des transitions dans la figure 1.1 permettent de différencier deux nombres de coordination. La symétrie et la multiplicité des états électroniques peuvent être déterminées à l'aide de la théorie du champ des ligands. Cette approche bien établie[11] est brièvement décrite dans la partie qui suit. À la base de l'attribution des bandes d'absorption par cette théorie est l'hypothèse d'un complexe rigide (géométrie fixe), les phénomènes vibroniques sont négligés. Les énergies calculées correspondent donc aux maxima des bandes d'absorption. La théorie ne fournit pas

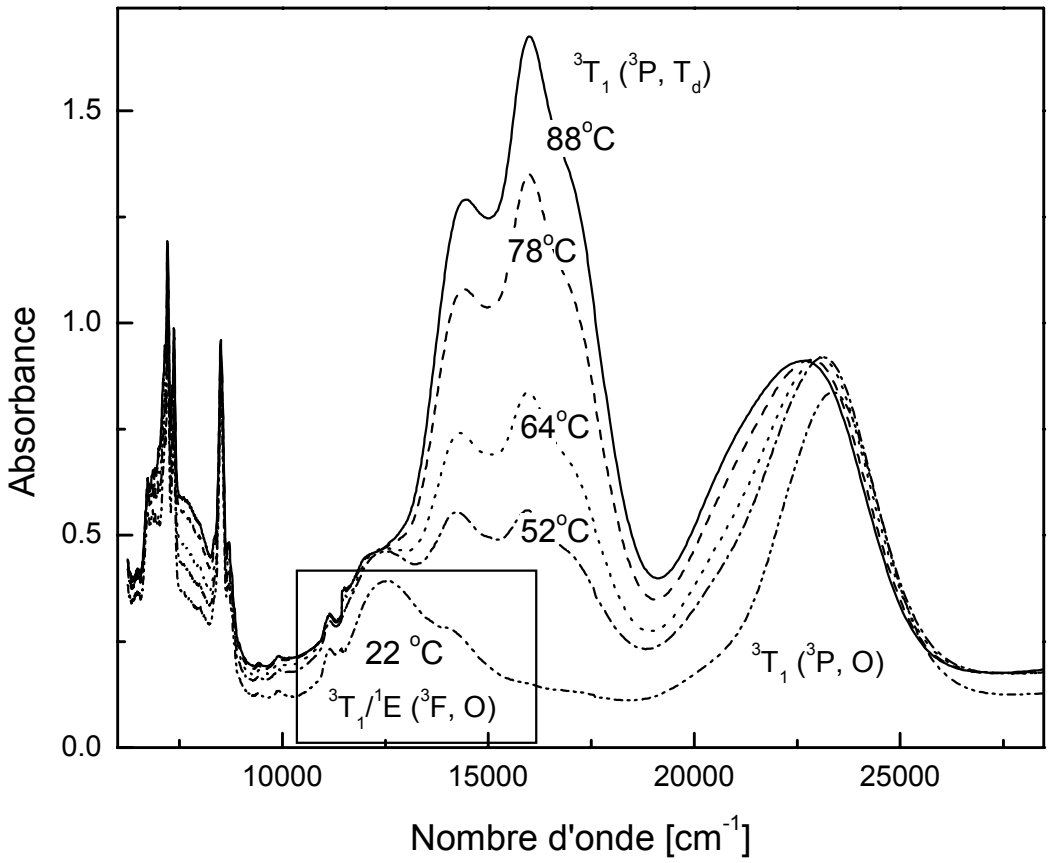

Figure 1.1 Spectres d'absorption de $Ni(DMSO)_n^{2+}$ (solution de $NiCl_2 \cdot 6H_2O$ dans le DMSO). On peut voir une forte augmentation de l'absorbance et un déplacement des bandes avec l'augmentation de la température. Ces caractéristiques sont typiques d'un changement du nombre de coordination pour les composés des métaux de transition.

de renseignement quantitatif sur la forme détaillée des bandes. Cette thèse est axée vers des situations où l'approche traditionnelle ne suffit plus.

La Figure 1.1 illustre les spectres d'absorption du complexe $Ni(DMSO)_n^{2+}$ en solution dans le diméthylsulfoxyde (DMSO). Au fur et à mesure que la solution est réchauffée, le nickel(II) passe d'une coordination octaédrique à tétraédrique. Ce changement du nombre de coordination se manifeste par une augmentation de l'intensité des transitions, par un changement des énergies des états électroniques et par une inversion de l'ordre des états électroniques. Les bandes d'absorption sont identifiées par l'état final de la transition. Traditionnellement un seul état est attribué à chaque bande. Cette approche est raisonnable pour toutes les bandes de la Figure 1.1, à l'exception de la bande encadrée, qu'il faut attribuer à deux états. C'est un premier exemple d'une situation d'intérêt pour cette thèse, et c'est le sujet du chapitre 2.

La Figure 1.2 montre cette inversion des états électroniques pour le nickel(II), de configuration électronique $[Ar]3d^8$, lors du passage d'une coordination octaédrique (groupe ponctuel O) vers une coordination tétraédrique (groupe ponctuel T_d). Cette Figure correspond aux spectres expérimentaux de la Figure 1.1. La symétrie des états électroniques est donnée par la théorie des groupes[12, 13]. Pour un complexe de configuration d^2 ou d^8 en coordination octaédrique ou tétraédrique, les énergies des états électroniques se calculent avec la théorie du champ des ligands en utilisant les équations[14]:

$$E(^3T_2) = 2Dq \qquad (1.1)$$

$$E(^3A_2) = 12Dq \qquad (1.2)$$

Dans ces équations, Dq représente la force du ligand. La séparation énergétique entre les orbitales t_2 (d_{xy}, d_{xz}, d_{yz}) et e ($d_{x^2-y^2}$, d_{z^2}) est de 10Dq[12, 13]. Pour le nickel(II) en coordination octaédrique, l'état fondamental est de symétrie $^3A_2$, et en coordination tétraédrique l'état fondamental est un des deux états $^3T_1$. L'énergie des deux états triplets de symétrie T_1 ne peut être calculée séparément à cause de l'interaction de configuration. Leurs énergies sont déterminées par le déterminant séculaire suivant[14]:

$$\begin{vmatrix} -6Dq - E_{T_1(F)} & 4Dq \\ 4Dq & 15B - E_{T_1(P)} \end{vmatrix} = 0 \qquad (1.3)$$

Le paramètre de Racah B est une mesure pour la répulsion interélectronique. La différence d'énergie entre les termes ^3F et ^3P pour un ion libre correspond à 15B. Dans un complexe, la valeur de B est plus faible que pour l'ion libre. Le couplage entre les états T_1 est de 4Dq et leurs énergies sont:

$$E_{T_1(F,P)} = 7.5B - 3Dq \pm \frac{1}{2}\sqrt{225B^2 + 100Dq^2 + 180DqB} \qquad (1.4)$$

Cette équation illustre les effets du couplage entre les états $^3T_1(^3F)$ et $^3T_1(^3P)$. Les deux états ne retiennent pas leur identité pure, mais le mélange de leur caractère est constant et ne dépend pas des propriétés détaillées des deux états, comme par exemple de leurs surfaces d'énergie potentielle. Les chapitres 2 à 5 montrent que cette approximation n'est pas suffisante et nous avons développé des modèles plus précis pour analyser ces situations.

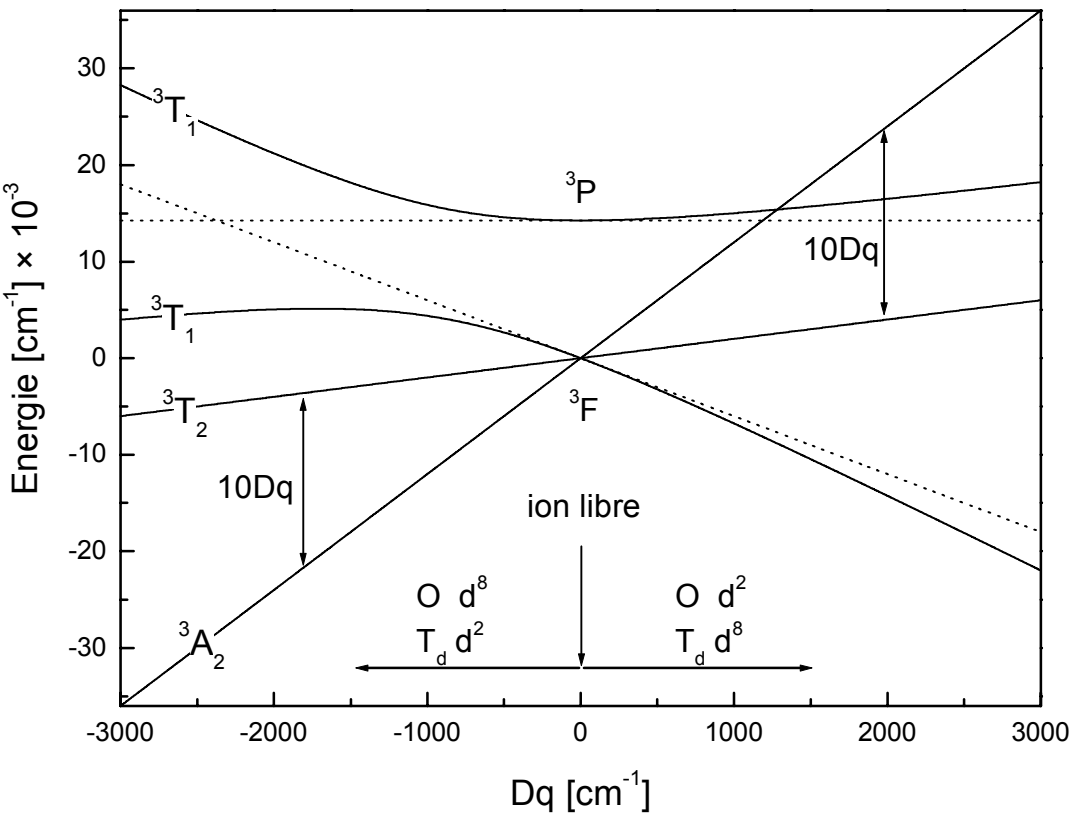

Figure 1.2 Diagramme des états électroniques pour des complexes métalliques avec les configurations d^2 et d^8. En parcourant l'axe des Dq des valeurs négatives vers les valeurs positives on passe d'une géométrie octaédrique (groupe ponctuel O) vers une géométrie tétraédrique (groupe ponctuel T_d) pour un complexe d^8. Le comportement est inversé pour un complexe de configuration d^2. Il est intéressant de noter que tous les états provenant du terme ^3F de l'ion libre se croisent à (0,0). Les lignes en pointillé sont les éléments diagonaux de l'équation 1.3, -6Dq et 15B, avec B=950 cm^{-1}.

Les équations 1.1 à 1.4 permettent de déterminer les énergies des états électroniques pour des complexes de métaux ayant la configuration d^2 en coordination octaédrique et d^8 en coordination tétraédrique pour des valeurs de Dq positives. En utilisant une valeur négative pour Dq, on obtient les énergies pour des complexes octaédriques avec la configuration d^8 et tétraédriques avec la configuration d^2. Un fait à noter est que la valeur de 10Dq fréquemment utilisée pour caractériser les complexes inorganiques[15], n'est autre que la différence d'énergie entre les états $^3A_2$ et $^3T_2$ (voir équations 1.1 et 1.2). Cette valeur de 10Dq correspond à l'énergie de la première transition électronique pour les complexes d^8 octaédriques et d^2 tétraédriques. Pour les complexes d^2 octaédriques et d^8 tétraédriques, 10Dq ne correspond pas à l'énergie de la première transition permise, il s'agit plutôt de la différence d'énergie entre les deux états excités $^3A_2$ et $^3T_2$ comme illustré à la Figure 1.2.

Les Figures 1.1 et 1.2 constituent un bon exemple de la richesse d'états électroniques différents des complexes des métaux de transition. Un aspect intéressant est le croisement évité des deux états $^3T_1$. Il est essentiel de comprendre l'interaction entre ces deux états pour décrire correctement la structure électronique des complexes de configuration d^2 ou d^8 dans la Figure 1.2, comme présenté au chapitre 5.

1.3. Surfaces d'énergie potentielle et couplage entre états: les manifestations spectroscopiques

D'un point de vue plus général, le passage d'un nombre de coordination de 6 à 4 illustré par les Figures 1.1 et 1.2 est une réaction chimique très simple où les croisements évités sont importants, une situation très courante en spectroscopie des complexes de métaux de transition. L'étude spectroscopique de ces complexes mène à la compréhension de systèmes plus compliqués où des croisements d'états électroniques sont importants, tel que les réactions photochimiques et la dynamique des réactions[16-19]. Nous avons choisi les complexes à étudier dans les chapitres suivants pour obtenir des modèles idéaux permettant l'étude approfondie et la compréhension du comportement de différents états électroniques couplés.

Ces phénomènes d'intérêt ne peuvent pas être analysés avec la théorie traditionnelle, approche illustrée dans la Figure 1.2, principalement parce qu'il faut tenir compte du mouvement vibrationnel et simultanément des états électroniques en interaction. Un exemple d'une manifestation expérimentale d'un tel effet est le double maximum dans l'encadré de la Figure 1.1. Cette partie du spectre d'un complexe octaédrique est profondément affectée par l'interaction entre deux états électroniques et par le mouvement de la molécule le long d'une coordonnée normale. L'origine de la double bosse était sujet à polémique dans la littérature de recherche et dans les livres d'enseignement[20-23]. Cette forme de bande est observée pour une gamme de complexes du nickel(II) avec des ligands coordinés par des atomes d'oxygène ou par des halogénures[24-28]. Nous avons développé un modèle rigoureux et général pour analyser cette signature spectroscopique.

Le livre de référence reconnu ‘Advanced Inorganic Chemistry’ de Cotton et Wilkinson[23] souligne que la double bosse dans le spectre du $[Ni(H_2O)_6]^{2+}$ en solution est le résultat du couplage spin-orbite. Les auteurs mentionnent également: ‘at higher resolution the spectra show much greater complexity and require much more sophisticated analysis’. Ces spectres nécessitent une analyse qui implique à la fois plusieurs états électroniques et les aspects vibroniques, dépassant les approches traditionelles. Nous utilisons cette complexité des spectres de cristaux à basse température pour notre analyse et pour vérifier rigoureusement notre modèle. Des double maxima pour certaines bandes d’absorption ont aussi été observées pour des ions de chrome(III) dopé dans des oxydes[29, 30]. Dans ces spectres, le minimum situé entre les deux maxima a été nommé une antirésonance de Fano.

Pour analyser ces effets spectroscopiques il est indispensable d’utiliser une théorie des énergies électroniques en combinaison avec une théorie vibronique pour bâtir un modèle quantitatif. L’ingrédient clé d’un tel modèle sont des surfaces d’énergie potentielle pour décrire les états électroniques. Cette approche mène à des niveaux d’énergie vibroniques, ce qui permet de caractériser les formes des bandes d’absorption en détail.

Le modèle vibronique le plus simple, appliqué souvent dans la littérature[31], décrit les états impliqués dans une transition électronique avec des surfaces harmoniques. La Figure 1.3 illustre ces surfaces en fonction d’une seule coordonnée normale Q. L’état excité est défini par:

$$V = \frac{1}{2} k(Q - \Delta Q)^2 + E_{00} \qquad (1.5)$$

La géométrie d'équilibre de l'état excité est décalée par ΔQ le long de la coordonnée normale. Dans cette équation, Q représente la coordonnée normale. Le minimum d'énergie de l'état excité est plus haut de E_{00} que l'état fondamental et k représente la constante de force harmonique. Ce modèle est basé sur le principe de Franck-Condon[32, 33]. Ce principe découle directement de l'approximation de Born-Oppenheimer[34] qui stipule que les électrons bougent beaucoup plus rapidement que les noyaux, ce qui implique que la fonction d'onde vibronique peut être écrite comme un produit des fonctions d'onde électronique et vibrationelle. Dans ce cas, la transition électronique se produit à une échelle de temps où les noyaux des atomes peuvent être considérés comme immobiles. On parle alors de transition verticale selon le principe de Franck-Condon. Cette transition est illustrée par la flèche verticale sur la Figure 1.3 et correspond au maximum de la bande d'absorption. L'enveloppe de la bande d'absorption pour cette situation est une distribution de Poisson dont la largeur dépend principalement de la grandeur de ΔQ. Si on observe la structure vibronique, l'écart entre les maxima est constant et correspond à la fréquence de vibration de l'état excité. Toutes les variables de l'équation 1.5 peuvent être déterminées directement à partir d'un spectre d'absorption de bonne qualité.

Dans les cas qui nous intéressent, les états électroniques ne sont pas isolés les uns des autres et plusieurs états excités rapprochés en énergie interagissent ensemble. Dans ce cas-ci l'approximation de Born-Oppenheimer n'est pas strictement observée. Pour deux états excités couplés la situation est décrite par un système de quatre courbes d'énergie potentielle qui sont désignés comme surfaces couplés à la

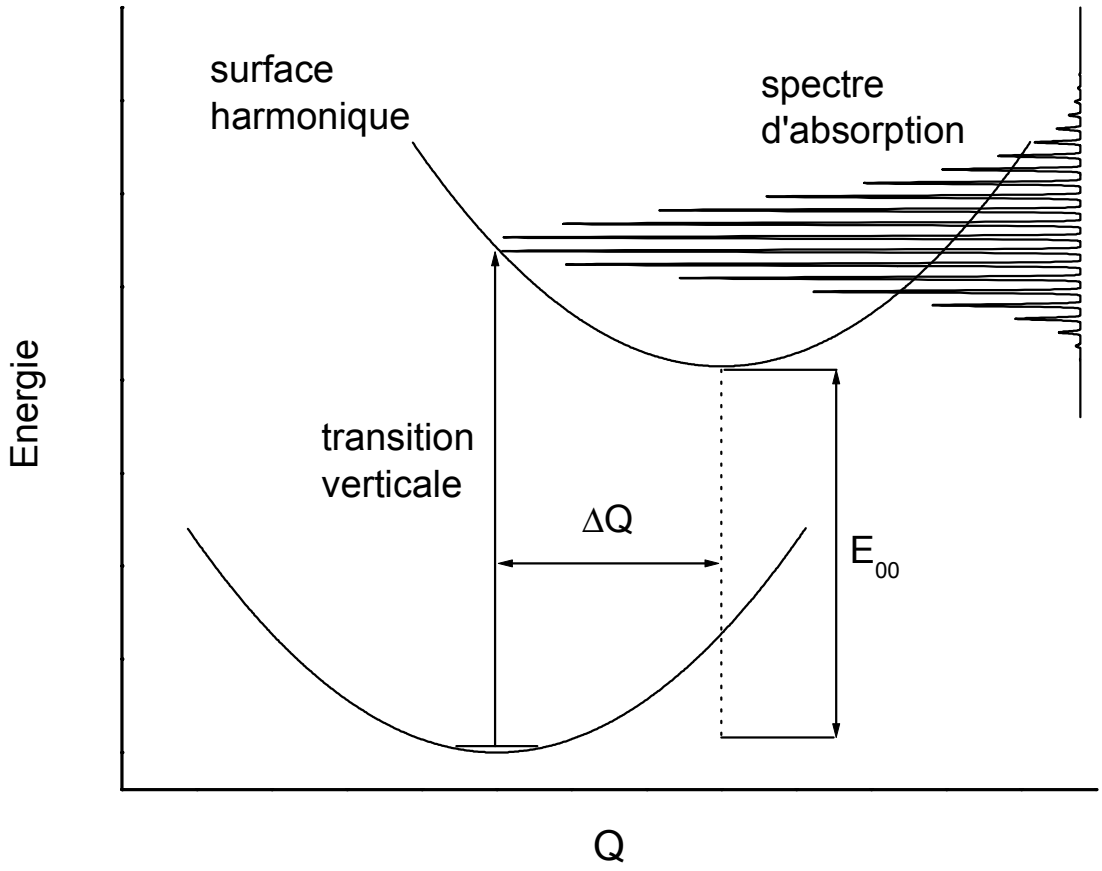

Figure 1.3 Spectre d'absorption calculé selon le principe de Franck-Condon avec des surfaces d'énergie potentielle harmoniques. Le décalage (ΔQ) le long d'une seule coordonnée normale Q et le concept de transition verticale sont illustrés. L'espacement entre les maxima du spectre d'absorption correspond à la fréquence vibrationnelle de la surface de potentiel harmonique de l'état excité. L'enveloppe de la bande est régulière et forme une distribution de Poisson.

Figure 1.4. Les courbes harmoniques en pointillé sont les éléments diagonaux d'un déterminant 2×2 dont les éléments hors-diagonaux correspondent à une constante de couplage tel que montré par l'équation 1.6. Les traits pleins sont les potentiels couplés et correspondent aux solutions du déterminant:

$$\begin{vmatrix} \frac{1}{2}k_1(Q-\Delta Q_1)^2 + E_{00(1)} - E_1 & V_{12} \\ V_{12} & \frac{1}{2}k_2(Q-\Delta Q_2)^2 + E_{00(2)} - E_2 \end{vmatrix} = 0 \qquad (1.6)$$

Les deux potentiels harmoniques sont définis par les mêmes variables que dans l'équation 1.5, en addition V_{12} est la constante de couplage. Cette équation est analogue à l'équation 1.3 où 4Dq est la constante de couplage. La différence la plus importante par rapport à l'équation 1.3 est que les énergies dépendent de la coordonnée Q. À l'instar de la théorie du champ des ligands, le mélange entre états n'est pas statique (ou constant) quand la molécule bouge. Comme le montre la Figure 1.4, l'enveloppe du spectre calculé pour ce modèle est très différente d'une distribution de Poisson et elle montre deux maxima, en ressemblance qualitative à la forme de la bande de l'encadré de la Figure 1.1. Les différences d'énergie entre les raies vibroniques du spectre calculé à haute résolution dans la Figure 1.4 ne correspondent plus simplement à la fréquence vibrationelle de l'état excité. L'étude et la compréhension de ces phénomènes sont présentées dans les chapitres 2 à 5.

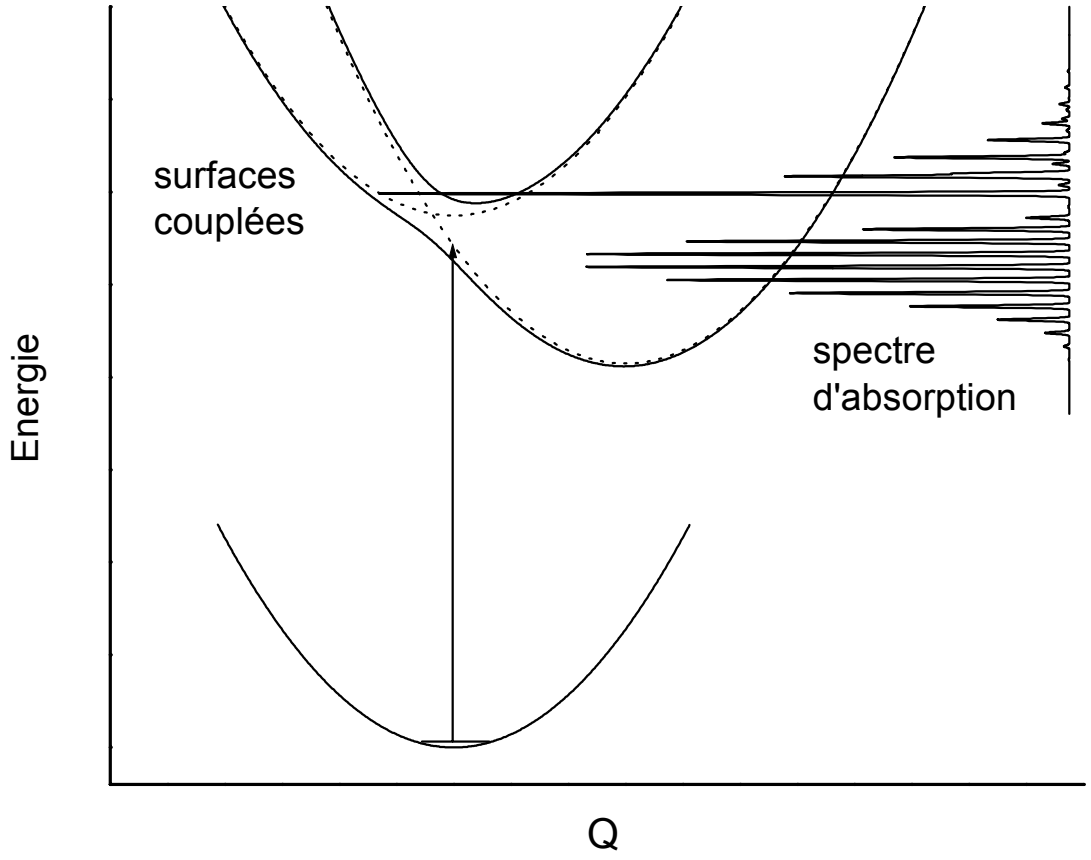

Figure 1.4 Spectre d'absorption calculé pour des surfaces d'énergie potentielle couplées. Les espacements entre les maxima du spectre d'absorption ne correspondent pas à la fréquence vibrationelle des surfaces harmoniques. La forme de la bande est irrégulière et comporte deux maxima séparés d'une région à très faible absorbance.

Dans un cas général on peut avoir *n* états électroniques interagissants. Dans ce cas on doit traiter *2n* surfaces d'énergie potentielle pour décrire correctement le système. En présence de ce système de surfaces d'énergie potentielle compliquées, le principe de Franck-Condon devient difficile à utiliser pour calculer le spectre résultant, parce qu'il faut calculer beaucoup de fonctions propres pour les puits couplés. Pour cette raison, et aussi pour pouvoir suivre l'évolution de notre modèle dans le temps, nous avons utilisé la théorie de la spectroscopie dépendante du temps[35] pour calculer les spectres d'absorption de systèmes couplés. Il s'agit d'une approche nouvelle en spectroscopie inorganique, qui illustre de façon très claire l'importance des différentes propriétés moléculaires, comme par exemple des changements des longueurs de liaison, des constantes de couplage spin-orbite ou des fréquences de vibration au cours d'une transition électronique.

1.4. Plan de la thèse

Nous avons, pour la première fois, utilisé le modèle quantitatif présenté de façon schématique à la Figure 1.4, combinant la théorie du champ des ligands et une théorie vibronique, pour expliquer la présence de deux maxima distincts dans le spectre d'absorption de la bande centrale du $[Ni(H_2O)_6]^{2+}$. Cette approche est présentée dans les chapitres 2 et 3. Nous commençons avec l'analyse du spectre du complexe $[Ni(H_2O)_6]^{2+}$ en solution à température ambiante qui montre le double maximum aussi observé dans l'encadré de la Figure 1.1, observation de base reconnue depuis longtemps en chimie de coordination. Le chapitre 3 confirme la validité du modèle pour analyser des spectres résolus. Les résultats de ces chapitres

montrent que le modèle résout deux problèmes classiques en spectroscopie inorganique: la présence d'un double maximum dans les spectres d'absorption de divers complexes du nickel(II) en solution et la présence d'antirésonances de Fano dans les spectres d'absorption de composés du chrome(III). Les analyses impliquent des spectres d'absorption polarisés de complexes ayant des symétries moléculaires différentes, comme décrit dans les chapitres 2 et 3.

Le modèle de la Figure 1.4 s'applique aussi aux spectres de complexes d'autres métaux de transition, qui ne montrent pas de double maximum évident comme les complexes du nickel(II). Ces résultats pour des complexes du vanadium(III), du cobalt(II) et du chrome(III) sont présentés au chapitre 4. Ces expériences démontrent que le modèle de la figure 1.4 peut être étendu à pratiquement tous les complexes des métaux de transition, mais nous avons aussi vu que d'autres phénomènes, par exemple l'effet Jahn-Teller, compliquent souvent l'interprétation des observations spectroscopiques. À partir des chapitres 2, 3 et 4, les manifestations spectroscopiques du couplage spin-orbite entre états électroniques sont analysés en profondeur.

Le chapitre 5 contient une analyse d'états électroniques couplés correspondant au croisement évité des deux états $^3T_1$ de la Figure 1.2. L'interaction entre ces deux états ne peut être caractérisée à partir des spectres d'absorption et nous utilisons des calculs *ab-initio*[36] pour mettre à terme cette analyse. Nous avons réussi à montrer les différents effets du couplage entre les états électroniques $^3T_1$ des complexes aquo du vanadium(III) (d^2) et du nickel(II) (d^8), ce qui nous a conduit à une meilleure compréhension de leur structure électronique. Ces calculs nous ont permis de montrer que les interactions entre états électroniques sont importantes, même pour des cas où les bandes d'absorption impliquant ces états ne montrent aucun recouvrement. Les

résultats de ce chapitre soulignent que l'attribution d'un seul état électronique à une bande d'absorption n'est souvent qu'une approximation imprécise.

Les chapitres 6 et 7 illustrent l'application des techniques de spectroscopie à deux catégories de matériaux différents des complexes des éléments de la série 3d. La première catégorie de matériaux que nous avons étudié sont des complexes des lanthanides avec des ligands nitronyl-nitroxyde qui sont des radicaux organiques. Ces composés sont d'intérêt à cause de leurs propriétés magnétiques provenant des électrons non pairés du centre métallique et des ligands[37, 38]. Le ligand ainsi que plusieurs des métaux utilisés ont des états excités dans le proche-IR et dans le rouge, de nouveau une situation où on peut s'attendre à des interactions entre états électroniques, mais cette fois les états sont centrés sur le métal et aussi sur les ligands, une différence importante par rapport aux situations examinées dans les chapitres 2 à 5. La structure vibronique des spectres d'absorption et de luminescence indique que cette interaction existe. Cette découverte est d'importance parce qu'elle démontre qu'il existe un lien entre les propriétés optiques (couleur, émission) et les propriétés magnétiques de ces matériaux.

La deuxième catégorie de matériaux que nous avons étudié a été choisie dans le but d'examiner les interactions entre états électroniques centrés sur plus de deux unités (ion métallique ou ligand) d'un solide. Dans le chapitre 6 nous présentons des spectres de luminescence, d'absorption et d'excitation d'agrégats de silicium, où le nombre d'atome formant l'agrégat et définissant sa taille détermine les propriétés optiques[39, 40].

Pour ces deux catégories de matériaux inorganiques modernes, nous identifions expérimentalement les phénomènes causés par les états électroniques en interaction.

À ce jour, aucun modèle quantitatif de même profondeur que ceux pour les complexes analysés dans les chapitres 2 à 5 n'est disponible.

Nous verrons donc dans cette thèse que les modèles traditionnels sont insuffisant pour expliquer adéquatement la structure électronique des molécules et matériaux inorganiques. Des modèles plus performants sont nécessaires en vue de comprendre leur structure électronique et éventuellement de contrôler leurs propriétés chimiques et physiques. La spectroscopie détaillée et les modèles avancés sont d'importance pour le développement de nouveaux matériaux ayant des propriétés magnétiques et optiques désirables, ce qui est un domaine très actif de la recherche moderne.

1.5. Techniques utilisées

En solution et à la température de la pièce, une analyse approfondie des bandes avec les modèles présentés aux Figures 1.3 et 1.4 n'est souvent pas possible, car en général seule l'enveloppe non résolue de la bande est observée dans ces conditions. L'analyse détaillée nécessite des spectres d'absorption de cristaux mesurés à l'aide de lumière polarisée et à des températures inférieures à 20 K pour observer les progressions vibroniques d'un spectre d'absorption. Ceci est illustré par les spectre du complexe *trans*-$[CoCl_2(H_2O)_4]$ de la Figure 1.5. Les énergies et intensités des bandes sont très différentes selon la polarisation de la lumière qui peut être parallèle (π) ou perpendiculaire (σ) à la direction des liens Co-Cl. On voit que la spectroscopie d'absorption à basse température donne énormément d'informations sur la structure

électronique et vibrationnelle de ce complexe. Le spectre à haute température est beaucoup moins résolu, particulièrement pour ce qui est de la bande de la Figure 1.5 centrée à 26000 cm^{-1}. Cette bande montre également un exemple typique d'une progression vibronique qui apparaît à basse température (20 K), mais qui est absente à 200 K. On peut voir sur la même figure un exemple typique de polarisation: La bande centrée à 22500 cm^{-1} n'apparaît que dans le spectre en π et est pratiquement absente en σ. Les maxima des bandes sont bien reproduits par la théorie du champ des ligands, comme indiqué par les lignes verticales en haut des bandes.

Les interactions entre états électroniques du complexe *trans*-$[CoCl_2(H_2O)_4](H_2O)_2$ peuvent, en principe, aussi être étudiées par spectroscopie RPE et par mesures de la susceptibilité magnétique. En symétrie idéalisée (groupe ponctuel O), l'état fondamental $^4T_1$ (^4F) est en interaction avec l'état excité $^4T_1$ (^4P). Cette situation correspond au croisement évité des deux états $^3T_1$ dans la Figure 1.2 et les méthodes magnétiques pourraient nous donner des renseignements supplémentaires sur cette interaction. Les Figures 1.5 à 1.7 illustrent les avantages de la spectroscopie d'absorption à l'état solide et à basse température par rapport à la spectroscopie RPE et aux mesures de susceptibilité magnétique. Les Figures 1.6 et 1.7 montrent les spectres RPE et les mesures de la susceptibilité magnétique d'un monocristal orienté, du même composé. Cette comparaison souligne encore que la spectroscopie optique est la méthodologie à choisir pour nos buts. Le signal RPE à 40 K est faible en raison de la relaxation rapide du spin électronique. Il atteint une intensité maximale à 20 K.

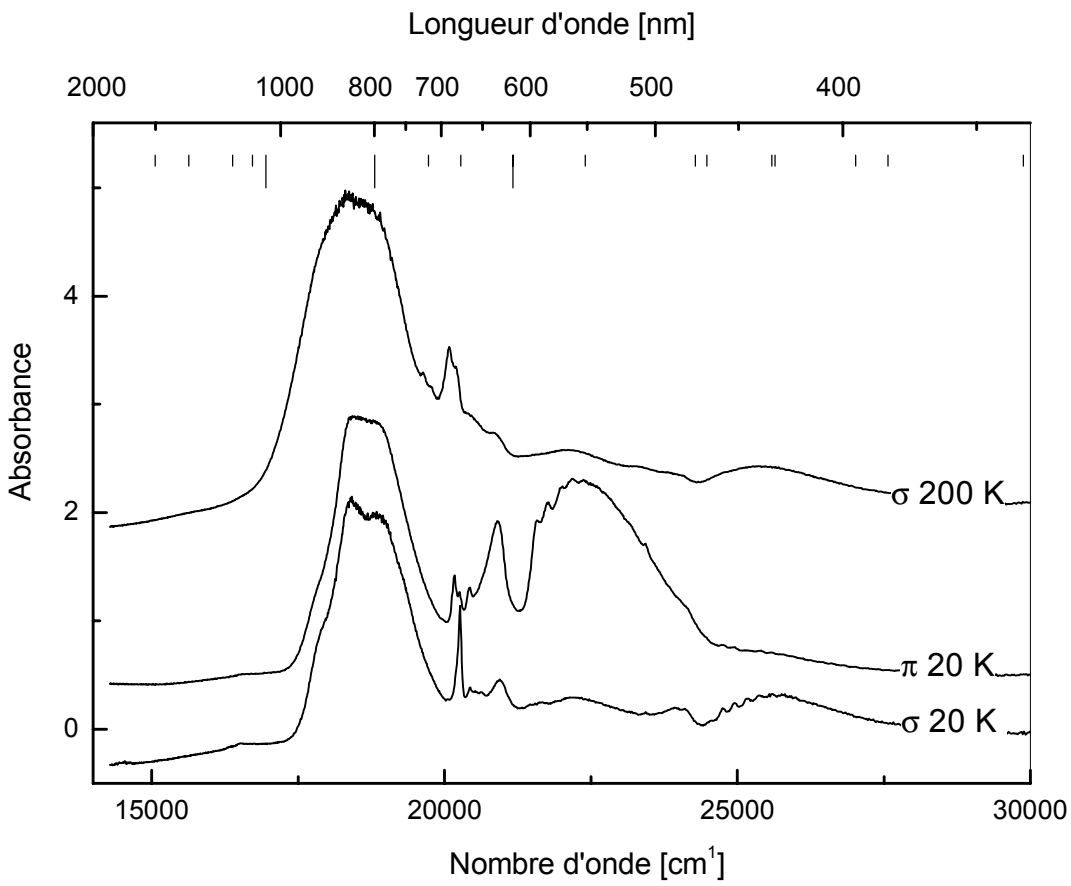

Figure 1.5 Spectres d'absorption polarisés de *trans*-$[CoCl_2(H_2O)_4](H_2O)_2$ à différentes températures. Les états électroniques calculés avec la théorie du champ des ligands sont représentés par des traits verticaux. Les traits longs représentent les états quadruplets (transitions permises par le spin) et les traits courts les états doublets (transitions interdites par le spin). On peut remarquer que la résolution vibronique autour de 25000 cm^{-1} apparaît seulement à basse température. Ce spectre est discuté plus en détail au chapitre 4.

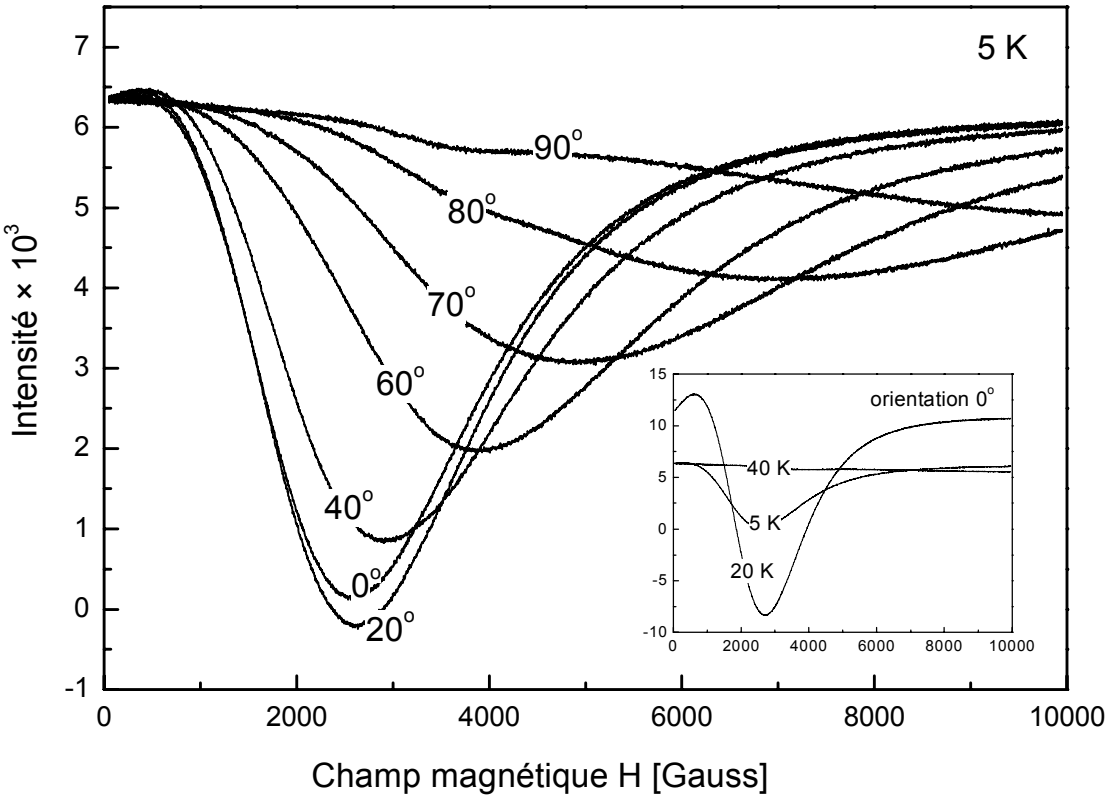

Figure 1.6 Spectre RPE d'un cristal orienté de $[CoCl_2(H_2O)_4](H_2O)_2$ à 5 K. L'angle entre le champ magnétique et l'axe cristallographique c est indiqué sur chaque courbe. Le panneau intérieur montre la variation du signal RPE avec la température pour l'orientation 0º. Le signal à 40 K est faible en raison de la relaxation rapide du spin électronique. Le signal atteint une intensité maximale à 20 K, la diminution de l'intensité à 5 K est due à un ordre antiferromagnétique à basse température dans le solide[41].

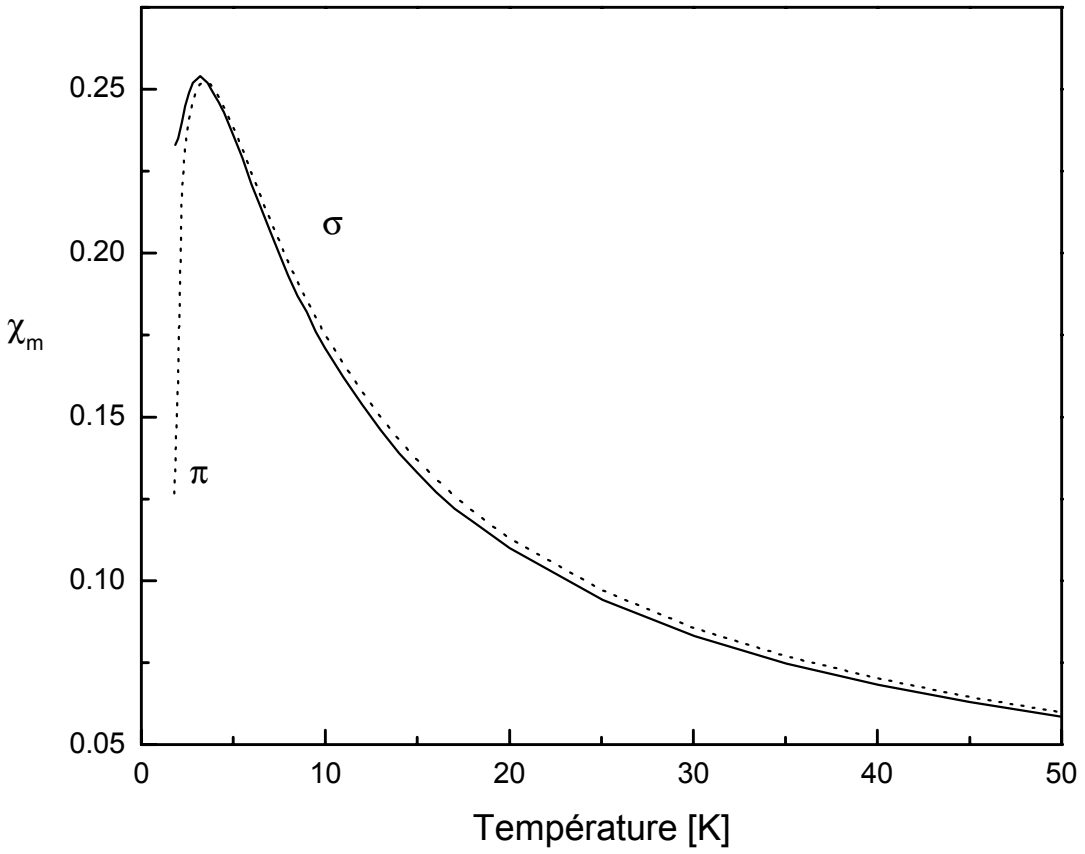

Figure 1.7 Mesures de la susceptibilité magnétique sur un cristal orienté de $[CoCl_2(H_2O)_4](H_2O)_2$ à 5 K. On voit le comportement magnétique différent pour deux orientations du champ magnétique, parallèle à l'axe à (π) et parallèle à l'axe b (σ). Le moment magnétique pour un champ perpendiculaire a l'axe c est plus faible [41], ce qui correspond au signal RPE plus faible à 90º de la Figure 1.6.

La diminution de l'intensité à 5 K est due à un ordre antiferromagnétique à basse température[41]. Ces spectres montrent donc beaucoup moins de détails que les spectres d'absorption. Les mesures de la susceptibilité magnétique dans la Figure 1.7 montrent que pour un champ perpendiculaire à l'axe c le moment magnétique est plus faible [41], ce qui correspond au signal RPE faible (90º) de la Figure 1.6.

La théorie du champ des ligands permet de faire le lien entre la spectroscopie optique et les mesures magnétiques, mais ces dernières ne fournissent pas assez d'information pour déterminer tous les paramètres nécessaires, comme illustré par l'exemple des Figures 1.5 à 1.7. Les mesures de susceptibilité magnétique ne fournissent qu'une quantité déterminé par le moment magnétique de l'état fondamental, qui contient beaucoup moins d'information qu'un spectre. La spectroscopie RPE ne montre pas une résolution suffisante pour détecter l'influence de l'interaction entre états électroniques. L'avantage principal de la spectroscopie optique est qu'elle nous permet de caractériser avec une bonne résolution l'état fondamental et les états excités. La spectroscopie optique s'avère une bonne méthode, très polyvalente et puissante pour étudier des interactions entre états électroniques, le sujet central de cette thèse.

Chapitre 2: Effets du couplage entre états électroniques sur des bandes d'absorption peu résolues en solution et dans des verres dopés.

Table des matières

2.1. Pourquoi la deuxième bande d'absorption dans le spectre du $Ni(H_2O)_6^{2+}$ a-t-elle deux maxima?

Why does the middle band in the absorption spectrum of $Ni(H_2O)_6^{2+}$ have two maxima?

Myriam Triest, Guillaume Bussière, Hugo Bélisle and Christian Reber

J. Chem. Ed. **2000**, *77*, 670
http://jchemed.chem.wisc.edu/JCEWWW/Articles/index.html

Abstract

The absorption band shape observed for the $^3A_{2g} \rightarrow {}^3T_{1g}(^3F),{}^1E_g$ crystal field transitions in the absorption spectrum of $Ni(H_2O)_6^{2+}$ is analyzed with a time dependent theoretical model and visualized in this electronic publication. The importance of fast intersystem crossings is illustrated by the model, as is the influence of the positions of the excited state potential energy surfaces, both along the energy and the normal coordinate axes. The model quantitatively reproduces the experimental spectrum between 550 nm and 900 nm and illustrates the important symmetry and bonding information that can be obtained from electronic spectra of transition metal compounds.

Introduction

The absorption spectra of octahedral complexes of nickel(II) are often used to illustrate basic aspects of metal-ligand bonding in coordination compounds. A number of practical guides for the analysis of such spectra in order to determine crystal field parameters or the equivalent quantities in the angular overlap molecular orbital model have been published[1, 2]. The band maxima of the spin allowed transitions are used to determine 10Dq and B and the spectrochemical series can be established from a comparison of absorption maxima for a series of compounds[3]. The goal of this work is to extend the traditional crystal field analysis and to give the undergraduate student an opportunity to explore quantitative models linking point group symmetry, electronic states and potential energy surfaces. Octahedral nickel complexes are well suited for this purpose as group theory provides a full description of their electronic states in the energy range of the absorption spectra[4]. The concept of molecules moving on one or several potential energy surfaces is important for many areas of chemistry; examples include detailed reaction dynamics[5] and electron transfer processes[6], where multiple potential energy surfaces similar to those presented in the following, are essential.

An aspect of the absorption spectra of some octahedral nickel(II) complexes that is discussed only in a very cursory manner in the standard texts concerns the shape of the absorption bands, leading to the following questions from our undergraduate students:

Why does the "middle" band in the absorption spectrum of $Ni(H_2O)_6^{2+}$ have two maxima (or a maximum and a shoulder), but only a single maximum for many other octahedral complexes, such as $Ni(NH_3)_6^{2+}$? And why do the other two bands have only one maximum?

The neglect of this spectroscopic observation in the conventional crystal field approach leaves a taste of lax analysis of experimental data, and we have not found a rigorous literature illustration of its physical origin suitable for undergraduate students. Several inorganic textbooks offer diverging discussions on the subject, as documented by an extensive set of references in a recent publication[7]. A very short assessment is given by Cotton and Wilkinson[8], assigning the bandshape to two energetically close excited states. We present in the following a full quantitative model that will allow us to calculate the band shape and characterize the two states. The double maximum is a consequence of interacting electronic states with potential energy surfaces crossing in the Franck-Condon region of the absorption spectrum.

Our model was developed for and rigorously tested against highly resolved polarized low-temperature absorption spectra of a series of nickel(II) complexes with octahedral, tetragonal and trigonal point group symmetry[7] and it is applied here to less resolved solution spectra. Even without a detailed understanding of the underlying theory, undergraduate students can use the Quicktime animations to explore the processes that define bandshapes.

Figure 2.1.1 presents absorption spectra of two octahedral nickel(II) complexes measured in our undergraduate coordination chemistry laboratory on a Varian Cary 5E spectrometer. The three spin allowed bands are clearly visible for both

compounds, and their maxima are used to determine 10Dq and B. The triplet excited states are easily assigned with a Tanabe-Sugano diagram for the d^8 electron configuration, as shown in Figure 2.1.2. Some absorption bands (most notably the highest energy $^3A_{2g} \rightarrow {}^3T_{1g}(^3P)$ bands) have only a single maximum for octahedral complexes of nickel(II), others, especially the "middle" $^3A_{2g} \rightarrow {}^3T_{1g}$ (^3F) band in spectra of nickel(II) complexes with halide or oxygen ligands, show a more complicated band shape with two maxima. This can be clearly seen in the spectrum of $Ni(H_2O)_6^{2+}$. Shoulders are sometimes observed in the lowest energy $^3A_{2g} \rightarrow {}^3T_{2g}$ band of complexes with nitrogen donor ligands[9]. A comparison of the experimental spectra with the Tanabe-Sugano diagram reveals that double maxima are observed for situations in the neighborhood of a crossing of the lowest-energy singlet excited state with the first or second triplet excited states. This situation will be investigated in the following.

Experimental Results

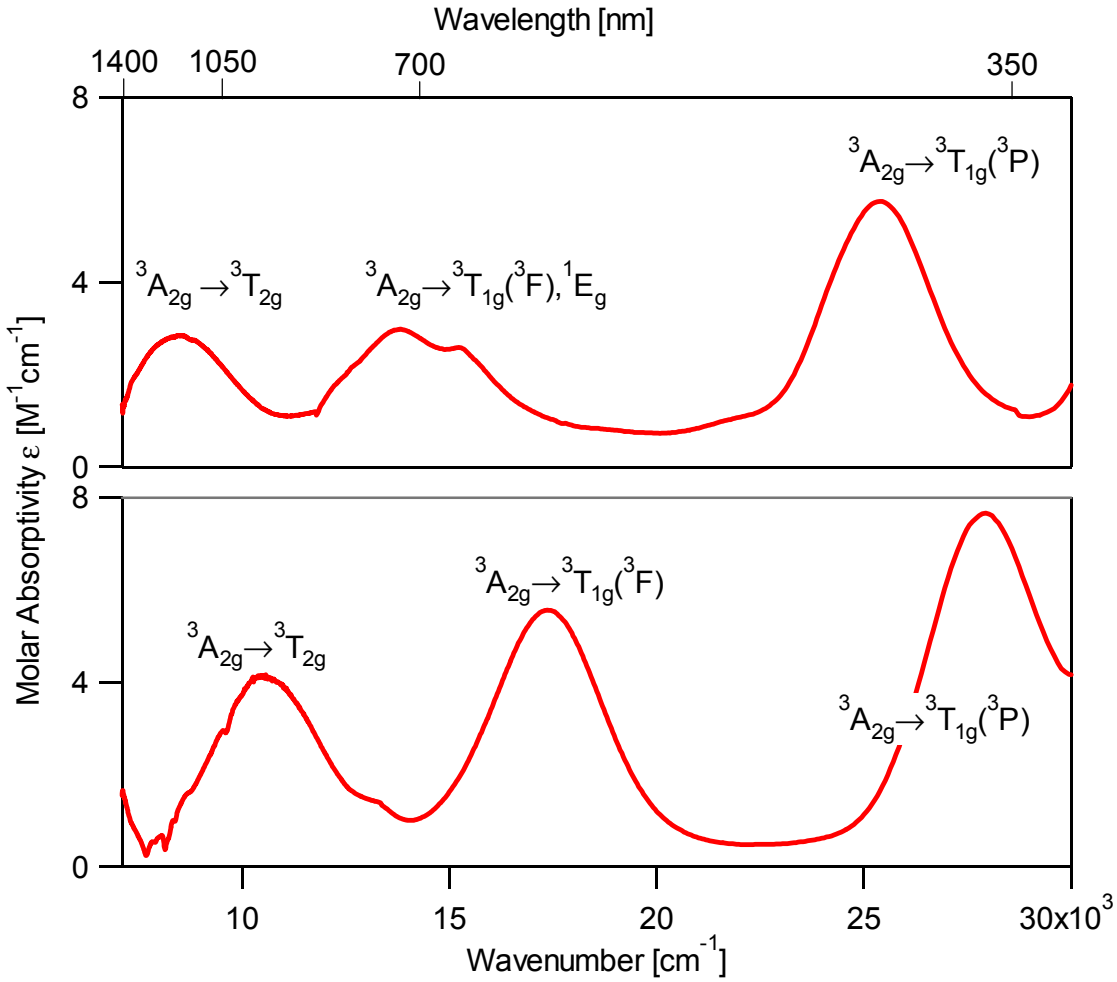

Figure 2.1.1 Absorption spectra showing all three spin allowed crystal field bands of $Ni(H_2O)_6^{2+}$ (upper trace, 0.101 M in aqueous solution) and $Ni(NH_3)_6^{2+}$ (lower, 0.315 M in aqueous NH_3 solution). Band assignments are given as illustrated in the Tanabe-Sugano diagram in Figure 2.1.2.

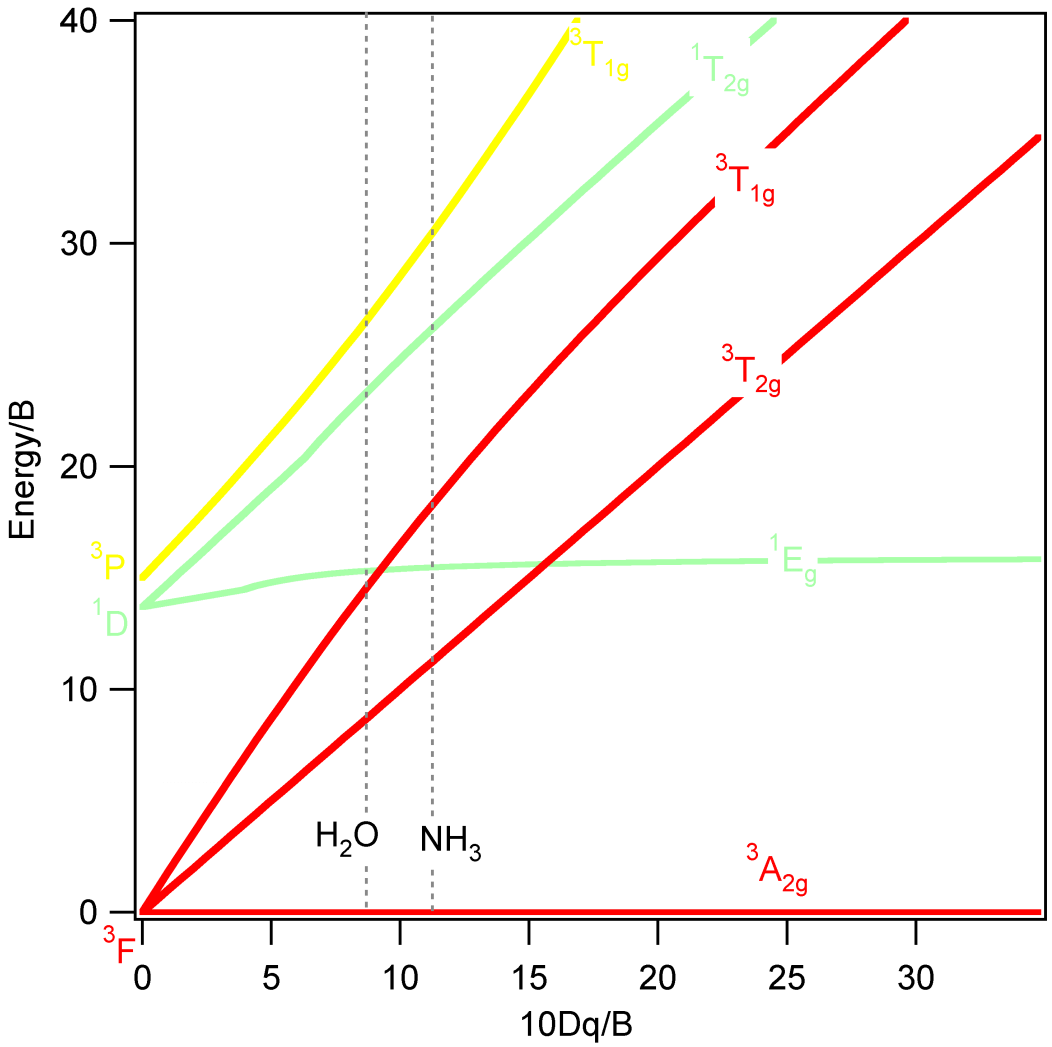

Figure 2.1.2 Tanabe-Sugano diagram for octahedral nickel(II) complexes. The bands observed in Figure 2.1.1 are shown as dotted lines for both complexes.

Theoretical Background

The three spin-allowed electronic transitions observed for nickel(II) complexes in Figure 2.1.1 are very broad, indicating that the molecules undergo important structural changes in the course of the electronic transition. This observation is easily rationalized with the overall bonding or antibonding character of the electron configurations from which the states arise: excited electronic states with a higher population of the σ-antibonding e_g orbitals are expected to have longer Ni^{2+} - ligand bond lengths than the ground state. These bond elongations result in broad absorption bands. In contrast, transitions to excited states arising from the same electron configuration as the ground state, with almost unchanged Ni^{2+} - ligand bond lengths, lead to narrow bands in the absorption spectrum. Often both types of bands can be observed experimentally[10]. The traditional quantitative approach to analyze band shapes in absorption spectra involves the Franck-Condon principle and overlap integrals of vibrational eigenfunctions, an approach based on the time-independent theory of spectroscopic transitions. This approach is easily applied to harmonic potential energy surfaces, but it becomes less obvious for situations with nonharmonic potentials and multiple states that have to be considered simultaneously, as is the case for the spectra in Figure 2.1.1.

Modern microcomputers have made an alternative, time-dependent approach feasible. In this approach, the evolution of the initial-state eigenfunction on the potential energy surface of the final state is calculated, providing an intuitively appealing picture of the behavior of a molecule that absorbs light. This approach is

compared to the standard Franck-Condon theory in a recent electronic publication in this journal[11]. The most important quantity for the calculation of an absorption spectrum is the time-dependent autocorrelation function $<\phi|\phi(t)>$, corresponding to the overlap of the wavefunction at time zero (ϕ) with the wavefunctions that evolve on the potential energy surfaces ($\phi(t)$). The Fourier-transform of the autocorrelation to the frequency domain is the calculated spectrum. The theoretical equations have been described in detail[12, 13]. Numerical algorithms to solve the time-dependent Schrödinger equation and to calculate the time-dependent wavefunction on potential surfaces have also been described in this journal before[14].

The first Quicktime animation illustrates the time-dependent approach to an absorption transition between one-dimensional harmonic potential energy surfaces. The vibrational motion of the wavefunction $\phi(t)$ is easily followed in Figure 2.1.3. The absolute value of the autocorrelation $|<\phi|\phi(t)>|$ is shown as a yellow trace in Figure 2.1.3. It decreases as the wavefunction $\phi(t)$ moves away from its initial position ϕ, then reaches a maximum after each vibrational period when returning to its starting position. All autocorrelation functions in the following are multiplied by a phenomenological damping factor that decreases their value with increasing time, leading to maxima in Figure 2.1.3 that are becoming smaller with time. The damping factor chosen for Figure 2.1.3 determines the width of each peak in the highly resolved calculated spectrum in Figure 2.1.4. A larger value leads to the calculated band without resolution, also included in Figure 2.1.4, representing a typical solution spectrum. It is obvious from this Figure that the damping factor does not change the

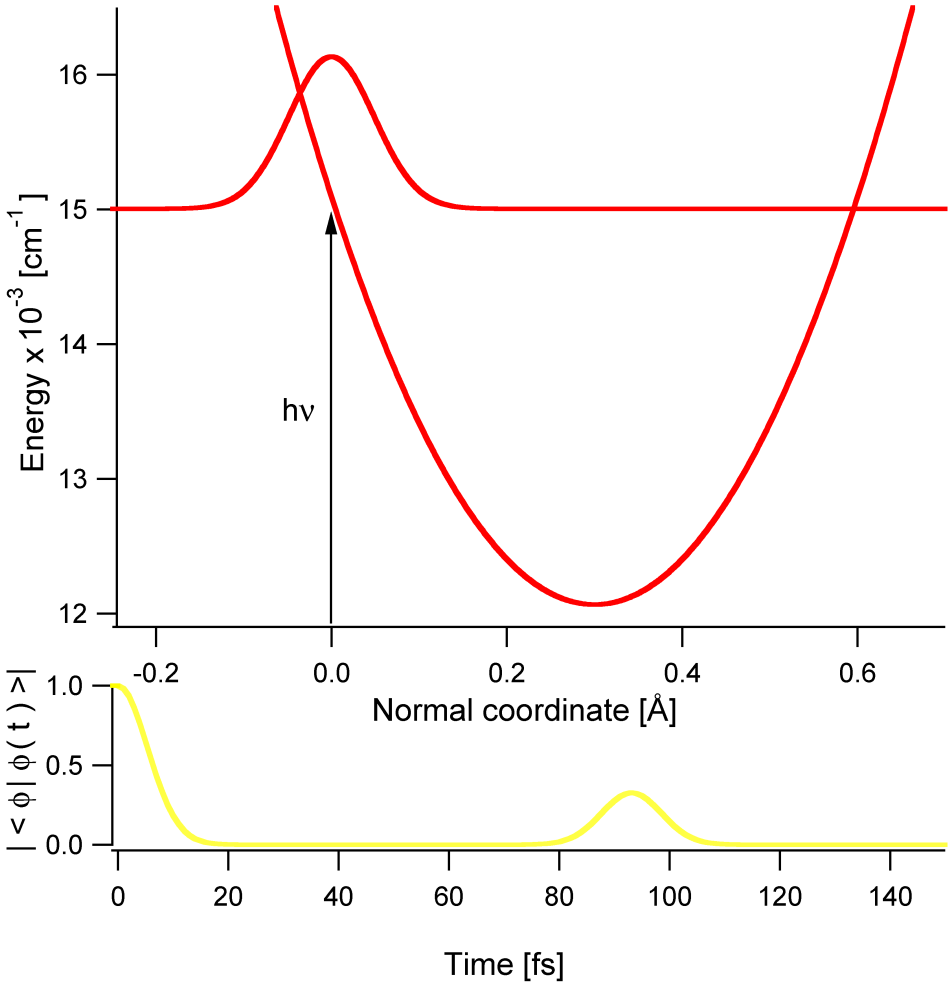

Figure 2.1.3 Animation of an electronic absorption transition between two harmonic surfaces. The top panel shows the time-dependent wavefunction $\phi(t)$ on the potential energy surfaces of the excited state, the bottom panel shows the absolute value of the autocorrelation function $|\langle\phi|\phi(t)\rangle|$ as a function of time. This quantity corresponds to the overlap of the time-dependent wavefunction $\phi(t)$ with the wavefunction ϕ at 0 fs. The time interval between frames is 1 fs.

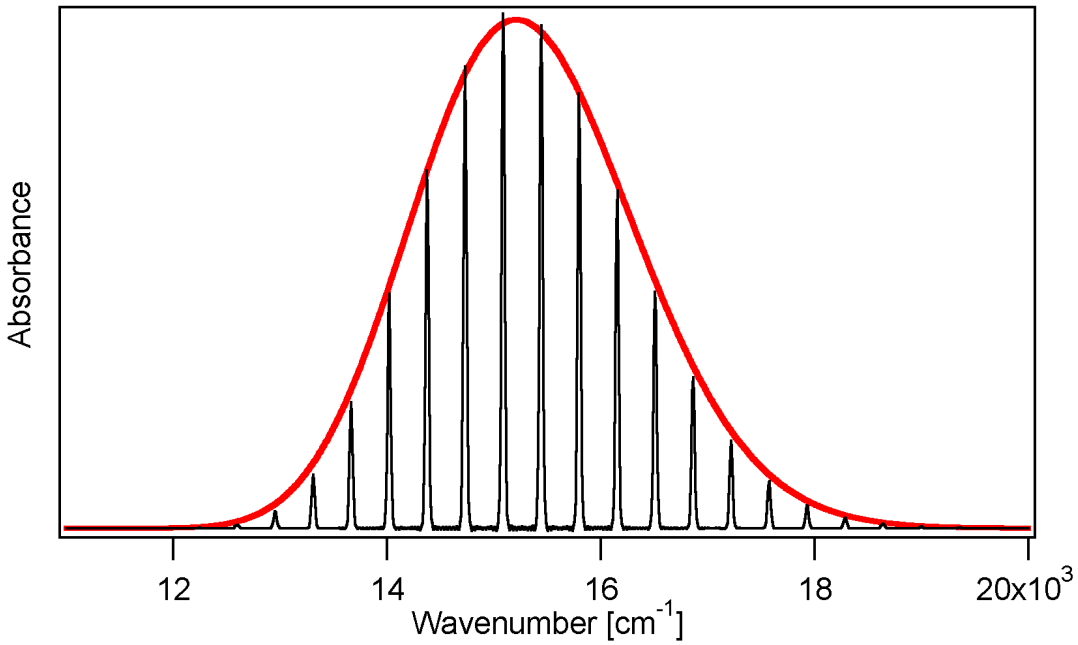

Figure 2.1.4 Calculated absorption spectra from the model in Figure 2.1.3. This spectrum was obtained by a Fourier transform of the autocorrelation in Figure 2.1.3. The resolved spectrum shows the vibronic structure of the band, the unresolved spectrum reproduces a typical solution absorption spectrum, such as the examples in Figure 2.1.1.

total width or overall envelope of the absorption spectrum, quantities that are entirely determined by the potential energy surfaces. The simple model involving only one excited state potential energy surface is appropriate for all absorption bands showing a single maximum in Figure 2.1.1.

Model calculations for $Ni(H_2O)_6^{2+}$ and $Ni(NH_3)_6^{2+}$

In this section, we focus on models analogous to those in Figure 2.1.3, but adapted to the situations for the "middle" absorption bands of $Ni(H_2O)_6^{2+}$ and $Ni(NH_3)_6^{2+}$, shown in Figure 2.1.1. The values of 10Dq and B obtained from the band maxima allow us to calculate the energies of all crystal field excited states of the complexes held "frozen" at their ground state equilibrium geometry. The calculations therefore give not only triplet but also singlet excited state energies, and we notice that for $Ni(H_2O)_6^{2+}$ the $^3T_{1g}(^3F)$ state is close to the lowest-energy singlet electronic state, ^1E_g. The energy separation of these two states is much larger for $Ni(NH_3)_6^{2+}$. The crystal field energies can be used to place the complexes along the horizontal axis of Figure 2.1.2.

A more detailed view of the electronic states of interest is given in Figure 2.1.5a. Spin-orbit coupling separates the $^3T_{1g}$ state into A_{1g} , E_g , T_{1g} and T_{2g} levels. A second E_g level arises from the ^1E_g excited state. The avoided crossing between the two E_g levels is caused by an off-diagonal matrix element, given in eq. 2.1.1, which depends on λ, the spin orbit coupling constant. The literature value of λ is -270 cm^{-1} for $Ni(H_2O)_6^{2+}$[15]. Spin-orbit coupling is not expected to influence metal-ligand

bond lengths and therefore all potential energy surfaces arising from $^3T_{1g}$ have their minima at the same position along Q. Molecular structures in excited states are often different from the ground state, leading to minima of excited state potentials that do not coincide with the ground state potential minimum. The minimum of the $^3T_{1g}$ excited state is at a larger value of Q than the minima of the ground state and the ^1E_g excited state, a direct consequence of the increased population of the σ-antibonding e_g orbitals in the triplet excited state. The $^3A_{2g}$ ground state and the lowest-energy singlet excited state arise from the same electron configuration and are therefore expected to have very similar bond lengths, leading to potential minima at the same value of Q, as shown in Figure 2.1.5b.

Of particular interest is the avoided crossing between the two E_g states. We describe their coupled potentials V_{E_g} as:

$$V_{E_g} = \begin{bmatrix} \frac{1}{2}K_S Q^2 + E_S & -\sqrt{6}\lambda \\ -\sqrt{6}\lambda & \frac{1}{2}K_T\left(Q_{a_{1g}} - \Delta Q_T\right)^2 + E_T \end{bmatrix} \qquad (2.1.1)$$

These potential energy surfaces are shown in Figure 2.1.5b for $Ni(H_2O)_6^{2+}$. The abscissa Q denotes the totally symmetric breathing mode of the octahedral complex. The origin of this axis is at the ground state equilibrium geometry. Experimental vibrational energies were used to calculate the force constants k_S and k_T of the harmonic potentials for the E_g states arising from the singlet (subscript S) and triplet

(subscript T) states, respectively. Their offsets E_S and E_T along the energy axis and the offset ΔQ along Q for the E_g level arising from the triplet excited state were adjusted to fit the experimental spectrum[7].

The absorption spectrum in the region of the middle band of $Ni(H_2O)_6^{2+}$ is a superposition of several transitions. The transitions to the A_{1g}, T_{1g} and T_{2g} states correspond exactly to the situation illustrated in Figures 2.1.3 and 2.1.4. The spectra for these transitions can therefore be easily calculated with the model in Figure 2.1.3. The situation is more complicated for the two potential energy surfaces describing the coupled E_g states arising from $^3T_{1g}$ and ^1E_g, respectively. These states are coupled by the off-diagonal matrix element in eq.2.1.1 and their potential energy surfaces have to be considered simultaneously in order to understand the observed absorption spectrum. The effects of coupling influence the absorption spectrum and lead to the double maximum measured for $Ni(H_2O)_6^{2+}$. The calculation of absorption spectra for these coupled surfaces is outlined in the following.

The potential energy surfaces for the coupled states are shown in Figure 2.1.5b. The first panel of this Figure shows harmonic surfaces for the singlet (gray) and triplet (black) excited states, not including any coupling. The second panel shows the surfaces that include the coupling, the adiabatic surfaces. It is important to realize that the singlet and triplet character of these surfaces changes along Q, as illustrated by the color change from gray to black. The comparison of the first two panels shows directly which character dominates the adiabatic surface for each value of Q. The full (combined) description of the model for two coupled electronic states is shown in the third panel of Figure 2.1.5b, and we will use this model for our calculations.

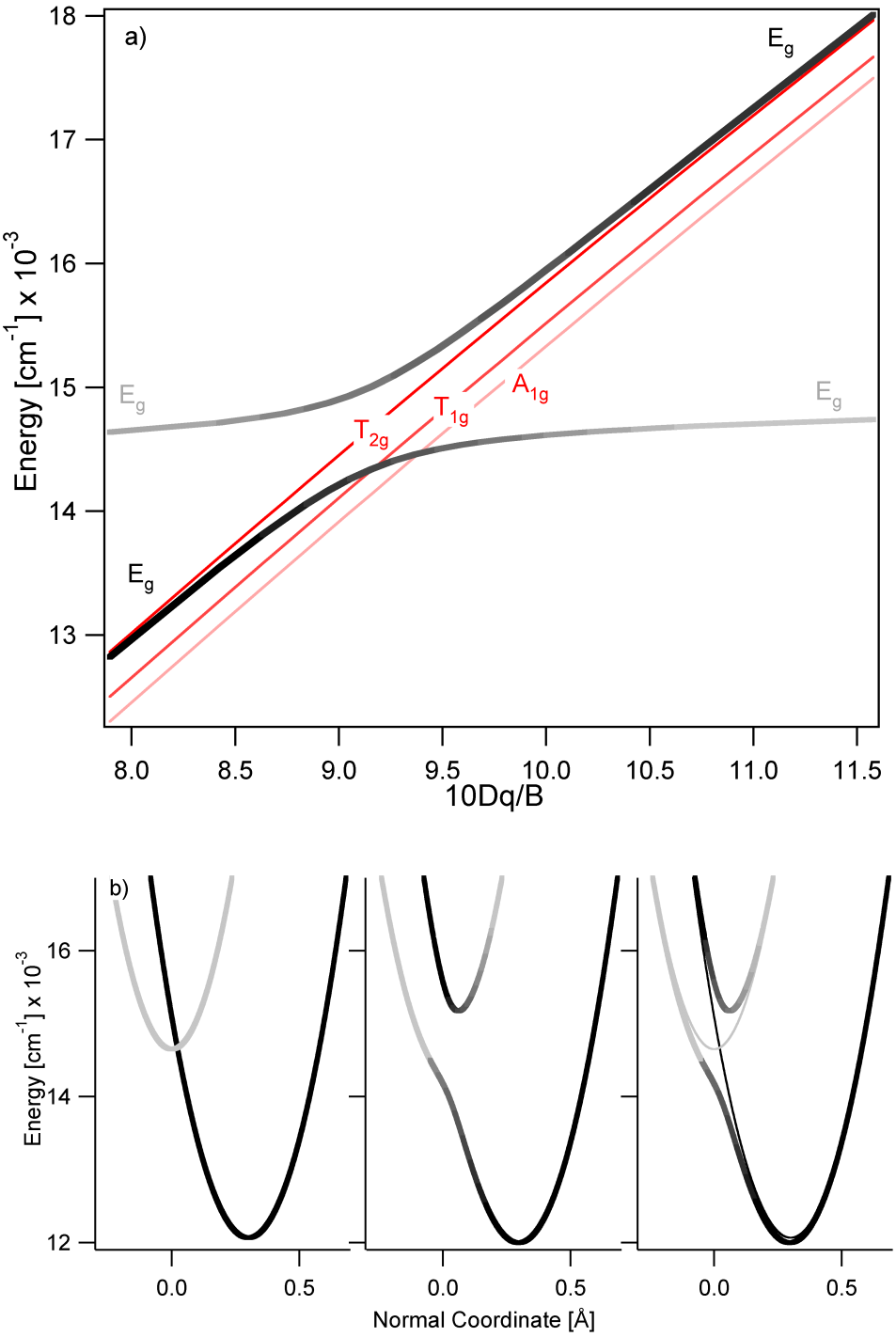

Figure 2.1.5 a) Calculated energy levels in the region of the $^3T_{1g}$, ^1E_g crossing. b) Coupled potential energy surfaces for the E_g (^1E_g) and E_g ($^3T_{1g}$) electronic states of $Ni(H_2O)_6^{2+}$.

The calculation of the spectrum involves an allowed electronic transition to the $^3T_{1g}$ excited state and a forbidden transition to the ^1E_g excited state. We assume for simplicity that all transitions are parity allowed by the same enabling mode of ungerade parity, not explicitly included in the model presented here. A full discussion of the intensity mechanisms is given elsewhere[7]. The model for $Ni(H_2O)_6^{2+}$ is shown in Figure 2.1.6. At t=0, the molecule is completely described by the wavefunction on the triplet surface. The amplitude on the singlet surface, is exactly zero because the transition to the singlet state is spin-forbidden. The evolution of the wavefunction and autocorrelation can be followed by playing the movie. It is obvious that there is very important amplitude transfer between the surfaces even at very short times. This is easily analyzed by following the evolution of the wavefunction frame by frame. We used 1 fs time intervals in the production of all Quicktime animations. At 0 fs, all amplitude is on the triplet surface. Approximately 5-10 fs later, the singlet surface has gained significant amplitude, an effect that leads to a steep drop of the autocorrelation function. At 18 fs, some of this amplitude has returned to the triplet surface, leading to a bump in the autocorrelation, which is not observed if only one potential energy surface is involved (Figure 2.1.3). The autocorrelation then drops to zero as wavefunction amplitude moves away from the initial region and only very little amplitude transfer occurs, as most amplitude is far from the region where the potential energy surfaces cross or change color. Important amplitude transfer occurs again after approximately one vibrational period, when the wavefunctions are again approaching this region.

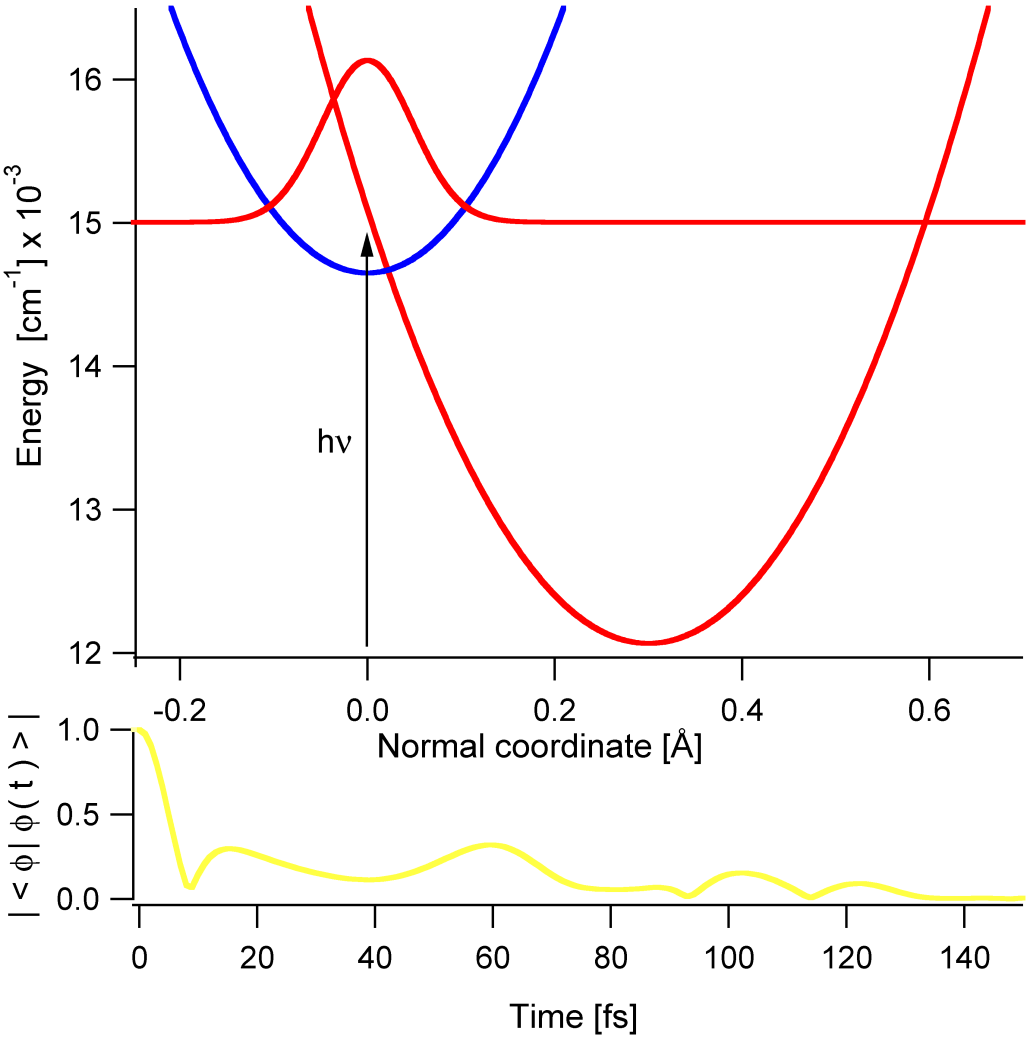

Figure 2.1.6 Time dependent wavefunctions $\phi(t)$ on the coupled surfaces of $Ni(H_2O)_6^{2+}$. The bottom panel shows the absolute value of the autocorrelation $|\langle\phi|\phi(t)\rangle|$.

The calculated absorption spectrum for this model is shown in Figure 2.1.7. The unresolved calculated spectrum consists of two bands with different maxima, the resolved calculated spectrum shows a much more complicated pattern of lines than the calculated spectrum in Figure 2.1.4. From the potential energy surfaces in Figure 2.1.5 we note that the maximum at higher energy qualitatively corresponds to levels in the narrow upper adiabatic surface. The broader band at lower energy corresponds to transitions to levels within the broad lower energy adiabatic surface. Model calculations on highly resolved single crystal spectra have confirmed this observation[7]. We note from the nature of the adiabatic surfaces that it is impossible to attribute meaningful singlet or triplet labels to each of the two absorption maxima, a finding that is emphasized by the varying color along each adiabatic surface in the Franck-Condon region. The intensity of the higher energy band is much too high for a formally spin-forbidden transition, but its width is relatively small, as expected for a transition to the undisplaced singlet state. The intensity of the lower energy band is too low for a spin-allowed transition, but the band is broad, as expected for a transition to the triplet surface which is displaced along the Q axis by ΔQ. This calculated spectrum shows that it is important to note which aspects of the experimental spectra have been used to assign labels of excited states to observed bands.

The total calculated spectrum is the sum of the spectra obtained for the transitions to each of the excited states in Figure 2.1.5a. The calculated spectra were normalized and then multiplied by the degeneracy of the final state. A degeneracy of 2 was used for the spectrum arising from the coupled E_g states, because intensity only

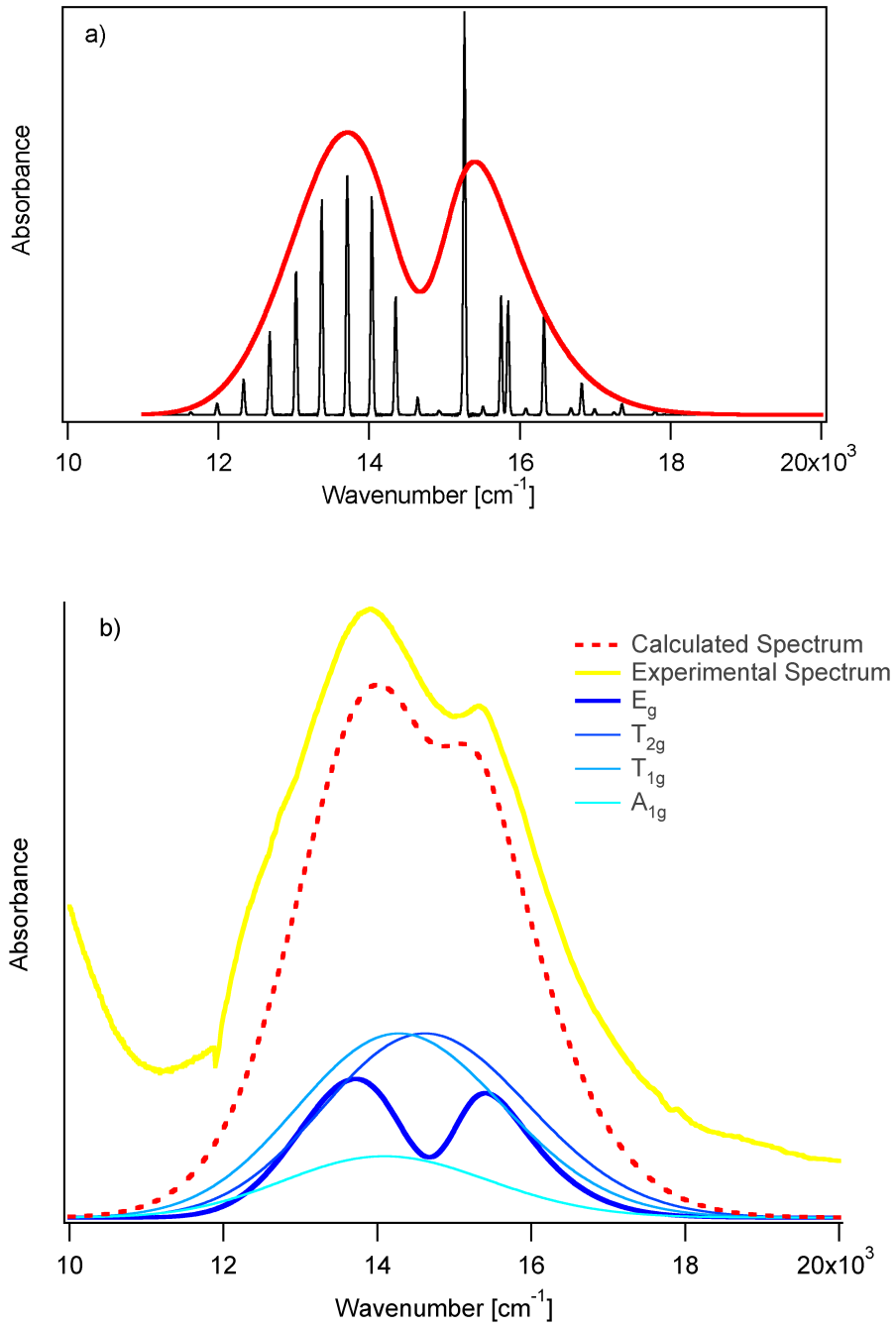

Figure 2.1.7 a) Calculated absorption spectrum for the transition to the two coupled E_g states of $Ni(H_2O)_6^{2+}$. b) Calculated absorption spectrum to all levels of the $^3T_{1g}$ / ^1E_g manifold shown in Figure 2.1.5a. The top trace shows the experimental spectrum for comparison.

arises from the E_g ($^3T_{1g}$) level. The sum of all the calculated absorption spectra was then scaled to the experimental molar absorptivity. The agreement between calculated and experimental spectra is very good and supports our model. The double maximum observed for $Ni(H_2O)_6^{2+}$ arises from the coupled E_g states because their potential energy surfaces cross in a region that is very close to the starting position of the wavefunction at 0 fs. This leads to important amplitude transfer at very short times, a new maximum in the autocorrelation and two maxima in the calculated absorption spectrum.

The third situation illustrated is the middle absorption band of the $Ni(NH_3)_6^{2+}$ complex. The potential energy surfaces for this complex are shown in Figure 2.1.8. They are again defined by eq.2.1.1. The off-diagonal coupling element between the E_g states is identical in magnitude to the one for $Ni(H_2O)_6^{2+}$. The stronger ligand field in the hexammine complex leads to a shift of the triplet excited state to higher energy, placing the color change of the adiabatic surfaces at a different location along Q than for $Ni(H_2O)_6^{2+}$ in Figure 2.1.5b.

The time evolution of the wavefunction is shown in Figure 2.1.9. It is obvious that much less amplitude transfer occurs at short times than for $Ni(H_2O)_6^{2+}$ in Figure 2.1.6. The autocorrelation therefore does not show an additional maximum and the calculated spectrum in Figure 2.1.10 resembles the spectrum obtained from the model involving only one excited state potential surface in Figure 2.1.3. It is much easier to attribute singlet and triplet electronic labels to the spectrum in Figure 2.1.10 than to the spectrum in Figure 2.1.7. We notice that the calculated intensity for the spin-forbidden transition to the singlet state is entirely borrowed from the allowed triplet transition.

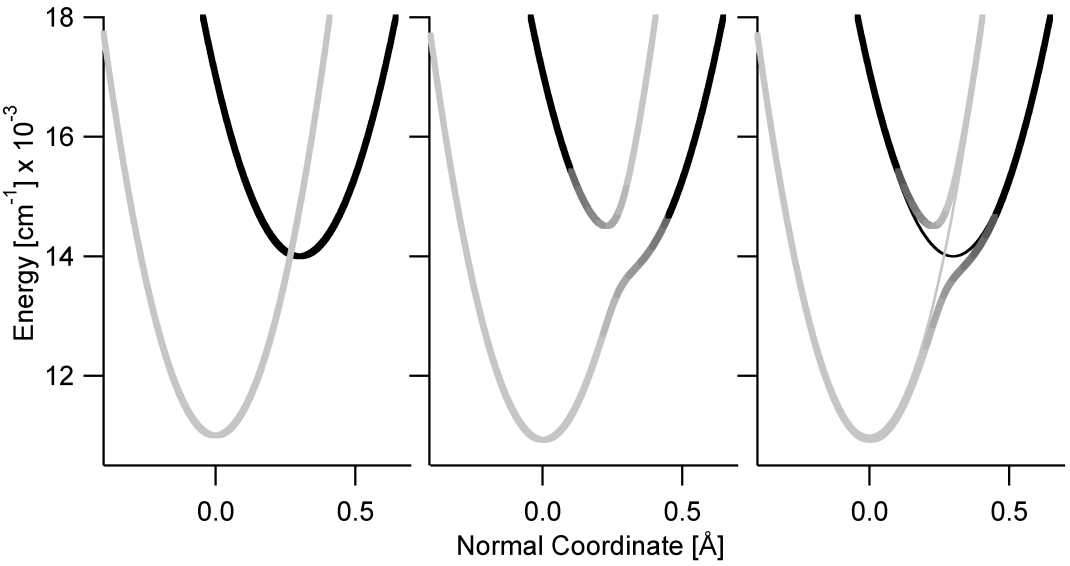

Figure 2.1.8 Coupled potential energy surfaces for $Ni(NH_3)_6^{2+}$.

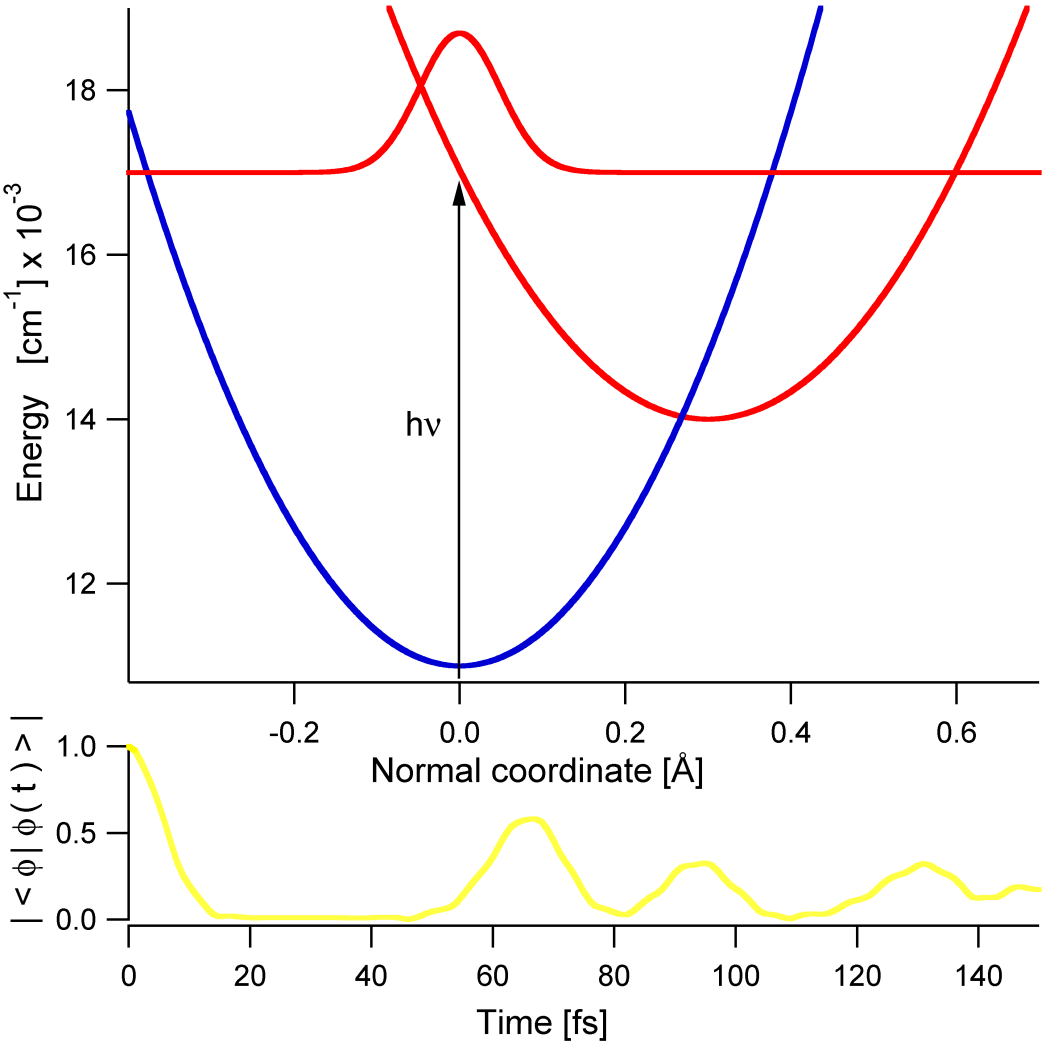

Figure 2.1.9 Time dependent wavefunction $\phi(t)$ on the coupled surfaces of $Ni(NH_3)_6^{2+}$, including the absolute value of the autocorrelation $|\langle\phi|\phi(t)\rangle|$ in the bottom panel.

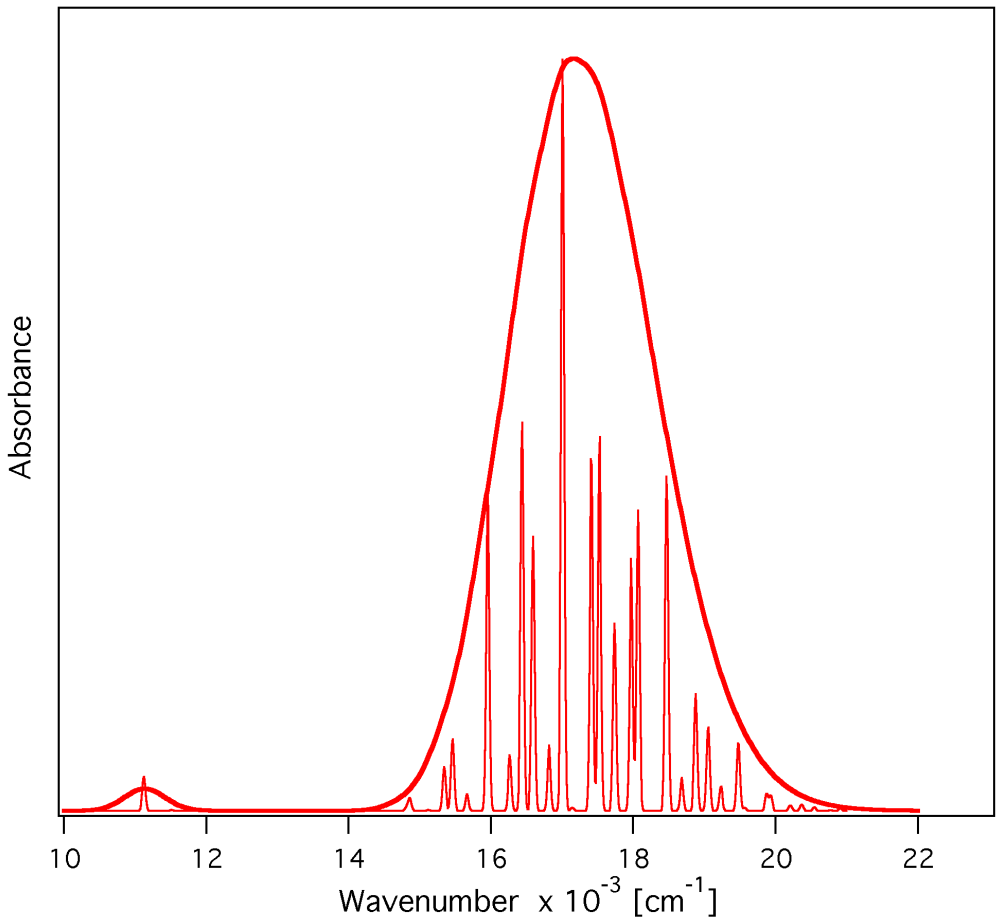

Figure 2.1.10 Absorption spectrum for the transitions to the two coupled E_g states of $Ni(NH_3)_6^{2+}$ calculated from the potential surfaces in Figure 2.1.9.

The time-dependent approach applied here to the middle band in the absorption spectra of $Ni(H_2O)_6^{2+}$ and $Ni(NH_3)_6^{2+}$ provides a quantitative illustration of the observed bandshapes in solution absorption spectra. It links the traditional crystal field symmetry analysis to the dynamic behavior of molecules on potential surfaces, illustrating the important insight provided by electronic spectroscopy.

Acknowledgement

This work was made possible by research grants from the Natural Sciences and Engineering Research Council (Canada) and by an intramural teaching grant from the Université de Montréal. We thank Véronique Nadeau and Lori Jinbachian for measuring the spectra in Figure 2.1.1 during their inorganic laboratory course.

2.2 Une alternative à la théorie dépendante du temps pour le calcul de la forme de la bande d'absorption sans résolution vibronique.

Introduction

Il a été démontré dans un article publié récemment[1] que la forme de la bande d'absorption pour deux états couplés s'apparente aux antirésonances de Fano[2]. Pour compléter les travaux présentés à la section 2.1, nous avons utilisé l'équation analytique de Neuhauser *et al.*[1] pour simuler certains spectres d'absorption de complexes inorganiques en solution et dans des verres dopés. L'approche théorique est décrite dans l'article: **"Analytical Derivation of Interference Dips in Molecular Absorption Spectra: Molecular Properties and Relationships to Fano's Antiresonance."** par Daniel Neuhauser, Tae-Jun Park, et Jeffrey I. Zink, *Phys. Rev. Lett*. **2000**, *85*, p. 5304-5307.

Comme les auteurs l'ont souligné, des antirésonances sont fréquemment observées dans les spectres de complexes des éléments de transition[3, 4]. Jusqu'à présent, ces antirésonances étaient interprétées dans le cadre de la théorie développée par Fano menant à des équations pour des transitions d'absorption atomique en présence d'un fond d'absorbance constant, un continuum[2]. Les spectres de molécules, contrairement aux atomes, ne présentent pas de continuum. Ils ont une absorption qui varie fortement en fonction de la longueur d'onde, comme illustré dans la Figure 1.3. L'équation développée par Neuhauser *et al*. utilise des paramètres qui sont significatifs du point de vue moléculaire, contrairement à l'équation de Fano.

Les équations analytiques

Neuhauser a utilisé une fonction Lorentzienne pour décrire la bande d'absorption sur laquelle se produit l'antirésonance[1]:

$$\beta \approx \frac{1}{\omega - \Delta + i\sqrt{\omega_0 \lambda}} \qquad (2.2.1)$$

Le paramètre Δ indique le maximum de la bande permise, la largeur de la bande est approximativement $\sqrt{\omega_0 \lambda}$ et $i = \sqrt{-1}$. La valeur ω_0 est la fréquence de vibration impliquée dans la transition permise et la quantité λ correspond à la différence d'énergie entre le maximum de la bande et le fond du puit de potentiel. Le nombre d'onde ω est l'abscisse du spectre d'absorption tel que montré à la figure 2.2.1. Les paramètres ω, Δ , ω_0 et λ sont en unités de cm^{-1}. Le spectre avec l'antirésonance est décrit par l'équation suivante[1]:

$$\sigma = -\frac{1}{\pi} \mathrm{Im}\left(\frac{\beta}{1 - \gamma^2 \beta \alpha} \right) \qquad (2.2.2)$$

Ici β est décrit par l'équation 2.2.1 et la valeur de σ est obtenue en utilisant la partie imaginaire d'une fonction complexe de β et α. La valeur γ est la constante de couplage entre les deux états électroniques en cm^{-1}. La fonction α est $1/(\omega - \varepsilon_{F_0} + i\Gamma)$ ou ε_{Fo} est l'origine de la transition interdite ($\varepsilon_{Fo}=\varepsilon_F+\omega_0/2$) et Γ son facteur d'élargissement en cm^{-1}. La Figure 2.2.1 compare les deux spectres obtenus avec les équations 2.2.1 et 2.2.2 en fonction de ω.

Nous avons réécrit la fonction σ en terme des paramètres moléculaires ω_0, λ, Γ, γ, ε_F, ε_A. Les paramètres ω_0, Γ, γ et ε_F, λ sont les mêmes que décrit précédemment et ε_A est l'origine électronique de la transition permise ($\varepsilon_A=\Delta-\lambda$). Pour simplifier l'équation, la même fréquence de vibration ω_0 a été utilisée pour les deux états excités:

$$\sigma = -\frac{A}{\pi} \times \frac{\left[\frac{-\sqrt{\omega_0 \lambda} - \frac{\Gamma \gamma^2}{a^2 + \Gamma^2}}{b^2 + \omega_0 \lambda} \right]}{\left[1 - \frac{\gamma^2 (ab - \Gamma \sqrt{\omega_0 \lambda})}{(a^2 + \Gamma^2)(b^2 + \omega_0 \lambda)} \right]^2 + \left[\frac{\gamma^4 (a\sqrt{\omega_0 \lambda} + b\Gamma)^2}{(a^2 + \Gamma^2)^2 (b^2 + \omega_0 \lambda)^2} \right]} \qquad (2.2.3)$$

où a = $\omega-\varepsilon_F-\omega_0/2$, b = $\omega-\varepsilon_A-\lambda$ et A est l'aire sous le spectre.

L'équation 2.2.3 a été programmée dans le logiciel Origin et les paramètres ont été optimisés par le logiciel pour obtenir le meilleur accord possible avec les spectres expérimentaux.

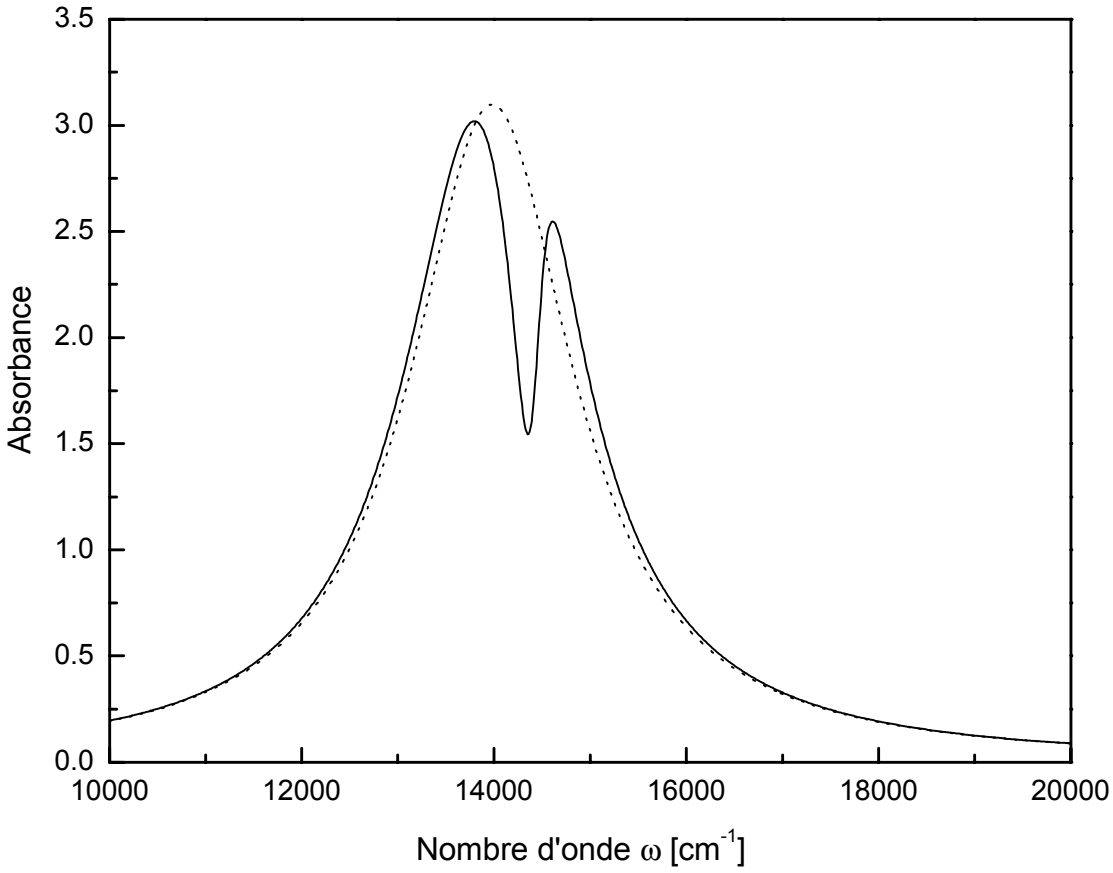

Figure 2.2.1 Comparaison entre la bande Lorentzienne (β) de l'équation 2.2.1 (en pointillé) et un spectre avec une antirésonance (σ) correspondant aux équations 2.2.2 et 2.2.3 (en trait plein). Un fait à noter est la perte d'intensité, ou antirésonance, près de 14500 cm^{-1}. L'aire sous chacune des courbes est normée à 1.

Comparaison avec les spectres d'absorption

La Figure 2.2.2 présente la deuxième bande d'absorption du $[Ni(H_2O)_6]^{2+}$ en solution à la température de la pièce. L'équation 2.2.3 a été utilisée pour simuler le spectre d'absorption. Pour reproduire la bande de façon plus réaliste, deux spectres calculés sont combinés pour reproduire la forme de la bande d'absorption. La partie imaginaire de la Lorentzienne β de l'équation 2.2.1 est utilisée pour simuler les composantes spin-orbite de l'état $^3T_{1g}$ qui n'interagissent pas avec l'état singulet et σ simule les deux états E_g couplés provenant des états $^3T_{1g}$ et ^1E_g. Cette figure correspond à la Figure 2.1.7 qui montre un calcul correspondant avec la théorie dépendante du temps. Les Figures 2.1.5 et 2.1.7 illustrent la séparation des composantes de l'état $^3T_{1g}$ sous l'effet du couplage spin-orbite et leur contribution individuelle à la bande d'absorption. Les Figures 2.2.2 et 2.2.3 comparent d'une façon similaire les spectres d'absorption au résultat d'une somme des fonctions σ et Im(β). Les paramètres R1 et R2 représentent la pondération de chacune des deux fonctions, ainsi (R1×A)/(R1+R2) donne l'aire sous la courbe pour la fonction σ et (R2×A)/(R1+R2) donne l'aire pour la fonction β. Les paramètres b et m simulent une ligne de base spectrale de forme y=mx+b. Le paramètre ε_β est l'énergie de l'origine électronique pour la bande non-couplée (fonction β).

Pour illustrer la versatilité de cette approche nous avons simulé la bande d'absorption du $[Ni(H_2O)_6]^{2+}$ en solution gelée dans le butanol à 80 K. On peut voir sur la Figure 2.2.3 que le modèle reproduit la forme de la bande tout en gardant des paramètres moléculaires raisonnables.

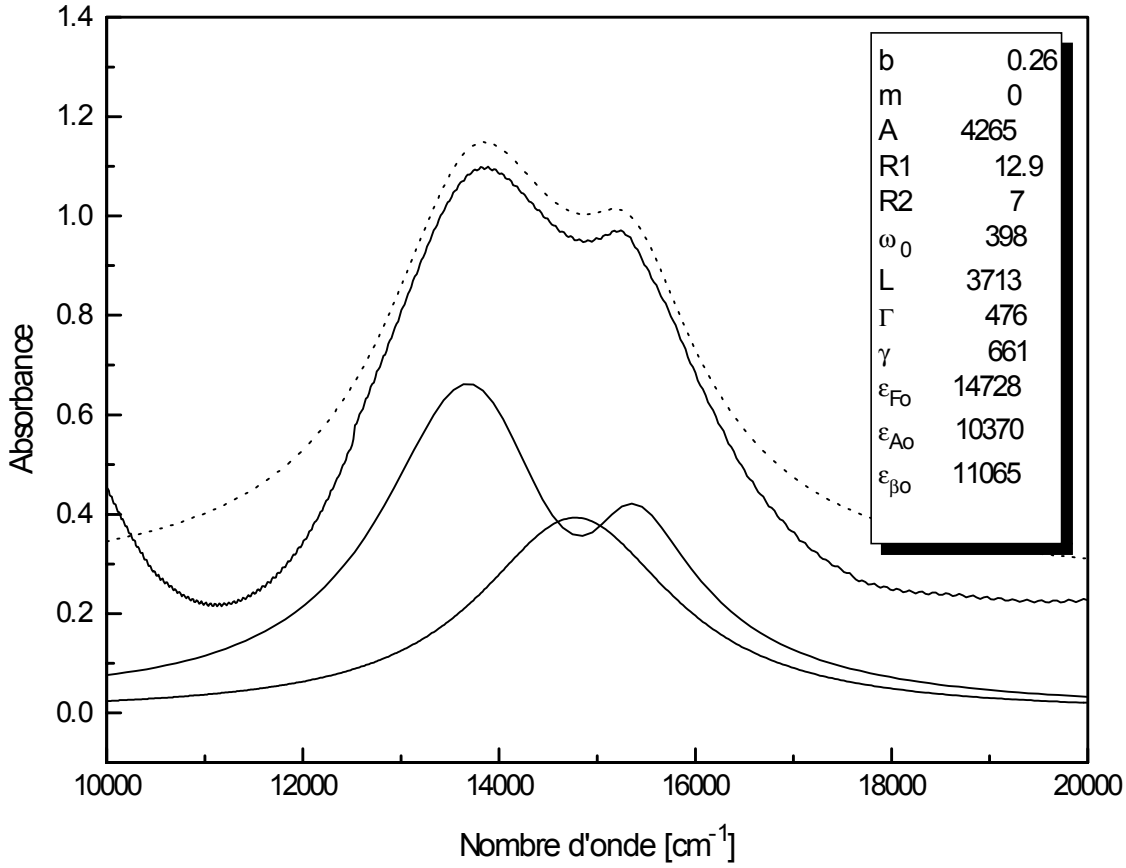

Figure 2.2.2 Spectre d'absorption de la région $^3T_{1g}/^1E_g$ de $[Ni(H_2O)_6]^{2+}$ en solution dans l'eau à la température ambiante, trace solide en haut, comparé avec le résultat de la simulation, en pointillé, utilisant la somme des deux fonctions β et σ. Les deux traces du bas montrent chacune des fonctions. Les spectres sont décalés en absorbance pour des raisons de clarté.

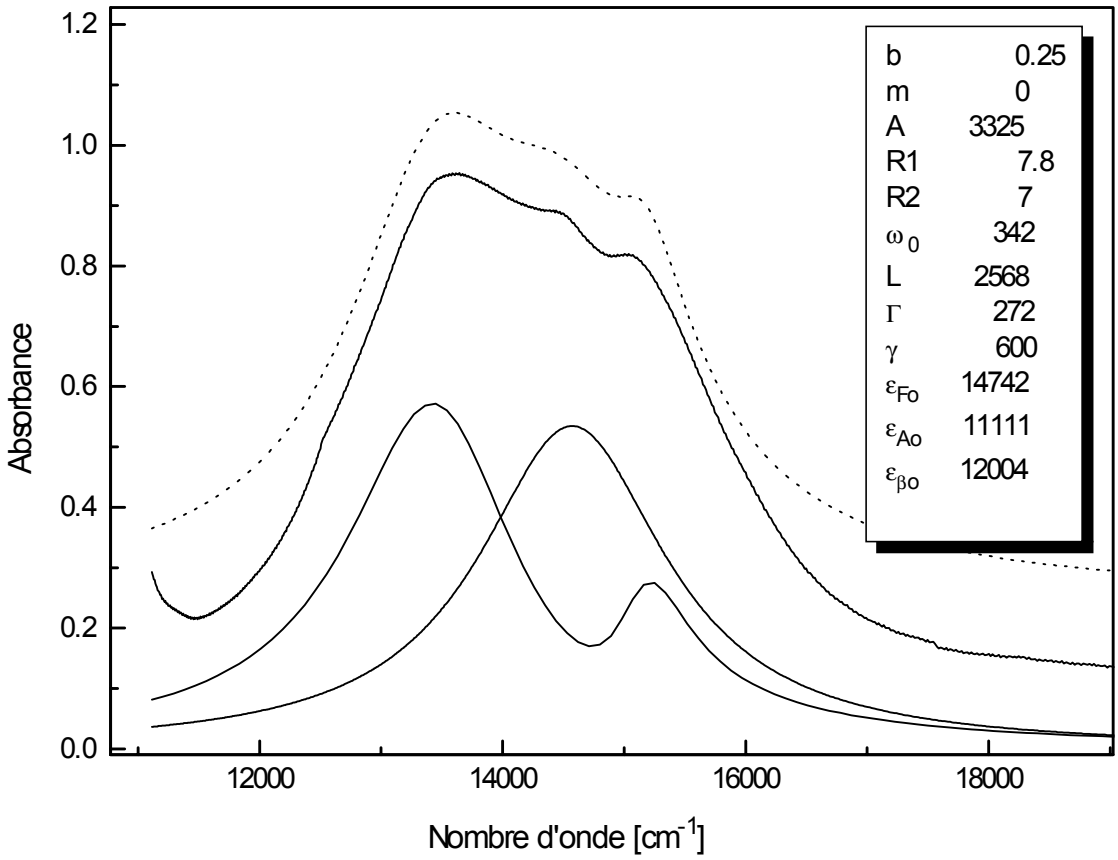

Figure 2.2.3 Spectre d'absorption de la région $^3T_{1g}/^1E_g$ de $[Ni(H_2O)_6]^{2+}$ en solution dans le butanol à 80 K, trace solide en haut, comparé avec le résultat de la simulation, en pointillé. Les deux traces du bas montrent chacune des fonctions. Les spectres sont décalés en absorbance pour des raisons de clarté.

La Figure 2.2.4 présente le spectre d'absorption à 5 K d'un zirconia cubique dopé avec 2% de chrome(III)[5]. La région de la première transition permise, $^4A_2 \rightarrow {}^4T_2$, est particulièrement intéressante puisque la surface d'énergie potentielle de l'état $^4T_2$ croise celles de deux états doublets, ^2E et $^2T_1$, ce qui donne lieu à deux antirésonances dans la bande. Cette région spectrale a été explorée pour plusieurs verres dopés et des antirésonances sont observés[2, 3]. Les auteurs utilisent l'équation de Fano pour décrire le phénomène, ce qui ne mène pas à des paramètres qu'on peut comparer aux propriétés moléculaires des états excités couplés.

Nous avons utilisé deux fonctions σ décrites par l'équation 2.2.3 pour simuler les deux antirésonances de la bande $^4T_2$. Pour simplifier le calcul, tous les paramètres sont identiques pour les deux fonctions σ excepté le poids de chacune d'elle, R1 et R2, et la position des deux doublets, ε_{F1} et ε_{F2}. L'équation 2.2.3 est ainsi utilisée pour reproduire l'expérience de la façon la plus simple possible.

Conclusion

La présence d'antirésonances semblables à celles de Fano est courante en spectroscopie inorganique. Les complexes du chrome(III) sont particulièrement intéressant puisque plusieurs d'entre eux ont un spectre d'absorption présentant des antirésonances évidentes[2, 3]. L'observation de ce phénomène n'est pas limitée à ce métal, tous les métaux de transition, de configuration d^2 à d^8 peuvent former des complexes présentant cette caractéristique spectroscopique. Les spectres d'absorption des complexes du nickel(II) sont un autre exemple avec cette particularité.

Dans la première partie du chapitre 2 nous avons vu que la théorie de la spectroscopie dépendante du temps est très utile en ce qui concerne la compréhension de ces particularités spectroscopiques. Si on compare le résultat présenté à la Figure 2.2.2 à la première partie du chapitre 2, on peut voir que l'équation analytique est une alternative simple à la théorie dépendante du temps pour analyser des spectres peu résolus.

Il faut cependant garder à l'esprit que cette équation analytique reste une approximation par rapport à la théorie dépendante du temps. Les deux principaux inconvénients de cette approche simplifiée sont au niveau de la forme de la bande d'absorption et des progressions vibroniques. L'équation ne peut pas reproduire les progressions vibroniques observées dans les spectres, phénomène illustré à la Figure 1.4, et pour cette raison elle ne peut être utilisée que pour des cas présentant peu de résolution spectrale. Les formes de bandes d'absorption simulées par les équations 2.2.1 à 2.2.3 sont Lorentziennes, ce qui provoque un élargissement à la base dans les spectres simulés présentés sur les Figures 2.2.2 à 2.2.4. Cet élargissement à la base n'est pas observé dans les spectres expérimentaux. Leur forme s'apparente plutôt à une distribution de Poisson, illustré à la Figure 1.3, ce qui est mieux simulé par la théorie dépendante du temps.

L'équation analytique présente cependant plusieurs avantages. Elle est moins difficile à utiliser et beaucoup plus simple que les logiciels utilisant la théorie dépendante du temps. Un autre avantage de l'équation 2.2.3 est qu'elle peut être entrée directement dans un logiciel commercial tel que Origin pour affiner les paramètres de façon automatique. Cet affinement est beaucoup plus efficace que celui

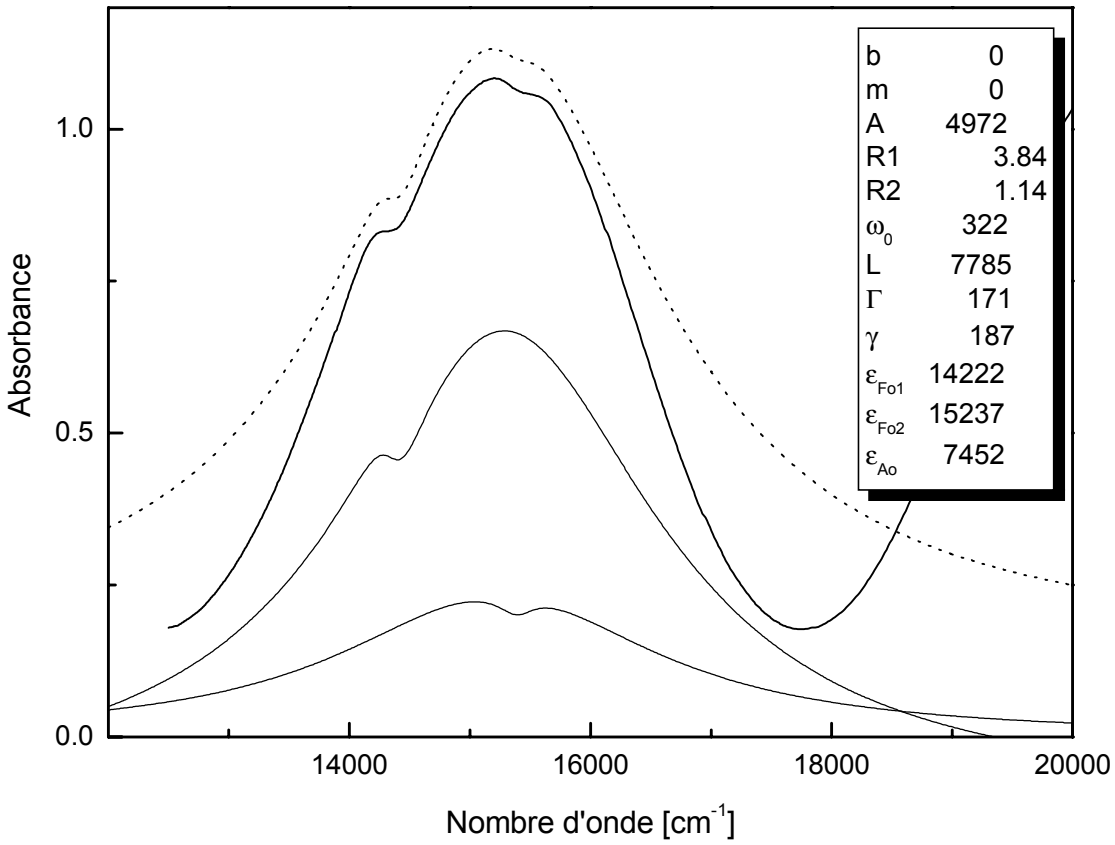

Figure 2.2.4 Spectre d'absorption en phase solide de ZrO_2/Y_2O_3 : 2% Cr(III) à 5 K (trait plein, en haut). La transition permise dans ce cas-ci, $^4T_2$, croise deux transitions interdites, ^2E et $^2T_1$. Deux fonctions σ, traces solides en bas, sont additionnées pour simuler l'expérience. Le spectre calculé total est donné en pointillé. Les spectres sont décalés en absorbance pour des raisons de clarté.

effectué au chapitre 3, où nous avons utilisé une approche automatisée pour l'affinement des paramètres par la théorie dépendante du temps[6].

Une équation analytique qui décrit la forme d'une bande d'absorption impliquant deux états électroniques en interaction ne peut être calulée qu'avec des formes Lorentziennes. Pour des bandes qui sont décrites par des distributions de Poisson, un calcul numérique est possible et efficace. L'approche de la référence[1] peut aussi être généralisée pour traiter des modèles où la surface d'énergie potentielle de l'état final est décalée le long de plusieurs coordonnées normales. Dans cette situation, la forme de la bande d'absorption dans la région des maxima varie en fonction des décalages le long des coordonnées normales et de leurs fréquences vibrationnelles[7]. Ce sont des situations qui pourraient être explorées de façon efficace à l'aide de l'approche théorique décrite dans ce chapitre.

Chapitre 3: Couplage entre états excités dans des complexes du nickel(II) étudié par spectroscopie d'absorption polarisée à basse température.

Table des matières

Coupled Excited States in Nickel(II) Complexes Probed by Polarized Absorption Spectroscopy

Guillaume Bussière and Christian Reber

J. Am. Chem. Soc. **1998**, *120*, 6306-6315

Abstract

The absorption spectra of $Ni(H_2O)_6^{2+}$, *trans*-$NiCl_2(H_2O)_4$ and $NiCl_6^{4-}$ show an unusual band shape for the $^3A_{2g} \rightarrow {}^3T_{1g}$, ^1E_g (O_h labels) electronic transitions in the near-infrared to visible wavelength range. A barely resolved broad band and an intense vibronic progression with a spacing larger than the totally symmetric ground-state metal-ligand vibrational frequency are superposed. Low-temperature polarized spectra are analyzed with a quantitative model and both the large interval and the band intensities are shown to arise from efficient intersystem crossings between the two excited states. Alternative assignments proposed in the literature are examined.

Introduction

Interactions between multiple electronic states are of key importance to many areas of chemistry, such as electron transfer processes and photochemical reactions[1, 2]. Transition metal compounds are ideal model systems for an investigation of interacting states because of their rich electronic structure with excited-state energies and other properties that can be controlled by simple chemical modifications such as ligand substitutions. The high symmetry of these molecules imposes rigid group theoretical constraints, and crystal field theory can be used for a complete identification of all low-energy electronic states. Electronic spectroscopy provides the detailed experimental information needed for a complete characterization of the interaction between excited states of the title compounds.

We apply polarized absorption spectroscopy to single crystals of three hexacoordinated nickel(II) complexes with aquo and chloro ligands. The electronic spectra of such complexes have attracted much interest in the past[3-8]. Among their most unusual features is an intense vibronic progression on the high-energy side of a spin allowed d-d band between approximately 500 nm and 1000 nm. Its spacing is significantly larger than the ground-state totally symmetric vibrational energy of all three complexes. We present a quantitative model to calculate the shape of the complete band system with its prominent vibronic structure, including the large spacing of the vibronic progression. Our analysis shows that the excited-state force constant of a bond is not the only factor determining the energy separation within a vibronic progression. The vibronic structure is also affected by the coupling between energetically close excited states, an effect neglected in conventional spectroscopic

assignments, despite its important influence on properties and reactivities of excited states. In the title compounds, the interaction between states of identical symmetry is caused by spin-orbit coupling and we derive and discuss its effects from quantitative calculations of the experimental absorption bandshapes. Our time dependent quantum mechanical model provides information on nonadiabatic transitions between coupled electronic states. Complexes with resolved d-d bands provide a unique opportunity to study such effects because the symmetry of all relevant states can be obtained from crystal field theory, leaving a very small number of adjustable parameters for the theoretical analysis. The influence of coupled excited states on spectra is not limited to crystal-field bands, it is an effect that is important in the electronic spectroscopy of other classes of compounds and materials.

A number of models and assignments have been proposed for the spectroscopic region of interest[3-6, 8], the most recent being a refined crystal field approach to nickel complexes with nitrogen and sulfur donor ligands[9]. The main emphasis of most models is on purely electronic transition energies calculated from the energy differences between states in Tanabe-Sugano diagrams or from electronic structure calculations. Energies and intensities of vibronic bands and progressions have received less detailed attention. Our approach unifies these facets and identifies the spectroscopic manifestations of intersystem crossings. Literature models for the vibronic structure include proposals such as a two-phonon progression in a non-totally symmetric mode to account for the unusual structure observed in hexacoordinated nickel(II) halides[10] or the textbook attribution of the double maximum in the region of interest of the absorption spectrum of $Ni(H_2O)_6^{2+}$ to a Jahn-Teller effect[11], while another very recent textbook concludes that there is no

agreed explanation for this splitting[12]. We comment on these explanations and on the long-standing controversy on singlet and triplet assignments for transition metal complexes with strongly coupled electronic states[3-6, 8].

Experimental Section

Crystals of *trans*-$NiCl_2(H_2O)_4 \cdot 2H_2O$ and $Ni(H_2O)_6(NO_3)_2$ were obtained by slow evaporation of saturated aqueous solutions of $NiCl_2 \cdot 6H_2O$ (Fisher Chemicals) and $Ni(NO_3)_2 \cdot 6H_2O$ (Biopharm) over several days. Samples for spectroscopic measurements were obtained through several recrystallizations. Infrared spectra are in excellent agreement with the literature[13]. $NiCl_2(H_2O)_4 \cdot 2H_2O$ crystallizes as very regular monoclinic green prisms. The crystal structure shows only one site for the $NiCl_2(H_2O)_4$ complex[14]. The shortest separation between nickel centers is 6.5 Å without shared ligands or bridging water molecules. Larger metal-metal distances in this structure involve hydrogen bonds through at least one non-coordinated water molecule. The crystals used for spectroscopic measurements had clearly defined optical extinction directions, determined between crossed polarizers. The molecular Cl-Ni-Cl axis is parallel to the crystallographic a axis which coincides with the long side of the crystals and one of the extinction directions[14]. Spectra were measured with the incident light beam perpendicular to the crystal surface containing the ab plane. The H_2O-Ni-OH_2 bonds are nearly perpendicular to the a axis in this arrangement. These crystals allow us therefore to measure spectra polarized along molecular axes.

$Ni(H_2O)_6(NO_3)_2$ crystallizes as blue-green triclinic crystals with less clearly defined extinction directions than $NiCl_2(H_2O)_4 \cdot 2H_2O$. Crystals were obtained from saturated aqueous solutions of $Ni(NO_3)_2 \cdot 6H_2O$ (Biopharm) within several days. The crystal structure of this compound again shows only one site for the Ni^{2+} ion[15], but the molecular axes do not coincide with the extinction directions.

The crystal growth and near-infrared spectroscopic properties of $CsMgCl_3:Ni^{2+}$ were described previously[16]. In the following, we analyze the absorption spectrum of a crystal used for the luminescence study in the literature[16].

Crystal thicknesses for absorption spectroscopy were between 0.5 mm and 1 mm. Low temperature polarized spectra were measured with a Varian Cary 5E spectrometer equipped with a pair of Glan-Taylor polarizers. All spectra are corrected for the baseline of the instrument. The sample temperature was controlled with an Oxford Instruments CF-1204 helium gas flow cryostat. Raman spectra were measured using the 488.2 nm blue line of a Coherent Innova 90-5 argon ion laser and a Spex 14018 monochromator with a photomultiplier (Hamamatsu R955) and a photon counting system (Spex DPC-2).

Spectroscopic Results

All three nickel(II) complexes show NIR-VIS absorption spectra with three spin-allowed transitions, as illustrated for $Ni(H_2O)_6^{2+}$ in Figure 3.1, where the bands are assigned in O_h symmetry. In the following, we focus on the region of the lowest-energy singlet-triplet intersection, involving the $^3T_{1g}(^3F)$ and ^1E_g excited states in the

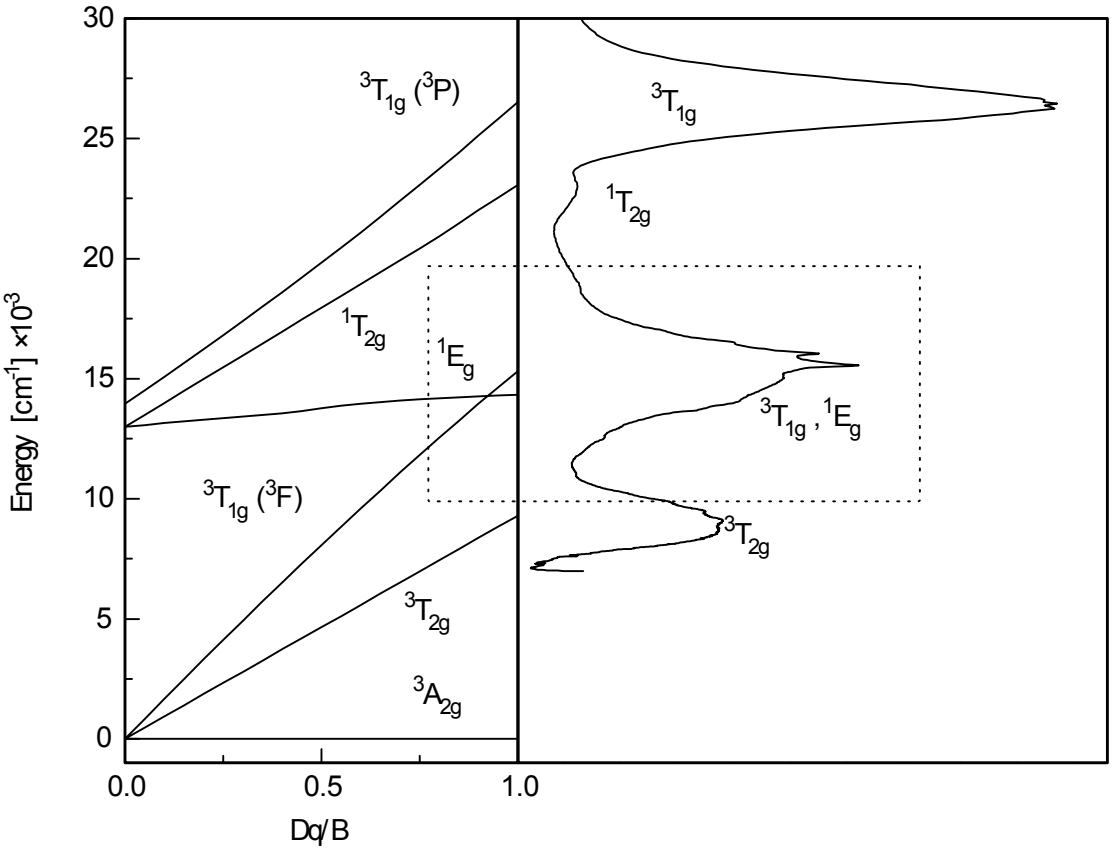

Figure 3.1 Overview absorption spectrum and band assignments for $Ni(H_2O)_6^{2+}$. The unpolarized experimental spectrum of $Ni(H_2O)_6(NO_3)_2$ was measured at 5 K and is identical to the literature data[8]. The dotted rectangle denotes the region of the first singlet-triplet intersection, shown in more detail in Figures 3.2, 3.4 and 3.5 for all compounds studied.

energy range of the middle spin-allowed band in the spectrum of Figure 3.1. This region is denoted by the dotted rectangle in the Figure.

The polarized single-crystal absorption spectra for *trans*-$NiCl_2(H_2O)_4 \cdot 2H_2O$ in the region of the $^3A_{2g} \rightarrow {}^3T_{1g}(^3F)$, ^1E_g transitions (O_h labels) are shown in Figure 3.2. The electronic transitions from the ground state to both excited states are parity forbidden and the oscillator strength in the wavelength range shown in Figure 3.2 is on the order of 5×10^{-6}, typical for this type of transitions. The oscillator strength increases by 27% between 5 K and 300 K. The temperature dependence of the spectrum does not provide evidence for structural phase transitions. A simple paramagnetic behavior is observed at temperatures down to 5 K, ruling out cooperative electronic excitations in our spectra[17]. The band system in the near-infrared to visible (NIR/VIS) range extends from approximately 12000 cm^{-1} to 18000 cm^{-1} and consists of a broad band and an intense vibronic progression. The maxima of the broad band are at 13240 cm^{-1} and 13430 cm^{-1} in σ and π polarization, respectively. Weak vibronic structure on the broad band is observed in both polarizations with an average spacing of 357 cm^{-1}, indicated schematically in Figure 3.2. The intense vibronic progression has its first maximum at 14780 cm^{-1} in σ polarization. The members of the progression in the σ polarized spectrum are separated by 430 ± 5 cm^{-1}, as marked in Figure 3.2. The π polarized spectrum shows two very similar 430 cm^{-1} progressions with an average separation of 75 cm^{-1} between corresponding maxima, indicated in Figure 3.2 for the second member of both progressions. The lowest energy maximum of the first progression is at 14760 cm^{-1}, overlapping the corresponding maximum of the higher energy

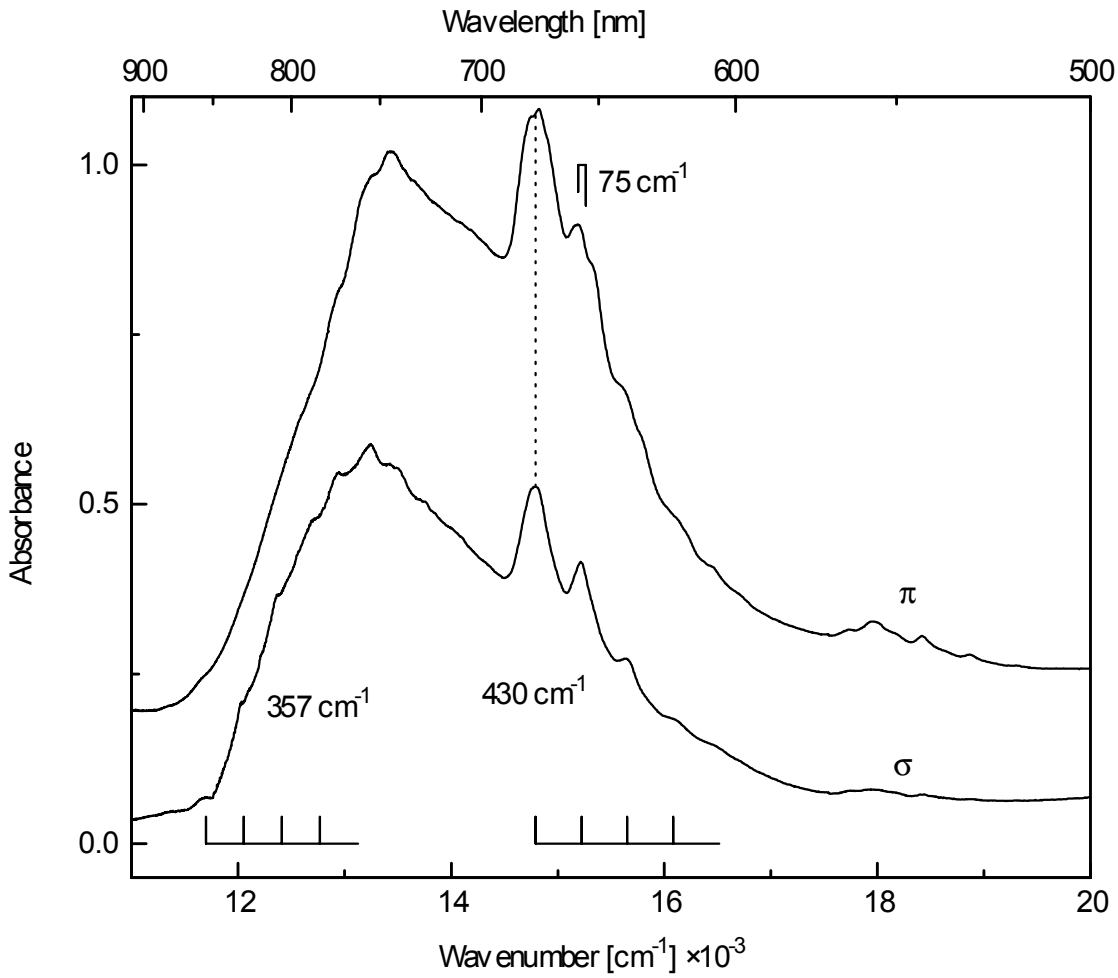

Figure 3.2 Polarized absorption spectra of *trans*-$NiCl_2(H_2O)_4 \cdot 2H_2O$ at 5 K in the region of the $^3A_{2g}$, ^3E_g and $^1A_{1g}$, $^1B_{1g}$ bands (D_{4h} labels). Polarization directions are given relative to the molecular Cl-Ni-Cl axis. The main vibronic progressions are indicated for the σ polarized spectrum. The π polarized spectrum is offset by 0.15 absorbance units for clarity.

progression at 14830 cm^{-1}. The progression in σ polarization has its maxima at energies close to the first progression in π polarization, as illustrated by the dotted line in Figure 3.2. The weak vibronic peaks at approximately 18000 cm^{-1} involve vibrational modes of the aquo ligands[8].

The Raman spectra of $NiCl_2(H_2O)_4 \cdot 2H_2O$ are shown in Figure 3.3 at room temperature and at 77 K. The vibrational energies are very similar at both temperatures, again indicating negligible structural changes of the chromophores as a function of temperature. Vibrational energies at 77 K are 532 cm^{-1}, 377 cm^{-1} and 364 cm^{-1}. The signal at 364 cm^{-1} in the room temperature spectrum is attributed to the totally symmetric Ni-H_2O stretching mode based on its polarization and on literature assignments[13]. We note that there is no Raman signal corresponding to the spacing of 430 cm^{-1} in the intense vibronic progression observed in the absorption spectra of Figure 3.2.

Our polarized single crystal absorption spectra of $Ni(H_2O)_6(NO_3)_2$ are identical to the literature spectra for this compound[8] and similar to the data reported for $Ni(H_2O)_6^{2+}$ in a variety of crystals and glasses[3, 6, 8]. An intense vibronic progression with a spacing of 490 ± 20 cm^{-1} is observed on the high-energy side of the broad band. The totally symmetric vibrational mode has a Raman frequency of 397 cm^{-1}, again lower in energy than the spacing of the intense vibronic progression. The average spacing of the resolved progression on the broad band is 355 cm^{-1} and the oscillator strength of the band system increases by 24% between 5 K and room temperature. The overall absorption spectrum is shown in Figure 3.1 and the region of interest is compared to our theoretical model in Figure 3.4.

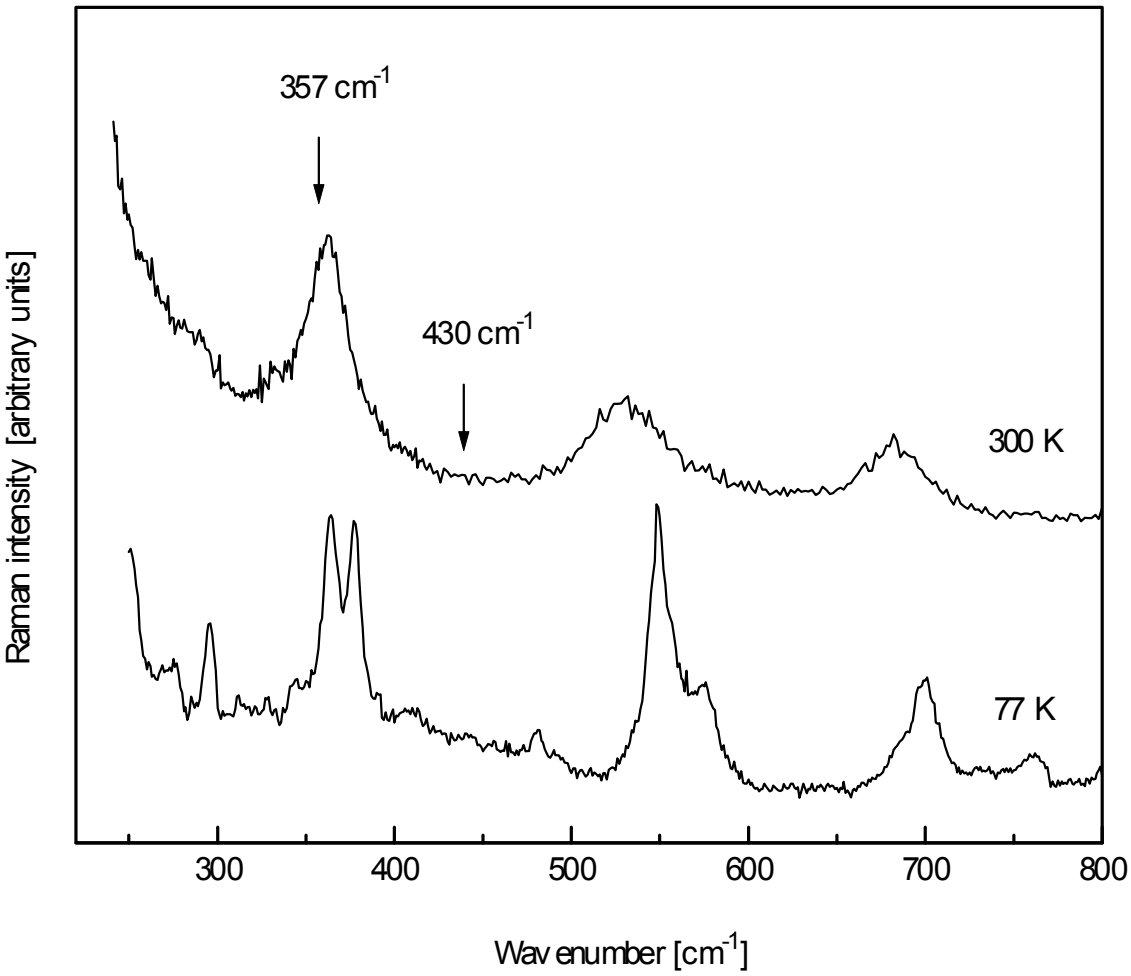

Figure 3.3 Unpolarized Raman spectra of *trans*-$NiCl_2(H_2O)_4 \cdot 2H_2O$. The arrows indicate the average spacing of the vibronic progressions in the absorption spectra of Figure 3.2.

The absorption spectrum of $CsMgCl_3:Ni^{2+}$ is identical to the literature spectra[18, 19] and it is compared to our theoretical model in Figure 3.5b. The band intensity increases by 30% between 15 K and room temperature. The broad band shows weak vibronic structure with an average spacing of 240 cm^{-1}. The spacing of the intense progression is 300 cm^{-1}, again higher than the a_{1g} vibrational frequency of 255 cm^{-1}[20]. Similar spectra are obtained for pure crystalline $CsNiCl_3$ and $CsNiBr_3$, with additional fine structure at low temperature due to magnetic ordering[19].

Discussion

We combine absorption energies and intensities, vibrational spectra and electronic states derived from crystal field theory to fully analyze the NIR/VIS band system for nickel(II) complexes with three different point group symmetries. Idealized O_h and D_{4h} point groups are used for $Ni(H_2O)_6^{2+}$ and $NiCl_2(H_2O)_4$, respectively. The Ni^{2+} centers doped into $CsMgCl_3$ occupy a site with exact D_{3d} symmetry. All crystal field states of interest can be derived from the relevant character tables[21] and are summarized in Scheme 3.1. Octahedral (O_h) symmetry corresponds to the simplest situation with only one pair of interacting singlet and triplet levels. These two levels have E_g symmetry and are connected by the dotted arrows in Scheme 3.1. Tetragonal (D_{4h}) symmetry offers two singlet states that can interact with one or two triplet states, and in trigonal (D_{3d}) symmetry we probe one singlet state interacting with several triplets at different energies. All pairs of interacting levels are indicated in Scheme 3.1. These pairs of coupled levels with

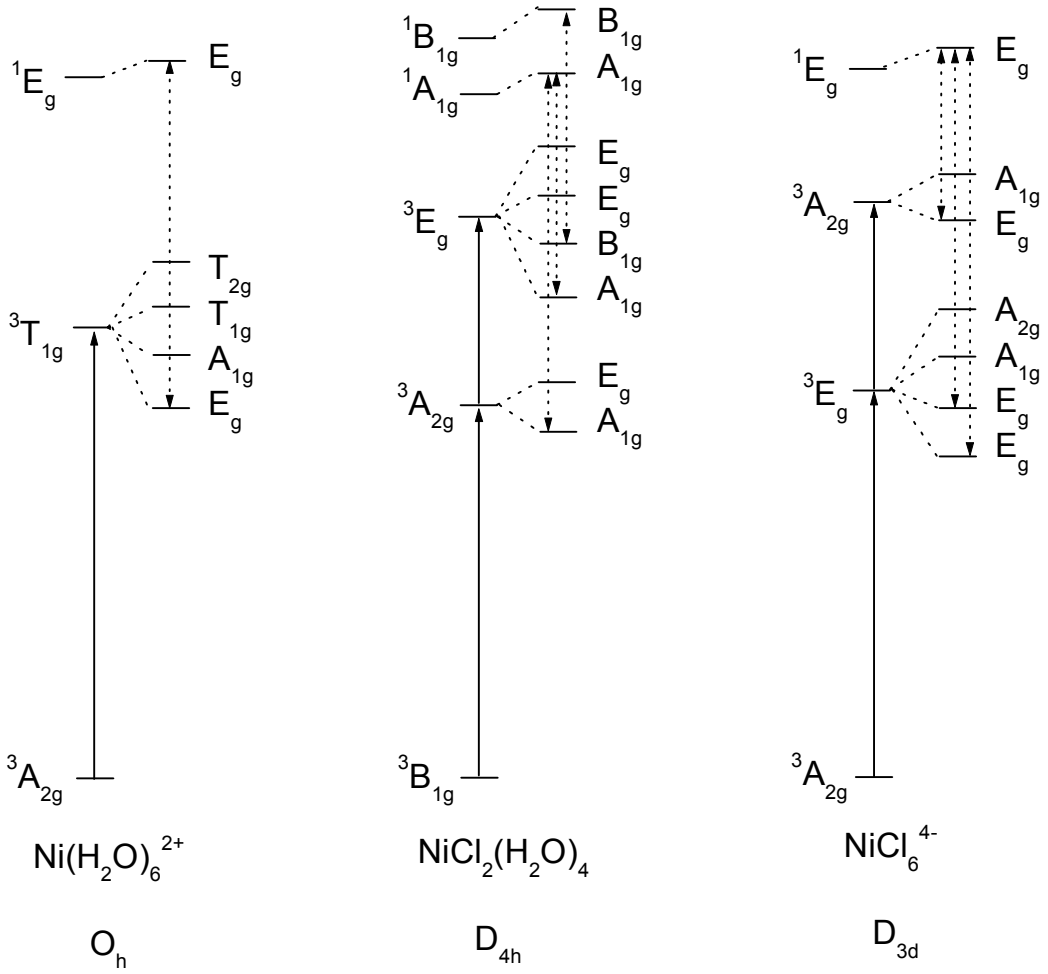

Scheme 3.1 Electronic states involved in the absorption bands in the region of the first singlet-triplet intersection for octahedral, tetragonal and trigonal complexes of nickel(II). The energetic order of triplet states and their spin-orbit sublevels is discussed in the text. Solid arrows denote spin allowed absorption transitions. Dotted arrows connect pairs of interacting levels.

their potential energy surfaces along a totally symmetric normal coordinate are the key aspect accounting for the unusually large vibronic spacings in the absorption spectra. The quantitative potential energy surfaces for the coupled states are used to calculate absorption spectra using time dependent theory, an approach that allows us to visualize the vibronic dynamics involving the coupled states and their spectroscopic consequences. The spectroscopic features observed in the three different symmetries will be unified with the model approach presented in the following. We will then briefly compare our analysis to several alternative assignments presented in the literature.

$Ni(H_2O)_6^{2+}$: O_h symmetry, one singlet-triplet interaction.

The quantitative analysis of this band shape proceeds through three main stages: first, the electronic states with their potential energy surfaces have to be defined, then the most efficient intensity mechanism for the transitions has to be determined and finally the resulting bandshapes have to be calculated. These three stages will be discussed in detail for $Ni(H_2O)_6^{2+}$, an analogous approach is then applied to $NiCl_2(H_2O)_4$ and $NiCl_6^{4-}$. Crystal field theory can be used to quantitatively define the energies of all electronic states for this complex in the NIR/VIS region. The parameters B and Dq were determined from the three spin allowed absorption bands of this complex[6] and the literature value of –270 cm^{-1} for the spin-orbit coupling constant λ, determined from EPR spectroscopy was used[22]. The energies of the relevant electronic states are calculated with these crystal field parameters and given in Table 3.1. Figure 3.4 summarizes our model and its comparison with the

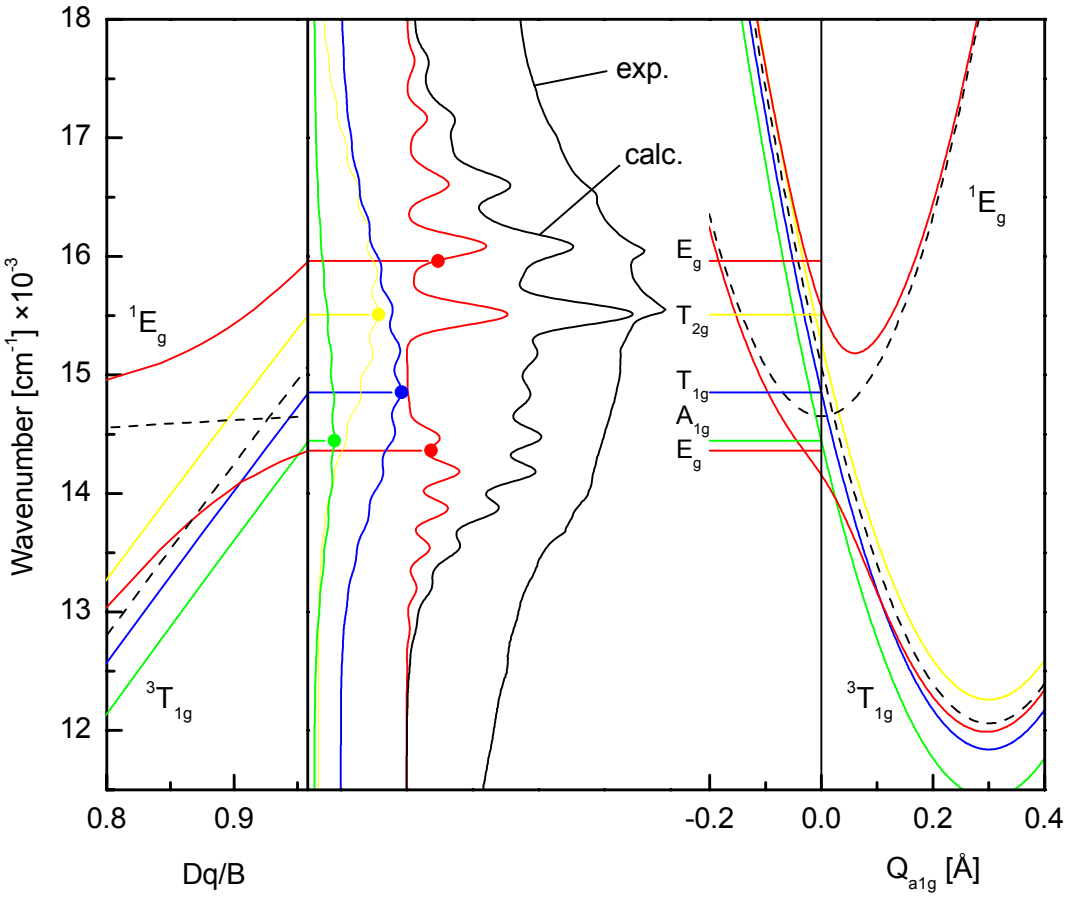

Figure 3.4 Crystal field states (left hand panel) and potential energy surfaces (right hand panel) for an octahedral complex of nickel(II) in the $^3T_{1g}/^1E_g$ energy range. Calculated spectra for the transition to each electronic state are shown in the central panel. Lines with markers connect electronic states and their corresponding calculated spectra. The total calculated spectrum (calc.) is obtained as the sum of the four individual spectra and is compared to the experimental spectrum of $Ni(H_2O)_6^{2+}$ measured at 5 K.

experimental absorption spectrum of $Ni(H_2O)_6^{2+}$. The left-hand panel of the Figure illustrates the crossing region between the ^1E_g and $^3T_{1g}(^3F)$ levels as a function of the ratio Dq/B and is identical to a standard Tanabe-Sugano diagram for the two excited states of interest. The dotted lines indicate the singlet-triplet crossing in the absence of spin-orbit coupling, as shown in Figure 3.1. The highest value of Dq/B shown in Figure 3.4 corresponds to the crystal field parameters in Table 3.1. The energetic order of the spin-orbit levels at this abscissa value is identical to Scheme 3.1 and given in the middle panel of Figure 3.4. The avoided crossing between the E_g levels arising from the singlet and triplet excited states is caused by the off-diagonal matrix element for spin-orbit coupling between the $E_g(^3T_{1g})$ and $E_g(^1E_g)$ states, given as $-\sqrt{6}\lambda$ in the literature[23]. This model applies to a complex with a rigid geometry corresponding to the ground state molecular structure and does not include vibronic effects.

A physically more meaningful description of the electronic states includes vibronic effects and requires potential energy surfaces. We limit our analysis to one-dimensional harmonic surfaces along the totally symmetric normal coordinate of the metal-ligand breathing mode Q_{a1g}, as shown on the right-hand side of Figure 3.4 for all singlet and triplet excited states given in Scheme 3.1. The minimum of the ground state surface defines the origin of the Q_{a1g} axis. The ^1E_g excited state potential has its minimum also at $Q_{a1g} = 0$ because it arises from the same $t_{2g}^6e_g^2$ electron configuration as the ground state. The $^3T_{1g}$ excited state is expected to have its minimum at $Q_{a1g} > 0$, a consequence of the increased antibonding character of its $t_{2g}^5e_g^3$ electron configuration. This offset and the resulting Ni-H_2O bond elongations

Table 3.1 Spectroscopic parameters for the ground (g.s) and excited (e.s.) electronic states

Parameter	$Ni(H_2O)_6^{2+}$	$NiCl_2(H_2O)_4$	$NiCl_6^{4-}$
$^3\Gamma$ origins [cm^{-1}]	12066 E_g ($^3T_{1g}$)[a] 11431 A_{1g} ($^3T_{1g}$)[a] 11840 T_{1g} ($^3T_{1g}$)[a] 12495 T_{2g} ($^3T_{1g}$)[a]	10365 A_{1g} ($^3A_{2g}$) 10500 E_g ($^3A_{2g}$)	10400 E_g (^3E_g) 10700 E_g (^3E_g) 11000 A_{1g} (^3E_g) 11200 A_{2g} (^3E_g) 11850 Eg ($^3A_{2g}$) 12100 A_{1g} ($^3A_{2g}$)
$^1\Gamma$ origin [cm^{-1}]	14651 E_g(^1E_g)a	14403 A_{1g} ($^1A_{1g}$)	12500 E_g (^1E_g)
vibrational frequencies [cm^{-1}]			
$\hbar\omega_{a1g}$, g.s.	397	364	255
$\hbar\omega_{\Gamma}$, $^3\Gamma$ e.s.	355	357	240
$\hbar\omega_S$, $^1\Gamma$ e.s.	397	364	255
potential minima			
ΔQ_T, $^3\Gamma$ e.s. [Å]	0.30	0.295	0.17
ΔQ_S, $^1\Gamma$ e.s. [Å]	0.00	0.05	0.00
coupling constant V_{ST} [cm^{-1}]	661	730	350
damping factor Γ [cm^{-1}]	60	100	60
transition dipole moments, μ_S/μ_T	0.00/1.00	0.09/0.91	0.00/1.00

[a]calculated with: Dq=910.7 cm^{-1}, B=950 cm^{-1}, C/B=4, λ=-270 cm^{-1} [22] (λ=0 for E_g states), crystal field triplet levels correspond to absorption maxima and are higher by 3013 cm^{-1} than the band origins given in the Table.

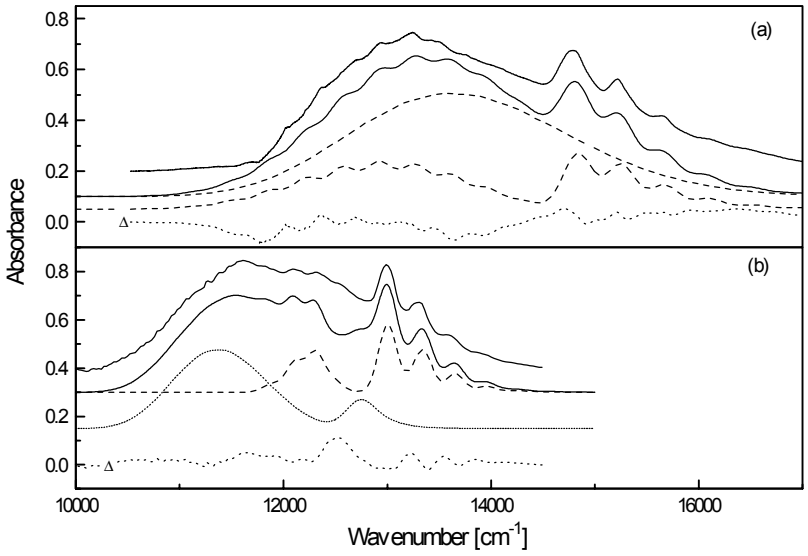

Figure 3.5 a) Calculated and experimental absorption spectra for *trans*-$NiCl_2(H_2O)_4 \cdot 2H_2O$ in σ polarization. The top trace (solid line) denotes the experimental spectrum, followed by the total calculated spectrum (solid line) separated from the experimental spectrum by 0.1 absorbance units for clarity. The two dotted traces denote the calculated spectra for the E_g and the coupled A_{1g} levels arising from $^3A_{2g}$ and $^1A_{1g}$. The difference trace between experimental and calculated spectra is denoted by Δ. b) Calculated and experimental absorption spectra of $CsMgCl_3:Ni^{2+}$ in σ polarization. The top trace (solid line) denotes the experimental spectrum, followed by the total calculated spectrum (solid line), separated from the experimental spectrum by 0.1 absorbance units. The calculated spectra for two sets of coupled E_g levels are represented by dotted lines. The difference trace between experimental and calculated spectra is denoted by Δ.

are assumed to be identical for all four spin-orbit levels arising from the $^3T_{1g}$ excited state. Spectroscopic data and calculated crystal field levels quantitatively define the potential energy surfaces for $Ni(H_2O)_6^{2+}$ with the parameter values summarized in Table 3.1. The frequency of the a_{1g} mode in the Raman spectrum of $Ni(H_2O)_6^{2+}$ is used to determine the harmonic potential energy surfaces for both the $^3A_{2g}$ and ^1E_g states. The vibrational frequency for the $^3T_{1g}$ excited state is lower than for the ground state and we use the frequency of 355 cm^{-1} from the resolved vibronic structure of the $^3T_{1g}$ band, a value in close agreement with the literature[8]. This vibrational energy is used for all four potential energy surfaces arising from the $^3T_{1g}$ state.

The potential energy surfaces for the coupled E_g states are represented by the matrix:

$$V_{E_g} = \begin{pmatrix} \frac{1}{2}k_S(Q_{a_{1g}} - \Delta Q_S)^2 & V_{ST} \\ V_{ST} & \frac{1}{2}k_T(Q_{a_{1g}} - \Delta Q_T)^2 \end{pmatrix} \qquad (3.1)$$

The diagonal elements correspond to the harmonic (diabatic) excited state potentials shown as dotted lines on the right-hand side of Figure 3.4, the diagonalized matrix defines the adiabatic potentials, shown as solid lines in the Figure. The indices S and T refer to singlet and triplet excited states, respectively, whose force constants $k_{S,T}$ are obtained from the vibrational frequencies given in Table 3.1. ΔE_{ST} denotes the energy difference between the origins of the transitions to coupled states of identical symmetry, given in Table 3.1. The coupling constant V_{ST} is set to the off-diagonal matrix element between the two E_g states, $-\sqrt{6}\lambda$, [23]using the numerical value of

-270 cm^{-1} for λ, the ground-state spin-orbit coupling constant[22] to obtain the coupling constant V_{ST} in Table 3.1. The offset ΔQ_T is assumed to be identical for all triplet states and is the only unknown model parameter.

The dominant contribution to the experimental oscillator strengths for the centrosymmetric complexes studied occurs via a vibronically induced electric dipole mechanism, illustrated by the magnitude and temperature dependence of the oscillator strength. The observed bands are therefore based on vibronic origins involving ungerade parity enabling modes onto which all progressions in totally symmetric modes are built. We base our model on a single effective vibronic origin offset by the same energy from the electronic origin for transitions to all four states arising from $^3T_{1g}$ and we neglect magnetic dipole progressions built directly on the electronic origins. The intensity distributions within a progression built on an electronic origin and on a corresponding vibronic origin are reported to be identical for a large number of transition metal compounds with resolved electronic spectra[24]. We assume that this is also the case for the title compounds. The energies of the effective vibronic origins are given in Table 3.1. The experimental bandwidths of the individual vibronic transitions in our spectra are too large to allow us to distinguish between several different vibronic origins, in contrast to a comprehensive literature study on $Ni(H_2O)_6^{2+}$[8], where two vibronic origins separated by 196 cm^{-1} were identified from a single crystal spectrum.

We use the time-dependent theory of electronic spectroscopy to calculate absorption spectra[25]. Its application to transition metal compounds has been discussed in detail previously[26, 27]. The absorption spectrum is given by

$$I(\omega) = C\omega \int_{-\infty}^{+\infty} e^{i\omega t} \left\{ \langle \phi | \phi(t) \rangle e^{-\Gamma^2 t^2 + \frac{iE_0}{\hbar} t} \right\} dt \qquad (3.2)$$

with I(ω) denoting the intensity at frequency ω in arbitrary units, E_0 the energy of the vibronic origin and Γ a phenomenological damping factor, determined from the width of each band forming the vibronic structure. Eq. 2 was used to calculate the spectra arising from the transitions to the A_{1g}, T_{1g}, T_{2g} and to the coupled E_g levels in $Ni(H_2O)_6^{2+}$.

The most important ingredient to eq. 3.2 is $<\phi|\phi(t)>$, the autocorrelation function of a wavepacket ϕ prepared on the potential energy surfaces of the final states at time t=0 in the course of the electronic transition. We assume transition dipole moments that are constant along Q_{a1g} and identical for all levels arising from the triplet excited state. The quantity ϕ in eq. 3.2 corresponds therefore to the lowest energy vibrational eigenfunction χ of the electronic ground state. The time-dependent wavefunction $\phi(t)$ is obtained with a split-operator algorithm[28] adapted to calculate wavepacket dynamics on one or two final electronic states[29-31].

The coupled potential surfaces in eq. 3.1 are used to calculate $\phi(t)$ for the E_g states. The time-dependent wavefunction is a vector quantity with two components, corresponding to the states of singlet and triplet parentage. The initial wavefunction ϕ is given by:

$$\phi = \begin{pmatrix} \phi_S(t=0) \\ \phi_T(t=0) \end{pmatrix} = \begin{pmatrix} \mu_S \chi \\ \mu_T \chi \end{pmatrix} \qquad (3.3)$$

with μ_S and μ_T denoting the dipole moments for the transitions to singlet and triplet excited states, respectively. In our model for $Ni(H_2O)_6^{2+}$ we use $\mu_T = 1$ for all triplet levels and set μ_S to zero, giving no intensity to the spin forbidden band in the absence of spin-orbit coupling. The intensity of the transition to the ^1E_g excited state is therefore entirely borrowed from the $^3T_{1g}$ band.

We calculate the total spectrum as a superposition of individual spectra for each of the A_{1g}, T_{1g} and T_{2g} levels with relative intensities of 1:3:3 based on the degeneracies of the final states, as suggested for $Ni(H_2O)_6^{2+}$ in the literature[5, 8]. These three spectra are shown on the left hand side of the central panel in Figure 3.4 and have their maxima at the calculated crystal field energies. The spectrum arising from the transition to the coupled E_g levels is given a relative intensity of 2, again assuming no intrinsic intensity for the $^3A_{2g} \rightarrow {}^1E_g$ transition, and it is added to the three Poisson bands for the transitions not involved in the singlet-triplet coupling. This total calculated spectrum and the experimental spectrum are shown as the two rightmost traces in the central panel to Figure 3.4. Their overall agreement is very good, especially considering that the model is based on an idealized point group and involves only a single adjustable parameter, ΔQ_T. We obtain a value of 0.30 Å for ΔQ_T, corresponding to an elongation of 0.12 Å for each Ni^{2+}-H_2O bond. This value is within the typical range determined in the literature for large d-d bands[26] and similar to the value of approximately 0.1 Å given in a semiquantitative configurational coordinate diagram[5]. The calculated spacing between members of

the progression on the high-energy side of the absorption band is 550 cm^{-1}, higher than the vibrational frequencies of all potential surfaces in the model calculation and in good agreement with the experimental separation of 490 cm^{-1}. To our knowledge this is the first *quantitative* calculation of both the energies and intensities of the vibronic structure for the $^3T_{1g}$ and ^1E_g excited states of $Ni(H_2O)_6^{2+}$.

The model in Figure 3.4 provides detailed insight on the singlet and triplet band assignments, which have caused some controversy in the literature[3-6, 8]. The singlet and triplet characters of the coupled E_g levels can easily be calculated from the crystal field eigenfunctions. At the left hand limit of the Dq/B abscissa the singlet character of the highest energy level, identified as ^1E_g, is 96%, the singlet character of the lower energy E_g level is only 4%. At the right-hand limit of the abscissa, the singlet character of the highest energy level decreases to 16%, the lower energy E_g level has singlet and triplet contributions of 83% and 17%, respectively. This electronic picture could lead us to attribute the lower energy band of the spectrum calculated for the coupled E_g states to the singlet and the higher energy band, which corresponds to the intense vibronic progression, to the triplet excited state. It is clear from the potential energy surfaces in Figure 3.4 that this assignment is not meaningful: the diabatic potential energy surface of the singlet excited state is placed higher in energy than the band assigned to the singlet based on electronic wavefunctions.

It is important to realize that all characterizations based on electronic wavefunctions apply to the rigid complex and implicitly involve the adiabatic approximation. Even in this approximation, the right hand panel to Figure 3.4 provides a more complete picture: the singlet and triplet character varies as the

complex moves along either the upper or lower adiabatic potential surface during a vibration. This variation is governed by the shapes and positions of the surfaces and the magnitude of the coupling constant V_{ST}, quantities that are only partially included in a purely electronic picture. Our analysis described in the preceding sections explicitly involves nonadiabatic transitions between the two surfaces, causing both the high intensity and the unusual vibronic splitting. The detailed spectra give therefore direct experimental information on the behavior of the complexes in coupled electronic states, a situation of current interest in photochemistry and molecular dynamics[1, 2].

Model calculations with inverted energetic order of the singlet and triplet diabatic potential energy surfaces did not lead to calculated spectra close to the experimental data, further corroborating our model analysis. Potential energy surfaces with minimum energies and positions similar to those in Figure 3.4 are also obtained for the following two compounds, where an automated and optimized search of parameter space was performed.

***trans*-$NiCl_2(H_2O)_4$: D_{4h} symmetry, two different singlets coupled to triplet states.**

In this point group the ^1E_g (O_h) excited state splits into $^1A_{1g}$ and $^1B_{1g}$ levels. The $^3T_{1g}$ state separates into $^3A_{2g}$ and ^3E_g, which are then further split by spin-orbit coupling, as illustrated in Scheme 3.1. The most important difference from O_h symmetry is that the $^3A_{2g}$ state can only interact with the $A_{1g}(^1A_{1g})$ state, whereas the ^3E_g state can couple to both $A_{1g}(^1A_{1g})$ and $B_{1g}(^1B_{1g})$.

The energetic order of triplet and singlet excited states in this tetragonal complex can be obtained from a crystal field calculation using the angular overlap formalism[32, 33]. The angular overlap parameters $e_\sigma(H_2O)$ and $e_\pi(H_2O)$ of 4380

cm^{-1} and 1000 cm^{-1} were determined from the spin allowed band maxima of $Ni(H_2O)_6(NO_3)_2$ at 5 K. The corresponding absorption maxima of $NiCl_6^{4-}$ in $CsCdCl_3$[34], $CsMgCl_3$[18, 19] and $NiCl_2$[10,35] were used to determine average values of 3700 cm^{-1} and 990 cm^{-1} for e_σ(Cl) and e_π(Cl), respectively. These values were then transferred to the mixed ligand complex $NiCl_2(H_2O)_4$. The Racah parameter B was set to 900 cm^{-1} (83% of the free ion value), the ratio C/B to 4 and the spin-orbit coupling constant ζ to 600 cm^{-1}. This calculation does not involve a fit, but it leads to spin allowed band maxima for $NiCl_2(H_2O)_4$ in satisfactory agreement with the experimental values obtained at 5 K. The first band maximum is broad and located between 8100 cm^{-1} and 8700 cm^{-1} (σ and π polarizations). It corresponds to the calculated maxima at 8114 cm^{-1} and 9200 cm^{-1} for the barycenters of the ^3E_g and $^3B_{2g}$ excited states, respectively. The second band is observed at 13240 cm^{-1} (σ) and 13430 cm^{-1} (π) and calculated at 13449 cm^{-1} ($^3A_{2g}(^3F)$) and 14183 cm^{-1} ($^3E_g(^3F)$). The narrow third band maximum is observed at 24300 cm^{-1} (σ and π), in good agreement with the calculated maxima at 24692 cm^{-1} ($^3A_{2g}(^3P)$) and 25258 cm^{-1} ($^3E_g(^3P)$).

The calculated energetic order of the excited states in the region of the NIR/VIS band system predicts the barycenter of the $^3A_{2g}$ state lower in energy by 735 cm^{-1} than the barycenter of the ^3E_g state. The $^1A_{1g}$ state is calculated at an energy lower by 178 cm^{-1} than the $^1B_{1g}$ state. This value compares favorably to the average separation of 75 cm^{-1} between the two progressions in the π polarized absorption spectrum in Figure 3.2, especially since no angular overlap parameters were fitted to the spectrum of $NiCl_2(H_2O)_4$. This qualitative energetic order is given in Scheme 3.1 and confirmed in the following.

The experimental spectrum of *trans*-$NiCl_2(H_2O)_4$ shows a double progression in π polarization, but only the lower energy progression appears in σ polarization. The band maximum of the broad band in σ polarization is at lower energy than in π polarization. Transition energies and vibronic patterns can be combined with the calculated crystal field energies and indicate that the σ polarized spectrum is dominated by the $^3B_{1g} \rightarrow {}^3A_{2g}$ band. This triplet excited state can only interact with the $^1A_{1g}$ state. The $^3B_{1g} \rightarrow {}^3E_g$ transition is expected at higher energy, as observed in π polarization. The ^3E_g state has A_{1g} and B_{1g} spin-orbit levels that can interact with both singlet excited states, leading to the two superposed progressions in the spectrum and confirming the energetic order derived from the angular overlap model. This experimental observation confirms that the singlet states gain most of their intensity from the triplet transitions, justifying the assumption made for the model in Figure 3.4.

The main contribution to the oscillator strength of the spectra in Figure 3.2 again arises from vibronic mechanisms involving ungerade parity enabling modes. These vibrational modes of $NiCl_2(H_2O)_4$ have been studied in detail[13], and several e_u, a_{2u} and b_{2u} vibrations with frequencies between 100 cm^{-1} and 400 cm^{-1} are reported[13]. The oscillator strength of the spectra in Figure 3.2 is most likely built on such low-energy vibronic origins. Absorption and MCD spectra of octahedral $Ni(H_2O)_6^{2+}$ complexes with resolved vibronic origins show that t_{1u} modes are the most efficient enabling modes[8]. The t_{1u} mode splits into e_u and a_{2u} in the D_{4h} point group, indicating that b_{2u} modes are less important as enabling modes. We use group theoretical selection rules to examine the possible enabling modes for the spin

allowed bands. In π polarization, the $^3B_{1g} \rightarrow {}^3E_g$ transition is only allowed with an e_u enabling mode and the $^3B_{1g} \rightarrow {}^3A_{2g}$ transition is not allowed with any of the ungerade parity enabling modes. The transition to the ^3E_g state therefore dominates the observed spectrum in π polarization and enabling modes of e_u symmetry are very efficient. In σ polarization, the $^3B_{1g} \rightarrow {}^3A_{2g}$ transition is allowed with e_u enabling modes, indicating that the experimental spectrum is dominated by this transition. The $^3B_{1g} \rightarrow {}^3E_g$ transition in σ polarization is allowed with a_{2u} or b_{2u} enabling modes which appear to be less efficient because no replica of the bandshape observed in π polarization, involving only the ^3E_g state, can be observed in the σ polarized spectrum of Figure 3.2. Both the group theoretical analysis of the observed polarizations and the comparison of calculated crystal field energy levels with experimental band maxima therefore confirm that the σ and π polarized spectra show predominantly the transitions to the $^3A_{2g}$ and ^3E_g states, respectively.

We use the same approach as presented for $Ni(H_2O)_6^{2+}$ in the preceding section, but we limit the calculation to the σ polarized spectrum involving the $^3A_{2g}$ and $^1A_{1g}$ excited states. The model involves coupled A_{1g} surfaces and a simple harmonic surface for the E_g level of the $^3A_{2g}$ state, leading to a Poisson bandshape. The intensity ratio of the two partial spectra is 1:2, again analogous to the calculation described for $Ni(H_2O)_6^{2+}$. The origins of the three transitions to singlet and triplet states, the offsets of the minima of both the triplet and singlet levels along Q_{a1g}, the vibrational frequency describing the harmonic potentials for the triplet excited states, the coupling constant V_{ST} and the transition moments μ_S and μ_T are all treated as adjustable parameters. We apply a simulated annealing technique to efficiently and

systematically search this parameter space[36]. All parameters resulting from this refinement were obtained from several different sets of initial guesses using different annealing temperature profiles, indicating that the fit parameters are unique and correspond to the global minimum in parameter space. Their final numerical values are summarized in Table 3.1 and lead to a very good agreement between calculated and experimental spectra, as illustrated in Figure 3.5a. The calculated spacing within the intense progression is 420 cm^{-1}, in excellent agreement with the experimental spacing of 430 cm^{-1}. The difference trace between experimental and calculated spectra is included in the Figure. The differences are largest in the region between maxima of the vibronic progressions, most likely a consequence of our neglect of low-frequency lattice modes. The maxima of the vibronic progressions are well reproduced by our model. The difference trace reflects mainly the limitation to one vibrational mode, the assumption of harmonic potentials for the electronic states and the neglected coupling to energetically far A_{1g} states. Errors of the parameters resulting from the fit are smaller than 0.5%, but these errors again are influenced by the intrinsic model assumptions. A more realistic evaluation of the fit results is obtained by a comparison of the results for all three nickel(II) complexes. Our fit leads to parameter values very similar to those for $Ni(H_2O)_6^{2+}$. It is reassuring that distortions ΔQ_T identical to three significant digits are obtained for the A_{1g} and E_g levels arising from the triplet excited state, despite their treatment as independent parameters in our fit procedure. The coupling constant V_{ST} resulting from the fit varies by only 10 % from the value used for $Ni(H_2O)_6^{2+}$, where it was not an adjustable parameter. The analysis for the tetragonal complex reveals therefore

excited states with properties almost identical to the octahedral complex described in the preceding section. We note that the fit leads to small but nonzero values for μ_S and ΔQ_S, slightly different from $Ni(H_2O)_6^{2+}$. These differences could be caused by the assumption of one dimensional potential energy surfaces for $NiCl_2(H_2O)_4$, a complex with two totally symmetric stretching modes involving aquo and chloro ligands.

$NiCl_6^{4-}$: D_{3d} symmetry, one singlet coupled to several triplet states.

The spectrum of $CsMgCl_3:Ni^{2+}$ in the region of interest is very similar in σ and π polarization, and we use only the σ polarization for the following analysis[18, 19]. The electronic states in D_{3d} symmetry are shown in Scheme 3.1. Both the $^3A_{2g}$ and ^3E_g excited states have E_g spin-orbit levels that can interact with the $E_g(^1E_g)$ state. The splitting between the two triplet states is larger than 1000 cm^{-1}, determined experimentally from luminescence spectra arising from a higher excited state[37]. This system gives us the opportunity to examine the effects of three energetically different E_g levels of triplet parentage on the E_g level arising from ^1E_g. We make three separate calculations for the three sets of coupled E_g levels. The spectroscopic effects of coupling between E_g levels arising from the triplet states are negligible because the states have potential surfaces that are only displaced along the energy axis but not along Q_{a1g}. The partial spectra for the coupled E_g states and the total calculated spectrum are shown in Figure 3.5b, with the spectra involving the two closely spaced E_g states at lowest energy added together for clarity. The total calculated spectrum is in excellent agreement with the experiment. The difference trace again shows

minimal differences in the region of the vibronic maxima and larger differences between maxima, most likely for the same reasons discussed for $NiCl_2(H_2O)_4$. We calculate a progression interval of 320 cm^{-1}, close to the experimental interval of 300 cm^{-1}. Adjustable parameters include the origins listed in Table 3.1, the vibrational frequency of the excited triplet states, the offsets ΔQ_S and ΔQ_T and the coupling constant V_{ST}. The energetic order of the $^3A_{2g}$ and ^3E_g states can not be independently confirmed from the complicated excited-state spectra in this region[37, 38]. The crystal field approach used for $NiCl_2(H_2O)_4$ is problematic for the hexachloride complexes because the crystal field potential appears to be significantly influenced by ions outside the first coordination sphere[16]. The energies of the triplet excited states resulting from our fit indicate that the ^3E_g state is lower than the $^3A_{2g}$ state, as summarized in Table 3.1.

The spectra for the sets of coupled E_g surfaces in Figure 3.5b show that energetically close levels of singlet and triplet parentage give rise to a band shape with two maxima of comparable intensity and a vibronic progression with a large spacing, whereas the band shape calculated for E_g states with a larger energy separation shows two unresolved bands of unequal intensity with the weaker transition attributed to the excited state with predominant singlet character. An experimental spectrum similar to the latter situation is reported for $CsCdCl_3:Ni^{2+}$[39], where the triplet and singlet maxima are separated by 2000 cm^{-1} and only a weak, narrow band is observed on the high energy side of the broad spin allowed transition. This trend justifies the limitation of our spectroscopic model to pairs of coupled states that are energetically close. A large energy separation between levels of the same

symmetry leads to very weak effects in the absorption spectra that can not be easily observed experimentally.

Origin of the large energy difference in the intense progression.

Both the intensity and the vibronic structure of the spin forbidden transition can be rationalized from the time dependent wavefunction on the coupled potential energy surfaces obtained from the calculation of the spectra. We use the autocorrelation function and time dependent populations of the diabatic surfaces for V_{ST}=0 and for the values of V_{ST} given in Table 3.1 and we neglect all levels with symmetries different from those of the coupled states. Figure 3.6 shows the coupled potentials for $NiCl_2(H_2O)_4$ and for $CsMgCl_3:Ni^{2+}$. The intersection of the singlet and triplet surfaces is close to the Franck-Condon region in both complexes. The absolute autocorrelation functions are shown in Figures 3.7a and 3.8a. The dotted curves for V_{ST}=0 show an initial drop and a recurrence after one vibrational period. Two important changes occur for nonzero values of the coupling constant: a new maximum appears at very short times (10-30 fs), and the maximum corresponding to one vibrational period has a more complicated shape with its initial rise at a shorter time than calculated for V_{ST}=0. These two effects lead to major changes of the band shape: the short-time maximum corresponds to spectral intensity at energies higher by autocorrelation functions are shown in Figures 3.7a and 3.8a. The dotted curves for V_{ST}=0 show an initial drop and a recurrence after one vibrational period. Two important changes occur for nonzero values of the coupling constant: a new maximum appears at very short times (10-30 fs), and the maximum corresponding to one vibrational period has a more complicated shape with its initial rise at a shorter

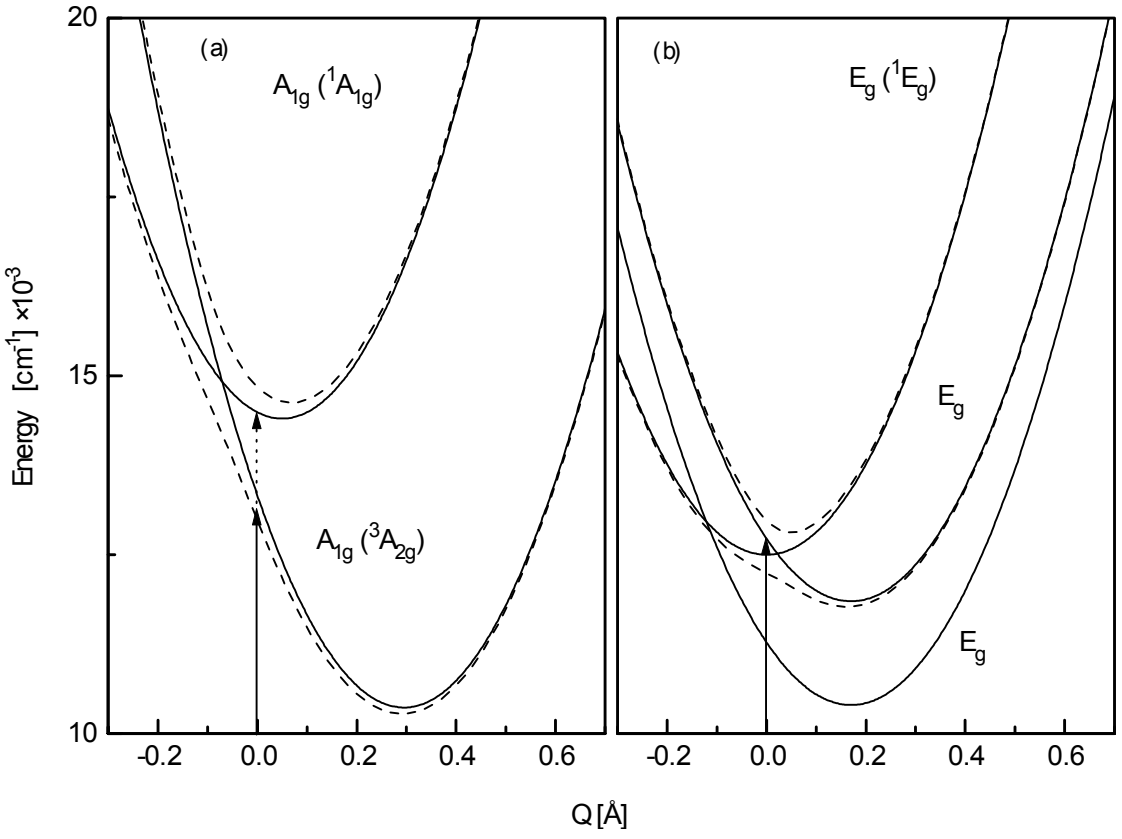

Figure 3.6 Potential energy diagrams for trans-$NiCl_2(H_2O)_4 \cdot 2H_2O$ (a) and $CsMgCl_3:Ni^{2+}$ (b) Diabatic and adiabatic potentials are shown as solid and dotted lines, respectively. Arrows denote Franck-Condon transitions from the ground state.

time than calculated for V_{ST}=0. These two effects lead to major changes of the band shape: the short-time maximum corresponds to spectral intensity at energies higher by consequence of intersystem crossings. The shorter time of the first recurrence after one vibrational time period accounts for the larger separation of the members of the progression. We note that the larger spacing between the vibronic levels of the singlet excited states is qualitatively anticipated from the shape of the upper adiabatic potential surface. For nonzero coupling, this surface is narrower than the harmonic (diabatic) potential and a larger spacing of the energy levels is expected, but the adiabatic limit does not allow us to calculate band intensities for both the singlet and triplet states.

The autocorrelation for coupled states is strongly influenced by the transfer of wavepacket amplitude between the two surfaces, as illustrated in Figures 3.7b, 3.8b and 3.8c on the same time scale as used for the autocorrelation functions in Figures 3.7a and 3.8a. The wavepacket amplitude is calculated by integrating ϕ_S and ϕ_T as defined in eq. 3.3 for each point along the time axis. These time dependent amplitudes or populations show a drop for the 'allowed' surface at short times, followed by a back transfer of amplitude within 15 fs, leading to a new maximum of the autocorrelation. This transfer occurs initially when the wavepacket moves through the crossing region and modulates the autocorrelation at short times, as illustrated by the comparison of the population and autocorrelation curves. The populations on the two surfaces remain approximately constant when the wavepacket is far from the crossing region. Large changes occur again after one vibrational time period, when the time-dependent wavefunction is back near the crossing. These population changes

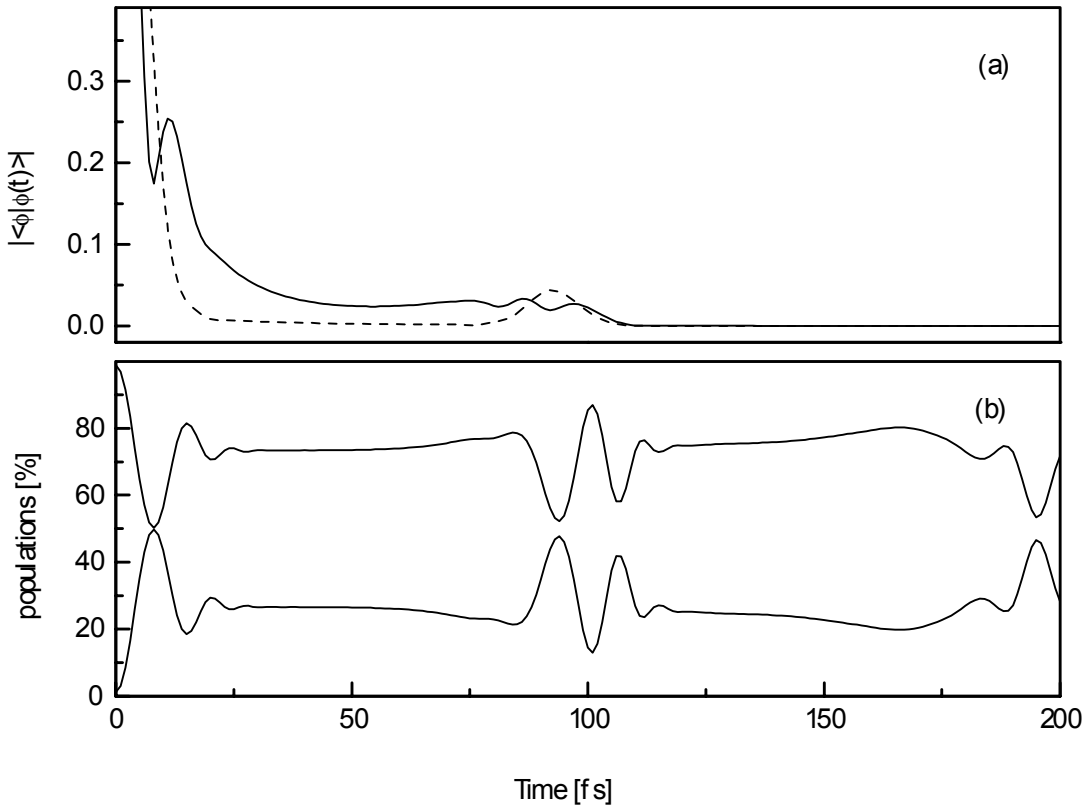

Figure 3.7 Absolute values of the autocorrelation (a) and time dependent populations (b) of the coupled $A_{1g}(^1A_{1g})$ and A_{1g} $(^3A_{2g})$ excited states in Figure 3.6a for *trans*-$NiCl_2(H_2O)_4 \cdot 2H_2O$. Solid lines indicate calculations with the coupling constant V_{ST} in Table 3.1, dotted lines denote calculations with $V_{ST} = 0$.

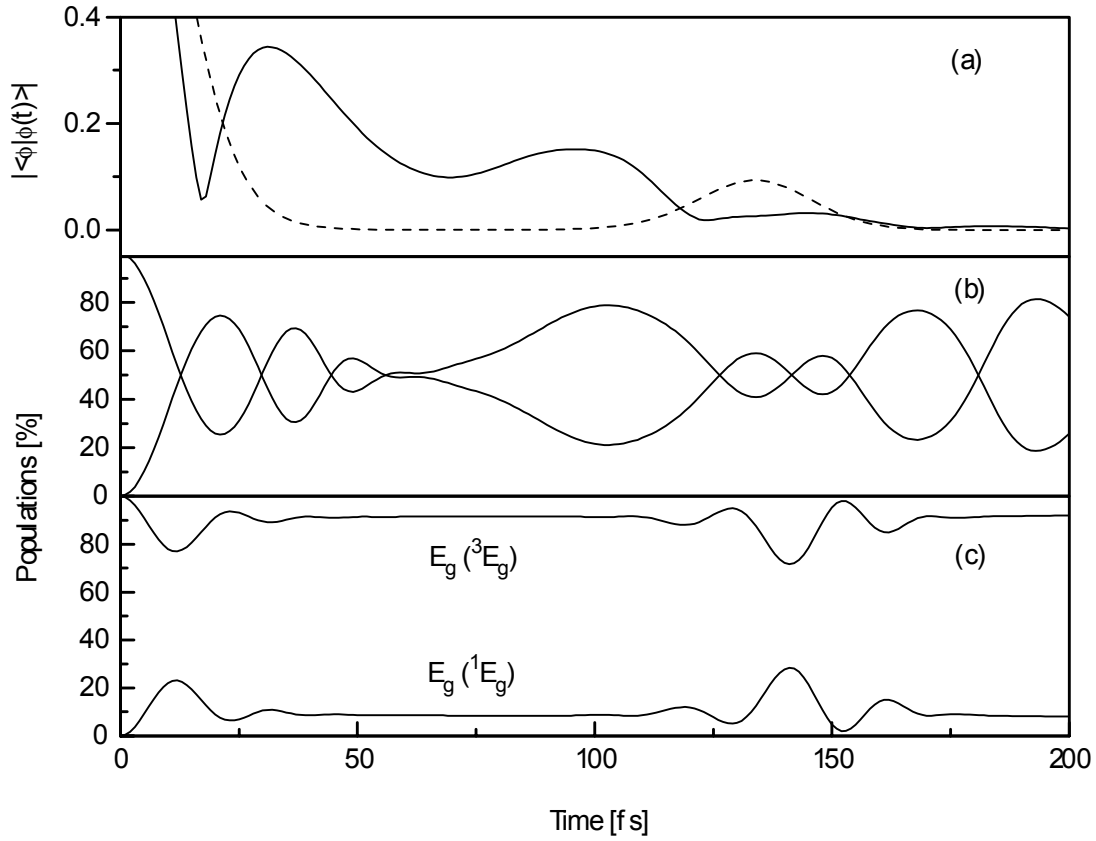

Figure 3.8 Absolute values of the autocorrelation (a) and time dependent populations (b) of the energetically close pair of E_g excited states in Scheme 3.1 and Figure 3.6b for $CsMgCl_3:Ni^{2+}$. Solid lines indicate calculations with the coupling constant V_{ST} in Table 3.1, dotted lines denote calculations with $V_{ST}=0$. The time dependent populations for the coupled E_g states with a large energy separation are shown for comparison in (c).

lead to the complicated shape of the first recurrence in the autocorrelation of the coupled system and to the large spacing of the vibronic progression.

The time dependent populations of the coupled states can also be used to examine the singlet and triplet assignments made for the title complexes. Figures 3.7b and 3.8c show that the average population of the triplet level is significantly higher than that of the singlet level, in intuitive agreement with the expectations for spin allowed and spin forbidden transitions. At certain times the populations can be equal or even inversed, a consequence of the time dependent wavefunction changing surfaces as it moves along Q_{a1g}, indicating the nonadiabatic behavior of the molecule in these interacting excited states and illustrating the difficulty of assigning singlet and triplet bands. Figure 3.8b shows the complicated crossover dynamics for states close in energy. The attribution of singlet and triplet character based on the time-dependent populations is impossible in this case, and physical and chemical properties of the singlet-triplet system can not be determined separately, illustrating the shortcomings of traditional spectroscopic assignments and of some analyses of photochemical reactivities.

Alternative interpretations of the band shape.

An alternative explanation of the double maximum observed in the room temperature absorption spectrum of $Ni(H_2O)_6^{2+}$, where the high-frequency progression is not resolved, assigns the band shape to a Jahn-Teller effect in the $^3T_{1g}$ state with no spectroscopic evidence for the ^1E_g state[11]. The experimental observation of similar spectra for complexes with very different symmetries presented in this work and in the literature[6, 8], and the absence of a significant Ham

quenching of the electronic origins of the $^3T_{1g}$ band[8] provide clear experimental evidence against a strong Jahn-Teller effect in the $^3T_{1g}$ state. Only a strong Jahn-Teller effect involving a significant distortion along the normal coordinates of the active modes could account for the large splitting of the observed absorption band. A comprehensive study of these bands in a large series of complexes at room temperature indicates that a double maximum of the $^3T_{1g}/^1E_g$ band system is only observed for a narrow range of crystal field parameters between $0.8<Dq/B<1.1$[6]. Such a strong dependence of the Jahn-Teller distortions on Dq/B is not expected.

We note that the large vibronic spacing observed in the title compounds can not be attributed to a missing mode effect (MIME), used to explain unusual spacings in a variety of transition metal complexes[40, 41]. The MIME arises from excited state distortions along multiple normal coordinates and can not lead to progression intervals that are larger than the largest vibrational frequency involved[40], as is the case for the title compounds.

A literature analysis of the absorption spectra of $NiCl_2$ and $NiBr_2$ proposes a two-phonon progression involving two quanta of the e_g vibration separating each member to account for the large progression interval[10]. The overall absorption spectra of these layered halides are very similar to those of $CsMgCl_3:Ni^{2+}$ and we compare the literature analysis to our model in the following. The experimental progression interval for $NiCl_2$ is 335 cm^{-1}[10]. The progression has five clearly discernible members and an intensity distribution similar to that of $CsMgCl_3:Ni^{2+}$, shown in Figure 3.5b. The point group of the $NiCl_6^{4-}$ unit is D_{3d}, but the distortion of the octahedral coordination sphere along the trigonal axis is a compression rather than an elongation as in $CsMgCl_3:Ni^{2+}$[42, 42]. The vibrational frequencies of the a_{1g} and

e_g modes of $NiCl_2$ are 269 cm^{-1} and 173 cm^{-1}, respectively[44]. Progressions involving two quanta between each member are possible for non-totally symmetric modes, such as the e_g vibration, based on symmetry arguments[10]. They are dominating the spectrum if the initial and final potential energy surfaces have different vibrational frequencies and if their minima are at exactly the same position along the normal coordinate. We examine a simple model of this situation based on the ground state frequency for the e_g mode and an excited state frequency of 167 cm^{-1}, corresponding to half the experimental spacing in the progression observed for $NiCl_2$. A calculation with these values leads to an intensity ratio of 1:0.0008 for the members of the progression involving 0 and 2 quanta of the e_g vibration, far from the ratio of 1:0.5 (±0.3) estimated from the experimental intensities of the intense progressions in Figures 3.2, 3.4 and 3.5. A displacement of the excited state potential surface by just 0.01 Å along the e_g normal coordinate leads to a progression with its members separated by only <u>one</u> quantum of the vibrational energy, i.e. only half the observed interval. The intensity ratio of the first and second members of this progression is 1:0.009, an intensity for the second band higher by an order of magnitude than the two-quanta sideband observed for zero displacement. It is therefore not possible to quantitatively rationalize the intense vibronic progression in $NiCl_2$ and $CsMgCl_3:Ni^{2+}$ as a two-phonon progression in the e_g mode. The special case of a strong $e_g \times E_g(^1E_g)$ Jahn-Teller effect in these trigonal systems should lead to dramatically different spectra from those observed for tetragonal complexes such as $NiCl_2(H_2O)_4$, where the singlet excited states are no longer degenerate. We therefore conclude that the intense progression observed in several nickel halides arises from

spin-orbit coupling between the singlet and triplet excited states, analogous to the situation for the $Ni(H_2O)_6^{2+}$ complex.

Conclusion

Our model rationalizes absorption band positions, intensities and the unusual vibronic structure observed for a variety of nickel(II) compounds and underlines the important influence of intersystem crossings in these complexes. The physical origins of the observed spectroscopic effects can be identified from low-temperature, polarized single-crystal spectra and are qualitatively similar to those of interference dips and intensity borrowing[45, 46]. Our experimental and calculated spectra illustrate that the intervals observed in vibronic progressions can depend on interactions between different electronic states, an effect that has traditionally been neglected.

Acknowledgments

This work was made possible by research grants from the NSERC (Canada). We thank Hans U. Güdel for allowing us to use the absorption spectrum of $CsMgCl_3:Ni^{2+}$, measured by C. R. in his laboratory.

Chapitre 4: Couplage entre états excités dans des complexes de type *trans*-$[MCl_2(H_2O)_4]^{n+}$ (M: Ni^{2+}, Co^{2+}, V^{3+}, Cr^{3+}) étudié par spectroscopie d'absorption et de luminescence.

Coupled electronic states in *trans*-$MCl_2(H_2O)_4^{n+}$ complexes (M: Ni^{2+}, Co^{2+}, V^{3+}, Cr^{3+}) probed by absorption and luminescence spectroscopy

Guillaume Bussière, Rémi Beaulac, Benoit Cardinal-David, and Christian Reber

Coord. Chem. Rev. **2001**, *219-221*, 549-583

Table des matières

This paper is dedicated to Professor Barry Lever on the occasion of his 65th birthday.

Abstract

The electronic spectra of *trans*-$MCl_2(X_2O)_4^{n+}$ complexes (M: Ni^{2+}, Co^{2+}, V^{3+}, Cr^{3+} and X: H, D) are analyzed in order to understand interactions between electronic states. We present detailed low temperature polarized absorption spectra of single crystals. Spectra were measured over a large range, from the NIR to the UV, and they show several spectroscopic effects arising from interactions between electronic states. The lowest-energy electronic transition in $VCl_2(H_2O)_4^+$ consists of sharp weak bands between 950 and 1030 nm, well separated from the more intense spin allowed bands. Observed energy differences and the temperature dependence of the transition intensities lead to a quantitative characterization of the ground state splitting. The analogous $CrCl_2(H_2O)_4^+$ chromophore has a much smaller energy separation between its lowest energy spin forbidden transition and the first spin allowed band. We examine the effect of this difference on the resolved spectra and compare it to related transition metal complexes. The strongest interaction between electronic states occurs in $NiCl_2(H_2O)_4$, where the lowest energy singlet state is very close in energy to a spin allowed crystal field band, giving rise to intense vibronic patterns. Experimental spectra are analyzed quantitatively using the time dependent theory of spectroscopy and established crystal field and Jahn-Teller approaches.

Keywords: Absorption spectroscopy; Emission spectroscopy; Raman spectroscopy; Nickel complexes; Vanadium complexes; Chromium complexes; Cobalt complexes.

1. Introduction

Effects arising from coupled electronic states are important to many areas of chemistry, especially for transition metal compounds, which have a rich electronic structure where many states can interact[1]. Intersystem crossings in transition metal compounds have been reported and were discussed qualitatively, but most often not quantitatively, by several authors in the past[2-6]. There are numerous experimental manifestations of coupling between electronic states, and we will present examples involving spin-orbit coupling, the Jahn-Teller effect and configuration interaction. Our study is based on experimental low temperature absorption and emission spectra of *trans*-$MCl_2(X_2O)_4^{n+}$ (M: V^{3+}, Cr^{3+}, Co^{2+}, Ni^{2+}; X: H, D) complexes. Spin-orbit coupling between electronic states of different multiplicity is present in all complexes, but the magnitude of the resulting spectroscopic effects depends strongly on parameters like the spin-orbit coupling constant, the energy difference between interacting states, their potential surfaces and the off-diagonal ligand field matrix element between the states. We compare quantitatively the spectroscopic consequences of spin-orbit interaction in a series of transition metal complexes with the *trans*-dichlorotetraaquo ligand environment.

Several spectroscopic investigations of the $MCl_2(H_2O)_4^{n+}$ chromophores are reported in the literature. McCarthy *et al.*[7, 8] have extensively studied the absorption spectra of $Cs_2CrCl_5{\cdot}4H_2O$ and $Cs_3VCl_6{\cdot}4H_2O$. Spectroscopic studies of $CoCl_2(H_2O)_4{\cdot}2H_2O$ were reported by Ferguson[9], Ferguson and Wood[10], Joy and Fogel[11] and Pappalardo[12]. The only spectroscopic study on $NiCl_2(H_2O)_4{\cdot}2H_2O$ reported before 1998 is by Gieleβen[13], who has also studied a series of other

complexes of divalent metals with this ligand sphere. His pioneering publication in 1935 predates most applications of quantum mechanical models to transition metal compounds. To our knowledge, no quantitative overall comparison of the spectra of *trans*-dichlorotetraaquo complexes has been published.

The time dependent theory of spectroscopy is used in order to quantitatively describe intersystem crossings in the title compounds. The calculation of absorption spectra by time dependent theory was established by Heller[14]. The application of the theory to transition metal complexes has been discussed in detail in previous publications[15, 16]. We have developed an approach for $NiCl_2(H_2O)_4$ and extend it to all compounds discussed here[1]. In view of the good agreement between experimental and calculated spectra, it appears that time dependent theory is an essential tool to understand electronic spectra and electronic structure of transition metal compounds.

2. Experimental Section

2.1. Nickel and cobalt complexes

Crystals of *trans*-$MCl_2(X_2O)_4 \cdot 2X_2O$ (X = H or D, M = Ni^{2+} or Co^{2+}) were obtained by slow evaporation of saturated solutions of MCl_2 in X_2O over several days (in a dessicator for D_2O). $NiCl_2(H_2O)_4 \cdot 2H_2O$ crystallizes as regular monoclinic green prisms[17]. The crystal used for spectroscopic measurements had clearly defined optical extinction directions, determined between crossed polarizers. The polarized low temperature absorption spectra were measured with the light beam perpendicular to the *ab* crystallographic plane. The projection of the molecular Cl-Ni-Cl axis in this

plane is parallel to the crystallographic *a* axis and perpendicular to the *b* axis. The crystal was oriented on a X-ray diffractometer and the axes which are parallel to the extinction directions were identified. The labels π and σ refer to the orientation of the molecular Cl-M-Cl axis relative to the electric vector of polarized light. $CoCl_2(H_2O)_4 \cdot 2H_2O$ crystallizes as regular monoclinic mauve prisms. The crystals are strongly dichroic and appear orange with the electric vector perpendicular to the *b* axis and mauve with the vector parallel to the *b* axis[9]. The orientation of the unit cell with respect to the crystal faces was also crystallographically determined in order to define the π and σ polarizations. Our analysis of the polarization directions is confirmed by the literature studies on $CoCl_2(H_2O)_4 \cdot 2H_2O$ which is isostructural to the nickel(II) analog[17, 18].

2.2. Vanadium and chromium complexes

Crystals of $Cs_3VCl_6 \cdot 4X_2O$ and $Cs_2CrCl_5 \cdot 4X_2O$ (X = H or D) were obtained by slow evaporation of saturated acidic solutions of CsCl and MCl_3 (XCl 2M in X_2O, X = H or D, M = V^{3+} or Cr^{3+}) over several days (in a dessicator for D_2O). $VCl_3 \cdot 6X_2O$ was prepared by hydrating (with H_2O or D_2O) anhydrous VCl_3. $CrCl_3 \cdot 6H_2O$ is available commercially and $CrCl_3 \cdot 6D_2O$ can be obtained by several recrystalizations in D_2O. Crystallographic studies confirm that these compounds contain the *trans*-$MCl_2(X_2O)_4^+$ chromophore[7, 8, 19-23]. Infrared spectroscopic measurements show that our deuterated compound contains less than 4% hydrogen. $Cs_3VCl_6 \cdot 4X_2O$ crystallizes as dark green rectangular prisms, with one side particularly longer than

the others. These crystals had clearly defined optical extinction directions, parallel to the crystallographic axes, determined between crossed polarizers. The molecular Cl-V-Cl axis is parallel to the crystallographic *a* axis, which coincides with the short side of the crystals. $Cs_2CrCl_5 \cdot 4X_2O$ forms dark green, slightly dichroic crystals[7]. $Cs_2CrCl_5 \cdot 4X_2O$ crystallizes in the monoclinic space group C2/m[21, 22].

2.3. Spectroscopic instrumentation

Crystal thicknesses for absorption spectroscopy were between 0.5 mm and 5 mm. Low temperature polarized spectra were measured with a Varian Cary 5E spectrometer equipped with a pair of Glan-Taylor polarizers. All spectra are corrected for the baseline of the instrument. The sample temperature was controlled with an Oxford Instruments CF-1204 helium gas flow cryostat. Raman spectra were measured using a Renishaw System 3000 Raman imaging microscope. The microscope was used to focus the laser light onto a spot approximately 1 μm in diameter and to collect the scattered light. Spectra were measured using four different excitation wavelengths: 782 nm (NIR diode laser), 632.8 nm (HeNe), 514.5 and 488.2 nm (argon ion) and the appropriate Renishaw notch filters allowing us to obtain clean spectra down to 100 cm^{-1} from the excitation wavelength. Back scattering Raman intensities were detected using a Peltier cooled CCD detector.

Emission spectra were taken using two different apparatus. The most sensitive instrument between 400 and 1050 nm is the Renishaw 3000 Raman imaging microscope. The Raman system was equipped with an elbow objective to focus the

laser on the sample and to collect the emitted light in the helium cryostat described above. The measurements between 1050 and 1650 nm were made with a Hamamatsu R5509-72 (serial No. JE-0156) photomultiplier tube cooled with liquid nitrogen. The 488 and 514 nm lines of a Coherent Innova CR-12 ion argon laser with the appropriate interference filters were used as excitation sources.

Lifetime measurements were made using a Continuum Minilite II Q-switched Nd:YAG pulsed laser at 532 nm. Measurements between 650 nm and 800 nm were made with a Hamamatsu R4632 photomultiplier connected to an optically triggered (Thorlabs FDS100 Si photodiode) Tektronix TDS380 digital oscilloscope.

3. *trans*-$NiCl_2(H_2O)_4$

3.1. $NiCl_2(H_2O)_4 \cdot 2H_2O$

We have reported previously [1] that nickel (II) aquo and chloro complexes are ideal models for a comprehensive study of interactions between electronic excited states. In fact, the $NiCl_2(H_2O)_4$ chromophore has the energetically closest electronic excited states of different spin multiplicity in the $MCl_2(X_2O)_4^{n+}$ series reported here. The energy separations between the first spin forbidden and spin allowed transitions vary in the order: $V^{3+} > Cr^{3+} > Ni^{2+}$, Co^{2+}. An advantage of the nickel(II) electronic structure for quantitative theoretical modeling is that the problem can be reduced to an interaction between two electronic states. This simple model cannot be used quantitatively to analyze more complicated cases, for instance the spectrum of the cobalt(II) complex in the visible spectral region. This d^7 ion has half-integer J values and double group symmetry labels have to be used, leading to interactions between

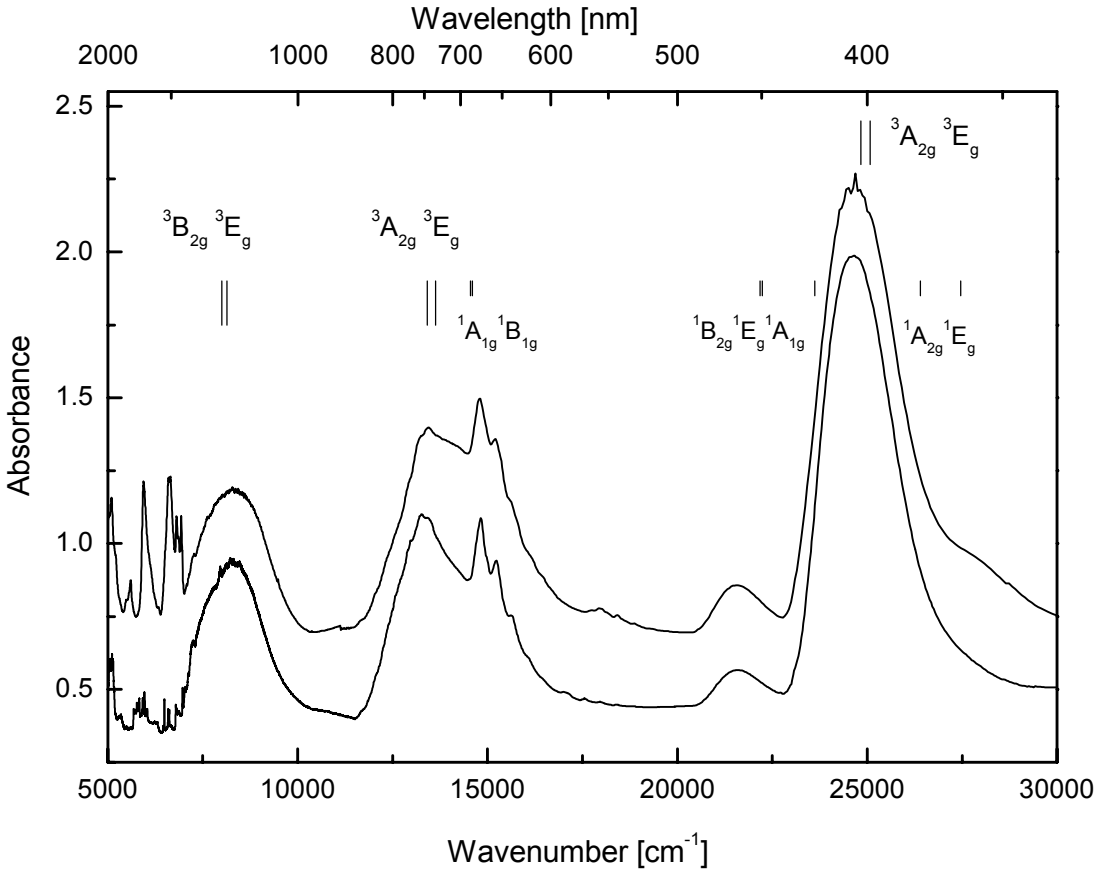

Figure 4.1 Unpolarized absorption spectra of $NiCl_2(H_2O)_4 \cdot 2H_2O$ (top trace) and $NiCl_2(D_2O)_4 \cdot 2D_2O$ (bottom trace) at 5 K. The vertical lines represent the AOM energies calculated with parameters from Table 4.2 with ζ=0. The tall lines represent spin-allowed transitions, the short lines the spin-forbidden transitions.

multiple electronic states, a situation that is hard to analyze quantitatively. Another characteristic of the nickel(II) system is the large matrix element between interacting states and the highest spin-orbit coupling constant λ of the metals studied here, as summarized in Table 4.1.

3.2. Spectroscopic results

The overall absorption spectrum of the $Ni(X_2O)_4Cl_2$ chromophore is presented in Figure 4.1 and it shows three spin-allowed crystal field bands and two spin forbidden transitions. The oscillator strengths for the spin allowed and the first spin forbidden bands in the unpolarized spectrum are on the order of 5×10^{-6} (band at 13459 cm^{-1}) and 3.6×10^{-7} (14820 cm^{-1}), respectively[1]. The value for the allowed transition is in the usual range but the value for the forbidden band is quite high, leading to an abnormally low intensity ratio $I_{triplet}$ / $I_{singlet}$ of 14. The main feature of this spectrum is the intense vibronic progression on the high-energy side of the middle band. This vibronic progression has a higher spacing than the ground state vibrational frequency of the totally symmetric nickel-aquo stretching mode. Such progressions are observed for many nickel(II) complexes in the $^3T_{1g}$ / ^1E_g (O_h labels) region of the spectrum, where crossing between allowed and forbidden states occurs. For the $NiCl_2(H_2O)_4$ chromophore, the σ polarized spectrum has a simple vibronic progression while a doubled pattern appears in π polarization, as shown in Figure 4.2.

Table 4.1 Comparison of parameters relevant for intersystem crossings in $MCl_2(H_2O)_4^{n+}$ complexes.

Chromophore symmetry of the coupled states (O_h point group)	Energy separation of the first forbidden and the closest allowed transition (between maxima)	Matrix element (coupling constant between the states)	Intensity ratio $I_{allowed}$ / $I_{forbidden}$ of coupled spin-orbit sublevels.	Relation between λ and ζ, λ value and percentage of the free ion value	λ and ζ for the free ion (cm^{-1}) [63]
$NiCl_2(H_2O)_4$ $^3T_{1g}/^1E_g$	1344 cm^{-1}	$-\lambda\sqrt{6}$ 730 cm^{-1}	6.1 $(A_{1g}/A_{1g})^{\dagger}$ 2.8 (calculated)	$\lambda = -\zeta/2$ -298 cm^{-1} (92%)	λ=-324 ζ=648
$CrCl_2(H_2O)_4^+$ $^2E_g/^4T_{2g}$	1979 cm^{-1}	$-3\lambda\sqrt{6}/\sqrt{5}^{*}$ -187 cm^{-1}	95 $(U/U)^{\dagger}$ 87 (calculated)	$\lambda = \zeta/3$ 57 cm^{-1} (63%)	λ=91 ζ=273
$VCl_2(H_2O)_4^+$ $^1T_{2g}/^3T_{2g}$	6687 cm^{-1}	$-\lambda\sqrt{6}^{**}$ -233 cm^{-1}	1118 (T_{2g} / T_{2g}) 1275 (calculated)	$\lambda = \zeta/2$ 95 cm^{-1} (91%)	λ=104 ζ=208
$CoCl_2(H_2O)_4$ $^4T_{2g}/^2E_g$	4000 cm^{-1}	0 cm^{-1}	-	$\lambda = -\zeta/3$ -172 (96%)	λ=-180 ζ=540

*Highest possible value[5, 43]

**For $^1T_{2g}$, it is 0 for ^1E_g[43]

†Error on experimental value is large due to the difficulty to separate the experimental spectrum into two bands

Table 4.2 Spectroscopic parameters and ligand field calculations for the title complexes.

	Raman frequencies 83K *(cm^{-1})*	**Absorption 5 K** *(cm^{-1}) [{D_{4h}} O_h (ion)]* *<polarization>*	**Calculated ligand-field energies** *[D_{4h} (spin-orbit)]*	**Emission 5 K** *(cm^{-1}) [D_{4h}]*	**angular overlap parameters for ligand field calculations** *(cm^{-1})*
$NiCl_2(H_2O)_4 \cdot 2H_2O$	296 364 377 548 701	8279 [$^3T_{2g}$] 13245 [{$^3A_{2g}$} $^3T_{1g}$] <σ> 13430 [{^3E_g} $^3T_{1g}$] <π> 14803 [^1E_g] 21614 [$^1A_{1g}$, $^1T_{2g}$] 24691 [$^3T_{1g}$ (^3P)]	8000 [$^3B_{2g}$]^b 8142 [^3E_g]^b 13416 [$^3A_{2g}$]^b 13634 [^3E_g]^b 15233 [(A_{1g})]^a 22023 [(B_{2g})]^a 24834 [$^3A_{2g}$]^b 25074 [^3E_g]^b		$e_\sigma(H_2O)$ 4000 $e_{\pi s}(H_2O)$ 1000 $e_{\pi c}(H_2O)$ 700 e_σ(Cl) 3700 e_π(Cl) 1000 B 950 C 3800 ζ 596
$Cs_2CrCl_5 \cdot 4H_2O$	150 228 241 286 440 484 734	13629 [$^4T_{2g}$]† 14438 [^2E_g] 14800 [?] 16630 [$^4T_{2g}$] 20690 [{$^2B_{2g}$} $^2T_{2g}$] 21760 [$^4A_{2g}$ $^4T_{1g}$] 23040 [^4E_g $^4T_{1g}$] 35130 [^4E_g $^4T_{1g}$]	14438 [(Γ_6)]^a 14822 [(Γ_7)]^a 16401 [$^4E_{2g}$]^b 17000 [$^4B_{2g}$]^b 21650 [(Γ_7)]^a 21297 [$^4A_{2g}$]^b 23636 [^4E_g]^b 35948 [^4E_g]^b 36688 [$^4A_2$]^b	12121 [^4E_g] 13655 [^4E_g]†	$e_\sigma(H_2O)$ 7000 $e_{\pi s}(H_2O)$ 1000 $e_{\pi c}(H_2O)$ 500 e_σ(Cl) 6000 e_π(Cl) 1000 B 599 C 3332 ζ 171
$Cs_3VCl_6 \cdot 4H_2O$	169 233 260 282 507	9717 [$^1T_{2g}$] 16447 [$^3T_{2g}$] <σ> 16502 [$^3T_{2g}$] <π> 19268 [$^3T_{2g}$] <σ> 23256 [$^3T_{1g}$ (^3P)] 33092 [{$^3B_{1g}$} $^3A_{2g}$]	8 [$^3A_{2g}$ (E)]^a 2443 [^3E_g]^b 9718 [(B_{2g})]^a 17038 [^3E_g]^b 18237 [$^3B_{2g}$]^b 24360 [^3E_g]^b 28204 [$^3A_{2g}$]^b 34637 [$^3B_{1g}$]^b	10234*	$e_\sigma(H_2O)$ 7000 $e_{\pi s}(H_2O)$ 1150 $e_{\pi c}(H_2O)$ 0 e_σ(Cl) 6000 e_π(Cl) 1000 B 622 C 2857 ζ 190
$CoCl_2(H_2O)_4 \cdot 2H_2O$	150 163 183 199 282 362 543 697 851	8060 [{^4E_g} $^4T_{2g}$] 8330 [{$^4B_{2g}$} $^4T_{2g}$] 16450 [{$^4B_{1g}$} $^4A_{2g}$] 18600 [{^4E_g} $^4T_{1g}$] 20268 [{^2E_g} $^2T_{1g}$] 22250 [{$^4A_{2g}$} $^4T_{1g}$] <π>	167 [(Γ_7) $^4A_{2g}$]^a 919 [^4E_g]^b 8054 [$^4B_{2g}$]^b 8297 [^4E_g]^b 16954 [$^4B_{1g}$]^b 18805 [^4E_g]^b 20273 [(Γ_7)]^a 21167 [$^4A_{2g}$]^b		$e_\sigma(H_2O)$ 4300 $e_{\pi s}(H_2O)$ 1000 $e_{\pi c}(H_2O)$ 400 e_σ(Cl) 3300 e_π(Cl) 1000 B 824 C 3626 ζ 516

† Electronic origin of the $^4T_{2g}$ state. [a] Calculated with parameters in the table, $\zeta \neq 0$. [b] Calculated with parameters in the table, $\zeta = 0$.
* $V(D_2O)_6^{3+}$ in $CsAl(SO_4)_2 \cdot 12D_2O$

The members of the progression in the σ polarized spectrum are separated by 430 ± 5 cm^{-1}. The same large separation is observed for the π polarization, but each member is twinned with an average 75 cm^{-1} separation, much smaller than the spacing of the progression. The weak vibronic peaks between 18000 and 19000 cm^{-1} involve vibrational modes of the aquo ligand.

The first allowed transition to $^3T_{2g}$ (O_h label) is in the near-infrared region, as shown in Figure 4.3. Magnetic dipole zero phonon lines are observed between 5500 and 7000 cm^{-1} for $NiCl_2(D_2O)_4 \cdot 2D_2O$. Ferguson and Wood[10] have observed similar transitions for the isostructural $CoCl_2(D_2O)_4 \cdot 2D_2O$. For $NiCl_2(H_2O)_4 \cdot 2H_2O$ these origins are not clearly observed because they overlap with more intense vibrational water overtones.

The Raman spectra at room temperature and 83 K show no vibrational transition at 430 cm^{-1}. The vibrational energies observed in the low temperature Raman spectrum are 532, 377 and 364 cm^{-1}. The signal at 364 cm^{-1} is attributed to the totally symmetric nickel-water stretching mode.

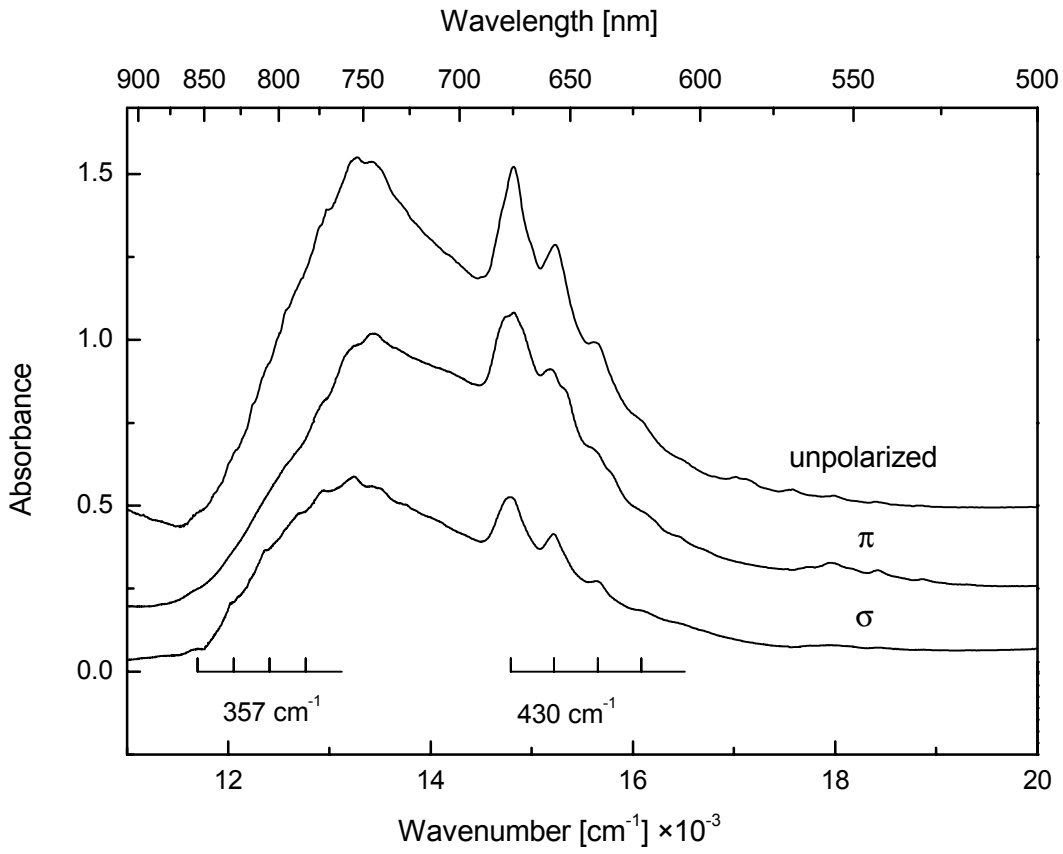

Figure 4.2 Unpolarized spectrum of the $^3T_{1g}$ / ^1E_g (O_h) region for $NiCl_2(D_2O)_4 \cdot 2D_2O$ (top trace) and polarized spectra of $NiCl_2(H_2O)_4 \cdot 2H_2O$ (bottom traces) at 5 K.

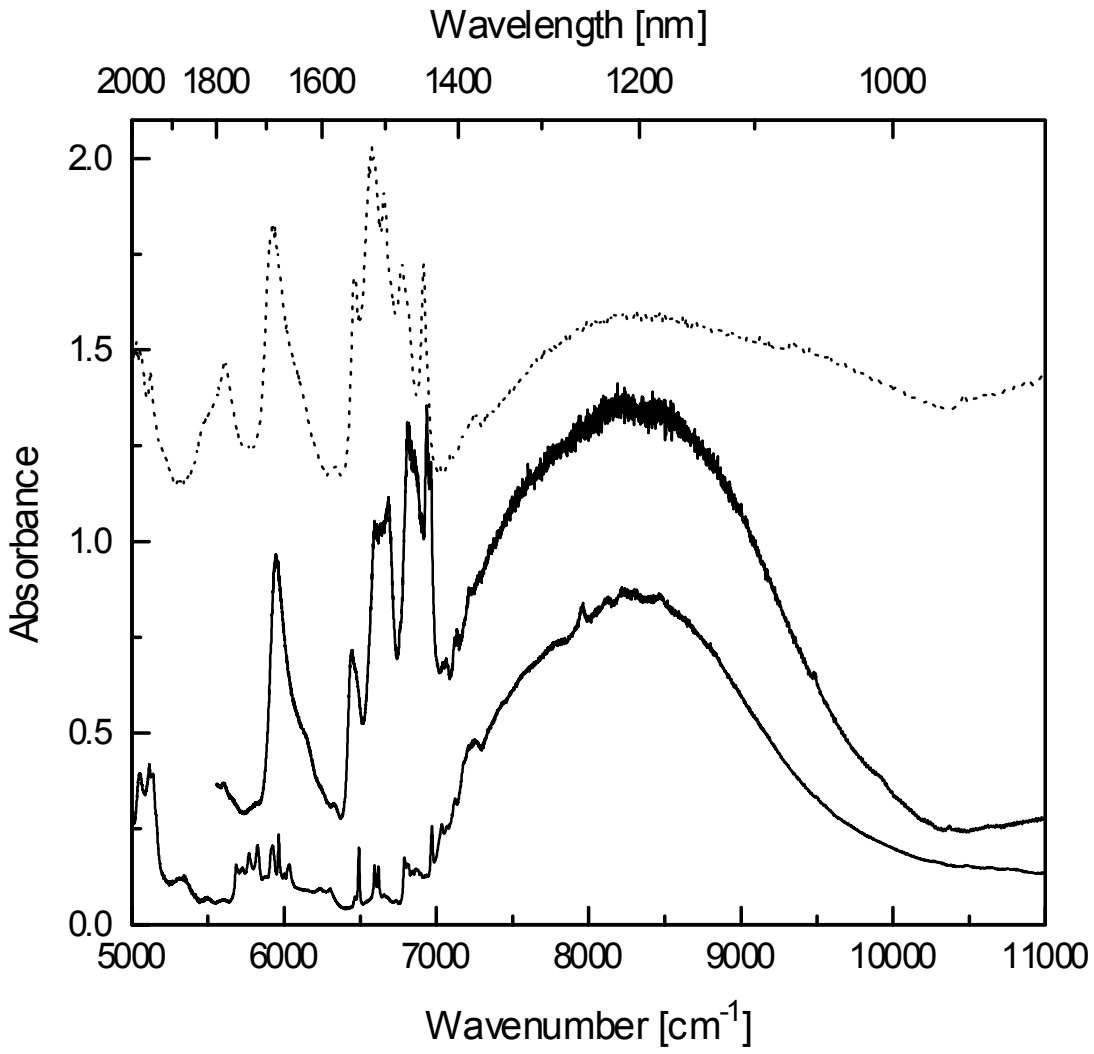

Figure 4.3 First electronic transition to the $^3T_{2g}$ state for *trans*-$NiCl_2(H_2O)_4 \cdot 2H_2O$ (top trace) and for *trans*-$NiCl_2(D_2O)_4 \cdot 2D_2O$ (bottom trace). The dotted trace shows the same region for $CoCl_2(H_2O)_4 \cdot 2H_2O$ with the water overtones very similar to those of nickel(II) analog.

3.3. Intersystem crossing and vibronic structure in the absorption spectra: strong effects caused by spin-orbit coupling

We used idealized D_{4h} point group symmetry to analyze the polarized spectra of the *trans*-$NiCl_2(H_2O)_4$ chromophore. The region of the $^3T_{1g}$ / ^1E_g (O_h) bands is of most interest and it is useful to use tetragonal symmetry to understand the features of this spectral region. In the D_{4h} point group, the ^1E_g (O_h) state is split into $^1A_{1g}$ and $^1B_{1g}$ levels. The $^3T_{1g}$ state separates into $^3A_{2g}$ and ^3E_g, which are then further split by spin-orbit coupling. The $^3A_{2g}$ state can only interact with the $^1A_{1g}$ state because there is no B_{1g} level among its spin-orbit components. This situation leads to a spectrum with a simple progression when the $^3A_{2g}$ state is involved in the transition and with a double progression when the ^3E_g state is involved. Considering the number of progressions observed and the fact that a transition to a doubly degenerate E_g level should have twice the oscillator strength of a transition to a nondegenerate A or B level, it is clear that in Figure 4.2 the $^3A_{2g}$ state dominates the σ polarized spectrum while the ^3E_g state appears prominently in π polarization.

The angular overlap model (AOM)[30,31] was used in order to obtain the energetic order of triplet and singlet excited states in this tetragonal chromophore. The angular overlap parameters $e_\sigma(H_2O)$, $e_{\pi s}(H_2O)$ and $e_{\pi c}(H_2O)$ were estimated from the spin-allowed band maxima of $Ni(H_2O)_6(NO_3)_2$ at 5 K[1, 24]. The corresponding absorption maxima of $NiCl_6^{4-}$ in $CsCdCl_3$, $CsMgCl_3$[25, 26] and $NiCl_2$[27, 28] were used to determine $e_\sigma(Cl)$ and $e_\pi(Cl)$, respectively. We set the parameters $e_\sigma(H_2O)$ and $e_{\pi s}(H_2O)$ to 4000 and 1000 cm^{-1}, respectively, while $e_\sigma(Cl)$ and $e_\pi(Cl)$ are set to 3700

and 1000 cm^{-1}, respectively, for the *trans*-dichlorotetraaquo nickel(II) complex. We analyze the spectra of the divalent nickel and cobalt ions with AOM e_σ and e_π parameters as close as possible to these values. Bencini *et al.* obtained mean values for $e_\sigma(H_2O)$ and $e_\pi(H_2O)$ of 3802 and 889 cm^{-1} (without π anisotropy) for divalent ions, summarized in their Table 5[29]. The same authors report values for chloride ligands in their Table 2 for divalent ions; their averages are 4496 and 1581 cm^{-1} for $e_\sigma(Cl)$ and $e_\pi(Cl)$, respectively, in relatively good agreement with the values we use here. For the trivalent chromium and vanadium complexes we set $e_\sigma(H_2O)$ and $e_\sigma(Cl)$ to 7000 and 6000 cm^{-1} respectively. Values of 7000 and 7500 cm^{-1} for $e_\sigma(H_2O)$ were suggested by Hitchman *et al.*[30] for $V(H_2O)_6^{3+}$, in agreement with the value used here. Hitchman *et al.* have also suggested that $e_{\pi c}(H_2O)$ should be quite small, on the order of 500 ± 500 cm^{-1}[30]. For all complexes, we set $e_{\pi c}(H_2O) < e_{\pi s}(H_2O)$, a condition consistent with a simple covalent model of the interaction between the water molecule and the metal ion where the p_x orbital of water does not contribute to the metal-ligand bonds because of its involvement in bonding to the hydrogen atoms[30, 31]. For all AOM calculations we assume an angle ψ=0, as the position of the hydrogen atoms is not known exactly for all title complexes. This assumption is justified in the case of nickel(II) and cobalt(II) complexes, where the position of hydrogen atoms has been deduced from X-ray crystallographic data [17, 18, 32]. The angle ψ between the plane of the H_2O ligands with the Cl-M-Cl axis is small, but not exactly zero. Our use of a fixed value of 0 for ψ could be an important reason for the variation of $e_{\pi c}(H_2O)$ between 0 and 700 cm^{-1}. The Racah parameter B was set to 950 cm^{-1} (88% of the free ion value), the ratio C/B to 4 and the spin-orbit coupling

constant ζ to 596 cm^{-1}. This AOM calculation does not involve a fit, but it leads to band maxima for $NiCl_2(H_2O)_4$ in satisfactory agreement with the experimental values obtained at 5 K, as shown in Figure 4.1 and Table 4.2.

The calculated energetic order of the excited states in the $^3T_{1g}$ / ^1E_g region (O_h) in the D_{4h} point group predicts that the barycenter of the $^3A_{2g}$ state should be lower in energy by 218 cm^{-1} than the barycenter of the ^3E_g state. The $^1A_{1g}$ state is calculated at an energy lower by 55 cm^{-1} than the $^1B_{1g}$ state. This value compares favorably to the average separation of 75 cm^{-1} between the two progressions in the π-polarized absorption spectrum in Figure 4.2, especially since no angular overlap parameters were fitted to the spectrum of $NiCl_2(H_2O)_4$.

The experimental spectrum of the *trans*-$NiCl_2(H_2O)_4$ chromophore shows a double progression in π polarization, but only the lower energy progression appears in σ polarization. The maximum of the broad band in σ polarization is at lower energy than in π polarization. The selection rules in the D_{4h} point group are given in Table 4.3. Transition energies and vibronic patterns can be combined with the calculated crystal field energies, indicating that the $^3B_{1g} \rightarrow {}^3A_{2g}$ band dominates the σ-polarized spectrum. This triplet excited state can only interact with the $^1A_{1g}$ state as established before. The $^3B_{1g} \rightarrow {}^3E_g$ transition is expected at higher energy, as observed in π polarization. The ^3E_g state has A_{1g} and B_{1g} spin-orbit levels that can interact with both singlet excited states, giving rise to a double progression in the spectrum and confirming the energetic order derived from the angular overlap model. It is clear from these observations that singlet states gain most of their intensities from the allowed triplet transitions and that intersystem crossings between excited

Table 4.3 Selection rules for electronic transitions in D_{4h} symmetry.

Electronic transition	Electric dipole allowed with Γ_u vibration in π polarization $\langle \Gamma_i \vert A_{2u} \vert \Gamma_f \rangle \Gamma_u = A_{1g}$	Electric dipole allowed with Γ_u vibration in σ polarization $\langle \Gamma_i \vert E_u \vert \Gamma_f \rangle \Gamma_u = A_{1g}$
$B_{1g} \rightarrow E_g$ or $E_g \rightarrow B_{1g}$	e_u	a_{1u}, a_{2u}, b_{1u}, b_{2u}
$B_{1g} \rightarrow A_{2g}$ or $A_{2g} \rightarrow B_{1g}$	b_{1u}	e_u
$B_{1g} \rightarrow B_{2g}$ or $B_{2g} \rightarrow B_{1g}$	a_{1u}	e_u
$A_{2g} \rightarrow E_g$ or $E_g \rightarrow A_{2g}$	e_u	a_{1u}, a_{2u}, b_{1u}, b_{2u}
$A_{2g} \rightarrow B_{2g}$ or $B_{2g} \rightarrow A_{2g}$	b_{2u}	e_u
$A_{2g} \rightarrow A_{2g}$	a_{2u}	e_u

states of different multiplicities can give rise to important vibronic features in the spectra of transition metal complexes.

The absorption band shape for the $^3B_{1g} \rightarrow {}^3A_{2g}$ / $^1A_{1g}$ transition has been calculated using the time dependent theory of spectroscopy[14, 33-36] and the result is compared to the experimental spectrum in Figure 4.4. Spectra of both A_{1g} and E_g spin-orbit levels of the $^3A_{2g}$ and $^1A_{1g}$ states are plotted in the Figure. The intensity ratio E_g/A_{1g} is 2:1, based on the degeneracies of the levels, and we assume that the intensity for the transition to the $^1A_{1g}$ state arises entirely from coupling to the triplet state. A simple harmonic surface is used for the E_g level of the $^3A_{2g}$ state, leading to a Poisson band shape. The coupled A_{1g} levels are represented schematically by the potential curves of Figure 4.5, the non-harmonic dotted curves clearly show the avoided crossing between the two A_{1g} levels. The relationship between electronic energies for a 'frozen' complex from the AOM calculation and the potential energy

surfaces, which correctly characterize the observed absorption spectrum, is illustrated in Figure 4.5. The calculated AOM energies define the potential energy surfaces in the Franck-Condon region as indicated in Figure 4.5. $NiCl_2(H_2O)_4 \cdot 2H_2O$ provides a clear example of an intersystem crossing where two excited states interact and where the influence from other electronic states is negligible. The one-dimensional potential curves in Figure 4.5 quantitatively rationalize all important aspects of the experimental spectrum: the unusually high spacing of the intense vibronic progression and the low intensity 'interference dip' before the onset of the intense progression. It has been shown that this model describes a molecular Fano antiresonance, and an analytical equation for unresolved spectra equivalent to Figure 4.4 has been published[37].

Table 4.4 Spectroscopic parameters for coupled electronic states.

Parameters (O_h labels)	$^1T_{2g}$-$^3T_{2g}$ $Cs_3VCl_6 \cdot 4H_2O$	$^1A_{1g}$-$^3T_{1g}$ $Cs_3VCl_6 \cdot 4H_2O$	$^3T_{1g}$ - ^1E_g $NiCl_2(H_2O)_4 \cdot 2H_2O$	$^4T_{2g}$ – ^2E_g $Cs_2CrCl_5 \cdot 4H_2O$
allowed transition origin(s) (cm^{-1})	14386 (all $^3T_{2g}$ s.o. sub-levels)	21000 (all $^3T_{1g}$ s.o. sub-levels)	10365 A_{1g} ($^3A_{2g}$) 10500 E_g ($^3A_{2g}$)	13722.5 U (^4E_g, $^4T_{2g}$) 13655.4 ($^4B_{2g}$, $^4T_{2g}$)
forbidden transition origin (cm^{-1})	9717 T_{2g} ($^1T_{2g}$) (O_h label)	19000 A_{1g} ($^1A_{1g}$) (O_h) label	14403 A_{1g} ($^1A_{1g}$)	14437.9 U (^2E_g)
Vibrational frequencies (cm^{-1})				
$\hbar\omega$ g.s.	507	507	364	286
$\hbar\omega$ allowed e.s.	507	507	357	286
$\hbar\omega$ forbidden e.s.	507	507	364	286
ΔQ_T, allowed (Å)	0.18	0.18	0.295	0.265
ΔQ_S, forbidden (Å)	0.0	0.0	0.05	0.0
Matrix element V_{ST} (cm^{-1})	-232.7 ($-\lambda\sqrt{6}$)	-268.7 ($-2\lambda\sqrt{2}$)	730 ($-\lambda\sqrt{6}$)	-187 ($-3\lambda\sqrt{6}/\sqrt{5}$)
Coupling constant λ (cm^{-1})	95	95	-270	57
Damping factor Γ (cm^{-1})	250 ($^3\Gamma$), 10($^1\Gamma$)	250	100	200 ($^4\Gamma$), 10($^2\Gamma$)
Transition dipole moments $\mu_{forbidden}/\mu_{allowed}$	0.00/1.00	0.00/1.00	0.09/0.91	0.00/1.00

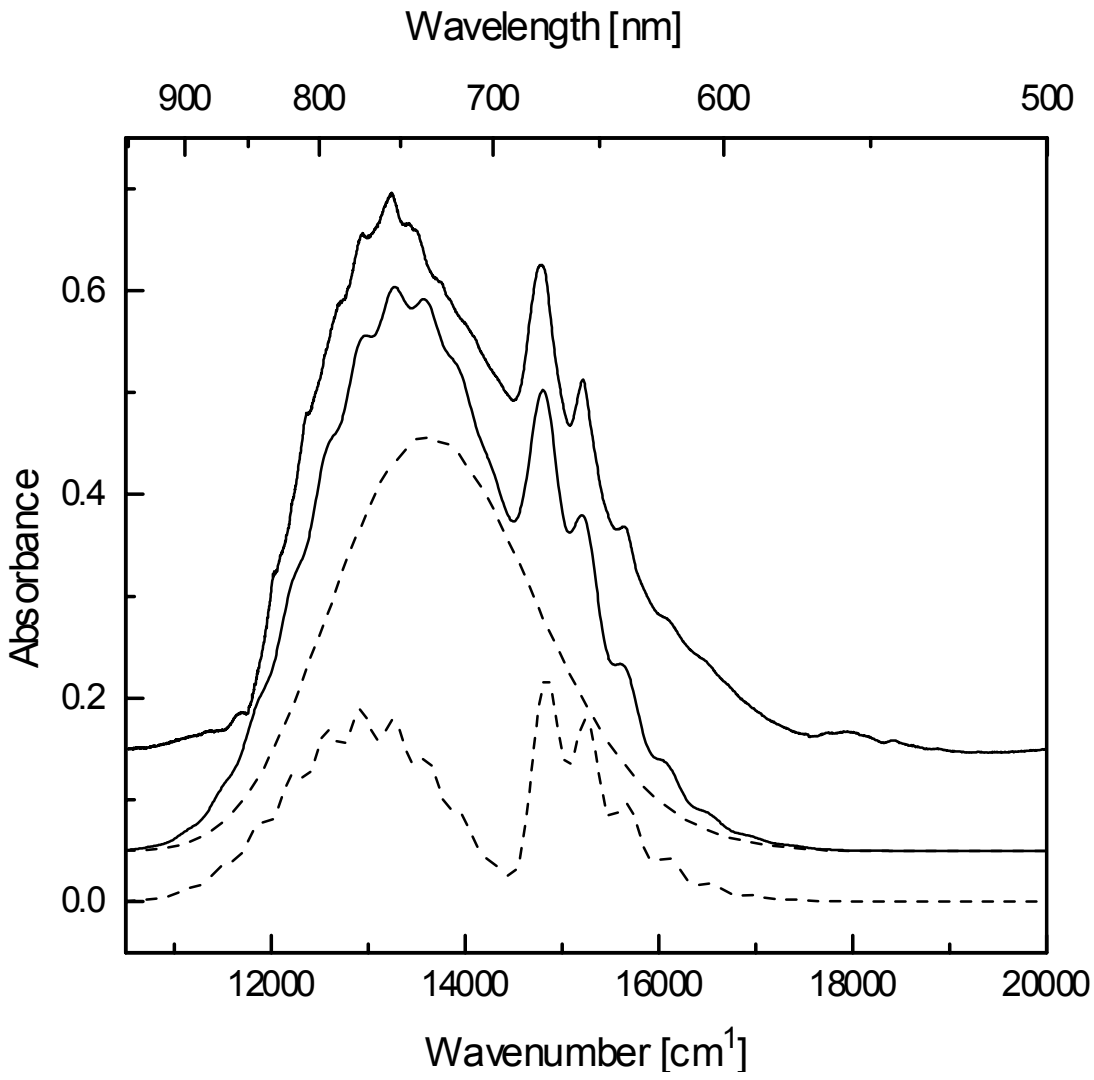

Figure 4.4 Calculated and experimental absorption spectra for *trans*-$NiCl_2(H_2O)_4 \cdot 2H_2O$ in σ polarization. The top trace denotes the experimental spectrum, followed by the total calculated spectrum (solid line) separated from the experimental spectrum by 0.1 in absorbance units for clarity. The two dotted traces denote the calculated spectra for the E_g and the coupled A_{1g} levels arising from $^3A_{2g}$ and $^1A_{1g}$.

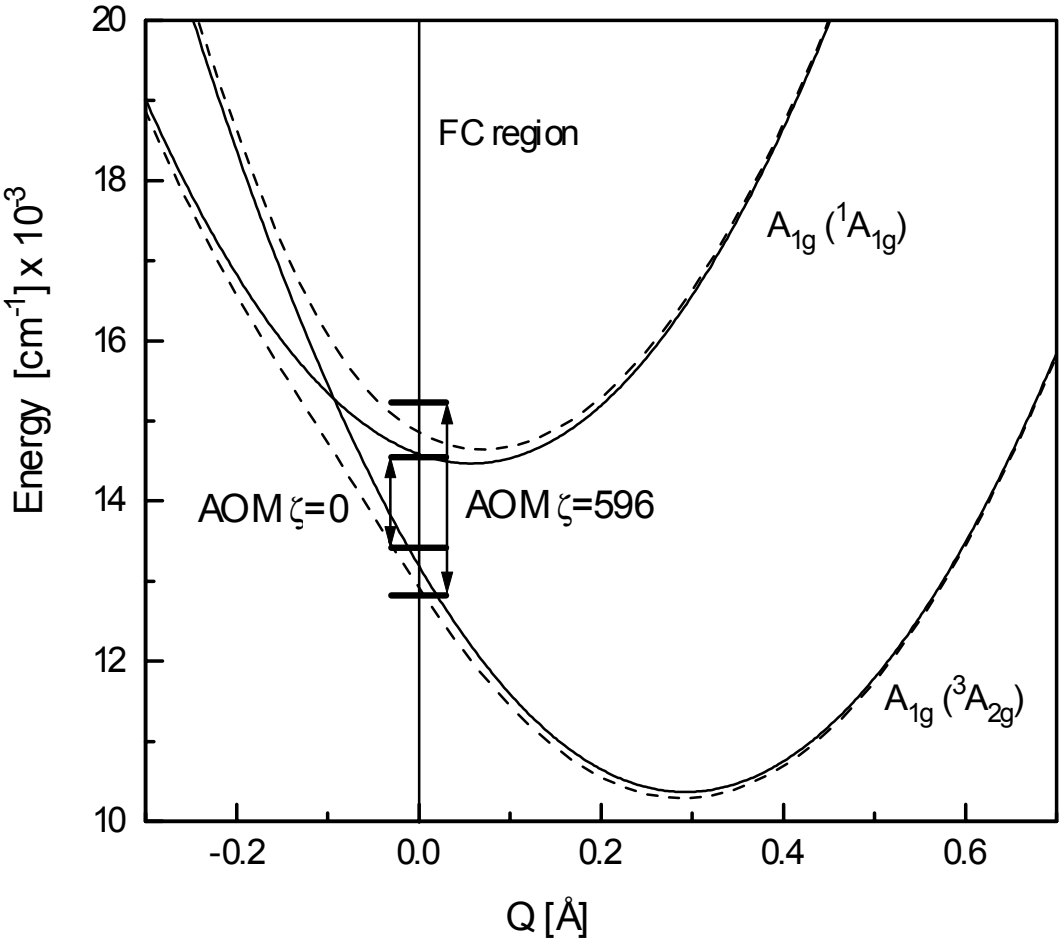

Figure 4.5 Potential energy surfaces for the coupled A_{1g} states of $NiCl_2(H_2O)_4 \cdot 2H_2O$. Diabatic and adiabatic potentials are shown as solid and dotted lines, respectively. The horizontal lines separated by arrows in the Franck-Condon (FC) region denote the energies of the A_{1g} states calculated with the angular overlap model. The short arrow represents the energy separation without spin-orbit coupling, the long arrow represents the energy separation with spin-orbit coupling.

4. *trans*-$VCl_2(H_2O)_4^+$

4.1. $Cs_3VCl_6 \cdot 4H_2O$

Recently several ligand field studies were reported for the $[V(H_2O)_6]^{3+}$ cation[30, 38-40]. Using the angular overlap model, it appears that the anisotropy of the π bonding of the water molecules explains the trigonal splitting observed in the experimental absorption spectra of vanadium(III) hexahydrate[30]. Analogous effects are important in chromium alums[41]. McCarthy *et al.*[8] have reported a detailed spectroscopic analysis of the $Cs_3VCl_6(X_2O)_4$ compound containing the tetragonal chromophore $VCl_2(X_2O)_4^+$ with X = H or D. The most intriguing feature observed in the literature spectra are two intense maxima separated by about 3000 cm^{-1} in the 500 to 700 nm region, corresponding to the lowest energy spin-allowed crystal field transition ($^3T_{1g} \rightarrow {}^3T_{2g}$ in O_h symmetry). We compare several quantitative models for this band system.

The lowest energy electronic transition occurs within the t_{2g}^2 strong field configuration between the $^3T_{1g}$ (^3F) ground state and the $^1T_{2g}$, ^1E_g excited states (O_h symmetry). We present the first experimental measurements of these sharp bands for *trans*-$VCl_2(H_2O)_4^+$ and explore the luminescence spectrum of vanadium(III) aquo complexes.

4.2. Spectroscopic results

The vanadium complexes show intense absorption bands in the UV-VIS range. Three spin-allowed transitions are expected which can be attributed as follows: $^3T_{2g}$ (15000 to 20000 cm^{-1}), $^3T_{1g}$ (23300 cm^{-1}) and $^3A_{2g}$ (33300 cm^{-1}) (O_h labels). Spin-forbidden absorption transitions can be seen in the NIR region (9600 to 10400 cm^{-1}) and are assigned to the ^1E_g and $^1T_{2g}$ (O_h labels). These NIR spectra show many interesting features and are presented in Figure 4.9. At least nine sharp transitions can be identified with widths at half height varying between 6 and 15 cm^{-1}. The overall oscillator strengths *f* are estimated to be $1.73 \cdot 10^{-8}$ and $5.8 \cdot 10^{-5}$ for the singlets and for the $^3T_{2g}$ transitions, respectively. The first value is typical for spin-forbidden and parity-forbidden transitions, while the second one, with an oscillator strength about three orders of magnitude higher, is in the range expected for the spin-allowed d-d bands.

An attempt to measure polarized absorption spectra for the singlet states (9600 to 10400 cm^{-1}) did not lead to well defined dichroic ratios. At the weak absorbance of the singlet states, the background noise of the spectrometer is increased due to the polarizers in this region of low detector sensitivity. With the instrumentation described before we were unable to detect any luminescence from $Cs_3VCl_6 \cdot 4D_2O$. This is due to the low quantum yield of each individual complex and to energy transfer processes in the concentrated solid. We did observe a sharp luminescence transition from $V(D_2O)_6^{3+}$ doped into $CsAl(SO_4)_2 \cdot 12D_2O$ at 10234 cm^{-1} (5 K), in exact agreement with the lowest-energy absorption transition (see Table 4.2 and ref. 38). This comparison shows that the weak intraconfigurational transitions are lower

in energy by approximately 520 cm^{-1} for the *trans*-$VCl_2(H_2O)_4^+$ than for $V(H_2O)_6^{3+}$ complexes[38], again underlying the very specific electronic structure of the title chromophores.

The 15000 to 20000 cm^{-1} region contains the most interesting polarization effects. Figure 4.6 shows that a single maximum is obtained in π polarization. In σ polarization, two maxima with a separation of about 3000 cm^{-1} are observed. McCarthy *et al*.[8] have reported the third polarization, in which the spectrum is almost identical to the σ spectrum of Figure 4.6. These observations agree with the expected polarization for a Jahn-Teller E_g state in D_{4h} symmetry, as established by Hougen[42].

The Raman spectra at 83 K are shown for both compounds in Figure 4.7. Five Raman active modes are expected for a seven-atom D_{4h} complex. It appears that they are all observed between 150 and 550 cm^{-1}. Three of them shift upon deuteration and are denoted by the arrows. The 507 cm^{-1} peak (482 cm^{-1} in the deuterated compound) can be assigned to the totally symmetric ν(V-O) mode. This frequency is close to the 530 cm^{-1} value recently observed for $V(H_2O)_6^{3+}$ in alums[38]. The other two modes involving the water ligand should be of b_{1g} and b_{2g} symmetry in the D_{4h} point group. Their assignment is doubtful, but the only deuteration sensitive peaks between 150 and 507 cm^{-1} are the 260 and 233 cm^{-1} bands (246 cm^{-1} and 221 cm^{-1} in the deuterated compound). The other two modes which do not significantly depend upon deuteration are assigned as the a_{1g} ν(V-Cl) and the e_g δ(V-Cl) vibrations.

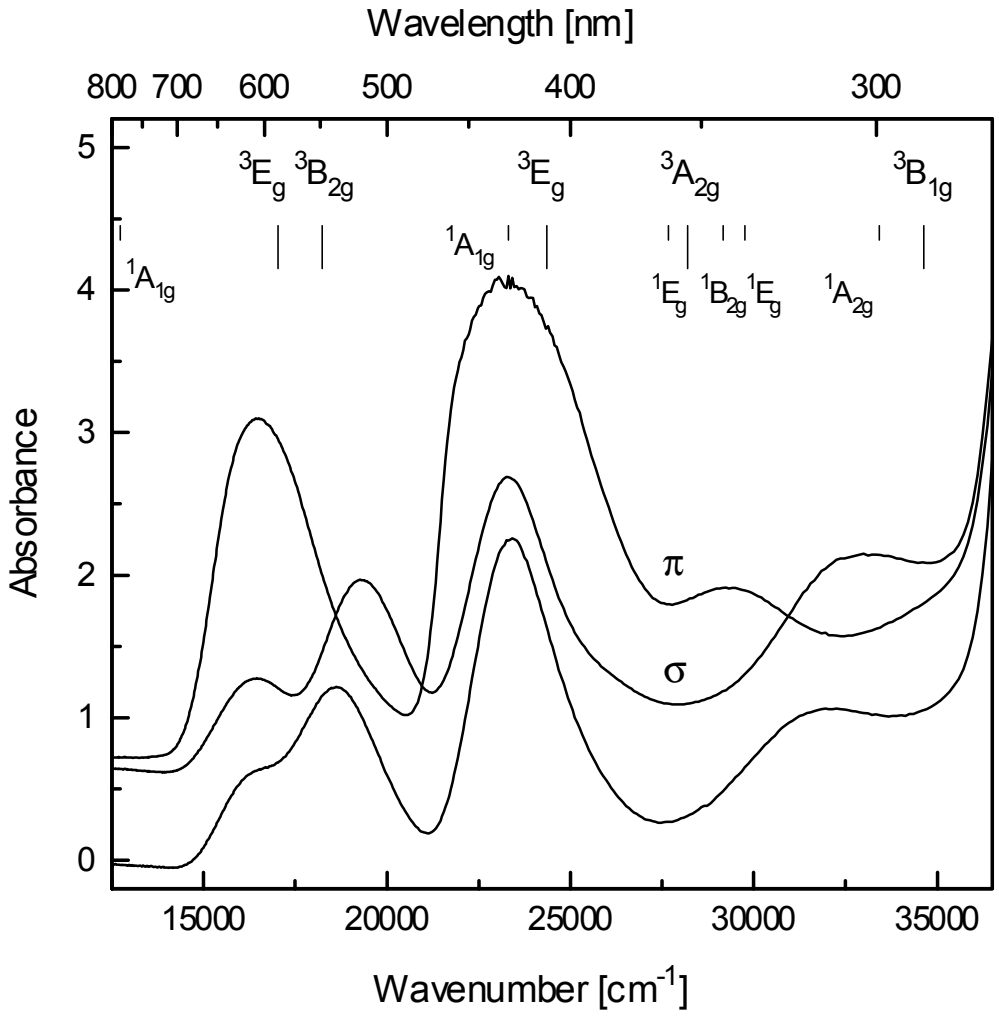

Figure 4.6 Polarized absorption spectra of $Cs_3VCl_6(H_2O)_4$ at 80 K (top). The polarization directions are given relative to the Cl-V-Cl axis of the trans-$VCl_2(H_2O)_4^+$ chromophore. The bottom trace is the σ polarized spectrum of $Cs_3VCl_6(D_2O)_4$ at 25 K. The π polarized spectrum of the deuterated compound is similar to the undeuterated π spectrum. The vertical lines represent the AOM energies calculated with parameters from Table 4.2 with ζ=0. The tall lines represent spin-allowed transitions, the short lines the spin-forbidden transitions.

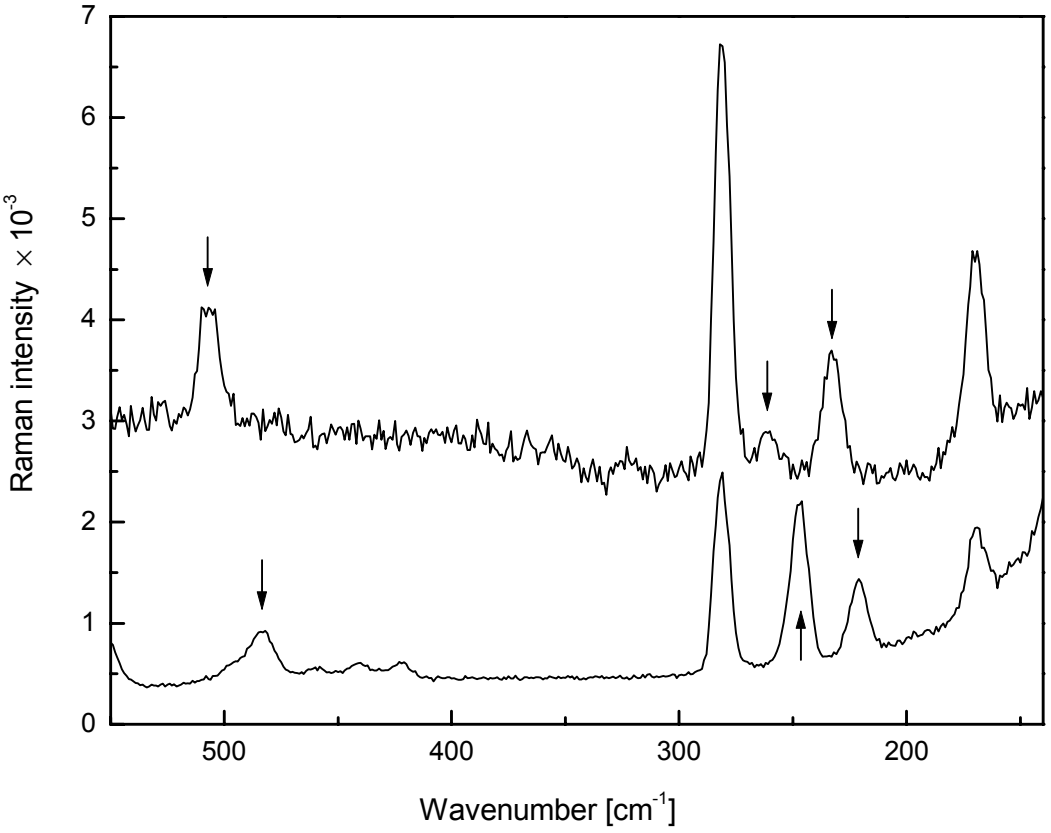

Figure 4.7 Unpolarized Raman spectra of $Cs_3VCl_6(H_2O)_4$ (top trace) and $Cs_3VCl_6(D_2O)_4$ (bottom trace) at 77 K. The arrows denote the three vibrational modes involving the water ligands.

4.3. The double maximum of the lowest energy triplet band: quantitative comparison of models

The absorption spectrum of the $VCl_2(H_2O)_4^+$ cation in $Cs_3VCl_6(H_2O)_4$ in σ polarization shows a splitting of 3000 cm^{-1} for the lowest energy triplet band, suggesting a separation of the first triplet excited state, $^3T_{2g}$ (O_h). The splitting in $Cs_3VCl_6{\cdot}4H_2O$ is too large to be explained by the tetragonal field and all attempts to reproduce it with the angular overlap formalism failed, even when π anisotropy for the water ligand is taken in account. We include energies calculated with the AOM model in Table 4.2 in order to illustrate this discrepancy. The calculated energy difference between the ^3E_g and $^3B_{2g}$ states arising from $^3T_{2g}$ (O_h) in D_{4h} symmetry is 1200 cm^{-1}, corresponding to less than 50% of the experimental energy difference of 2800 cm^{-1} between the two maxima in the sigma polarized spectrum in Figure 4.6. McCarthy *et al*. have suggested that the splitting is due to bands involving vibronic OH modes[8], but the intensity of the band is quite high in comparison to many other transition metal aquo complexes (see Figure 4.16), where only weak transitions involving OH stretching modes are observed[24].

We have shown that spin-orbit coupling between triplet and singlet states of nickel(II) complexes is of importance and is essential to explain many spectroscopic observations[1]. The two maxima observed for the vanadium(III) complex could be attributed to a singlet and a triplet state, in direct analogy with the nickel(II) spectra discussed in the preceding section. A $^1A_{1g}$ state is expected for the $VCl_2(H_2O)_4^+$ cation in the 500 nm region, but there are substantial differences between the

vanadium(III) and the nickel(II) complexes. First and most important, the spin-orbit coupling constant (λ) for vanadium(III) is expected to be approximately 95 cm^{-1}, much lower than for the nickel(II) ion. Second, the matrix element between the $^1A_{1g}$ and the $^3T_{2g}$ (O_h) states is zero. In D_{4h} symmetry coupling can occur, but the nonzero matrix element are smaller by approximately two orders of magnitude than for the nickel(II) complexes discussed in the preceding section. The AOM calculations show that several of these small matrix element can influence the bandshape, but the calculated intensity changes are too small by orders of magnitude to cause the double maximum in Figure 4.6. One can consider coupling with the higher energy $^3T_{1g}$ (O_h) state, but in this case the splitting is approximately 3700 cm^{-1} and the matrix element is $-2\lambda\sqrt{2}$. The splitting should be on the order of two times the absolute value of the matrix element and the intensity of the forbidden band decreases rapidly for larger splitting[43]. We are therefore not able to explain the observation with spin-orbit coupling in a reasonable way. The separation of the singlet and triplet states is too large and the matrix element too small.

A first alternative explanation involves vibronic coupling with OH stretching modes, as suggested by McCarthy *et al.*[8]. The hypothesis of progressions in OH or OD totally symmetric stretching modes (a_{1g}) was tested with aquo and deuterated compounds. As shown in the top panel of Figure 4.8, a calculated spectrum with a progression in the OH stretching a_{1g} mode is in good agreement with the two maxima of the experimental spectrum of $Cs_3VCl_6 \cdot 4H_2O$. The correlation for the OD vibration is not as good as for OH. The parameters used for the simulations are shown in Table 4.5. Figure 4.8 shows that the third and fourth members of the progression have no

equivalent in the experimental spectra. Only an ungerade parity vibronic origin can account for the lack of further vibronic members in the progression. All ungerade parity vibrations which can lead to electric dipole allowed vibronic origins are given in Table 4.3. It is unusual, but not without precedent, that a vibronic origin occurs in a high-frequency mode. A detailed analysis of such a spectrum with resolved vibronic structure was recently given for the organometallic compound $Ta(CO)_6$, where a high-frequency C≡O mode acts as a vibronic origin[44]. This explanation is qualitatively reasonable for $VCl_2(H_2O)_4^+$, and it shows the importance of coordinate dependent transition dipoles. This model can explain why a double maximum is observed for $VCl_2(H_2O)_4^+$, but it cannot account for its absence in the spectrum of $V(H_2O)_6^{3+}$. Vibronic origins involving high-frequency modes of the H_2O ligands of the title complexes are compared in the final section of this article and in Figure 4.16.

A second alternative explanation for the observed double maximum involves a Jahn-Teller effect. In the D_{4h} point group, the $^3T_{2g}$ state (O_h) is split by the tetragonal field into a $^3B_{2g}$ and a ^3E_g state. Two maxima can occur due to a Jahn-Teller effect involving the ^3E_g state and the b_{1g} and b_{2g} modes. The observed spectra could be a combination of both a Jahn-Teller effect along metal-ligand modes with a contribution from OH (or OD) vibrational modes, as discussed in the preceding paragraph. In Figure 4.8, we present a model calculation involving a Jahn-Teller effect involving the b_{1g} and b_{2g} metal ligand modes. We use a model based on an $E_g \otimes (b_{1g}, b_{2g})$ Jahn-Teller effect[42, 45]. In our approach, we neglect spin-orbit coupling, which is quite small for V^{3+} compounds. Ballhausen[45] has shown that for low spin-orbit coupling ($\lambda \approx 100$ cm^{-1}) in tetragonal molecules, the overall band shape

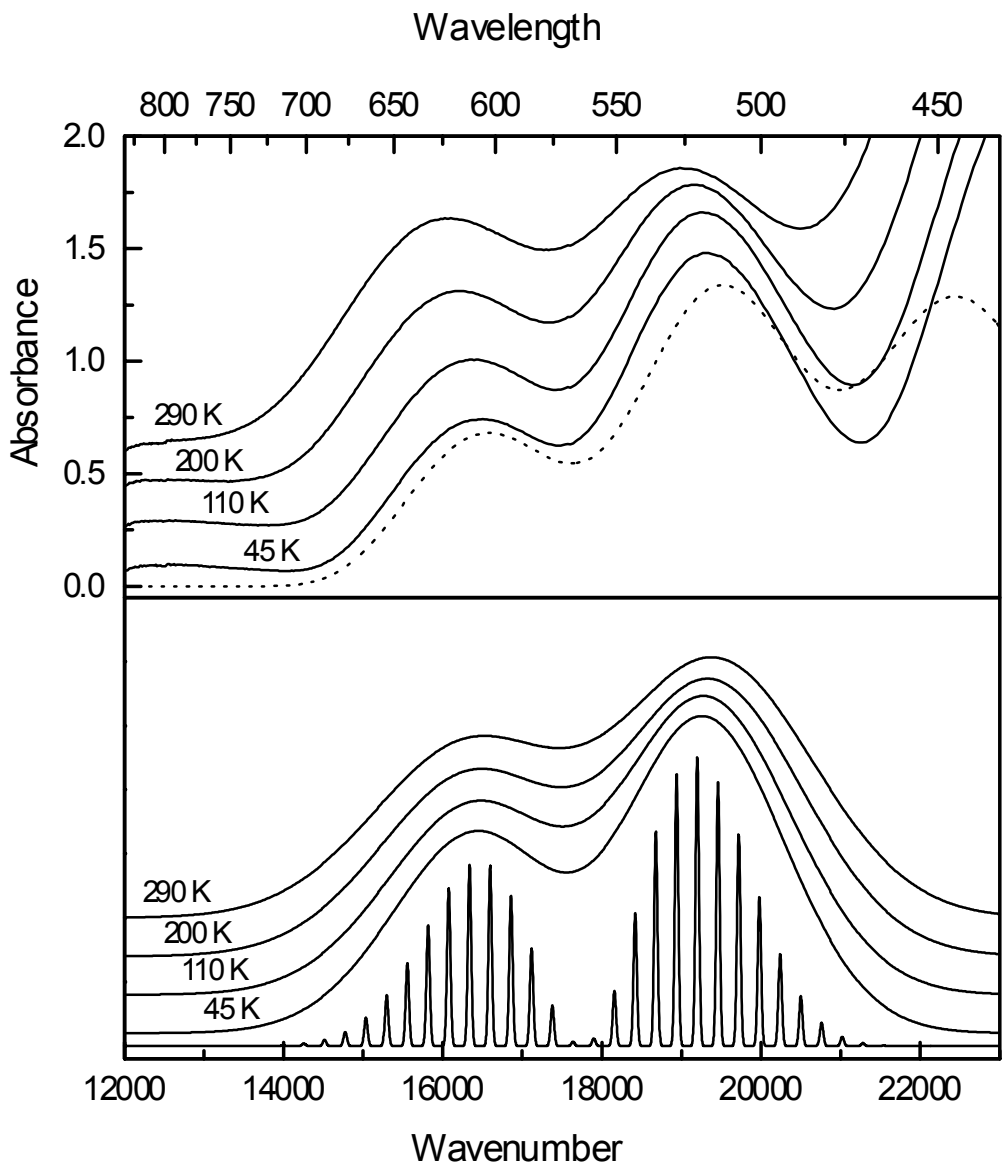

Figure 4.8 Temperature dependence of the $^3T_{2g}$ (O_h label) σ polarized absorption spectrum of $Cs_3VCl_6(H_2O)_4$ (top panel). The dotted trace denotes a calculated spectrum involving a progression in the OH totally symmetric stretching mode. The bottom panel shows the calculated temperature dependence, using the Jahn-Teller model described in the text with the calculated resolved vibrational structure shown as the bottom trace.

Table 4.5 Spectroscopic parameters for the $^3T_{2g}$ (O_h) state in $Cs_3VCl_6 \cdot 4H_2O$.

Parameters	Jahn-Teller ^3E_g	OH Vibration		
$^3\Gamma$ origin (cm^{-1})	11000	12380		
Vibrational frequencies (cm^{-1})	260	3000	507 υ(VO)	282 υ(VCl)
Distorsion, ΔQ (Å)		0.196	0.152	0.145
κ^2[48]	50			
Damping factor Γ (cm^{-1})	550-700	100		

of the E_g state is not changed by spin-orbit coupling, but only the resolved fine structure is affected. Since no resolved vibronic structure is observed for this compound in the region of the $^3B_{2g}$ and ^3E_g transitions, we neglect spin-orbit coupling to simplify the problem. The experimental temperature dependence of the σ polarized absorption spectrum is shown in the top panel of Figure 4.8 and compared to the calculated temperature dependence using the model described here in the bottom panel of Figure 4.8.

In an octahedrally coordinated compound, it is tempting to assume that a $T \otimes e_g$ Jahn-Teller effect can be responsible for such a splitting. For low spin-orbit coupling, when only a twofold degenerate e_g vibration is involved, this is impossible due to the orthogonality of the three T electronic states[46, 47]. In contrast, it is known that an $A \rightarrow E$ electronic transition can give rise to a large splitting of the absorption band[46, 48]. This shows that the tetragonal symmetry of the molecule plays a crucial role in the observation of the double maximum. It could also explain the absence of a double maximum for the corresponding band in $V(H_2O)_6^{3+}$.

We use two Jahn-Teller active vibrational frequencies ω_1 and ω_2 of b_{1g} and b_{2g} symmetry with Jahn-Teller couplings of f_1 and f_2, respectively. We can describe three limiting cases[42]: 1) f_1 or $f_2 = 0$, a case where only one vibrational frequency remains and the E_g level is split into two orthogonal electronic states. The vibrational levels of the two electronic states are degenerate, a situation known as accidental Born-Oppenheimer degeneracy[42]. 2) If $f_1 = f_2$ and $\omega_1 = \omega_2$ the problem is identical to an $E_g \otimes e_g$ Jahn-Teller problem in octahedral symmetry. In this case, the potential surface has a cylindrical symmetry and this problem has been solved by Longuet-Higgins *et al*.[48]. 3) For arbitrary values of ω_1, ω_2, f_1 and f_2, the problem is more difficult to solve. In that case, the potential surface has twofold symmetry about the energy axis[46]. If by chance $\omega_1 = \omega_2$, the potential surface happens to have cylindrical symmetry[46].

We make the following approximations: 1) ω_1 and ω_2 are sufficiently close to assume cylindrical symmetry of the potential surface. The vibronic intervals of 260 and 233 cm^{-1} in Figure 4.9 confirm this assumption. 2) f_1 and f_2 are sufficiently close to allow rotation of the molecule between an elongated and a rhombic configuration[45]. If these conditions are respected, then the problem is reduced to an $E_g \otimes e_g$ Jahn-Teller interaction.

We use a one-dimensional model in which the potential surface is a slice through the more complex two-dimensional cylindrical $E_g \otimes e_g$ potential surface. In that approximation, the vibrational wavefunctions of the degenerate E_g state are harmonic and degenerate. The probability distribution of the first vibrational wave function of the non-degenerate A electronic ground state in the cylindrical potential is

$2\alpha^2\rho e^{-\alpha^2\rho^2}$. The parameter α is defined as $(K\mu/\hbar^2)^{1/4}$ and ρ denotes the radius in the cylindrical coordinate system. We apply the simple model developed by Longuet-Higgins *et al*.[48] in which the E state is split by a linear coupling constant of the form κρ. In this model $\kappa^2 = 2\Delta E/\hbar\omega$ and the parameters used for the simulation are shown in TABLE 4.5. The potential energy surfaces for the E_g states are represented by the matrix:

$$V_{E_g} = \begin{pmatrix} \frac{K\rho^2}{2} & \kappa\rho \\ \kappa\rho & \frac{K\rho^2}{2} \end{pmatrix} \qquad (4.1)$$

The experimental band with its double maximum can not be rationalized with purely electronic models, such as AOM calculations. Vibronic effects have the most important influence on the spectrum. The change of the energy difference between maxima with deuteration is evidence for vibronic origins involving OH and OD modes, and the observation of the double maximum only in D_{4h} symmetry is a signature of a possible Jahn-Teller effect involving only the ^3E_g state. It is likely that a combination of these two vibronic effects occurs, but the unresolved experimental spectrum does not allow us to determine their individual contributions.

4.4. Ground state splitting and spin-orbit interaction between the lowest energy singlet and triplet states

Angular overlap model calculations were also made in order to verify that the band positions could be reproduced without major discrepancies (except for the splitting of the lowest energy triplet band). Using the zero field splitting of $Cs_3VCl_6{\cdot}4H_2O$ reported by Carlin *et al*.[49], we set $^3A_{2g}$ (D_{4h}) as the ground state with a splitting of 8 cm^{-1}. The second component of the $^3T_{1g}$ (O_h) ground state, the ^3E_g (D_{4h}) level, is expected to be around 1000 cm^{-1}[49]. We use the angular overlap model with spin-orbit coupling to exactly reproduce the 8 cm^{-1} splitting of the ground state. The spin orbit coupling constant ζ was set to 190 cm^{-1} (λ=95 cm^{-1}) for all calculations, see Tables 1 and 4. Table 4.2 and Figure 4.6 show that the positions of the bands are reasonably reproduced.

The well resolved NIR absorption transitions allow us to derive quantitative information on singlet-triplet interactions and the splitting of the electronic ground state. The temperature dependence of the lowest energy singlet absorption for $Cs_3VCl_6{\cdot}4H_2O$ and for $Cs_3VCl_6{\cdot}4D_2O$ is plotted in Figure 4.9. The bottom panel shows that the intensity of the transition decreases from 80 to 5 K. We use Boltzmann statistics (Equation 2) to fit this temperature dependence assuming a 8 cm^{-1} splitting d of the ground state[49].

$$I(T) = \frac{2Ee^{-(d/0.693816T)}}{1+2e^{-(d/0.693816T)}} + \frac{A}{1+2e^{-(d/0.693816T)}} \qquad (4.2)$$

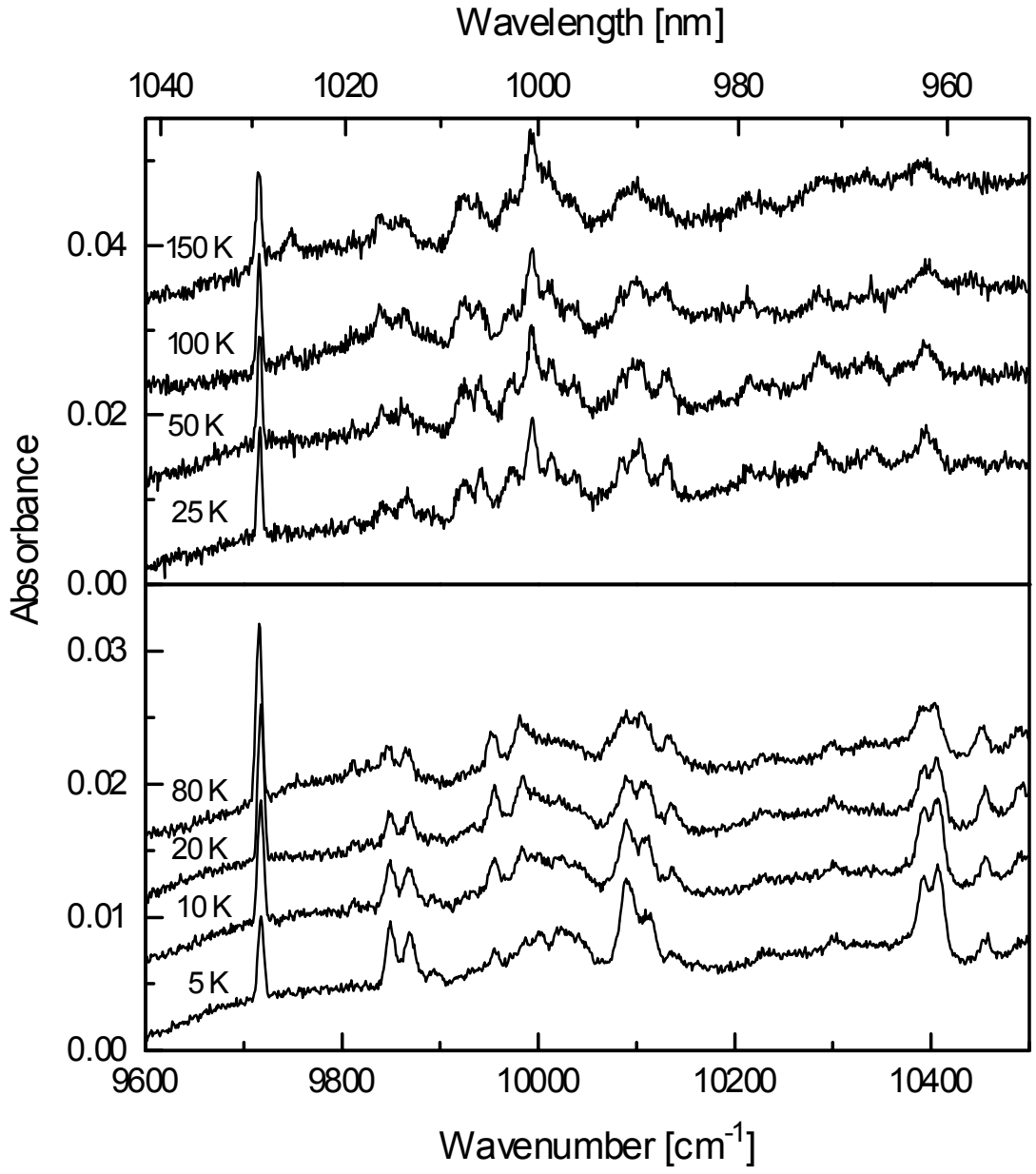

Figure 4.9 Temperature dependence of the unpolarized absorption spectra in the region of ^1E_g and $^1T_{2g}$ (O_h labels) spin-flip transitions of $Cs_3VCl_6(D_2O)_4$ (top panel) and $Cs_3VCl_6(H_2O)_4$ (bottom panel).

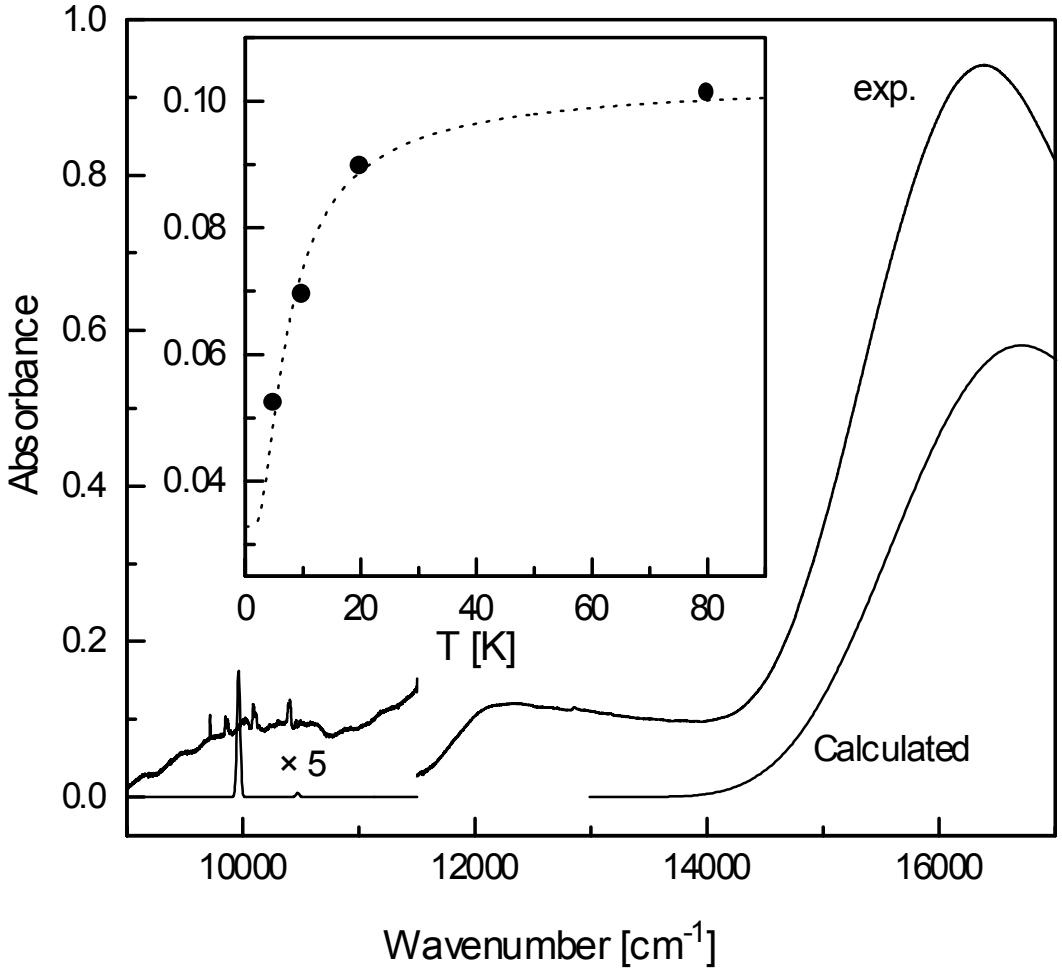

Figure 4.10 Calculation of the lowest $^1T_{2g}$ and $^3T_{2g}$ (O_h labels) bands in $Cs_3VCl_6{\cdot}4H_2O$. The calculated triplet intensity is normalized to the unpolarized $^3T_{2g}$ band in the 15000 to 20000 cm^{-1} region. The dots show the temperature dependence of the intensity of the first NIR absorption peak centered at 9717 cm^{-1} for $Cs_3VCl_6(H_2O)_4$. The dashed line is obtained from the fit of Equation 4.2 to the experiment, with a zero field splitting of 8 cm^{-1}.

Spin-orbit effects are quite weak in vanadium(III) complexes, as indicated by the low intensity of the singlet transitions in comparison to the triplet bands. We report a spin-orbit calculation for the first singlet and triplet bands in the absorption spectrum of $Cs_3VCl_6 \cdot 4H_2O$ in Figure 4.10. The calculated ratio $I_{triplet}/I_{singlet}$ is near the experimental ratio of 1118, a much higher value than for the nickel(II) and chromium(III) complexes. The singlet and triplet bands are well separated in the vanadium(III) complexes and the experimental ratio of intensities can be accurately calculated. We include both maxima observed between 14000 and 22000 cm^{-1} to calculate the intensity of the spin-allowed band. If only the first or only the second band is integrated to calculate the intensity, the experimental ratio is 2.5 times higher than the calculated one. All models discussed for this band indicate that both maxima are part of the triplet transition and we obtain a calculated $I_{triplet}/I_{singlet}$ ratio of 1275, slightly higher than the experimental value of 1118, as shown in Table 4.1. This excellent agreement again indicates that the double maximum discussed in the preceding section corresponds to a transition to a single excited electronic state, and not to the two states arising from $^3T_{2g}$ (O_h) in D_{4h} symmetry, illustrating again that the bandshape of the first spin allowed band in *trans*-$VCl_2(H_2O)_4^+$ is defined by vibronic effects.

5. *trans*-$CrCl_2(H_2O)_4^+$

5.1. $Cs_2CrCl_5 \cdot 4H_2O$

Crystallographic studies reveal that the green $CrCl_3 \cdot 6H_2O$ and $Cs_2CrCl_5(H_2O)_4$ crystals contain the *trans*-$CrCl_2(H_2O)_4^+$ chromophore[21-23]. $Cs_2CrCl_5(H_2O)_4$ is more suitable for spectroscopic investigations because it is more stable and its crystals are of higher optical quality than those of $CrCl_3 \cdot 6H_2O$[7]. The intensity of the first spin forbidden transition in this *trans*-dichlorotetraaquo chromophore is intermediate between those for the nickel(II) and vanadium(III) analogs. The separation between this transition and the first allowed band is also intermediate, as expected from their intensities. In a simple perturbation treatment, the intensity of the forbidden transition varies proportionally to $\zeta^2/\Delta E^2$[43], where ΔE is the separation of the doublet and the closest quartet states and ζ is the spin-orbit coupling constant. The chromium(III) complex clearly illustrates the intermediate case between strong (nickel) and weak (vanadium) coupling.

5.2. Spectroscopic results

The low temperature single crystal absorption spectra of $Cs_2CrCl_5(X_2O)_4$ are shown in Figure 4.11. The spectra of this dicesium compound are identical to those reported previously by McCarthy *et al*.[7]. Only the first quartet states which all arise from the ^4F free ion term can be clearly seen in the absorption spectra shown in Figure 4.11. The transitions to the ^2E_g and $^2T_{1g}$ (O_h) doublet states are reported in

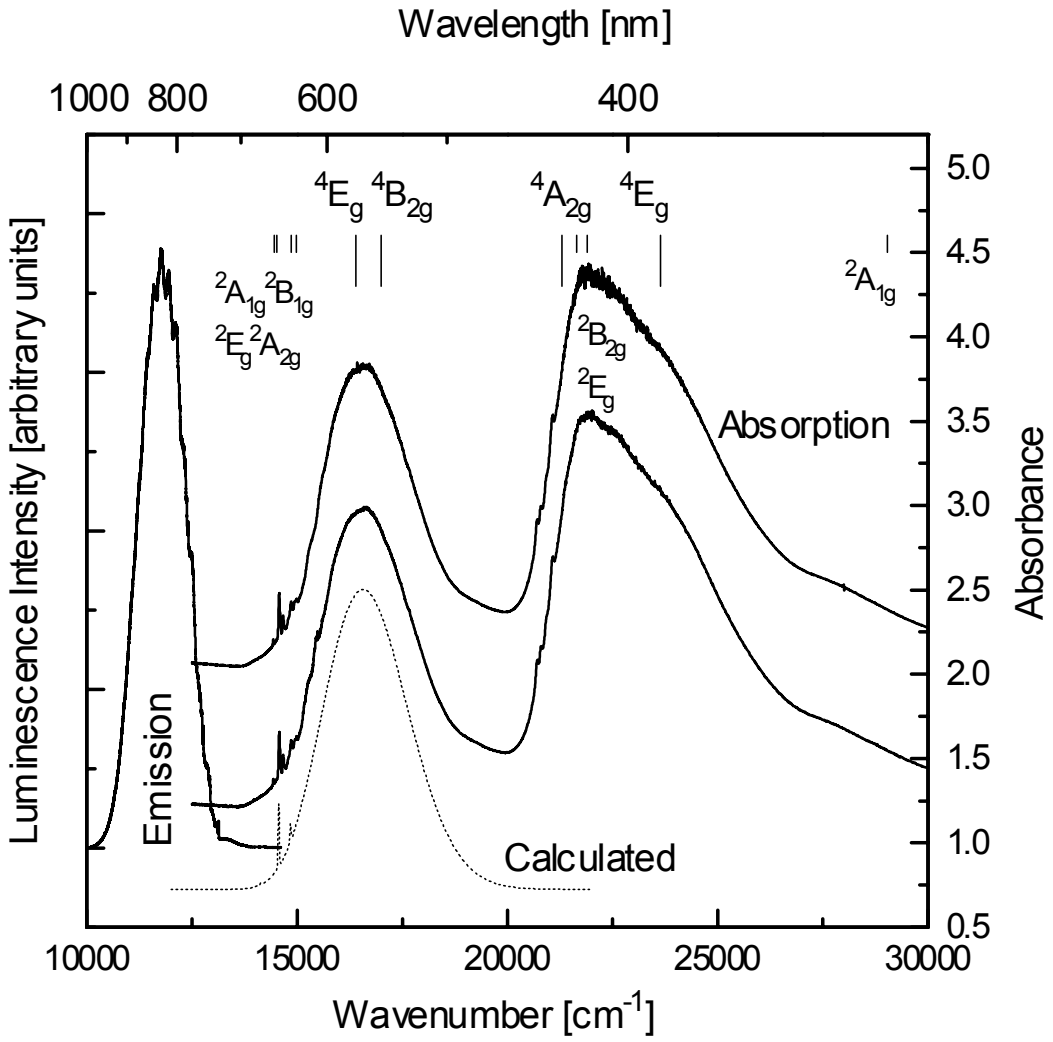

Figure 4.11 Unpolarized absorption spectra of $Cs_2CrCl_5 \cdot 4H_2O$ (bottom trace) and $Cs_2CrCl_5 \cdot 4D_2O$ (top trace) at 5 K. The trace at lower energy than the absorption spectra is the emission spectrum of $Cs_2CrCl_5 \cdot 4H_2O$ at 5 K. The dotted trace denotes the calculated spectrum for the first quartet and doublet states. The vertical lines represent the AOM energies calculated with parameters from Table 4.2 with ζ=0. The tall lines represent spin-allowed transitions, the short lines the spin-forbidden transitions.

detail in Figure 4.12. The origin of the first doublet band is at 14438 cm^{-1}, expected to be a component of ^2E_g (O_h) split by the tetragonal field. The exact position of the $^2T_{1g}$ state is not easily assigned within the sharp peaks between 14500 and 16000 cm^{-1}[7]. A higher $^2T_{2g}$ state (O_h) is seen around 22000 cm^{-1}, but the exact position of its electronic origin cannot be precisely determined due to overlap with more intense allowed transitions.

We compare the observed transition energies in Figure 4.11 to AOM calculations. The angular overlap parameters $e_\sigma(H_2O)$, $e_{\pi s}(H_2O)$ and $e_{\pi c}(H_2O)$ for the chromium(III) complex are 7000, 1000 and 500 cm^{-1}, respectively. For $e_\sigma(Cl)$ and $e_\pi(Cl)$, values of 6000 and 1000 cm^{-1} were used. The ligand-field parameters B and C and the energies in Table 4.2 are in reasonable agreement with the values reported by McCarthy *et al*.[7], and the overall agreement between calculated and observed transitions is good, as illustrated in Figure 4.11. A recent paper on the energy levels of tetragonal chromium(III) complexes in solution[50] reports calculated energies that are not significantly different from ours.

There are numerous emission spectra of hexaaquochromium(III) reported in the literature[41, 51-53], and chromium(III) halide complexes have also been studied by luminescence spectroscopy[54, 55], but only a few luminescence spectra of tetragonal chromium complexes are reported[56]. To our knowledge, no luminescence spectra of dichlorotetraaquochromium(III) have been published. The emission spectrum of $Cs_2CrCl_5{\cdot}4H_2O$ is shown in Figures 4.11 and 4.13. At 5 K, a large emission band from $^4T_{2g}$ (O_h) can be observed as shown in Figure 4.11 and its electronic origin is clearly detected at 13655 cm^{-1}, as indicated by the arrow in Figure 4.13. The broad

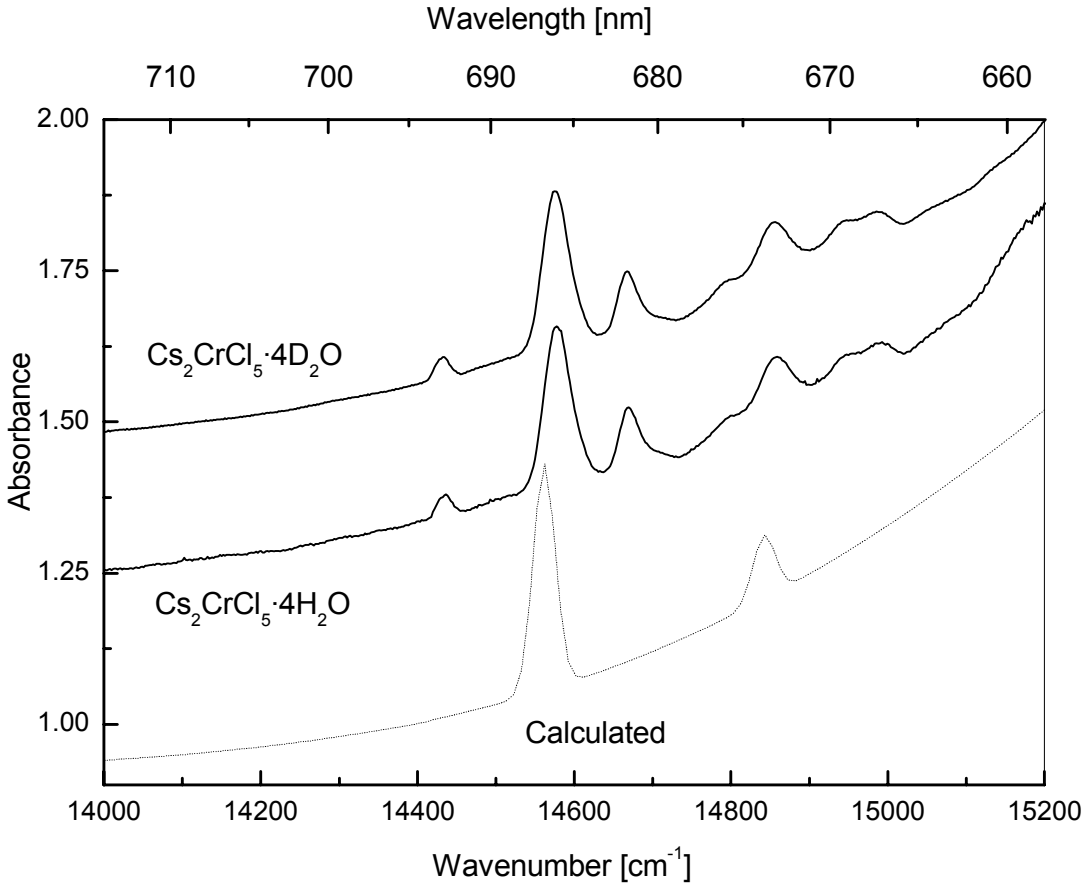

Figure 4.12 First transitions to ^2E_g and $^2T_{1g}$ (O_h notation) in $Cs_2CrCl_5 \cdot 4H_2O$ (bottom trace) and $Cs_2CrCl_5 \cdot 4D_2O$ (top trace). The dotted trace denotes the calculated spectrum.

band indicates that emission occurs from the lowest energy quartet state. High temperature fluorescence for chromium(III) aquo complexes has been reported by Forster[52], but to our knowledge Figures 4.11 and 4.13 present the first quartet-quartet emission with resolved vibronic structure observed at low temperature for a chromium(III) complex with aquo ligands.

We have also measured the luminescence spectra of the *trans*-dichlorotetraaquochromium chromophore in green $CrCl_3 \cdot 6H_2O$ and in green $Cr:AlCl_3 \cdot 6H_2O$, illustrated in Figure 4.14. Both spectra are similar. The high-energy region in the spectrum of $Cr:AlCl_3 \cdot 6H_2O$ is probably due to luminescence from $Cr(H_2O)_6^{3+}$. It is well known that different chloroaquochromium(III) isomers are formed in solution[23]. $Cr(H_2O)_6^{3+}$ doped into $AlCl_3 \cdot 6H_2O$ leads to sky-blue crystals[52], while $CrCl_2(H_2O)_4^{+}$ and $CrCl(H_2O)_5^{2+}$ lead to green crystals. The luminescence spectra in Figure 4.14 consist of a series of sharp bands arising all from the ^2E_g (O_h) state. In $Cs_2CrCl_5 \cdot 4H_2O$, the electronic origin of the quartet state is at lower energy than the origin of the emitting doublet states in Figure 4.14. This is the main spectroscopic difference between this solid and the green $CrCl_3 \cdot 6H_2O$, which contains luminophores with a very similar ligand sphere. The two chloride ligands of *trans*-dichlorotetraaquo chromium(III) appear to be sufficient to lead to a quartet emitting state, as observed for the limiting situation of a ligand environment consisting entirely of chloride ligands in $CrCl_6^{3-}$[55].

Other factors favoring luminescence from a quartet state include a strong splitting of the $^4T_{2g}$ (O_h) state lowering the electronic origin of a quartet component below the origin of the ^2E_g (O_h) state. The Jahn-Teller splitting of the ^4E_g state (D_{4h})

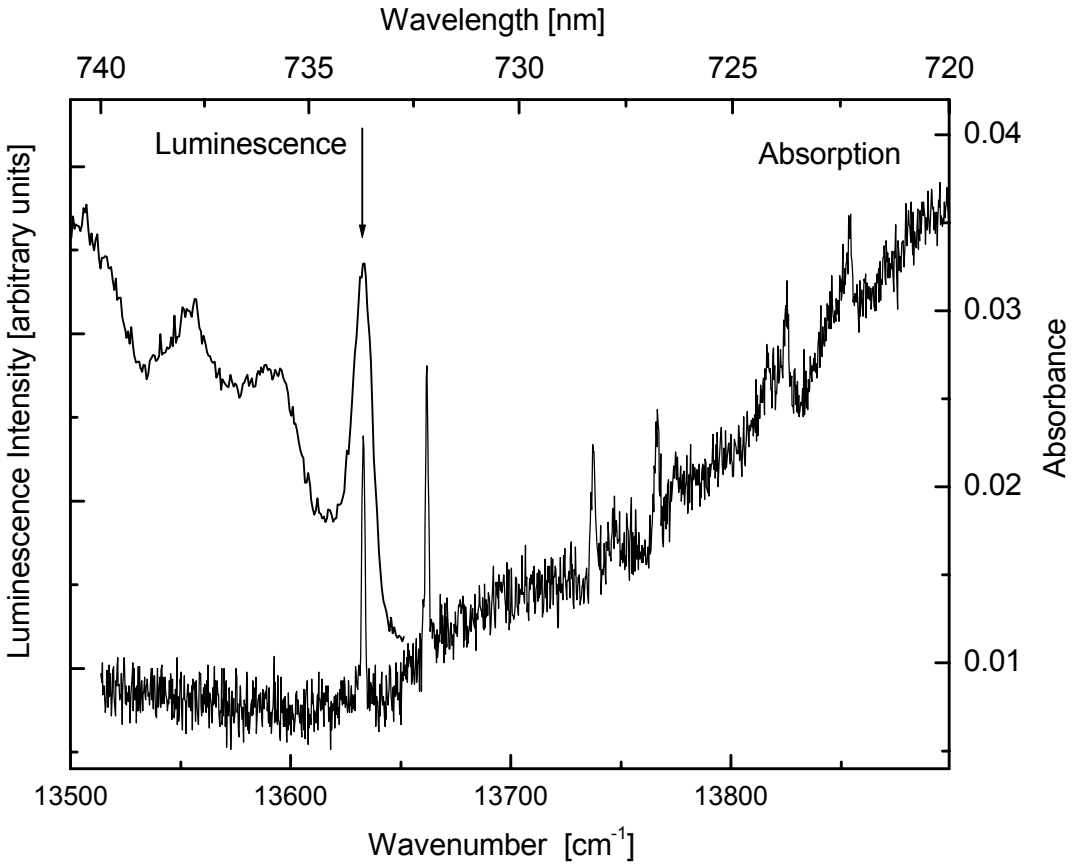

Figure 4.13 Unpolarized absorption spectrum of $Cs_2CrCl_5 \cdot 4H_2O$ (bottom trace) and emission spectrum (top trace) at 5 K. The arrow denotes the origin of the emission spectrum at 5 K.

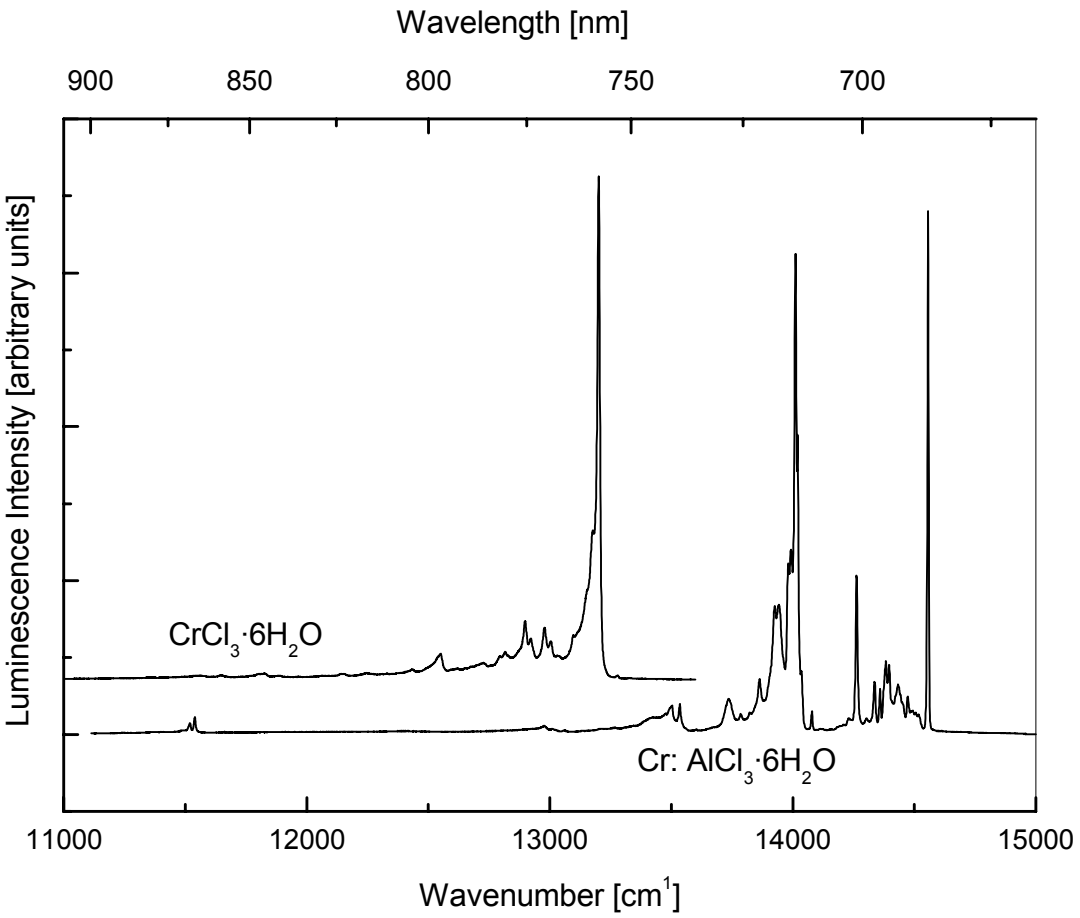

Figure 4.14 Emission spectra of green $CrCl_3 \cdot 6H_2O$ (top trace) and green $Cr{:}AlCl_3 \cdot 6H_2O$ (bottom trace) at 5 K. Both samples contain the $CrCl_2(H_2O)_4^+$ chromophore, but $AlCl_3 \cdot 6H_2O$ can also contain the $Cr(H_2O)_6^{3+}$ and $CrCl(H_2O)_5^{2+}$ chromophores.

could also lead to a particularly low-energy quartet component. The $t_{2g}^2e_g^1$ electronic configuration of the ^4E_g state is susceptible to a strong Jahn-Teller effect, and the main progression observed in the luminescence spectrum (see Figure 4.11) has an energy interval of 200 cm^{-1}, significantly different from the totally symmetric ν(Cr-Cl) and ν(Cr-O) modes observed in the Raman spectrum (286 cm^{-1} and 484 cm^{-1} respectively, see Table 4.2). This is evidence for distortions involving non-totally symmetric modes in the quartet excited state. All these effects are likely to play an important role in the luminescence behavior of $Cs_2CrCl_5 \cdot 4H_2O$.

The photophysics and photochemistry of aquo-chromium(III) complexes has been extensively studied in the past by several authors[52, 57-60]. We report new lifetime measurements on $CrCl_3 \cdot 6H_2O$, $Cr(H_2O)_6^{3+}$ (in $AlCl_3 \cdot 6H_2O$) and $Cr(D_2O)_6^{3+}$ (in $ND_4Al(SO_4)_2 \cdot 12D_2O$). For $Cr(D_2O)_6^{3+}$ we obtained a value for $(\tau p^0)^{-1}$ of 2805 sec^{-1} (τ=357 μs at 5 K) which is very close to the value of 2860 sec^{-1} (τ=350 μs) obtained by Camassei and Forster for $Cr(D_2O)_6^{3+}$ in $AlCl_3 \cdot 6D_2O$[52]. We have measured the values of $(\tau p^0)^{-1}$ for $Cr(H_2O)_6^{3+}$ and $CrCl_2(H_2O)_4^+$ (in green $CrCl_3 \cdot 6H_2O$) of 105165 (τ=9.5 μs) and 47740 s^{-1} (τ=21 μs), respectively, at 5 K. The lifetime of the *trans*-dichloro compound is more than twice the lifetime of the hexaaquo complex, a difference possibly due to the lower number of OH oscillators in the $CrCl_2(H_2O)_4^+$ chromophore. This comparison shows that lifetimes are very dependent on the number of water molecules coordinated to the chromium(III) cation, indicating that the main relaxation process is non-radiative. $Cr(D_2O)^{3+}$ and $Cr(H_2O)^{3+}$ are both emitting from ^2E_g state, but the deuterated compound has a lifetime that is more than 30 times longer. This comparison indicates that lifetime measurements on

these compounds cannot give reliable information on the spin multiplicity and other characteristics of the emitting state, since the non-radiative decay is always faster by order of magnitude than radiative processes.

The Raman spectrum of $Cs_2CrCl_3(H_2O)_4$ at 83 K is very similar to the spectrum of the analogous vanadium compound showing the five Raman active modes expected for a seven-atom D_{4h} complex. Their vibrational frequencies are observed between 150 and 550 cm^{-1} and they differ by only a few wavenumbers from those of the vanadium. A recent publication reports the infrared and Raman spectroscopy of the green pseudotetragonal form of $CrCl_3 \cdot 6H_2O$ and its deuterated analog at room temperature[61] and two strong bands at 463 cm^{-1} υ(Cr-O) and 295 cm^{-1} υ(Cr-Cl) were observed, frequencies that compare well with our results in Table 4.2.

5.3. Intersystem crossing and vibronic structure: intermediate effects caused by spin-orbit coupling

The intensity of the first forbidden transition in the aquo-chloro complexes of chromium(III) is intermediate between those of the vanadium(III) and nickel(II) analogs. The first singlet band of the $VCl_2(H_2O)_4^+$ chromophore is very weak and hard to detect in absorption experiments. The first forbidden doublet of the $CrCl_2(H_2O)_4^+$ chromophore is easily seen, but its intensity is much lower than that of the first spin-forbidden band of $NiCl_2(H_2O)_4$ (see Table 4.1).

There are two doublet states around 700 nm (14300 cm^{-1}) for the chromium compound, ^2E_g and $^2T_{1g}$ (O_h). Spin-orbit coupling transforms the ^2E_g to U and the $^2T_{2g}$

to E' and U. These levels can all interact with the $^4T_{2g}$ state which is split into E', E'' and 2U. Only the twofold degenerate E'' component of the quadruplet remains uncoupled to the doublet states in O_h symmetry[5]. There is no U state in D_{4h} symmetry, all levels are of E' or E'' symmetry. This particularity of the D_{4h} point group leads to very complicated interactions due to a large number of states of identical symmetry that can couple together and for that reason we treat the problem in approximate O_h symmetry. The model presented in the following is based on two coupled electronic states whose potential energy surfaces are defined along a single normal coordinate. It is therefore a semi-quantitative model, able to reproduce the intensity ratio between the allowed and forbidden bands, but not the resolved structure observed in Figure 4.12. We have recently analyzed the effect of multiple normal coordinates on the corresponding transitions of $Cr_2F_9^{-3}$[62]. It is likely that the quartet state of *trans*-$CrCl_2(H_2O)_4^+$ is also offset along several coordinates, but for the present analysis the one-dimensional model developed for the two preceding sections is sufficient.

The absorption band shape was calculated for the unpolarized spectrum of $Cs_2CrCl_5 \cdot 4H_2O$ at 5 K using time dependent theory in a similar way than for the $NiCl_2(H_2O)_4$ chromophore. Only the coupling between the ^2E_g (U) and $^4T_{2g}$ (U) (O_h labels) was taken into consideration. The large off-diagonal matrix element coupling these two states is $-\zeta\sqrt{6}/\sqrt{5}$ [5, 43]. The calculation involves the totally symmetric Cr-Cl stretching mode; the excited state vibrational frequency is assumed to be 286 cm^{-1}, identical to the ground state Raman frequency. The origin of the quartet state in the calculation was set to 13655 cm^{-1}, the value observed experimentally in emission

at 5 K, as shown in Figure 4.13. The spin-orbit coupling constant λ was set to 57 cm^{-1} (63% of the free ion value), as obtained from EPR measurements on $Cr(H_2O)_6^{3+}$ in alums[63], a value that was also used for ligand-field calculations on chromium(III) ions doped into oxides by Wood *et al*.[64]. All parameters in this model calculation are determined experimentally, except the excited state distortion ΔQ of the quartet state, which was adjusted to obtain a good agreement between experimental and calculated spectra. Parameter values are summarized in Tables 4.1 and 4.4. The calculated absorption intensity of the ^2E_g state using the model is in good agreement with the observed spectra. The calculated spectrum is show as a dotted trace on Figures 4.11 and 4.12.

6. *trans*-$CoCl_2(H_2O)_4$

6.1. $CoCl_2(H_2O)_4 \cdot 2H_2O$

The $CoCl_2(H_2O)_4 \cdot 2H_2O$ compound is isostructural to the nickel(II) analog[17, 18]. The low temperature polarized absorption spectra show many unusual bandshapes for forbidden and allowed bands. The cobalt(II) ion has a d^7 electron configuration and Kramer's degeneracy is expected for all states. The density of states in the visible part of the spectrum is very high (see Figure 4.15), and effects of coupled states are important. The close proximity of coupled states with identical symmetry makes this region of the cobalt(II) spectra unsuitable for a quantitative analysis with our model, which involves only two coupled electronic states of different spin multiplicity. The electronic absorption spectra of the cobalt(II)

compound in Figure 4.15 show very rich electronic and vibronic structure, similar to the spectroscopic results obtained for complexes in the preceding sections.

6.2. Spectroscopic results

Three quartet bands are expected for cobalt(II) compounds in octahedral symmetry. The first one is seen in the near-infrared region of the spectrum, involving the $^4T_{2g}$ state (O_h symmetry), split into ^4E_g and $^4B_{2g}$ in the D_{4h} point group. The assignment of the other two quartet bands is uncertain. For a mixed water and chloride ligand sphere, the $^4A_{2g}$ and $^4T_{1g}$ (O_h) states should be near a crossing point. Ferguson and Wood[10] have reported the $^4A_{2g}$ (O_h) state to be at 16450 cm^{-1} ($^4B_{1g}$ in D_{4h}) and the $^4T_{1g}$ state (O_h), to be split into ^4E_g and $^4A_{2g}$ (D_{4h}) at 18600 and 22250 cm^{-1}, corresponding to the strong bands in Figure 4.15.

The Raman spectrum of the $[CoCl_2(H_2O)_4]$ chromophore is very similar to the analogous nickel(II) compound[65], confirming that the two compounds are isostructural. The comparison of frequencies in Table 4.2 shows that some vibrational frequencies are similar for metals with identical oxidation states. For example, the ratio $\upsilon_{(CoO)}/\upsilon_{(NiO)}$ is about 0.99 for the totally symmetric stretching metal water mode. These frequencies are significantly different for trivalent ions, as illustrated by the ratio $\nu_{(CoO)}/\nu_{(VO)}$, which is 0.71. We carried out single crystal EPR and magnetic susceptibility measurements in order to determine the zero field splitting of the ground state. In both experiments, exchange effects dominate at low temperature and

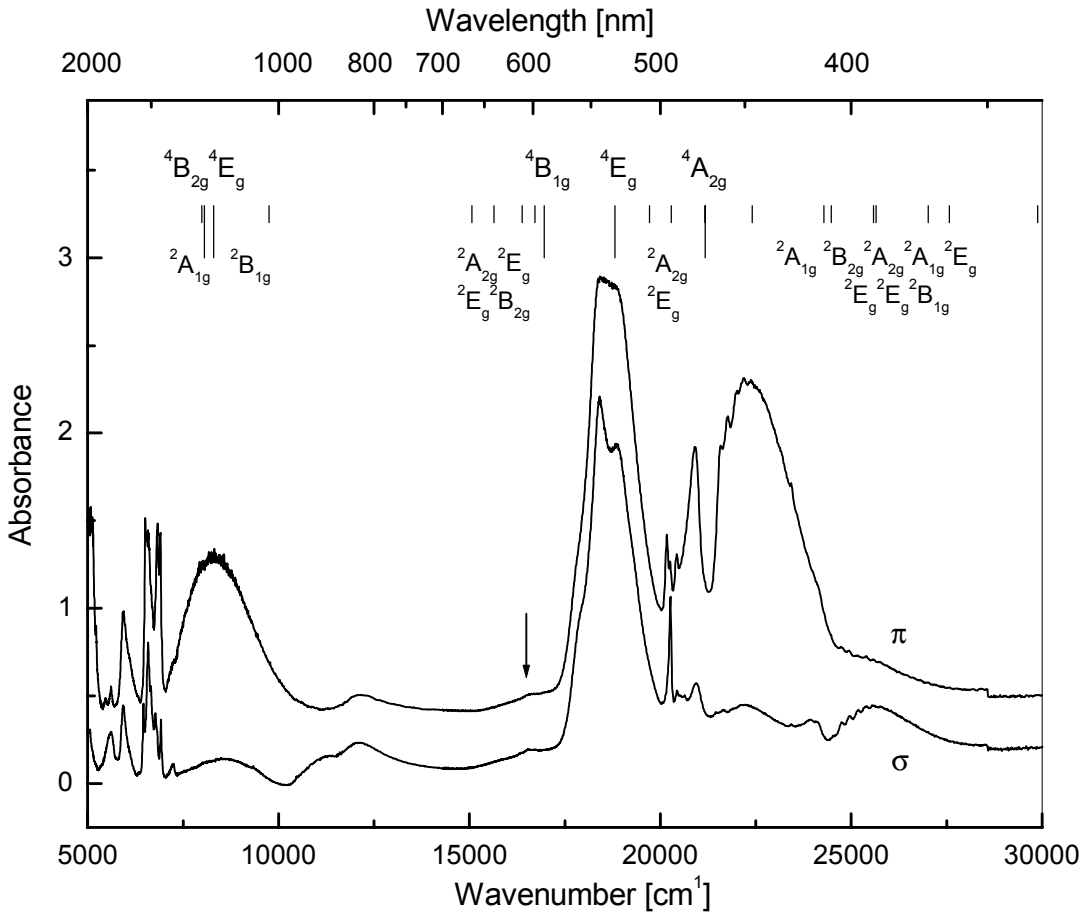

Figure 4.15 Polarized absorption spectra of $CoCl_2(H_2O)_4 \cdot 2H_2O$ at 5 K. The vertical lines represent the AOM energies calculated with parameters from Table 4.2 with ζ=0. The tall lines represent spin-allowed transitions, the short lines the spin-forbidden transitions.

it is not possible to determine energy levels for an individual complex in the concentrated crystal.

6.3. Effects of spin-orbit coupling between multiple states and vibronic transitions involving OH modes

The cobalt(II) ion with its d^7 electron configuration has the same 120 microstates as chromium(III). In the D_{4h} point group, a large number of doublet and quartet states are expected between 15000 and 30000 cm^{-1}. Numerous ligand field calculations have been reported for cobalt(II) complexes, supported by magnetic susceptibility and heat capacity measurements[66-69]. Four spectroscopic publications on $CoCl_2(H_2O)_4 \cdot 2H_2O$ include ligand field calculations, three of these in tetragonal symmetry[9-11] while one uses octahedral symmetry[12]. Due to the complexity of the absorption spectrum, the assignment of the bands is problematic and there are substantial differences between the assignments given by different authors.

We are particularly interested in tetragonal symmetry and for that reason we have compared our spectra and analyses to those of Ferguson and Wood and Joy and Fogel[10, 11]. The main differences between the assignments in these two publications concern the splitting of the ground state and the splitting of the first excited state in the near-infrared. The literature assignments are in agreement for the complicated part of the spectrum between 15000 and 30000 cm^{-1}. Joy and Fogel[11] assign the first NIR transition to the $^4B_{2g}$ state at 6600 cm^{-1} while Ferguson and Wood assign the first transition to be a ^4E_g at 8060 cm^{-1} [10]. In Table 4.2 we use the value

of Ferguson and Wood because there is no experimental evidence for a d-d transition at 6600 cm^{-1}, as this region is dominated by water overtones. Ferguson and Wood found magnetic dipole zero phonon lines in the near infrared located at 7092 and 7018 cm^{-1} (for $CoCl_2(H_2O)_4 \cdot 2H_2O$) and at 7122 and 7052 cm^{-1} (for $CoCl_2(D_2O)_4 \cdot 2D_2O$)[10]. These results show that an electronic transition located at 6600 cm^{-1} (below the electronic origins) is unlikely. The comparison to the water overtones in the spectra of the nickel(II) analog shows that both spectra are very similar in that region, as illustrated in Figure 4.3. It is well known that nickel(II) aquo compounds have no electronic transitions at these low energies.

A particularity of this spectrum is the transition to the $^4B_{1g}$ (D_{4h}) state ($^4A_{2g}$ in O_h). In two reports[10, 11], the authors locate it at approximately 16450 cm^{-1}, as denoted by the arrow in Figure 4.15. At first sight, the transition seems to be weak for an allowed band but the electron configuration of its final state is $t_{2g}^3 e_g^4$ and the intensity for such a two electron excitation is expected to be low. For the $^4B_{1g}$ (D_{4h}) state of the cobalt(II) complex there is no strong coupling possible with states arising from other crystal field or charge transfer electronic configurations. The charge transfer bands of the cobalt complex occur at energies higher than 40000 cm^{-1}. This energy difference of more than 25000 cm^{-1} greatly reduces the efficiency of coupling, and intensity borrowing. It is interesting to note that none of the spin-allowed crystal field bands is particularly weak for the nickel(II) complex in Figure 4.1, despite the fact that the $t_{2g}^4 e_g^4$ configuration, corresponding to a two electron excitation, contributes to the $^3T_{1g}$ states. We have shown with *ab-initio* calculations that these states arise from strongly mixed $t_{2g}^5 e_g^3$ and $t_{2g}^4 e_g^4$ configurations[70] and that

therefore no unperturbed double excitations can be observed, in contrast to the cobalt complex in Figure 4.15.

AOM calculations confirm the assignment of the $^4B_{1g}$ (D_{4h}) state. It is calculated at 16954 cm^{-1} with AOM parameters not too far from those of the related nickel(II) complex, as seen from Table 4.2. From magnetic susceptibility and heat capacity measurements, the position of the first two Kramer's doublets above the lowest energy state have been estimated at 152 cm^{-1} and 630 cm^{-1}[67]. We were able to approximately reproduce the position of these doublets at 167 and 868 cm^{-1}.

The near-infrared part of Figure 4.15 shows two maxima, the first one above 8000 cm^{-1} while the second is located near 12000 cm^{-1}. In π polarization, the first maximum is more intense than the second one. In octahedral symmetry, two states of different multiplicity are expected in this region of the spectrum, a $^4T_{2g}$ and a ^2E_g state. With aquo and chloro ligands, these two states should have potential energy surfaces with a crossing point near the Franck-Condon region and strong effects of coupling on the spectrum can be expected. The electronic configuration for the $^4T_{2g}$ state is $t_{2g}^4e_g^3$ while it is $t_{2g}^6e_g^1$ for the ^2E_g state. This difference of two electrons between the two configurations leads to a value of zero for the spin-orbit coupling matrix element. The only quartet which can couple to this ^2E_g state is the ground state. Strong spin-orbit interaction between excited electronic states of different spin multiplicity can arise only in the visible part of the spectrum, in Figure 4.15, for this cobalt(II) complex. Due to the high density of states that can interact in that spectral region, our simple model implying only two coupled states is inaccurate for a quantitative analysis of the spectrum. To avoid misuse of our model it is useful to

remember the selection rules for spin-orbit coupling between states: the electronic configurations should not differ by more than one electron, the product of $\Gamma_1 \times \Gamma_2$ should contain T_1 (for the O point group) and the spin difference $\Delta S=0,\pm1$[43]. The intensity of the weak ^2E_g band ($t_{2g}^6 e_g^1$) in π polarization is therefore mostly borrowed from the $^4T_{1g}$ ($t_{2g}^5 e_g^2$) ground state, the matrix element with all other quartets ($t_{2g}^4 e_g^3$ and $t_{2g}^3 e_g^4$) should be zero to respect the first selection rule.

The σ polarized transition between 25000 and 27000 cm^{-1} shows a vibronic progression with an interval of about 200 cm^{-1}. This frequency is observed in the Raman spectrum, as seen from Table 4.2. We found two strong bands at 183 and 199 cm^{-1}, in agreement with a literature study[65]. Ferguson and Wood have discussed this transition in terms of an anomalous band. The position of the band shifts to lower energy upon deuteration[10], and it appears that an OH vibrational mode is involved in the transition, a situation similar to the first triplet band of the vanadium(III) complex discussed in section 4.3. Weak bands involving OH modes are observed for nickel(II) aquo complexes[1, 24] and for the chromium(III) complex[7]. Figure 4.16 shows a comparison of this vibronic effect for all complexes. From this Figure it is easy to see that all complexes discussed in this paper exhibit a transition similar to the band of the cobalt(II) compound. The vanadium(III) complex shows the most dramatic effect, its anomalous band is stronger than the normal band in σ polarization. The origin of the vanadium(III) side band has been discussed in detail in section 4.3, testing several hypothesis that could also be considered for the other spectra in Figure 4.16. The vibronic band is σ polarized for all complexes, except for $NiCl_2 \cdot 6H_2O$, and its intensity varies from very weak to strong. This comparison

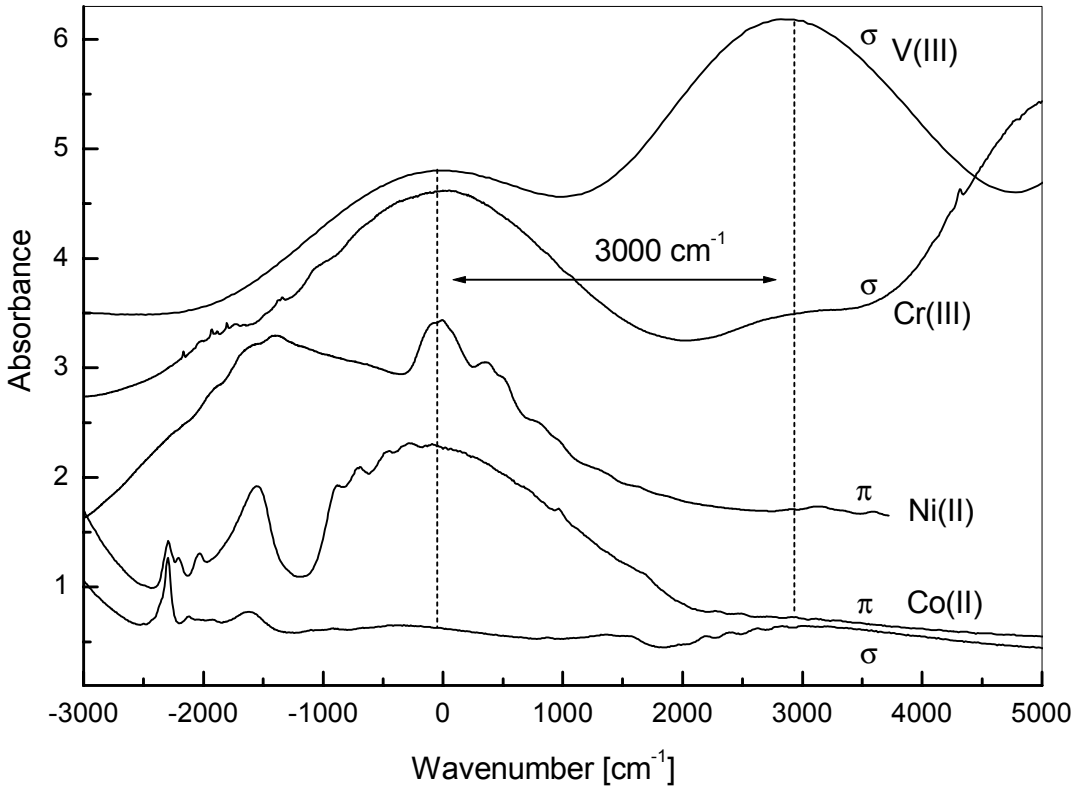

Figure 4.16 Absorption spectra of *trans*-dichlorotetraaquo complexes showing the OH vibrations, from top to bottom: $Cs_3VCl_6{\cdot}4H_2O$, $Cs_2CrCl_5{\cdot}4H_2O$, $NiCl_2{\cdot}6H_2O$ and $CoCl_2{\cdot}6H_2O$. The maxima of the transitions of interest were set to 0 cm^{-1} for this comparison. Each spectrum shows a second maximum near 3000 cm^{-1}, corresponding to a vibronic transition involving a high frequency OH mode.

illustrates the subtle characteristics of the metal-centered d-d transitions of the title complexes, which provide detailed information on aspects of the electronic structure extending beyond the metal-ligand bonds.

7. Conclusion

Intersystem crossing effects are observed in the spectra of many transition metal complexes. The title complexes show several different manifestations of intersystem crossings in their spectra. The sources of coupling are numerous and often hard to identify, but spin-orbit coupling always affects the band shapes and transition energies. The effect of spin-orbit coupling can be small and the forbidden bands can be hard to detect, like in the vanadium(III) complexes, or the effect can be drastic, increasing the vibronic interval in the spectra and the intensity of the formally forbidden transition, as observed for the nickel(II) complex.

Our calculations show that a simple model based on two coupled states allows us to quantitatively characterize the effects of intersystem crossing in many spectra. The calculated intensity ratios $I_{allowed}/I_{forbidden}$ vary by three orders of magnitude and are in good agreement with the experimental observations. Our model illustrates the relationship between ligand field theory (AOM) and vibronic effects involving potential energy surfaces. These two aspects have to be unified for a comprehensive and meaningful description of electronic states of transition metal complexes.

Acknowledgments

We thank Philip W. L. Tregenna-Piggot (Universität Bern) for the crystals of $CsAl(SO_4)_2 \cdot 12D_2O$: $V(D_2O)_6^{3+}$ and for help with the EPR measurements and Dominique Luneau (CEA Grenoble) for help with the magnetic measurements. This work was supported by grants from the Natural Sciences and Engineering Research Council (Canada).

Chapitre 5: Couplage entre états triplet des complexes $[Ni(H_2O)_6]^{2+}$ et $[V(H_2O)_6]^{3+}$: analyse par spectroscopie d'absorption et calculs *ab-initio* CASSCF/CASPT2.

Table des matières

Triplet electronic states in d^2 and d^8 complexes probed by absorption spectroscopy: a CASSCF/CASPT2 analysis of $[V(H_2O)_6]^{3+}$ and $[Ni(H_2O)_6]^{2+}$

Julie Landry-Hum [a], Guillaume Bussière [a], Chantal Daniel [b], and Christian Reber [a]

Département de chimie, Université de Montréal, Montréal QC H3C 3J7, Canada. and Laboratoire de Chimie Quantique, UMR 7551 CNRS/Université Louis Pasteur, Institut Le Bel, 4 Rue Blaise Pascal, 67 000 Strasbourg, France

[a] Université de Montréal

[b] Laboratoire de chimie quantique, CNRS/Université Louis Pasteur

Inorg. Chem. **2001**, *40*, 2595-2601

Abstract

Octahedral complexes of transition metal ions with d^2 and d^8 electron configurations have triplet electronic states with identical T_{2g}, A_{2g}, T_{1g} (^3F) and $T_{1g}(^3P)$ symmetry labels. CASSCF and CASPT2 calculations indicate the predominant electronic configurations for each triplet state. The two $^3T_{1g}$ states show strong configuration mixing in the d^8 complex $[Ni(H_2O)_6]^{2+}$, but much weaker mixing occurs between these states in the d^2 compound $[V(H_2O)_6]^{3+}$. Calculated vibrational frequencies and equilibrium geometries for the triplet states are used to obtain theoretical absorption spectra that are in agreement with the experimental data.

Synopsis

The interaction between the two $^3T_{1g}$ excited states of $[Ni(H_2O)_6]^{2+}$ leads to potential energy surfaces with mixed electronic character and minima at similar values along the normal coordinate, in contrast to $[V(H_2O)_6]^{3+}$, where a large offset between minima is expected. CASSCF and CASPT2 calculations characterize this effect. Absorption spectra calculated from the CASPT2 potential surfaces are in good agreement with experimental data.

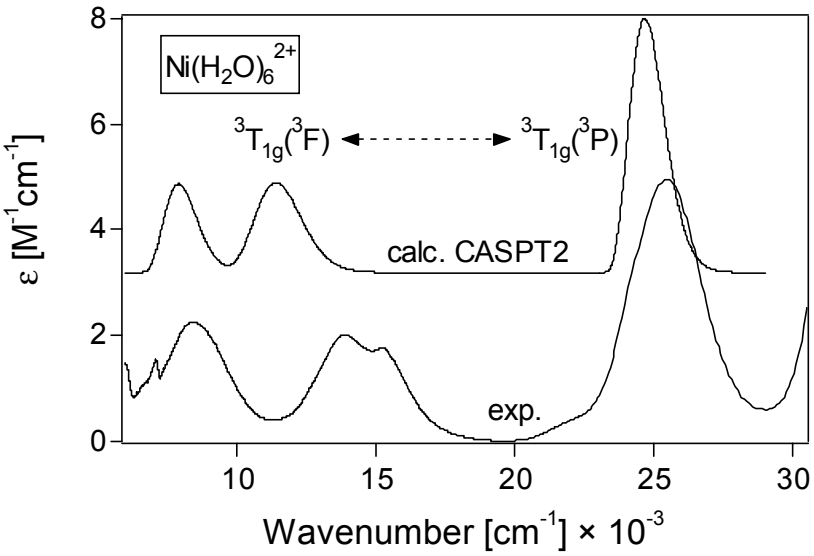

Introduction

Broad bands arising from spin-allowed d-d transitions in the visible and near-infrared dominate the absorption spectra of many transition metal compounds. An excellent qualitative description of the electronic states involved in these transitions is obtained from crystal field theory for a complex in a "frozen" molecular configuration, excluding any vibronic processes. Potential energy surfaces are needed for a more complete description of the vibronic transitions, which always involve changes in the molecular structure[1]. These potential energy surfaces are traditionally determined from a Franck-Condon analysis of the experimental vibronic spectra. Particularly precise information can be obtained from spectra with resolved vibronic progressions[2]. Such empirical potential energy surfaces do not, in general, allow us to characterize electronic configurations or coupling between electronic states and it is usually assumed that the electronic configuration obtained from the crystal field model for a single molecular geometry does not vary along the normal coordinates.

Optical absorption and luminescence spectra have been used to obtain experimental information on coupling effects between electronic states in specific situations. We have illustrated such effects for singlet and triplet states in $[Ni(H_2O)_6]^{2+}$[3, 4] and related complexes of metal ions with a d^8 configuration, as well as for *trans*-dioxo complexes of rhenium(V) and osmium(VI) complexes, metal centers with a d^2 configuration[5]. In the nickel(II) complexes, unusual progressions appear in the absorption spectrum due to a crossing between the lowest energy singlet state and a triplet excited state. The luminescence spectra of the rhenium and osmium

complexes show vibronic structure that reveals coupling effects between the singlet ground state and several excited states. The coupling in all these complexes involves states with different spin multiplicity and its effects can be analyzed from experimental spectra with resolved vibronic structure.

In the following, we investigate interactions between states with identical spin multiplicity that lead to absorption bands without resolved structure. For our model study, we choose the low energy triplet excited states of $[Ni(H_2O)_6]^{2+}$ and of $[V(H_2O)_6]^{3+}$. These states arise from different electronic configurations and we compare our quantitative results to the expectations from crystal field theory. We present potential energy curves (PEC) based on CASSCF and CASPT2 calculations and focus on the contributions of different electronic configurations for the two $^3T_{1g}$ states along the single normal coordinate used in our model. Absorption spectra calculated from these potential curves involve no adjustable parameters and we compare calculated band maxima, band widths and vibrational frequencies to the experimental spectra. We take advantage of the electron-hole analogy to illustrate the interacting $^3T_{1g}$ states for the d^2 and d^8 electronic configurations and to explore the vibronic spectra that can be expected from these coupled states. The ground state properties of the title compounds and many other aquo complexes have been explored by detailed electronic structure calculations[6], but effects involving coupled excited states have not been investigated.

Six-coordinate nickel(II) centers doped into halide lattices show absorption spectra similar to $[Ni(H_2O)_6]^{2+}$. These solid materials have unusual spectroscopic properties, such as luminescence from higher energy excited states, allowing for the observation of intriguing optical effects[7-12]. A very important factor leading to

these properties is the large energy separation between the two $^3T_{1g}$ states, to which the states mixing contributes, as discussed in the following for our two model complexes. Our calculations rationalize this energy separation and underline the importance of mixing between electronic states of transition metal chromophores.

Experimental Section and Spectroscopic Results

$[Ni(H_2O)_6]^{2+}$ was crystallized as the Tutton salt $(NH_4)_2Ni(SO_4)_2 \cdot 6H_2O$ from H_2O and D_2O, respectively, and an aqueous solution of $[V(H_2O)_6]^{3+}$ was prepared from $VCl_3 \cdot 6H_2O$ dissolved in 2M H_2SO_4. Absorption spectra were measured on a Varian Cary5E spectrometer and Raman spectra were obtained with a Renishaw System 3000 spectrometer using the 514.5 nm line of an Ar^+ ion laser as excitation source.

The spin allowed transitions to triplet crystal field excited states are easily observed in near infrared and visible absorption spectra of the two title complexes and have been reported in the literature[3, 4, 13-16]. Our spectra of $[V(H_2O)_6]^{3+}$ are identical to those in the literature[13-15,17]. The triplet crystal field bands of both $[Ni(H_2O)_6]^{2+}$ and $[V(H_2O)_6]^{3+}$ do not show resolved vibronic structure at room temperature. In contrast, the lowest-energy band of $[Ni(H_2O)_6]^{2+}$ crystallized as the Tutton salt shows well resolved structure for both the H_2O and D_2O ligands at low temperature. To the best of our knowledge, resolved spectra for this transition have not been reported before for $[Ni(H_2O)_6]^{2+}$.

Figure 5.1a shows the solution absorption spectra of $[Ni(D_2O)_6]^{2+}$ and $[V(H_2O)_6]^{3+}$ and the assignments of their spin allowed bands are given in idealized O_h

symmetry, used for simplicity throughout the following. We dissolved the nickel complex in D_2O in order to obtain a better spectrum in the region of the onset to the lowest-energy triplet band, where vibrational overtones of H_2O mask the crystal field transition. The band maxima observed in solution do not vary significantly between $[Ni(H_2O)_6]^{2+}$ and $[Ni(D_2O)_6]^{2+}$ for the level of detail shown in Figure 5.1a. The transition to the $^3A_{2g}$ excited state of $[V(H_2O)_6]^{3+}$ can not be unambiguously identified from the literature spectra and from our own measurements and it is therefore not included in our discussion.

Low-temperature spectra in the energy region of the onset of the lowest energy absorption band are given in Figure 5.1b for the crystalline $[Ni(H_2O)_6]^{2+}$ and $[Ni(D_2O)_6]^{2+}$ complexes. The crystals have well defined extinction directions, but the relative intensities of the resolved transitions do not show distinct polarization effects. We therefore report unpolarized spectra obtained on approximately 3 mm thick crystals in Figure 5.1b. The spectra show resolved vibronic structure, in contrast to the higher energy spin allowed bands of $[Ni(H_2O)_6]^{2+}$ and to all spin allowed transitions of $[V(H_2O)_6]^{3+}$, where the resolution of the spectra is significantly inferior to Figure 5.1b.

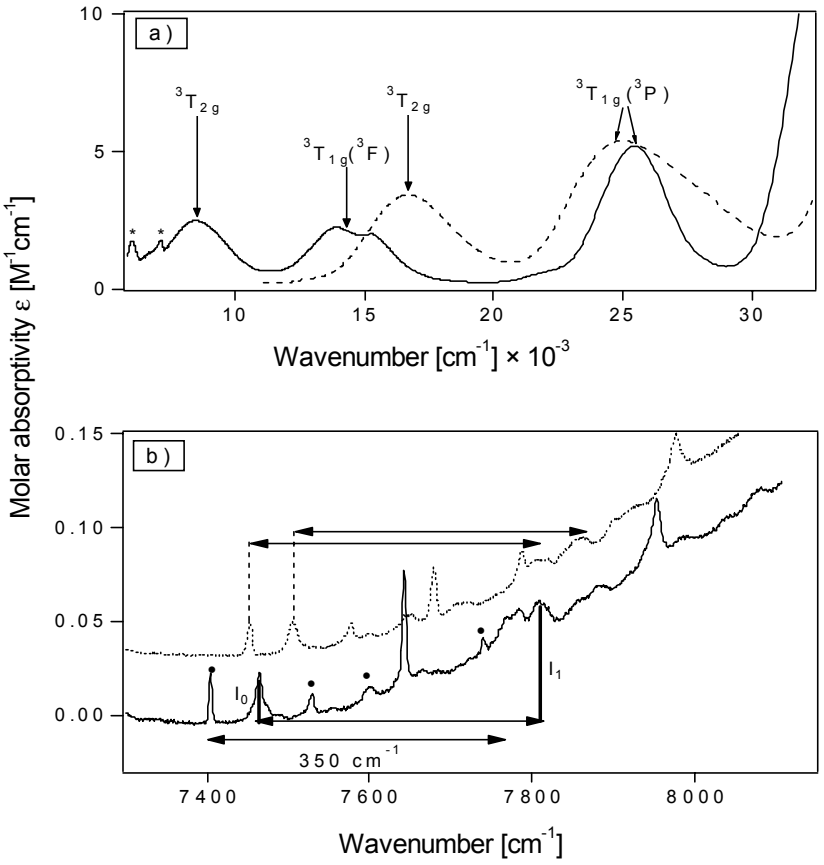

Figure 5.1 (a) Visible and near infrared solution absorption spectra of $Ni(D_2O)_6]^{2+}$ (solid line) and $[V(H_2O)_6]^{3+}$ (broken line) at room temperature with the assignment for all spin-allowed crystal field bands. The asterisks in the spectrum of $[Ni(D_2O)_6]^{2+}$ denote vibrational overtones or instrumental artifacts. (b) Single crystal absorption spectra of crystalline $(NH_4)_2Ni(SO_4)_2{\cdot}6(H_2O)$ (solid line) and its deuterated analogue (dotted line) at 5 K in the origin region of the lowest energy electronic transition. The dots denote transitions separated by equal energy intervals in the hydrated and deuterated complexes.

The well resolved peaks in Figure 5.1b correspond to transitions to the individual components of the $^3T_{2g}$ state, which is split by spin-orbit coupling and the low site symmetry of the complex in the crystal[18]. It is important to note that both spectra in Figure 5.1b show distinct progressions with an interval of approximately 350 cm^{-1}. This frequency corresponds to the totally symmetric Ni-H_2O stretching mode observed at 397 cm^{-1} in the Raman spectrum at 77 K. The low-temperature spectrum shows barely resolved shoulders separated by 350 cm^{-1} across the band, and progressions in this mode have been reported for the $^3T_{1g}(^3F)$ excited state in a detailed study of $[Ni(H_2O)_6]^{2+}$ in a series of crystal lattices[16]. This is therefore the most important mode determining the overall bandwidth. The spectrum is much less resolved at energies higher than the wavenumber range shown in Figure 5.1b, making it impossible to observe and analyze long progressions and even to observe the first member of the 350 cm^{-1} progression on some of the higher-energy vibronic origins. Weaker progressions in a mode with a frequency of approximately 200 cm^{-1} are also observed. They probably correspond to one of the Jahn-Teller active e_g and t_{2g} modes in the idealized O_h symmetry. These modes have frequencies of 299 cm^{-1} and 232 cm^{-1} in the ground state, as determined from the Raman spectra at 77 K.

The comparison between the spectra of $[Ni(H_2O)_6]^{2+}$ and $[Ni(D_2O)_6]^{2+}$ in Figure 5.1b allows us to identify vibronic transitions. The difference between the lowest energy peak and higher energy resolved transitions is systematically lowered for vibronic transitions of the deuterated complex. This comparison indicates that the transition at 7464 cm^{-1} denoted as I_0 on the lower trace of Figure 5.1b and the intense bands observed at 7642 cm^{-1} and 7954 cm^{-1} for $[Ni(H_2O)_6]^{2+}$ are vibronic origins. The bands whose energy difference from the lowest energy transition does not change

with deuteration are marked with dots in Figure 5.1b. It is tempting to assign these four bands as the electronic origins of transitions to the four spin orbit components E_g, T_{1g}, T_{2g} and A_{2g} expected in O_h symmetry, as the NiO_6 fragment of the complex does not deviate significantly from O_h symmetry[18]. These spin-orbit levels cover an energy range of approximately 600 cm^{-1} for crystal field parameters that reproduce all spin allowed d-d bands and the lowest energy spin forbidden transition. The ground state spin orbit coupling constant λ of –270 cm^{-1} was used for the calculations[3, 19, 20]. The bands marked with dots in Figure 5.1b span a range of approximately 300 cm^{-1}. This reduction is possibly a consequence of a Ham effect, in analogy to the corresponding lowest energy $t_{2g} \rightarrow e_g$ excitation studied in detail for a number of chromium(III) complexes[21,22]. We do not attempt to quantitatively analyze this splitting pattern due to the lack of information on electronic origins that could be hidden in the higher-energy region of the band, which shows significantly less resolution than the wavenumber range shown in Figure 5.1b. Large splitting of the $^3T_{2g}$ state cannot be ruled out for the title complexes due to the influence of anisotropic π bonding, which depends strongly on the position of the hydrogen atoms in each water ligand. This effect is not explored in the model calculations discussed in the following.

Computational Methods

The molecular structures of $[M(H_2O)_6]^{n+}$ (M=Ni, V; n=2,3) used for the calculations are based on the experimental structures of $Ni(H_2O)_6(NO_3)_2$[23], $NiCl_2(H_2O)_4$[24]

and $Cs_4V(H_2O)_6(SO_4)_2 \cdot 6H_2O$[25], $Cs_3VCl_6 \cdot 4H_2O$[26] with metal-oxygen distances of 2.06 Å and 1.97 Å for Ni-O and V-O, respectively. The model geometry and coordinate system used in the calculations are shown in Figure 5.2. These bond lengths are varied to obtain the potential energy surfaces shown in the following. The ligands are defined by O-H distances of 1.04 Å and H-O-H angles of 104.5°. Their structure and the orientation of the H_2O plane are not varied for our calculations.

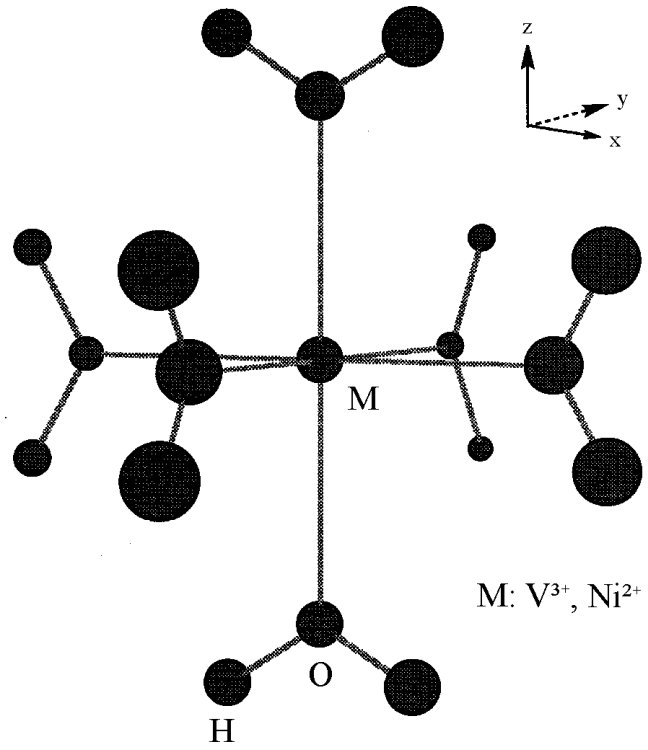

Figure 5.2 Molecular structure and coordinate system used for the CASSCF/CASPT2 calculations.

The electronic configuration of $[Ni(H_2O)_6]^{2+}$ in its $^3A_{2g}$ ground state is $(3d_{xy})^2(3d_{xz})^2(3d_{yz})^2(3d_{x2-y2})^1(3d_{z2})^1$, corresponding to $(t_{2g})^6(e_g)^2$ in the O_h point group, whereas the $^3T_{1g}$ electronic ground state of $[V(H_2O)_6]^{3+}$ is given by $(3d_{xy})^{2/3}(3d_{xz})^{2/3}(3d_{yz})^{2/3}(3d_{x^2-y^2})^0$ $(3d_{z^2})^0$, corresponding to $(t_{2g})^2(e_g)^0$ in the O_h point

group. In order to analyze the spectroscopy of $[M(H_2O)_6]^{n+}$ the low-energy triplet excited states generated by the single and double excitations within the 3d orbitals manifold have been calculated. Averaged CASSCF calculations in which eight electrons ($M=Ni^{2+}$) or two electrons ($M=V^{3+}$) have been correlated in thirteen active orbitals (the five 3d orbitals of the metal centers, the 3d of correlation and some diffuse orbitals delocalized over the oxygen atoms and the metal center) have been performed in order to generate the zero-order wavefunctions used as references in subsequent CASPT2 calculations that include the dynamical correlation effects. This active space was chosen to be identical for both title complexes in order to provide calculated spectroscopic properties that can be compared. The correlated calculations have been driven in D_{2h} symmetry and a level shift correction of 0.4 has been applied in the case of the nickel complex to eliminate intruder states[27, 28]. Spin-orbit effects are not included in the present calculations. The spin-orbit splitting of the triplet states in first-row transition metal complexes does not exceed a few hundreds of wavenumbers, a small effect compared to the nonadiabatic coupling on the order of thousands of wavenumbers, which is of interest here.

Let us note that the CASPT2 method, which is essentially monoconfigurational, should be used with care in situations of states mixing. In such cases, the zero order CASSCF wavefunction has to correctly describe this mixing in order to avoid erroneous results from the perturbational treatment. This is a potentially serious problem in the nickel complex. However, the stability of the CASPT2 calculation is assured by a nearly constant reference weight ω of approximately 0.70 in the case of

the vanadium complex and 0.76 in the case of the nickel compound for all electronic states and geometry variations investigated here.

On the basis of the experimental spectroscopic data, the totally symmetric average elongation of the M-O bonds along the normal coordinate ΔQ_{a1g} has been retained as the most important mode of deformation of the molecules in the crystal-field triplet excited states investigated here. The origin of the ΔQ_{a1g} axis is set at the ground state equilibrium geometry. The PEC associated to these low-lying triplet states are calculated as a function of this coordinate at the CASSCF and CASPT2 levels. Harmonic frequencies and the positions of the potential minima along the abscissa, denoted as ΔQ_{a1gmin}, were obtained from these calculations as summarized in Tables 5.1 and 5.2. We note that the rather large energy separation between the $^3T_{1g}(^3F)$ and $^3T_{1g}(^3P)$ states of $[Ni(H_2O)_6]^{2+}$ complex justifies *a posteriori* the computational method which describes the mixing at the zero-order only (CASSCF).

The basis sets which are of generally contracted atomic natural orbital (ANO) type are the following[29]: for the nickel and vanadium atoms a (17s, 12p, 9d, 4f) set contracted to [5s, 4p, 3d], for the oxygen atoms a (10s, 6p, 3d) set contracted to [3s, 2p, 1d] and for the hydrogen atoms a (7s, 3p) set contracted to [2s, 1p].

The calculations have been performed with the program system MOLCAS4.1[30].

Computational Results and Discussion

Crystal field states.

We present crystal field energy level diagrams to illustrate the electronic states important for the following discussion. The Tanabe-Sugano diagrams for $[V(H_2O)_6]^{3+}$ and $[Ni(H_2O)_6]^{2+}$ are given in Figures 5.3a and 5.3b, respectively. The coupling between the $^3T_{1g}$ states is obvious for both configurations and the d^8 diagram shows a prominent avoided crossing near the Dq range for the H_2O ligand. The corresponding effect is also visible in the d^2 diagram, where the two $^3T_{1g}$ states are closest at Dq=0, far from the region of the H_2O ligand.

The electronic energies of the coupled states are calculated as the eigenvalues of the weak-field energy matrix[31]:

$$\begin{vmatrix} -6Dq - E(^3T_{1g}(^3F)) & 4Dq \\ 4Dq & 15B - E(^3T_{1g}(^3P)) \end{vmatrix} = 0 \qquad (5.1)$$

The dotted lines in Figure 5.3 denote the diagonal elements of this matrix. The coupling constant between the states is 4Dq and the solid lines denote the energies of the $^3T_{1g}$ crystal field states. We note that the corresponding strong-field matrix leads to the same eigenvalues as eq. 5.1[31]. Numerical values for pairs of parameters Dq, B are 910 cm^{-1}, 950 cm^{-1}[3] and 1860 cm^{-1}, 665 cm^{-1}[32] for $[Ni(H_2O)_6]^{2+}$ and $[V(H_2O)_6]^{3+}$, respectively, as indicated on the abscissa of Figure 5.3.

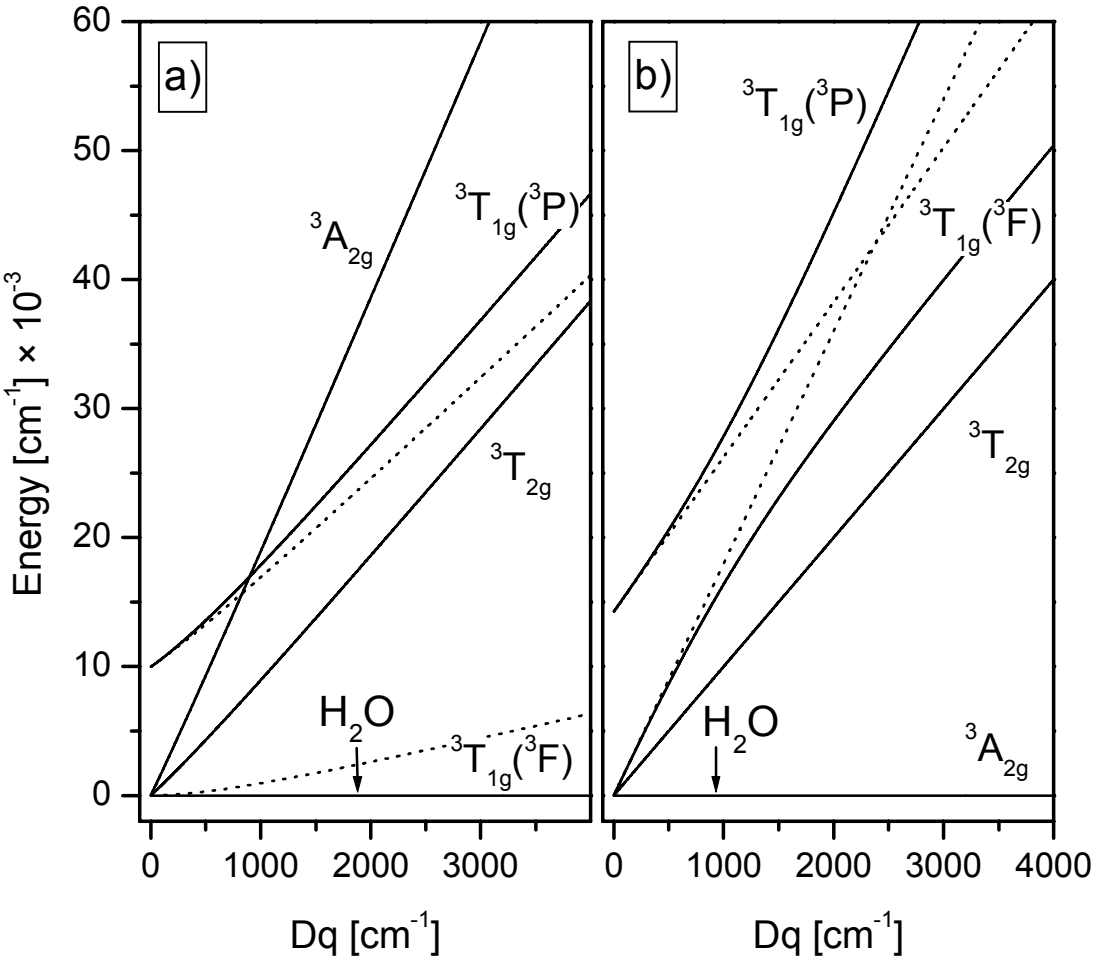

Figure 5.3 Tanabe-Sugano diagram for (a) $[V(H_2O)_6]^{3+}$ and (b) $[Ni(H_2O)_6]^{2+}$. The diagrams include only the triplet states discussed in this study. The position of the H_2O ligand for both complexes is indicated on the Dq axis. The broken lines give the energies of the $^3T_{1g}$ states if the off-diagonal matrix element coupling these states is set to zero.

Crystal field energies for all triplet states define the point of each excited state potential energy surface directly above the ground state equilibrium geometry. Both diabatic and adiabatic potentials for the two $^3T_{1g}$ states can be obtained by adding harmonic terms in ΔQ_{a1g} to the diagonal elements of eq. 5.1[3]. These surfaces are shown as dotted and solid lines in Figure 5.4. The offset of the minima along the abscissa is qualitative and increases with the number of electrons in the σ-antibonding e_g orbitals of the predominant electronic configurations of the two coupled states. We expect the ground state potential energy minimum for the vanadium(III) complex at a lower value of ΔQ_{a1g} than for the excited state, which arises from the $(t_{2g})^1(e_g)^1$ configuration, with a higher e_g σ-antibonding electron density than the ground state (Figure 5.4a). The adiabatic potentials are calculated with the coupling constant of 4Dq given in eq. 5.1 and the experimental vanadium-water stretching frequency of 530 cm^{-1}[15]. These adiabatic potentials retain the essential aspects of the harmonic diabatic surfaces: the V-O bond length is shorter in the $^3T_{1g}$ ground state than in the excited state with $^3T_{1g}$ symmetry. The minimum of the adiabatic potential curve in Figure 5.4a is lower in energy by 2330 cm^{-1} than the minimum of the diabatic curve. The vertical lines denote the positions of the minima of the adiabatic potentials. They are slightly closer to each other than the minima of the harmonic potentials, which are separated by 0.2 Å. The separation remains large, as shown by the horizontal double arrow in Figure 5.4a and leads to the broad $^3T_{1g}(^3F) \rightarrow {}^3T_{1g}(^3P)$ absorption band.

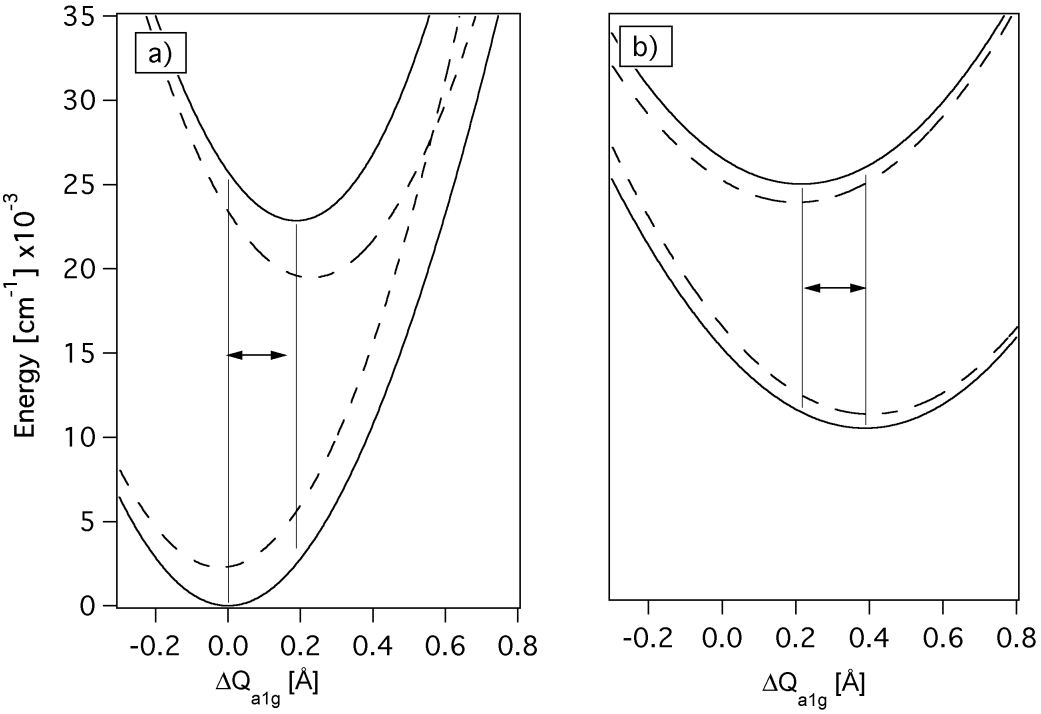

Figure 5.4 Schematic potential energy surfaces for the $^3T_{1g}$ states of (a) $[V(H_2O)_6]^{3+}$ and (b) $[Ni(H_2O)_6]^{2+}$. Solid and broken lines denote adiabatic and diabatic potentials, respectively.

The situation is different for the nickel complex, as shown in Figure 5.4b. The diabatic potentials are calculated with a vibrational frequency of 350 cm^{-1}, determined from the resolved spectra in Figure 5.1b and their minima are separated by 0.2 Å, the same value used for the corresponding states in Figure 5.4a. The $^3T_{1g}(^3F)$ excited state arises from the $(t_{2g})^4(e_g)^4$ configuration (in the formalism used for eq. 5.1) and its diabatic potential has a larger offset along the abscissa than the higher energy $^3T_{1g}(^3P)$ excited state, which arises from the $(t_{2g})^5(e_g)^3$ configuration with less e_g σ-antibonding electron density. We illustrate this difference by the position of the minima of the diabatic potential along Q. The minimum of the state arising from $(t_{2g})^5(e_g)^3$ is at 0.2 Å and the minimum of the state arising from $(t_{2g})^4(e_g)^4$ is at 0.4 Å, assuming an identical increase along Q for each electron placed into the σ-antibonding orbitals. The character of the adiabatic potentials is strongly mixed and varies along Q. This mixing leads to potential minima that are closer together than for the corresponding states in Figure 5.4a, as illustrated by the vertical lines and the shorter double arrow in Figure 5.4b. These similar potential curves rationalize the comparable bandwidths observed for the two transitions to $^3T_{1g}$ excited states shown in Figure 5.1a. Crystal field calculations give only a qualitative description of this variation, because they strongly depend on the choices made for the parameters Dq, B and C[13, 33, 34] and only d electronic configurations are considered. The most important aspect of the qualitative $^3T_{1g}$ potentials in Figure 5.4b is that they no longer strictly reflect the different electronic configurations of the two diabatic states. In analogy to the electronic energies in Figure 5.3, there are several different ways of defining diabatic potentials that lead to identical adiabatic potential surfaces. In the

crystal field approach, the two traditional ways are the weak-field and strong-field formalisms. This problem has been discussed in detail in the literature[35].

The qualitative PEC in Figure 5.4 shows that coupled potentials cross very far from the Franck-Condon region. We therefore use the adiabatic approximation to calculate absorption spectra throughout the following. In order to obtain a more quantitative picture of the potentials illustrated in Figures 5.4a and 5.4b, *ab-initio* calculations presented in the following section have been performed using the CASSCF/CASPT2 approach.

Potentials associated to the triplet crystal field states of $[V(H_2O)_6]^{3+}$.

The CASPT2 PEC calculated as a function of ΔQ_{a1g} and associated to the $^3T_{1g}(^3F)$ electronic ground state and to the low-lying $^3T_{1g}(^3P)$ and $^3T_{2g}$ excited states of $[V(H_2O)_6]^{3+}$ are represented in Figure 5.5a. The corresponding calculated vibrational frequencies, minimum energies and equilibrium M-O distances are reported in Table 5.1. Values reported in this table and in the Figure are obtained from one representative of the $^3B_{1g}$, $^3B_{2g}$, $^3B_{3g}$ states arising from each $^3T_{1g,2g}$ state in the D_{2h} symmetry of our model shown in Figure 5.2.

The potential minima of the $^3T_{2g}$ and $^3T_{1g}(^3P)$ excited states are shifted along ΔQ_{a1g} by 0.22 and 0.19 Å, respectively, at the CASPT2 level. As expected from the schematic picture in Figure 5.4a, the minima of the $^3T_{1g}$ ground and excited states do not coincide. Obviously, CASSCF calculations give only a qualitative picture of the potentials and associated properties, as illustrated by the values listed in Table 5.1. For instance, the minimum of the ground state PEC is obtained at an unphysically

large value of the normal coordinate from the CASSCF calculations and at a much more reasonable position with respect to experimental bond lengths at the CASPT2 level. This is due to the dynamical correlation effects (not included at the CASSCF level), which are very large in transition metal complexes. These correlation effects arise form the multiple excitation of the CASSCF inactive electrons and in general vary for different electronic states and as a function of the normal coordinate Q. As a consequence, the shape and relative positions of the CASPT2 potentials generally differ significantly from those obtained at the CASSCF level, but different electronic states are not affected to the same amount.

The lowest singlet excited state is calculated at 9270 cm^{-1} and 9890 cm^{-1} with CASSCF and CASPT2, respectively, very close to the corresponding sharp experimental absorption band observed at 10200 cm^{-1} for $[V(H_2O)_6]^{3+}$ doped into a cesium aluminum alum lattice[15]. We have recently measured the highest-energy luminescence transition for $[V(D_2O)_6]^{3+}$ at 10234 cm^{-1}. This good agreement between experimental and calculated energies of the lowest spin-flip transition further corroborates the validity of our model calculations.

Potentials associated to the crystal field triplet states of $[Ni(H_2O)_6]^{2+}$.

The CASPT2 PEC calculated as a function of ΔQ_{a1g} and associated to the $^3A_{2g}$ electronic ground state and to the low-lying $^3T_{1g}(^3F)$, $^3T_{1g}(^3P)$ and $^3T_{2g}$ states of $[Ni(H_2O)_6]^{2+}$ are represented in Figure 5.5b. The corresponding calculated vibrational frequencies, minimum energies and equilibrium Ni-O bond length changes are summarized in Table 5.2. Values reported in this Table are obtained from one

Table 5.1 Calculated equilibrium distances ΔQ_{a1gmin}, minimum energies E_{min} and vibrational frequencies $\hbar\omega$ for the triplet crystal field states of $[V(H_2O)_6]^{3+}$. Experimental values are given in parentheses.

Electronic state	CASSCF			CASPT2		
	ΔQ_{a1gmin} [Å]	E_{min} [cm^{-1}]	$\hbar\omega$ [cm^{-1}]	ΔQ_{a1gmin} [Å]	E_{min} [cm^{-1}]	$\hbar\omega$ [cm^{-1}]
$^3T_{1g}(^3F)$	0	0	124	0	0	253 (530[b])
$^3T_{2g}$	-0.71	9660	227	0.23	9830 (13400[a])	320
$^3T_{1g}(^3P)$	-0.73	23680	222	0.19	19930 (20700[a])	318

[a] estimated from Fig. 5.1a

[b] from [15]

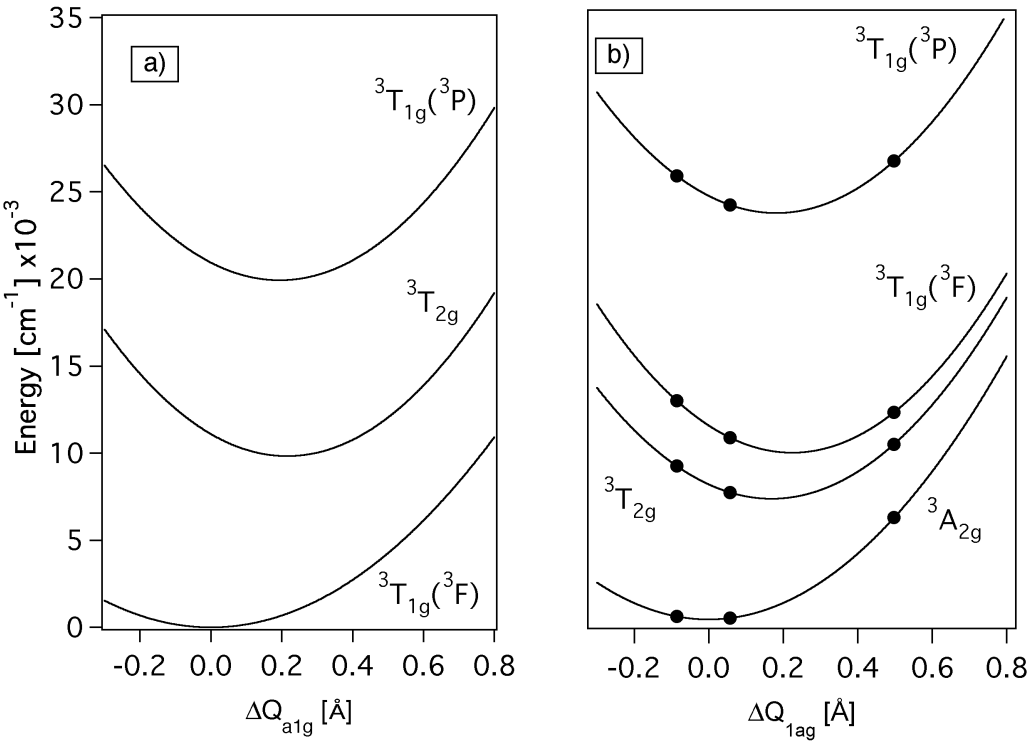

Figure 5.5 CASPT2 potentials for (a) $[V(H_2O)_6]^{3+}$ and (b) $[Ni(H_2O)_6]^{2+}$. Dots indicate molecular geometries for which configuration state functions are given in Table 5.3.

representative of the $^3B_{1g}$, $^3B_{2g}$, $^3B_{3g}$ states arising from each $^3T_{1g,2g}$ state in the D_{2h} symmetry of the model structure shown in Figure 5.2.

The resolved vibronic structure of the $^3T_{2g}$ band of $[Ni(H_2O)_6]^{2+}$ in Figure 5.1b allows us to estimate the position of the minimum ΔQ_{a1gmin} of this excited state PEC with respect to the ground state equilibrium geometry. The intensities of the first two members of the progression in the totally symmetric M-H_2O stretching mode are given as I_0 and I_1 in Figure 5.1b. The ratio I_1/I_0 is not significantly different for the deuterated complex and we determine a value of 2.2 from the spectra. The value of ΔQ_{a1gmin} is given as[1, 2]:

$$\Delta Q_{a_{1g}\,\min} = \frac{8.2118\sqrt{\frac{I_1}{I_0}}}{\sqrt{\hbar\omega m}} \qquad (5.2)$$

where $\hbar\omega$ denotes the vibrational frequency of the excited state, determined as 350 cm^{-1} from Figure 5.1b, and m is the mass of the ligand, 18 g/mole. We calculate a value of 0.15 Å from eq. 5.2, in excellent agreement with the value of 0.16 Å from the CASPT2 results in Table 5.2, again illustrating the good quality of the calculations. A similar analysis for the other excited states is not possible because the absorption bands do not show resolved structure.

Table 5.2 Calculated equilibrium distances ΔQ_{a1gmin}, minimum energies E_{min} and vibrational frequencies $\hbar\omega$ for the triplet crystal field states of $[Ni(H_2O)_6]^{2+}$. Experimental values are given in parentheses.

Electronic state	CASSCF			CASPT2		
	ΔQ_{a1gmin} [Å]	E_{min} [cm^{-1}]	$\hbar\omega$ [cm^{-1}]	ΔQ_{a1gmin} [Å]	E_{min} [cm^{-1}]	$\hbar\omega$ [cm^{-1}]
$^3A_{2g}$	0	0	318	0	0	300 (397[b])
$^3T_{2g}$	0.12	5678	346	0.17	7039 (6600[a])	332
$^3T_{1g}(^3F)$	0.17	8308	356	0.23	9724 (11300[a])	343 (350[c])
$^3T_{1g}(^3P)$	0.14	24850	350	0.18	23703 (23000[a])	337

[a] estimated from Fig. 5.1a.

[b] Raman, 77 K, this work.

[c] ref.[16]

Table 5.3 CASSCF weights of the configuration state functions for the triplet excited states of $[Ni(H_2O)_6]^{2+}$.

ΔQ_{a1g} [Å]	$^3T_{2g}$	$^3T_{1g}(^3F)$		$^3T_{1g}(^3P)$	
	$(t_{2g})^5(e_g)^3$	$(t_{2g})^4(e_g)^4$	$(t_{2g})^5(e_g)^3$	$(t_{2g})^4(e_g)^4$	$(t_{2g})^5(e_g)^3$
-0.0859	97%	70%	26%	27%	73%
0.0567	97%	72%	25%	25%	63%
0.4974	97%	76%	21%	21%	67%

The CASPT2 vibrational energies and minima of the PEC are in the range of the experimental values. Recent calculated frequencies reported in the literature for the ground state of several chromium(III) halide complexes deviate by up to 30% from the experimental frequencies measured for single crystals[36, 37], comparable to the differences we report in Tables 5.1 and 5.2. Another recent study on manganese(IV) doped into a fluoride lattice reports discrepancies of up to 20% between calculated and experimental ground state frequencies[38]. These studies involve isotropic metal-ligand π bonds, in contrast to the present work, where anisotropic π bonding occurs and is represented by the model structure in Figure 5.2. We examine only the variation of the metal-oxygen bond lengths and neglect the effects that an optimization of the orientation of the plane of each water ligand could have on vibrational frequencies in all electronic states of interest. Some of the literature studies include the crystal environment in the calculations, a second aspect

that was neglected in the present study, but could also influence vibrational frequencies and transition energies. In view of these simplifications, the agreement between calculated and observed frequencies is satisfactory. Excited state frequencies are usually not reported in the literature. The higher frequencies calculated for some excited states are counterintuitive, but the difference is within the variation between experimental and calculated values for the ground state.

In contrast to the vanadium complex, where the PEC calculated for the two $^3T_{1g}$ states have their minima close to the values expected without considering coupling between states, we observe here important effects due to mixing between these two electronic states as a function of the totally symmetric normal coordinate ΔQ_{a1g}. This is illustrated by the CASSCF weights of the configuration state functions reported in Table 5.3. For instance, we observe an increase of the $(t_{2g})^4(e_g)^4$ configuration from 70 to 76% in the $^3T_{1g}(^3F)$ state with the Ni-O bond elongation over the range given by the solid circles in Figure 5.5b. Even though this mixing occurs far from the crossing region, it will cause significant spectroscopic effects, illustrated by the relative positions of the potential minima associated to the two $^3T_{1g}$ states, which are within 0.06 Å despite their different electronic character. For comparison, in the vanadium complex, these states remain nearly pure (89% $(t_{2g})^2(e_g)^0$ for $^3T_{1g}(^3F)$, 92% $(t_{2g})^1(e_g)^1$ for $^3T_{1g}(^3P)$), and their character varies by less than 3% over the same range of ΔQ_{a1g}, leading to minima separated by 0.19 Å, a much larger value than for the nickel complex. Finally we note that the character of the $^3T_{2g}$ state for the nickel complex does not vary at all at the geometries in Table 5.3, again confirming the relevance of the state mixing calculated for the $^3T_{1g}$ excited states.

Calculated absorption spectra.

The spectroscopic effects induced by coupling between the $^3T_{1g}$ states are illustrated by the calculated spectra in Figure 5.6, which were obtained from the CASPT2 potentials in Figure 5.5. All absorption spectra were calculated using equal transition dipoles for each band. This assumption is justified by the experimental spectra of the nickel(II) complex, which do not show an unusually weak band for the transition corresponding predominantly to the two-electron excitation. Even in some vanadium(III) complexes, whose spectra contain an unusually weak band for the formal two-electron excitation from the $^3T_{1g}$ ground state to the $^3A_{2g}$ excited state, the experimental intensity of this band has been shown to be higher by orders of magnitude than estimated from the mixing coefficients[39]. Other factors, such as the efficiency of various ungerade parity enabling modes, appear to have a more important influence than the mixing coefficients. The absorption spectrum is calculated as[1, 2]:

$$I_{abs}(\omega) = \omega \int_{-\infty}^{\infty} e^{i\omega t} \left\langle \phi \middle| \phi(t) \right\rangle e^{-\Gamma^2 t^2 + \frac{iE_{00}}{\hbar} t} dt \qquad (5.3)$$

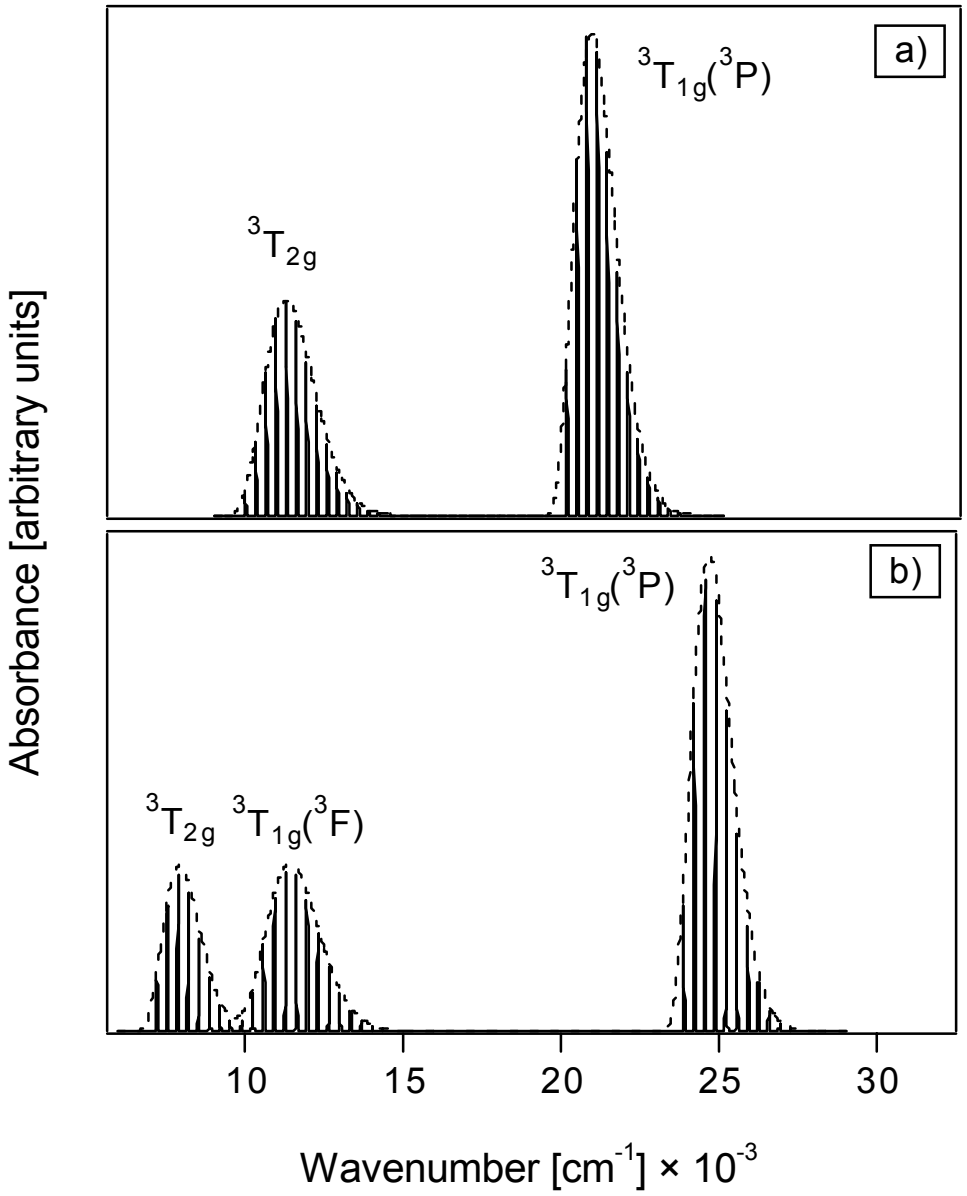

Figure 5.6 Absorption spectra for the spin-allowed transitions calculated from the CASPT2 potential curves for (a) $[V(H_2O)_6]^{3+}$ and (b) $[Ni(H_2O)_6]^{2+}$.

The linear frequency factor ω causes the different relative intensities of the calculated bands in Figure 5.6. The autocorrelation functions and Fourier transforms were calculated as described in detail before[3]. The origins E_{00} of the calculated bands for $[V(H_2O)_6]^{3+}$ are at 9830 cm^{-1} and 19930 cm^{-1} and compare well to the origin energies estimated from the experimental spectra at 13400 cm^{-1} and 20700 cm^{-1} respectively. The calculated bands are narrower by 25% to 50% than the experimental bands. The most likely reasons for this discrepancy are effects neglected in our model, such as Jahn-Teller distortions, and excited state splittings due to low site symmetry[18], energy differences between vibronic origins, which give rise to the main observed intensity, and spin-orbit coupling. All these effects lead to experimental bands that are larger than the calculations based on the PECs in Figure 5.5. The overall agreement between experiment and calculations is satisfactory.

Figure 5.6b shows the calculated absorption spectrum with all spin-allowed transitions of the nickel complex. As for the vanadium complex, the spectrum is obtained from the CASPT2 potential curves using identical transition dipoles for each band. The calculated electronic origins of the three bands are at 7039 cm^{-1}, 9724 cm^{-1} and 23703 cm^{-1} and the calculated spectrum shows a large energy gap of 13280 cm^{-1} between the two $^3T_{1g}$ band maxima. This energy difference is larger by almost a factor of two than the energy difference between the ground state and the lowest energy excited state, where the band maximum is calculated at 7910 cm^{-1}. The mixing of the $^3T_{1g}$ states contributes significantly to their large energy separation, illustrated by the schematic potential energy surfaces in Figure 5.4b. The calculations rationalize the experimental observation of very similar bandwidths for the two $^3T_{1g}$

bands in many octahedral nickel(II) complexes, even though the two states formally arise from different electronic configurations.

The comparison of the two calculated spectra in Figure 5.6 shows that the first band is at lower energy for the divalent nickel complex than for the trivalent vanadium complex, in agreement with the higher 10Dq value expected for the vanadium ion with its higher charge. The calculated spectra also confirm the experimental observation that the transition to the $^3T_{1g}(^3P)$ excited state occurs at higher energy in the nickel complex than in its vanadium analog. This is due to the higher energy of the atomic ^3P parent term in the nickel complex and to the steeper slope of the $^3T_{1g}(^3P)$ state as a function of Dq, as illustrated in Figure 5.3b. The steeper slope is a consequence of the significant 27% contribution of the electronic configuration with two additional electrons in the e_g orbitals to $^3T_{1g}(^3P)$, a direct energetic manifestation of the configuration mixing in the nickel complex

The *ab-initio* calculations show that the potential minima of the $^3T_{1g}(^3F)$ and $^3T_{1g}(^3P)$ states in the nickel complex are at very similar positions along the ΔQ_{a1g} axis, as illustrated in Table 5.2. This model study reveals that even states separated by a large energy difference can interact in ways that affect the experimental absorption spectrum.

Conclusion

Our combined experimental and theoretical study focuses on the effects of coupling between electronic states in $[V(H_2O)_6]^{3+}$ and $[Ni(H_2O)_6]^{2+}$, model

complexes with the d^2 and d^8 electronic configurations, respectively. The main qualitative trends are illustrated by a simple crystal field analysis. Quantitative spectroscopic properties have been extracted from CASSCF/CASPT2 potentials associated to the low lying triplet states and calculated as a function of a single normal coordinate, the totally symmetric M-H_2O stretching mode. The theoretical approach has enabled us to describe and to analyze the significant mixing between the two $^3T_{1g}$ states in $[Ni(H_2O)_6]^{2+}$. This strong interaction characterizing the nickel compound leads to potentials with minima at almost the same position along the normal coordinate, in contrast to the vanadium analog, where they are separated by approximately 0.2 Å. The interaction between states is an important reason for the observation of two $^3T_{1g}$ bands with nearly identical widths in the experimental spectra of many octahedral nickel complexes.

Acknowledgments

This work was made possible by grants and fellowships (to J. L.-H. and G. B.) from the Natural Sciences and Engineering Research Council (Canada) and by a visiting faculty fellowship (to C.R) from the Ministère des relations internationales (Province of Quebec) and the Ministère des affaires étrangères (France). We thank Myriam Triest (Université de Montréal) for helpful discussions. The calculations have been carried out either at the IDRIS (Orsay, France) through a grant of computer time from the Conseil Scientifique or at the LCQS (Strasbourg, France).

Chapitre 6: Luminescence de certains complexes de lanthanides avec des ligands nitronyl-nitroxyde.

Ligand-centered near-infrared luminescence from lanthanide complexes with chelating nitronyl nitroxide free radicals

Christophe Lescop [a], Dominique Luneau [a],
Guillaume Bussière [b], Myriam Triest [b], Christian Reber [b]

[b] Département de chimie, Université de Montréal
[a] Service de Chimie Inorganique et Biologique (UMR No. 5046), Département de Recherche Fondamentale sur la Matière Condensée, CEA-Grenoble, 38054 Grenoble cedex 09, France

Inorg. Chem. **2000**, *39*, 3740-3741.

Abstract

Luminescence spectra between 700 nm and 1000 nm are reported for a nitronyl nitroxide free radical and for its complexes with trivalent lanthanum, europium and gadolinium. The energy of the electronic origin is approximately 14,500 cm^{-1} and varies by 400 cm^{-1} between the free ligand and the metal complexes. At temperatures below 10 K resolved vibronic structure is observed in both absorption and luminescence spectra. The energy intervals and vibronic intensity distributions illustrate the influence of the lanthanide-radical coordination on the luminescence properties.

Several lanthanide complexes with free radical ligands have been prepared and characterized recently[1-4]. These compounds show a wide variation of magnetic properties, illustrated by gadolinium(III) complexes, for which both ferromagnetic[1, 4] and antiferromagnetic[2, 3] interactions between the unpaired electrons on the ligand and on the lanthanide center are observed. The nature of this ground-state magnetic coupling has been investigated in detail by comparing complexes with free radical and related diamagnetic ligands[4].

The excited electronic states and the luminescence properties of these new lanthanide complexes have not been explored. Electronic emission and absorption spectroscopy is used to gain insight on the ground and lowest-energy excited states of a series of new complexes of the nitronyl nitroxide radical shown in Scheme 6.1 (denoted as NITBzImH in the following) with trivalent lanthanum, europium and gadolinium ions. We describe the preparation, crystal structure and solid-state luminescence spectroscopy of the lanthanide-radical complexes and we compare the results to the spectra of the free ligand. The magnetic properties of all materials have been measured and will be reported and analyzed in a comprehensive study.

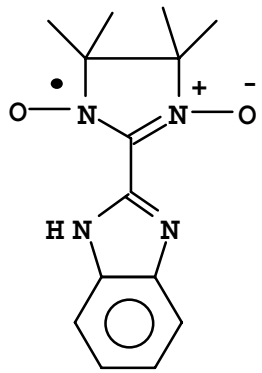

Chart 6.1. *NITBzImH Ligand*

Complexes of formula [Ln(III)(NITBzImH)$_2$(NO$_3$)$_3$] (Ln= La, Gd, Eu) were synthesized as air stable single crystals by slowly evaporating a solution mixture of NITBzImH, prepared as described in ref. 5, with stoechiometric amounts of [Ln(III)(NO$_3$)$_3$(H$_2$O)$_n$] in ethanol[6]. These compounds are isostructural and crystallize in the non-centrosymmetric group Pna2$_1$[7]. A view of the molecular structure is shown for the gadolinium complex in Figure 6.1. The lanthanide ion is coordinated by two nitronyl nitroxide ligands through one oxygen atom of the NO groups and one nitrogen atom of the benzimidazole moiety. The two radicals are not symmetry related. Three nitrate anions in η^2 mode complete the coordination sphere to a coordination number of 10. Similar molecular structures have been previously reported for lanthanide complexes with a closely related nitronyl nitroxide radical substituted with a triazole group[1, 4].

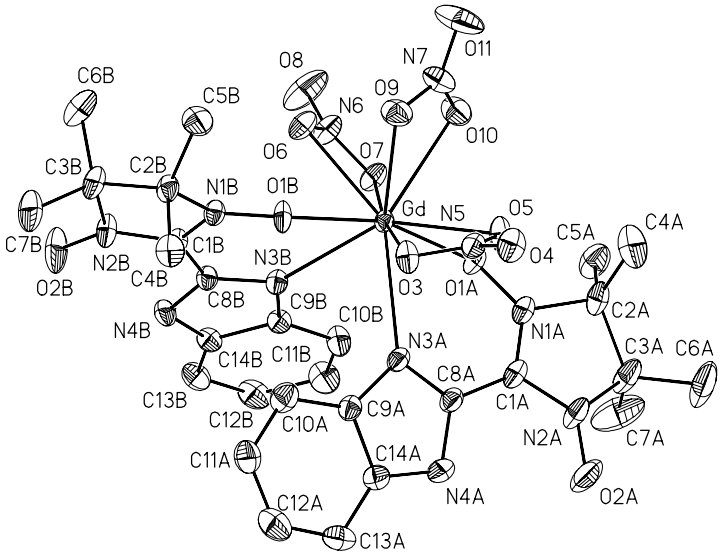

Figure 6.1 Representation of Gd(NITBzImH)$_2$(NO$_3$)$_3$ with thermal ellipsoids at the 30% probability level.

Figure 6.2 summarizes the luminescence properties of the free NITBzImH ligand and the three lanthanide complexes. All luminescence measurements were made with crystalline samples on instruments described in detail before[8, 9]. The onset of the lowest energy absorption band for all four solids is included in Figure 6.2 for comparison.

The luminescence spectra of the solid ligand are given at 5 K and 50 K at the bottom of Figure 6.2. The ligand shows a well-defined luminescence onset at 14,700 cm^{-1}. The spectrum is less resolved than the absorption spectrum and than the luminescence spectra of the lanthanide complexes. The luminescence onset coincides with the lowest energy absorption, indicating that the observed luminescence does not arise from deep traps. The 5 K absorption spectrum shows vibronic maxima separated by 230± 20 cm^{-1}. The first peak is most intense, its structure most likely corresponds to a short vibronic progression in a low-frequency mode.

The La complex shows a structured low-temperature luminescence spectrum with an onset at 14,300 cm^{-1}, lower in energy by 400 cm^{-1} than for the free ligand. The absorption band shows a corresponding shift to lower energy. Resolved structure with an average interval of 200± 20 cm^{-1} is observed in luminescence at 5 K, compared to the shoulders separated by 170± 20 cm^{-1} in absorption. This energy difference is smaller than for the free ligand and the intensity distribution is distinctly different: the main intensity of the ligand spectrum is at the first peak of the progression, in contrast to all lanthanide complexes, where the main intensity occurs after the second member of the progression in absorption and at approximately the third member of the progression in the resolved luminescence spectra. Figure 6.2 shows that the luminescence spectra of the lanthanide complexes have a larger overall

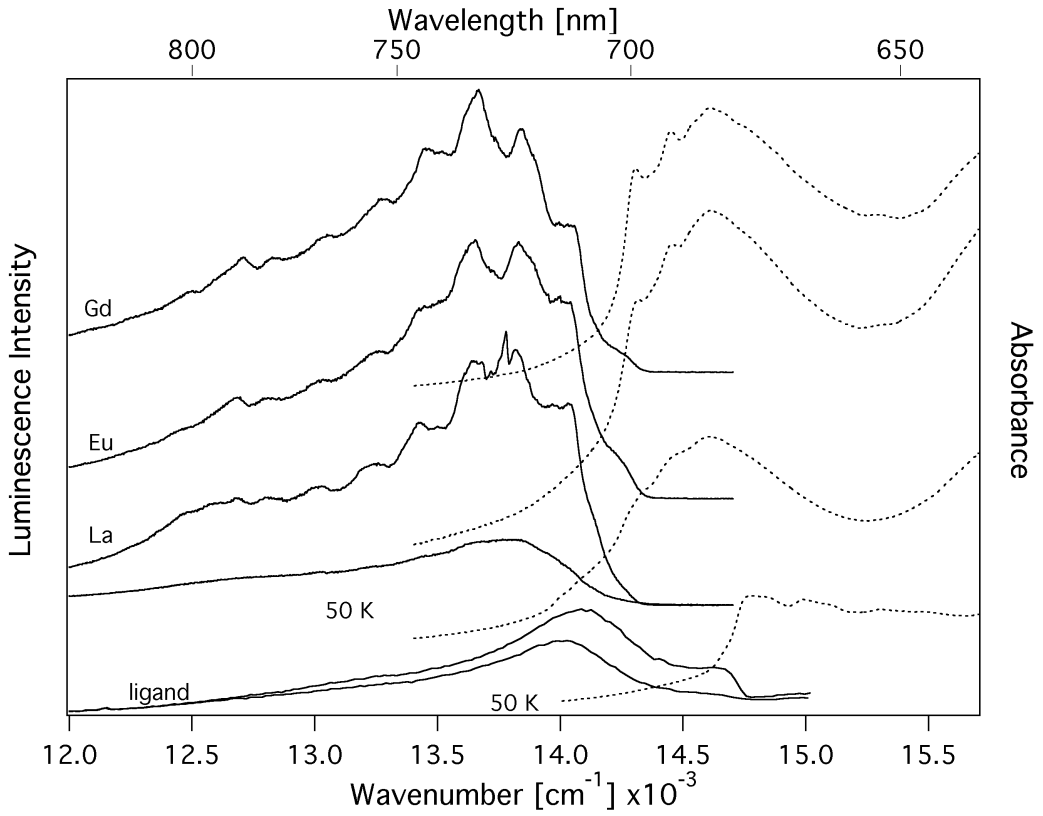

Figure 6.2 Top to bottom: luminescence (solid lines) and absorption spectra (dotted lines) of $Gd(NITBzimH)_2(NO_3)_3$, $Eu(NITBzimH)_2(NO_3)_3$, $La(NITBzimH)_2(NO_3)_3$ and NITBzimH (ligand). All spectra were measured at 5 K unless indicated otherwise in the Figure.

width than the band of the uncoordinated ligand, indicating that distortions along low frequency normal coordinates that are absent for the ligand occur for the lanthanide complexes. A likely reason for all these observations is that the change of the π electron density within the ligand caused by the electronic transition influences metal-ligand bonding and leads to progressions in low-frequency metal-ligand modes, which are not observed in the spectrum of the free ligand. The electronic structure of a model nitronyl nitroxide related to the ligand in Scheme 6.1 has been explored by detailed density functional calculations[10] and qualitatively illustrates these changes of π electron density involving both the nitronyl nitroxide and imidazole groups of the ligand. The lowest-energy electronic transition of the free ligand has been classified as $n \rightarrow \pi^*$[11]. The spectra of the lanthanide complexes in Figure 6.2 occur in a very similar energy range as for the uncoordinated ligand and we conclude that this qualitative overall assignment still applies. The resolved spectra of the lanthanide complexes in Figure 6.2 reveal the influence of metal-ligand bonding.

The luminescence spectra of the europium and gadolinium complexes are similar to those of the lanthanum compound. Their onsets show an additional weak shoulder at 14,400 cm^{-1} and the positions of their vibronic maxima vary slightly. A well resolved low-energy progression with an interval of 190± 10 cm^{-1} is observed in the absorption spectra of both the europium and gadolinium complexes. These progressions are again longer than for the uncoordinated ligand. The luminescence of the three metal complexes becomes weaker with temperature, as illustrated by the comparison of the 5 K and 50 K spectra for the La complex in Figure 6.2, but it can still be measured at room temperature.

To our knowledge, Figure 6.2 depicts the first luminescence spectra of a nitronyl nitroxide ligand and its lanthanide complexes. The spectra show more resolution than observed in the absorption spectra of transition metal complexes with nitronyl nitroxide ligands[12, 13]. Detailed absorption, MCD and Raman spectra have been reported for octahedral (β-diketonato)nickel(II) complexes with one nitronyl nitroxide ligand[14]. A luminescence maximum at 12,000 cm^{-1} is mentioned for $Cr(acac)_2$(NIT2-pyridine)[15], significantly lower in energy than the onset of the ligand absorption and the luminescence spectra shown in Figure 6.2.

The luminescence spectra of lanthanide complexes with nitronyl nitroxide ligands correspond to ligand-centered transitions. Their resolved vibronic structure is affected by the lanthanide coordination. We will further explore the potential of the title compounds as materials with combined optical and magnetic properties.

Acknowledgment

This research was supported by the "Commissariat à l'énergie atomique (CEA)", the CNRS (France) and the Natural Sciences and Engineering Research Council (Canada). We acknowledge travel grants from the "Ministère des Affaires Etrangères" and the "Ministère des Relations Internationales" (France-Quebec collaborations) and from the "Centre Jacques Cartier" (France).

Chapitre 7: Luminescence d'agrégats de silicium de taille nanométrique.

7.1 Introduction

Nous avons vu dans les chapitres précédents que les transitions électroniques dans les complexes inorganiques sont généralement centrées sur le métal. Dans d'autres conditions les transitions sont plutôt centrées sur un ligand en particulier, comme c'est le cas pour la luminescence des complexes de radicaux nitronyl-nitroxyde que nous avons observée. Dans certains cas spéciaux, il est possible que le principal facteur influençant l'énergie des états électroniques soit ni un centre métallique, ni un ligand. Pour un agrégat de taille nanométrique ayant des électrons délocalisés sur son ensemble, ce ne sont pas les orbitales atomiques ou les états électroniques moléculaires qui déterminent les niveaux d'énergie, mais plutôt un effet quantique relié à la taille de l'agrégat. Cette possibilité est souvent négligée malgré sa simplicité. On peut visualiser son impact avec une image bien connue reliant taille et énergie, celle de la particule dans une boîte. Dans ce modèle, les différences d'énergie entre les niveaux augmentent si les dimensions de la boîte diminuent. Ici, nous illustrons cette tendance par spectroscopie de luminescence, d'excitation et d'absorption.

Certains auteurs ont montré que l'on peut obtenir un effet de confinement quantique avec du silicium poreux[1, 2]. La taille des pores peut varier de 20 à 500 nm et les agrégats de silicium sont luminescent vers 800 nm dans ces conditions. La luminescence du silicium est normalement observée à une énergie plus basse, la

bande à 800 nm est donc une manifestation de la petite taille des agrégats.

Nous avons observé la luminescence d'agrégats de silicium de taille nanométrique (~1 nm) dans un film de silice mésoporeuse. Les travaux ont été effectués en collaboration avec l'Université de Toronto et sont publiés[3]. Ce chapitre décrit notre contribution à ce projet et présente l'ensemble de nos données spectroscopiques sur les agrégats de silicium.

7.2 Absorption, excitation et luminescence des agrégats et de la matrice de silice poreuse

La Figure 7.1 montre les spectres de luminescence en fonction de la température d'agrégats de silicium de taille nanométrique dans une matrice de silice poreuse. La matrice est un film d'une épaisseur d'environ 10 μm qui émet de la lumière autour de 455 nm, tel que présenté à la Figure 7.2. Les agrégats de silicium de taille nanométrique ont une luminescence peu intense à la température de la pièce. On peut voir sur la Figure 7.1 que les agrégats ont un maximum de luminescence autour de 570 nm à basse température. La Figure 7.3 compare les luminescences de la matrice de silice seule et avec les agrégats de silicium à basse température. Sur cette figure, on distingue clairement la composante due à la luminescence de la matrice de celle due aux agrégats de silicium. On peut remarquer que la luminescence de la matrice de silice est peu dépendante de la température alors que la luminescence des agrégats est fortement dépendante de la température. Le spectre d'absorption de la

matrice de silice est polarisé car celle ci à une structure ordonnée. La luminescence des agrégats de silicium est dépolarisée[3].

La Figure 7.4 montre la comparaison des spectres d'absorption et de luminescence d'un film qui contient des agrégats de silicium. Le recouvrement des bandes d'absorption et de luminescence est important dans une large région de 500 à 650 nm. Ce recouvrement indique qu'il y a probablement une distribution d'agrégats de tailles variables et que les spectres observés sont une superposition des spectres de différents chromophores. Le spectre d'excitation de la Figure 7.5 entre 450 et 550 nm est semblable au spectre d'absorption et ne nous permet pas d'observer le spectre d'un type d'agrégat en particulier.

L'étude spectroscopique de ces agrégats est préliminaire puisque la fabrication de ces matériaux est encore récente. Nous avons souligné le fait que l'émission de la matrice est polarisée[3] alors que celle des agrégats ne l'est pas. L'observation de cette polarisation avec le micro-spectromètre Renishaw pourrait être utile pour séparer l'émission de la matrice de silice de celle des agrégats de silicium. Quatre combinaisons sont possibles en orientant la polarisation de la source laser et en polarisant le signal.

La résolution spatiale du système Raman pourrait aussi être utilisée pour étudier la forme de la bande de luminescence des agrégats de silice. Les observations faites en luminescence portent sur une partie macroscopique de l'échantillon et la forme de bande semble très proche d'une Gaussienne. Pour un grand nombre d'agrégats on s'attend effectivement à une distribution normale des énergies. Si la largeur naturelle du spectre d'émission pour un seul agrégat est plus étroite que la bande observée expérimentalement en mode macroscopique, il devrait être possible d'observer une

bande plus étroite avec une résolution spatiale suffisante. La résolution spatiale du Raman (1 μm) est trop faible par rapport à la taille des agrégats (1 nm) pour les observer individuellement. Une expérience intéressante peut cependant être effectuée: voir si l'échantillon est homogène à l'échelle micrométrique. Dans le cas où les agrégats seraient distribués de façon hétérogène à cette échelle, l'étude de la relation entre la taille de ceux-ci et la longueur d'onde serait grandement facilitée. En prenant un spectre sur une surface d'environ 1 μm^2 on pourrait observer la luminescence d'un nombre plus petit d'agrégats et, avec de la chance, plus homogènes quant à leur taille, donc un spectre plus étroit. Dans le cas contraire, si la distribution des agrégats est très homogène à l'échelle micrométrique, on s'attend à voir le même spectre, peu importe l'endroit où on se trouve sur l'échantillon, ce qui est beaucoup moins intéressant. Peu importe le cas dans lequel on se trouve, une résolution spatiale très grande pourrait être très utile pour l'avancement de ce projet. L'utilisation d'une source d'excitation dans l'ultra-violet combinée à un appareil sensible et précis tel que le système Raman de Renishaw pourrait aussi être très utile puisque, comme on peut le voir sur les figures 7.4 et 7.5, l'excitation la plus efficace se fait autour de 400 nm.

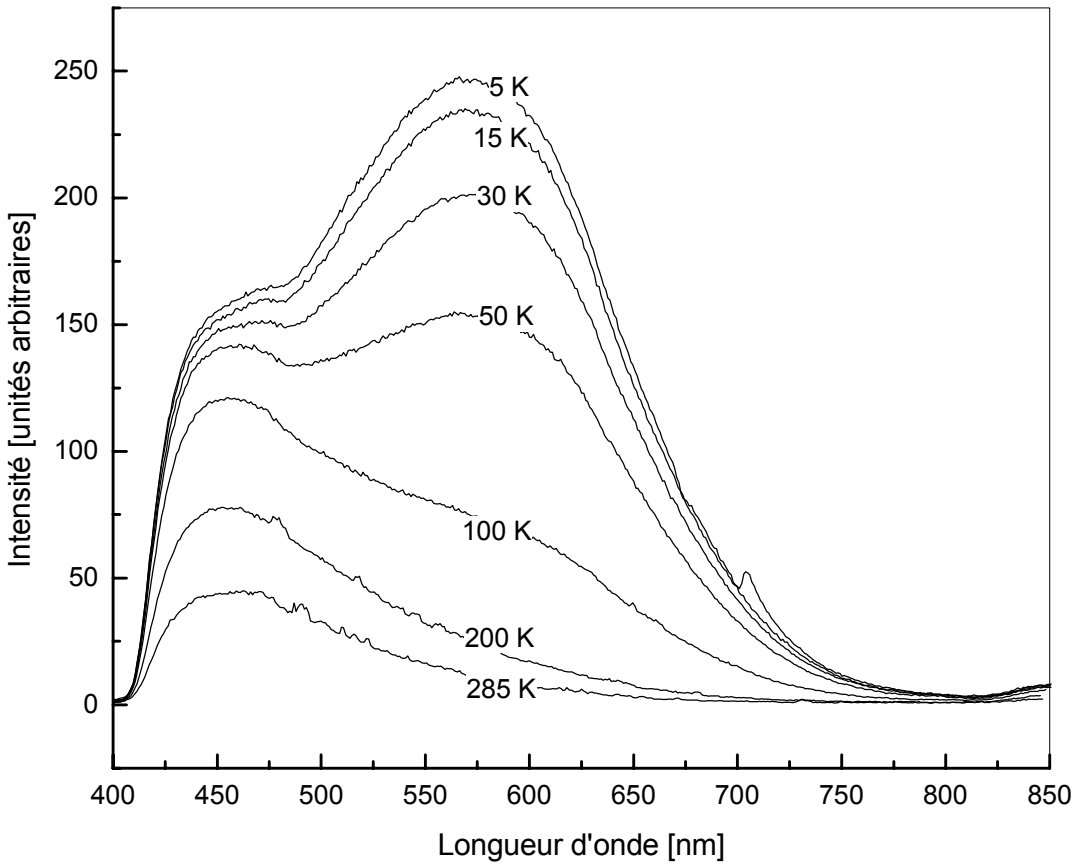

Figure 7.1 Spectres de luminescence des agrégats de silicium dans un film de silice poreuse d'une épaisseur d'environ 10 μm. La bande centrée à 570 nm est due aux agrégats de silicium (~1 nm). La partie à plus haute énergie (~455 nm) et due à la matrice de silice et est responsable pour la majeure partie de la luminescence bleue qu'on observe à la température de la pièce. A basse température, la luminescence jaune-orange des agrégats de silicium devient plus importante.

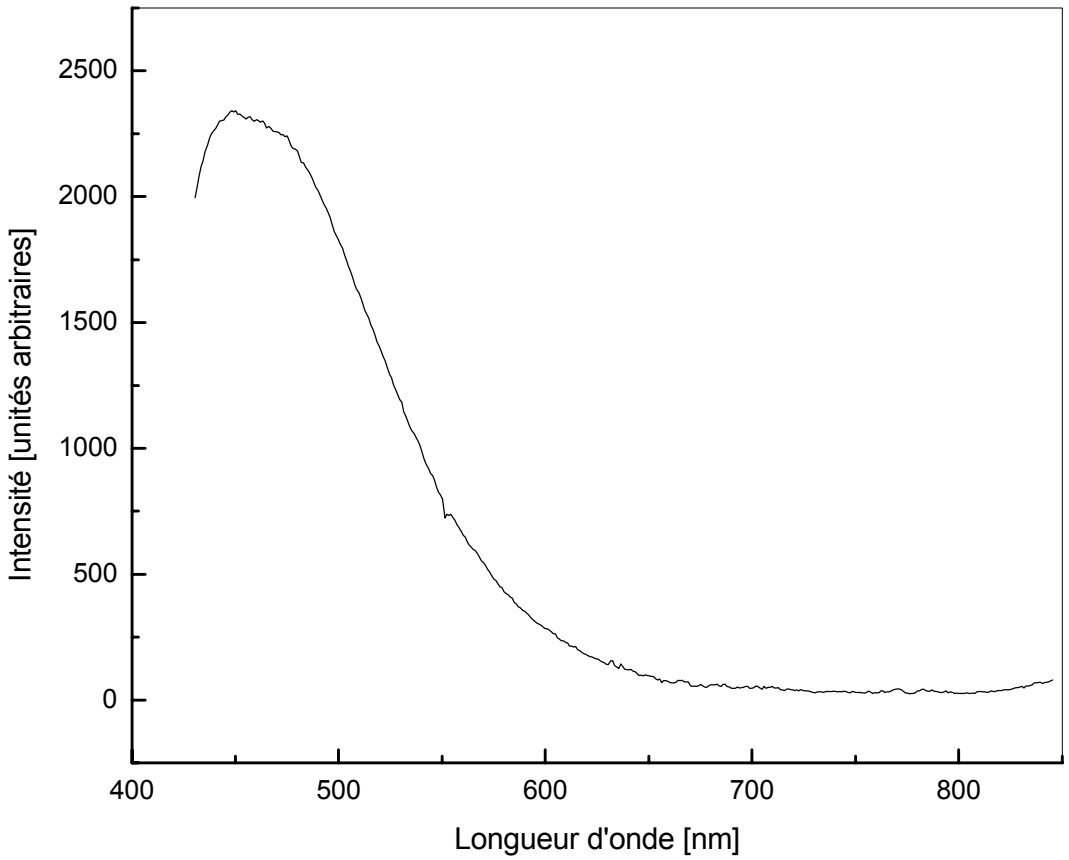

Figure 7.2 Spectre de luminescence de la matrice de silice poreuse à 5 K. Le film est d'une épaisseur d'environ 10 μm et ne contient pas d'agrégats de silicium. On voit que le maximum de la bande est centré autour de 455 nm et qu'il y a très peu d'intensité à 570 nm.

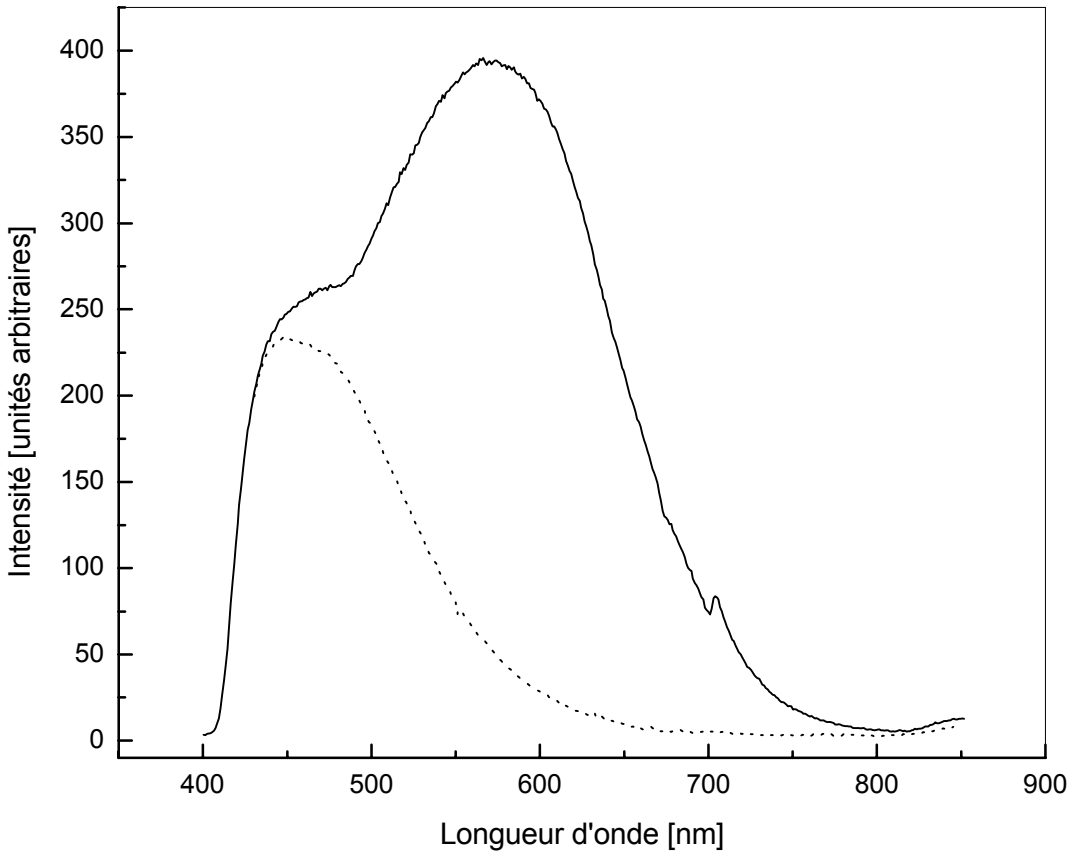

Figure 7.3 Comparaison entre la luminescence de deux films de silice poreuse d'une épaisseur d'environ 10 μm avec et sans agrégats de silicium à 5 K. Le spectre en trait plein est celui de la matrice en présence d'agrégats et en trait pointillé celui de la matrice seule. On peut voir aisément les contributions respectives de la matrice et des agrégats de silicium à la forme de la bande en trait plein.

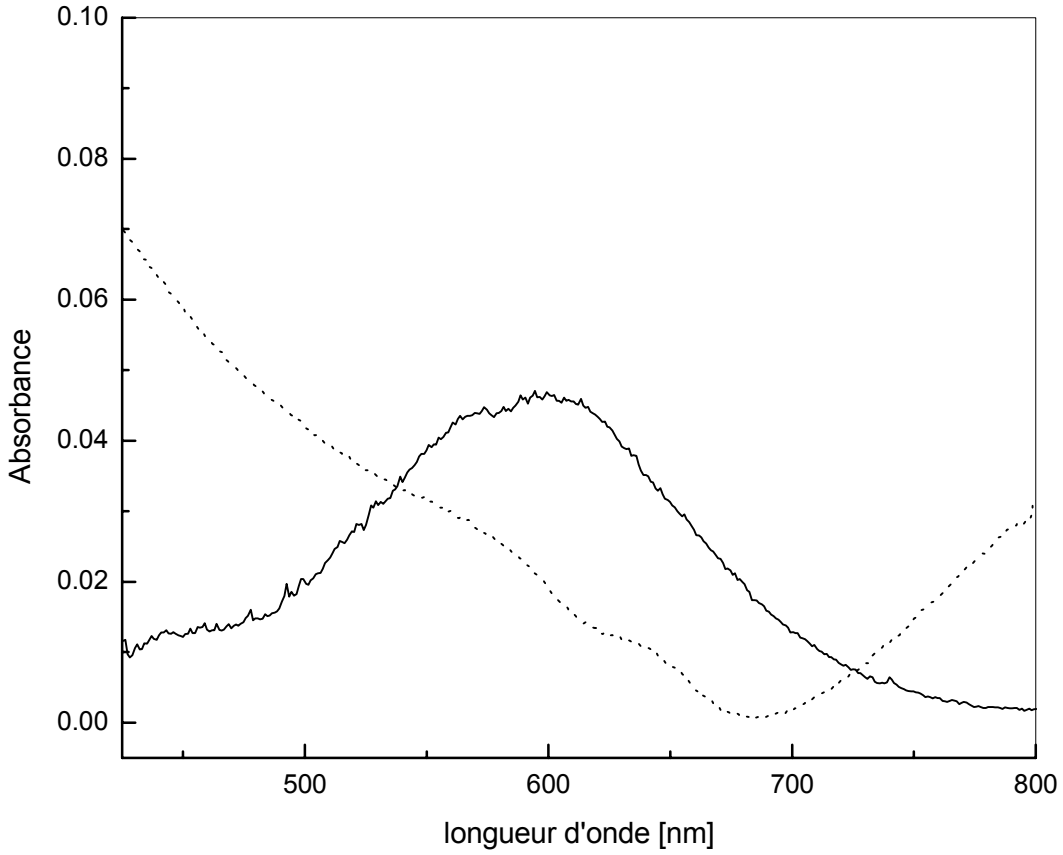

Figure 7.4 Comparaison entre la luminescence et l'absorption d'un film de silice poreuse d'une épaisseur d'environ 5 μm avec des agrégats de silicium. Le spectre de luminescence à 5 K est en trait plein, le spectre d'absorption, non polarisé, à 80 K est en trait pointillé.

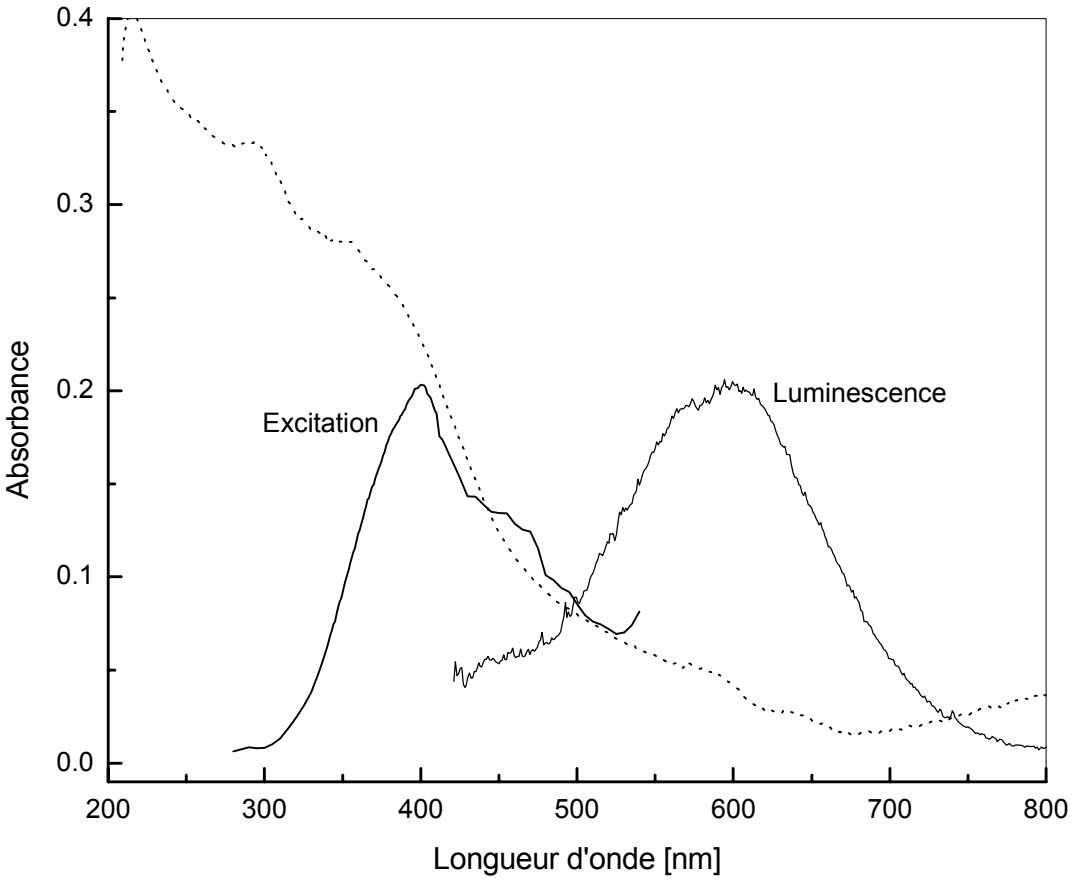

Figure 7.5 Comparaison entre la luminescence, l'absorption polarisée et l'excitation d'un film de silice poreuse d'une épaisseur d'environ 5 μm avec des agrégats de silicium. Le spectre de luminescence (5 K) et le spectre d'excitation (5 K) sont en trait plein. Un spectre d'absorption polarisé à 80 K est en trait pointillé.

Chapitre 8: Conclusion

Nous avons vu que les métaux de transition et leurs complexes ont une structure électronique riche qui est très utile pour l'étude des interactions entre états électroniques. Un exemple typique est la deuxième bande ($^3A_2 \rightarrow {}^3T_1$, groupe O) du $[Ni(H_2O)_6]^{2+}$ qui montre une double bosse en solution à la température de la pièce. L'auteur du livre 'Physical Inorganic Chemistry' a constaté qu'il n'y avait en ce moment aucune explication satisfaisante pour la double bosse observée[1]. L'auteur précise que deux hypothèses sont en concurrence pour expliquer la présence de deux maxima: l'effet Jahn-Teller et le couplage spin-orbite. Nous avons utilisé la théorie dépendante du temps pour calculer la forme de la bande en présence de couplage spin-orbite entre l'état $^3T_1$ et l'état ^1E. Le résultat est décrit dans les chapitres 2 et 3. La conclusion principale de ces travaux est que le couplage spin-orbite détermine la forme détaillée de ces spectres d'absorption. Une alternative à la théorie dépendante du temps pour décrire la forme de la bande a aussi été étudiée et fait l'objet du chapitre 2.2. L'interaction entre les deux états excités implique aussi le couplage spin-orbite mais elle est décrite par une équation analytique. L'équation analytique donne de bons résultats, mais elle s'applique seulement à des cas sans résolution vibronique. Elle a aussi l'avantage d'être beaucoup plus simple à automatiser que l'approche basée sur la théorie dépendante du temps. Nous avons démontré la première application pratique de cette équation analytique.

Comme les spectres en solution sont peu résolus, il a été nécessaire de travailler

dans d'autres conditions pour confirmer notre interprétation de la forme de la bande. Pour ce faire, des spectres d'absorption polarisés à basse température et à l'état solide cristallin sont nécessaires, ce qui fait l'objet du chapitre 3. La structure vibronique des états $^3T_1/^1E$ à basse température pour les complexes $[NiCl_6]^{4-}$, *trans*-$[NiCl_2(H_2O)_4]$ et $[Ni(H_2O)_6]^{2+}$ est reproduite par notre modèle utilisant la théorie dépendante du temps. Cet accord confirme de façon détaillée que le couplage spin-orbite est responsable pour le double maximum observé en solution, peu importe la symétrie du complexe. Ce résultat n'exclut cependant pas complètement la possibilité d'un effet Jahn-Teller dans l'état $^3T_1$, qui a une configuration $t_2^5e^3$ dans l'approximation du champ fort. Cette configuration électronique est très propice à l'effet Jahn-Teller car elle a une occupation non symétrique des orbitales e, qui sont orientées directement vers les ligands pour une coordination octaédrique. Pour comprendre le comportement de l'état $^3T_1$ nous avons fait des calculs *ab-initio* sur les complexes $[Ni(H_2O)_6]^{2+}$ (configuration $[Ar]3d^8$) et $[V(H_2O)_6]^{3+}$ (configuration $[Ar]3d^2$). Nous avons profité de l'analogie électrons-trous pour étudier le caractère de l'état $^3T_1$ dans deux situations différentes. La configuration électronique de l'état $^3T_1(^3F)$ pour $[Ni(H_2O)_6]^{2+}$ a été obtenue par ces calculs, présentés au chapitre 5. Le résultat nous indique que l'état $^3T_1(^3F)$ interagit fortement avec l'état $^3T_1(^3P)$ de configuration $t_2^4e^4$. Cette configuration électronique a une occupation symétrique des orbitales e, ce qui en fait une configuration très peu susceptible à un effet Jahn-Teller. L'état $^3T_1(^3F)$ pour $[Ni(H_2O)_6]^{2+}$ est donc un hybride entre les configurations $t_2^5e^3$ et $t_2^4e^4$ avec une contribution beaucoup plus faible d'autres configurations électroniques. La configuration $t_2^5e^3$ n'est pas clairement dominante. Cette caractéristique rend peu probable l'hypothèse selon laquelle l'effet Jahn-Teller serait responsable de la double

bosse observée pour la transition vers l'état $^3T_1(^3F)$ de $[Ni(H_2O)_6]^{2+}$ en solution. La combinaison de la spectroscopie d'absorption, de l'analyse théorique des spectres et de calculs *ab-initio* permet donc d'identifier l'origine des formes inhabituelles des transitions électroniques.

Nous avons aussi étudié les effets du couplage spin-orbite pour des complexes *trans*-dichlorotétraaquo du chrome(III), du vanadium(III) et du cobalt(II). Le même modèle a été utilisé et les résultats obtenus sont en accord avec les observations expérimentales, ce qui confirme une fois de plus que le couplage spin-orbite peut avoir un effet considérable sur l'apparence des spectres d'absorption des complexes inorganiques.

La spectroscopie des complexes aquo des métaux de transition de la première série est très bien comprise et de nombreuses études ont été réalisées sur le sujet. Plusieurs points restent à être éclaircis. Par exemple, un nombre de ces complexes présentent une série de transitions d'intensité faible, mais bien résolues, du côté à basse énergie de leur première transition permise [Ti(III), Cr(III), Ni(II), Co(II)]. Il y a très peu d'études en littérature sur ce sujet parce que ces transitions se situent dans le rouge et le proche-IR. Il n'est pas clair si les bandes en question correspondent à une ou plusieurs progressions vibroniques, à des origines vibroniques ou à une scission de l'état final de la transition permise sous l'effet du couplage spin-orbite. Un autre phénomène intrigant est la présence systématique de progressions vibroniques dans un mode impliquant la vibration OH à une fréquence d'environ 3000 cm^{-1}. Dans certains cas, l'effet Jahn-Teller semble être important et l'intensité de ces transitions varie de très faible à très intense. Jusqu'à ce jour aucune explication satisfaisante n'a été proposée pour rendre compte de ces observations.

Une partie de cette thèse est axée vers l'étude d'états électroniques à caractère différent des états provenant des orbitales 3d. Nous avons observé les premiers spectres d'absorption et de luminescence de radicaux organiques nitronyl-nitroxydes, ce qui fait l'objet du chapitre 6. Ces radicaux sont utilisés comme ligands pour former des complexes avec des métaux de transition et des lanthanides. Le but à long terme de ce projet est de mieux comprendre les interactions entre les états électroniques centrés sur le métal et le ligand, effets qui donnent lieu à des propriétés magnétiques intéressantes.

Des spectres d'émission ont été observés pour les radicaux libres et de leurs complexes avec des lanthanides. Une propriété intéressante a été observée lorsque le radical est coordiné à l'europium(III): la luminescence vient parfois du radical seulement, parfois du métal seulement et parfois des deux dans un même spectre. Cet exemple démontre que ces systèmes sont d'une grande richesse spectroscopique et que les deux catégories d'états électroniques sont en interaction. Plusieurs effets peuvent être en cause dans ce phénomène qui implique probablement un transfert d'énergie du métal vers le ligand ou l'inverse. Le comportement observé pour ces composés pourrait aussi avoir un lien avec leurs propriétés magnétiques, ceci fait partie d'un projet en cours.

Nous avons mesuré la luminescence et l'absorption d'agrégats de silicium de taille nanométrique, ce qui est le sujet du chapitre précédent. Dans ces matériaux, nous avons montré que la structure électronique et les propriétés optiques sont déterminées par la taille. Un aspect intéressant pour des travaux futurs pourrait être l'analyse de l'uniformité des tailles des agrégats par microspectroscopie.

Ce travail nous a permis de constater que la spectroscopie détaillée est

d'importance primordiale pour la compréhension de la structure électronique des complexes et matériaux modernes. Nous avons aussi vu que même les calculs *ab-initio* de bonne qualité ne donnent pas encore des prédictions fiables des énergies et propriétés d'états électroniques excités. Cependant, ces calculs décrivent bien certains aspect des interactions entre états et sont utiles pour comprendre la nature des états électroniques. La spectroscopie est une méthode très performante pour étudier des matériaux inorganiques modernes. Il reste par contre énormément de défis expérimentaux et théoriques à relever pour maîtriser cette approche.

Références

Chapitre 1

(1) Basolo, F.; Pearson, R.G.; Mechanisms of Inorganic Reactions; John Wiley: New York, **1967**.

(2) Bloomquist, D.R.; Willett, R.D.; *Coord. Chem. Rev.* **1982**, *47*, 125.

(3) Gütlich, P.; Hauser, A.; Spiering, H.; *Angew. Chem. Int. Ed. Engl.* **1994**, *33*, 2024.

(4) Stephens, D.R.; Drickamer, H.G.; *J. Chem. Phys.* **1961**, *34*, 937.

(5) Bray, K.L.; *Topics in Current Chemistry*, **2001**, *213*, 1.

(6) Grey, J.; Butler, I.; *Coord. Chem. Rev.* **2001**, *219-221*, 713.

(7) Gütlich, P.; Garcia, Y.; Goodwin, H.A.; *Chem. Soc. Rev.* **2000**, *29*, 419.

(8) Physical Methods in Bioinorganic Chemistry, L. Que Jr. Ed.; University Science Boooks: Sausalito, **2000**.

(9) Solomon, E.I.; *Inorg. Chem.* **2001**, *40*, 3656.

(10) Day, P.; *Angew. Chem. Int. Ed. Engl.* **1980**, *19*, 290.

(11) Shriver, D.F.; Atkins, P.W.; Chimie Inorganique; DeBoeck-Université: Paris, Bruxelles, **2001**, p. 437.

(12) Bethe, H.; *Ann. Phys.*, **1929**, *3*, 133.

(13) Ballhausen, C.J.; Introduction to Ligand Field Theory; McGraw-Hill: New York, **1962**.

(14) König, E.; *Struct. Bond*. **1971**, *9*, 175.

(15) Figgis, B.N.; Introduction to Ligand Fields; John Wiley: New York, **1966**.

(16) Butler, L.J.; *Annu. Rev. Phys. Chem*., **1998**, *49*, 125.

(17) Dixon, R.N.; Hwang, D.W.; Yang, X.F.; Harich, S.; Lin, J.J.; Yang, X.; *Science*, **1999**, *285*, 1249.

(18) Conroy, D.; Aristov, V.; Feng, L.; Sanov, A.; Reisler, H.; *Acc. Chem. Res*., **2001**, *34*, 625.

(19) Plastina, F.; Piperno, F.; *J. Opt. B: Quantum Semiclass. Opt*., **2000**, *2*, 140.

(20) Griffith, J.S.; The Theory of Transition Metal Ions; Cambridge University Press: New York, **1961**.

(21) Lee, J.D.; Concise Inorganic Chemistry, 4th ed.; Chapman and Hall: London, **1991**, p. 960.

(22) Kettle, S.F.A.; Physical Inorganic Chemistry; University Science Books: Sausalito, **1996**, p. 175.

(23) Cotton, F.A.; Wilkinson, G.; Advanced Inorganic Chemistry, 5th ed.; Wiley-Interscience: New York, **1988**, p. 745.

(24) Solomon, E.I.; Ballhausen, C.J.; *Mol. Phys.* **1975**, *29*, 279.

(25) Kozielski, M.; Pollini, I.; Spinolo, G.; *J.Phys. C: Solid State Phys.* **1972**, *5*, 1253.

(26) McPherson, G.L.; Stucky, G.D.; *J. Chem. Phys.* **1972**, *57*, 3780.

(27) Ackerman, J.; Holt, E.M.; Holt, S.L.; *J. Sol. State Chem.* **1974**, *9*, 279.

(28) Benedek, G.; Pollini, I.; Piseri, L.; Tubino, R.; *Phys. Rev. B* **1979**, *20*, 4303.

(29) Lempicki, A.; Andrews, L.; Nettel, S.J.; McCollum, B.C.; Solomon, E.I.; *Phys. Rev. Lett.* **1980**, *44*, 1234.

(30) Rodríguez-Mendoza, U.R.; Rodríguez, V.D.; Lavín, V.; Martín, I.R. Nuñez, P.; *Spectrochim. Acta, Part A* **1999**, *55*, 1319.

(31) Brunold, T.; Güdel, H. U.; dans Inorganic Electronic Structure and Spectroscopy, Solomon, E.I. and Lever, A.B.P., Ed.; John Wiley: New York, **1999**, vol. 1, p 259.

(32) Franck, J.; *Trans. Farad. Soc*., **1925**, *21*, 536.

(33) Condon, E.U.; *Phys. Rev*., **1928**, *32*, 858.

(34) Born, M.; Oppenheimer, J.R.; *Ann. Phys.*, **1927**, *84*, 457.

(35) Heller, E.J.; *Acc. Chem. Res.* **1981**, *14*, 368.

(36) Les méthodes ab-initio utilisées au chapitre 5 sont CASSCF et CASPT2. Ici, CAS signifie 'Complete Active Space', SCF signifie 'Self-Consistent Field' et PT2 'Perturbation Theory, 2nd order', une méthode de perturbation effectuée à partir d'un calcul CASSCF. Ces méthodes sont des extensions de la méthode de Hartree-Fock. Leurs caractéristiques sont résumés d'une perspective de chimiste non-théorique dans: Simons, J.; *J.Phys. Chem.* **1991**, *95*, 1017.

(37) Lescop, C.; Luneau, D.; Belorizky, E.; Fries, P.; Guillot, M.; Rey, P.; *Inorg. Chem.* **1999**, *38*, 5472.

(38) Lescop, C.; Luneau, D.; Bussière, G.; Triest, M.; Reber, C.; *Inorg. Chem.* **2000**, *39*, 3740.

(39) Schuppler, S.; Friedman, S.L.; Marcus, M.A.; Adler, D.L.; Xie, Y.-H.; Ross, F.M.; Harris, T.D.; Brown, W.L.; Chabal, Y.J.; Brus, L.E.; Citrin, P.H.; *Phys. Rev. Lett.* **1994**, *72*, 2648.

(40) Dag, Ö.; Ozin, G.A.; Yang, H.; Reber, C.; Bussière, G.; *Adv. Mater.* **1999**, *11*, 474.

(41) Taiichiro, H.; *J. Phys. Soc. Jpn.*, **1960**, *15*, 483.

Chapitre 2.1

(1) König, E.; *Struct. Bond*. **1971**, *9*, 175.

(2) Drago, R.S.; Physical Methods for Chemists, 2nd Ed.; Saunders College Publ.: Fort Worth, Toronto, **1992**. p. 735,

(3) Reedijk, J.; Van Leeuwen, P.W.N.M.; Groeneveld, W.L.; *Rec. Trav. Chim. Pays-Bas*, **1968**, *87*, 129.

(4) Smith, D.W.; *J. Chem. Ed*. **1996**, *73*, 505.

(5) Alexander, A.J.; Zare, R. N.; *J. Chem. Ed*. **1998**, *75*, 1105.

(6) Lewis, N.A.; *J. Chem. Ed*. **1980**, *57*, 478.

(7) Bussière, G.; Reber, C.; *J. Amer. Chem. Soc*. **1998**, *120*, 6306.

(8) Cotton, F.A.; Wilkinson, G.; Advanced Inorganic Chemistry, Fifth Edition; John Wiley: New York, **1988**, p. 745.

(9) Stranger, R.; McMahon, K.L.; Gahan, L.R.; Bruce, J.I.; Hambley, T.W.; *Inorg. Chem.* **1997**, *36*, 3466.

(10) Eaton, S.S.; *J. Chem. Ed.* **1979**, *56*, 635.

(11) Henderson, G.; Rittenhouse, R.C.; Wright, J.C.; Holmes, J.L.; *J. Chem. Ed.* **1979**, *56*, 631 et *J. Chem. Ed.* **1994**, *71*, 300, http://jchemed.chem.wisc.edu/JCEWWW/Articles/index.html

(12) Heller, E. J.; *Acc. Chem. Res.* **1981**, *14*, 368.

(13) Zink, J.I.; Kim Shin, K.-S.; *Adv. Photochem.* **1991**, *16*, 119.

(14) Tanner, J.J.; *J. Chem. Ed*. **1990**, *67*, 917.

(15) Abragam, A.; Bleaney, B. Electron Paramagnetic Resonance of Transition Metal Ions; Clarendon Press: Oxford, **1970**, p. 451.

Chapitre 2.2

(1) Neuhauser, D.; Park, T.J.; Zink, J.I.; *Phys. Rev. Lett*. **2000**, 85, 5304.

(2) Fano, U.; *Phys. Rev.* **1961**, *124*, 1866.

(3) Rodríguez-Mendoza, U.R.; Rodríguez, V.D.; Lavín, V.; Martín, I.R. Nuñez, P.; *Spectrochim. Acta*, Part A **1999**, *55*, 1319.

(4) Lempicki, A.; Andrews, L.; Nettel, S.J.; McCollum, B.C.; Solomon, E.I.; *Phys. Rev. Lett.* **1980**, *44*, 1234.

(5) Gutzov, S.; Wasgestian, F.; Barthel, T.; Assmus, W.; *Z. Phys. Chem.* **1998**, *205*, 41.

(6) Bussière, G.; Reber, C.; *J. Amer. Chem. Soc*. **1998**, *120*, 6306.

(7) Schenker, R.; Triest, M.; Reber, C.; Güdel, H.U.; *Inorg. Chem.* Sous presse.

Chapitre 3

(1) Bernardi, F.; Olivucci, M.; Robb, M.A.; *Chem. Soc. Rev.* **1996**, 322.

(2) Romstad, D.; Granucci, G.; Persico, M.; *Chem. Phys.* **1997**, *219*, 21.

(3) Jørgensen, C.K.; *Acta Chem. Scand.* **1955**, *9*, 405.

(4) Jørgensen, C.K.; *Acta Chem. Scand.* **1955**, *9*, 1362.

(5) Pryce, M.H.L.; Agnetta, G.; Garofano, T.; Palma-Vittorelli, M.B.; Palma, M.U.; *Philos. Mag.* **1964**, *10*, 77.

(6) Reedijk, J.; Van Leeuwen, P.W.N.M.; Groeneveld, W.L.; *Rec. Trav. Chim. Pays-Bas* **1968**, *87*, 129.

(7) Ferguson, J.; *Progr. Inorg. Chem.* **1970**, *12*, 159.

(8) Solomon, E.I.; Ballhausen, C.J.; *Mol. Phys.* **1975**, *29*, 279.

(9) Stranger, R.; McMahon, K.L.; Gahan, L.R.; Bruce, J.I.; Hambley, T.W.; *Inorg. Chem.* **1997**, *36*, 3466.

(10) Benedek, G.; Pollini, I.; Piseri, L.; Tubino, R.; *Phys. Rev.* B **1979**, *20*, 4303.

(11) Lee, J.D.; Concise Inorganic Chemistry, 4th Ed.; Chapman and Hall: London, **1991**, p. 960.

(12) Kettle, S.F.A.; Physical Inorganic Chemistry; University Science Books: Sausalito, **1996**, p. 175.

(13) Adams, D.M.; Lock, P.J.; *J. Chem. Soc.* A **1971**, 2801.

(14) Mizuno, J.; *J. Phys. Soc. Jpn.* **1961**, *16*, 1574.

(15) Bigoli, F.; Braibanti, A.; Tiripicchio, A.; Tiripicchio, C.; *Acta Crystallogr.* **1971**, B*27*, 1427.

(16) Reber, C.; Güdel, H.U.; *Inorg. Chem.* **1986**, *25*, 1196.

(17) Haseda, T.; Kobayashi, H.; Date, M.; *J. Phys. Soc. Jpn.* **1959**, *14*, 1724.

(18) McPherson, G.L.; Stucky, G.D.; *J. Chem. Phys.* **1972**, *57*, 3780.

(19) Ackerman, J.; Holt, E.M.; Holt, S.L.; *J. Sol. State Chem.* **1974**, *9*, 279.

(20) Johnstone, I.W.; Jones, G.D.; Lockwood, D.J.; *Solid State Commun.* **1981**, *39*, 395.

(21) Salthouse, J.A.; Ware, M.J.; Point group character tables and related data; Cambridge University Press: New York, **1972**.

(22) Abragam, A.; Bleaney, B.; Electron Paramagnetic Resonance of Transition Metal Ions; Clarendon Press: Oxford, **1970**, p. 451.

(23) Griffith, J.S.; The Theory of Transition Metal Ions; Cambridge University Press: New York, **1961**, p. 307.

(24) Flint, C.D.; *Coord. Chem. Rev.* **1974**, *14*, 47.

(25) Heller, E.J.; *Acc. Chem. Res.* **1981**, *14*, 368.

(26) Zink, J.I.; Kim Shin, K.-S.; *Adv. Photochem.* Volman, D. H.; Hammond, G.S.; Neckers, D.C.; John Wiley: New York, **1991**; *16*, p. 119.

(27) Reber, C.; Zink, J.I.; *Comm. on Inorg. Chem.* **1992**, *13*, 177.

(28) Feit, M.D.; Fleck Jr., J.A.; Steiger, A.; *J. Comp. Phys.* **1982**, *47*, 412.

(29) Alvarellos, J.; Metiu, H.; *J. Chem. Phys.* **1988**, *88*, 4957.

(30) Jiang, X.-P.; Heather, R.; Metiu, H.; *J. Chem. Phys.* **1989**, *90*, 2555.

(31) Engel, V.; Schinke, R.; Hennig, S.; Metiu, H.; *J. Chem. Phys.* **1990**, *92*, 1.

(32) Larsen, E.; LaMar, G.N.; *J. Chem. Ed.* **1974**, *51*, 633.

(33) Adamsky, H.; AOMX - an angular overlap program; Institut für Theoretische Chemie, Heinrich-Heine-Universität Düsseldorf: Düsseldorf, Germany, **1995**. http://www.theochem.uniduesseldorf.de/Computing/Progs/aomx/Welcome.html

(34) Oetliker, U.; Riley, M.J.; Güdel, H.U.; *J. Lumin.* **1995**, *63*, 63.

(35) Kozielski, M.; Pollini, I.; Spinolo, G.; *J. Phys.* C: *Sol. Stat. Phys.* **1972**, *5*, 1253.

(36) Press, W.H.; Teukolsky, S.A.; *Computers in Physics* **1991**, *5*, 426.

(37) May, P.S.; Güdel, H.U.; *Chem. Phys. Lett.* **1989**, *164*, 612.

(38) May, P.S.; Güdel, H.U.; *J. Lumin.* **1990**, *47*, 19.

(39) May, P.S.; Güdel, H.U.; *J. Lumin.* **1990**, *46*, 277.

(40) Tutt, L.; Zink, J. I.; *J. Am. Chem. Soc.* **1986**, *108*, 5830.

(41) Preston, D.M.; Güntner, W.; Lechner, A.; Gliemann, G.; Zink, J.I.; *J. Am. Chem. Soc.* **1988**, *110*, 5628.

(42) De Haan, Y.M.; Molecular Dynamics and Structure Carter, R.S.; Rush, J.J.; Natl. Bur. Std.: Washington, **1969**; Natl. Bur. St. Spec. Publ. Vol. 301, p. 233.

(43) Achiwa, N.; *J. Phys. Soc. Japan.* **1969**, *27*, 561.

(44) Pollini, I.; Spinolo, G.; Benedek, G.; *Phys. Rev.* **1980**, B *22*, 6369.

(45) Reber, C.; Zink, J.I.; *J. Chem. Phys.* **1992**, *96*, 2681.

(46) Wexler, D.; Zink, J.I.; Reber, C.; *J. Phys.* Chem. **1992**, *96*, 8757.

Chapitre 4

(1) Bussière, G.; Reber, C.; *J. Am. Chem. Soc.* **1998**, *120*, 6306.

(2) Jørgensen, C.K.; *Acta Chem. Scand.* **1955**, *9*, 405.

(3) Pryce, M.H.L.; Agnetta, G.; Garofano, T; Palma-Vittorelli, M.B.; Palma, M.U.; *Philos. Mag.* **1964**, B *10*, 477.

(4) Lempicki, A.; Andrews, L.; Nettel, S.J.; McCollum, B.C.; Solomon, E.I.; *Phys. Rev.* Lett. **1980**, *44*, 1234.

(5) Reisfeld, R.; Jørgensen, C.K.; *Struct. Bonding* (Berlin) **1988**, *69*, 63.

(6) Rodríguez-Mendoza, U.R.; Rodríguez, V.D.; Lavín, V.; Martín, I.R.; Nuñez, P.; *Spectrochim. Acta*, Part A **1999**, *55*, 1319.

(7) McCarthy, P.J.; Lauffenburger, J.C.; Skonezny, P.M.; Rohrer, D.C.; *Inorg. Chem.* **1981**, *20*, 1566.

(8) McCarthy, P.J.; Lauffenburger, J.C. Schreiner, M.M.; Rohrer, D.C.; *Inorg. Chem.* **1981**, *20*, 1571.

(9) Ferguson, J.; *J. Chem. Phys.* **1960**, *32*, 533.

(10) Ferguson, J.; Wood, T.E.; *Inorg. Chem.* **1975**, *14*, 184.

(11) Joy, W.H.; Fogel, N.; *J. Phys.* Chem. **1975**, *79*, 345.

(12) Pappalardo, R.; *Philos. Mag.* **1959**, *B4*, 219.

(13) Gieleβen, J.; *Ann. Phys.* **1935**, *5*, 537.

(14) Heller, E.J.; *Acc. Chem. Res.* **1981**, *14*, 368.

(15) Reber, C.; Zink, J.I.; *Comments Inorg. Chem.* **1992**, *13*, 177.

(16) Zink, J.I.; Kim Shin, K.S.; *Adv. Photochem.* **1991**, *16*, 119.

(17) Mizuno, J.; *J. Phys. Soc. Jpn.* **1961**, *16*, 1574.

(18) Mizuno, J.; *J. Phys. Soc. Jpn.* **1960**, *15*, 1412.

(19) Horner, S.M.; Tyree, S.Y.; *Inorg. Chem.* **1964**, *3*, 1173.

(20) Podmore, L.P.; Smith, P.W.; *Aust. J. Chem.* **1972**, *25*, 2521.

(21) Morosin, B.; *Acta Crystallogr.*, Sect. C: *Cryst. Struct. Commun.* **1966**, *21*, 280.

(22) Dance, I.G.; Freeman, H.C.; *Inorg. Chem.* **1965**, *4*, 1555.

(23) Magini, M.; *J. Chem. Phys.* **1980**, *73*, 2499.

(24) Solomon, E.I.; Ballhausen, C.J.; *Mol. Phys.* **1975**, *29*, 279.

(25) May, P.S.; Güdel, H.U.; *J. Lumin.* **1990**, *46*, 277.

(26) May, P.S.; Güdel, H.U.; *Chem. Phys.* Lett. **1989**, *164*, 612.

(27) Kozielski, M.; Pollini, I.; Spinolo, G.;
J. Phys. C: *Solid State Phys.* **1972**, *5*, 1253.

(28) Benedek, G.; Pollini, I.; Piseri, L.; Turbino, R.; *Phys. Rev.* **1979**, B *20*, 4303.

(29) Bencini, A.; Benelli, C.; Gatteschi, D.; *Coord. Chem. Rev.* **1984**, *60*, 131.

(30) Hitchman, M.A.; McDonald, R.G.; Smith, P.W.; Stranger, R;
J. Chem. Soc., *Dalton Trans.* **1988**, 1393.

(31) Schäffer, C.E.; *Struct. Bonding* (Berlin) **1968**, *5*, 68.

(32) Waizumi, K.; Masuda, H.; Ohtaki, H.; Tsukamoto, K.; Sunagawa, I.;
Bull. Chem. Soc. Jpn. **1990**, *63*, 3426.

(33) Feit, M.D.; Fleck, J.A.; Steiger, A.J.; *J. Comput. Phys.* **1982**, *47*, 412.

(34) Alvarellos, J.; Metiu, H.; *J. Chem. Phys.* **1988**, *88*, 4957.

(35) Jiang, X.-P.; Heather, R.; Metiu, H.; *J. Chem. Phys.* **1989**, *90*, 2555.

(36) Engel, V.; Schinke, R.; Hennig, S.; Metiu, H.; *J. Chem. Phys.* **1990**, *92*, 1.

(37) Neuhauser, D.; Park, T.J.; Zink, J.I.; *Phys. Rev. Lett*. **2000**, 85, 25, 5304.

(38) Tregenna-Piggott, P.L.W.; Best, S.P.; Güdel, H.U.; Weihe, H.; Wilson, C.C.; *J. Solid State Chem.* **1999**, *145*, 460.

(39) Meier, R.; Boddin, M.; Mitzenheim, S.; Schmid, V.; Schönherr, T.; *J. Inorg. Biochem.* **1998**, *69*, 249.

(40) Schönherr, T.; Schmid, V.; Meier, R.; *Spectrochim. Acta*, Part A **1998**, *54*, 1659.

(41) Armstrong, R.S.; Berry, A.J.; Cole, B.D.; Nugent, K.W.; *J. Chem. Soc.*, *Dalton Trans.* **1997**, 363.

(42) Hougen, J.T.; *J. Mol. Spectrosc.* **1964**, *13*, 149.

(43) Griffith, J.S.; The Theory of Transition Metal Ions; Cambridge University Press: New York, **1961**, p. 307.

(44) Bitner, T.W.; Zink, J.I.; *J. Am. Chem. Soc.* **2000**, *122*, 10631.

(45) Ballhausen, C.J.; *Theor. Chim. Acta* **1965**, *3*, 368.

(46) Sturge, M.D.; *Solid State Physics, Advances in Research and Applications* **1967**, *20*, 91.

(47) Liehr, A.D.; *J. Phys. Chem.* **1963**, *67*, 389.

(48) Longuet-Higgins, H.C.; Öpik, U.; Pryce, M.H.L.; Sack, R.A.; *Proc. R. Soc. London*, **1958**, A *244*, 1.

(49) Carlin, R.L.; O'Connor, C.J.; Bhatia, S.N.; *Inorg. Chem.* **1976**, *15*, 985.

(50) Kurzak, K.; *Spectrochim. Acta*, Part A **1991**, *47*, 1041.

(51) Goldsmith, G.J.; Shallcross, F.V.; McClure D.S.;

J. Mol. Spectrosc. **1965**, *16*, 296.

(52) Camassei, F.D.; Forster, L.S.; *J. Chem. Phys.* **1969**, *50*, 2603.

(53) Riesen, H.; Dubicki, L.; *Inorg. Chem.* **2000**, *39*, 2206.

(54) Ferguson, J.; Guggenheim, H.J.; Wood, D.L.; *J. Chem. Phys.* **1971**, *54*, 504.

(55) Güdel, H.U.; Snellgrove, T.R.; *Inorg. Chem.* **1978**, *17*, 1617.

(56) Riesen, H.; Krausz, E.; Dubicki, L.; *J. Lumin.* **1989**, *44*, 97.

(57) Chatterjee, K.K.; Forster,`L.S.; *Spectrochim. Acta*, Part A **1964**, *20*, 1603.

(58) Andrews, L.J.; Lempicki, A.; McCollum, B.C.; *J. Chem. Phys.* **1981**, *74* 5526.

(59) Forster, L.S.; *Chem. Rev.* **1990**, *90*, 331.

(60) Kirk, A.D.; *Chem. Rev.* **1999**, *99*, 1607.

(61) Šopotrajanov, B.; Stefov, V.; Žugic, M.; Petruševski, V.M.;

J. Mol. Struct. **1999**, *482-483*, 109.

(62) Schenker, R.; Triest, M.; Reber, C.; Güdel, H.U.; submitted

(63) Abragam, A.; Résonance paramagnétique électronique des ions de transition,

Presses Universitaires de France, **1971**

(64) Wood, D.L.; Ferguson, J.; Knox, K.; Dillon J.F. Jr.;

J. Chem. Phys. **1963**, *39*, 890.

(65) Adams, D.M.; Lock, P.J.; *J. Chem. Soc.*, *Dalton Trans.* **1971**, 2801.

(66) Taiichiro, H.; *J. Phys. Soc. Jpn.* **1960**, *15*, 483.

(67) Uryû, N.; Skalyo, J.; Friedberg, S.A.; *Phys. Rev.* A **1966**, *144*, 689.

(68) Figgis, B.N. Gerloch, M.; Lewis, J.; Mabbs, F.E.; Webb, G.A.;

J. Chem. Soc., *Dalton Trans.* **1968**, 2086.

(69) Gerloch, M.; Quested, P.N.; Slade, R.C.;

J. Chem. Soc., *Dalton Trans.* **1971**, 3741.

(70) Landry-Hum, J.; Bussière, G.; Daniel, C.; Reber, C.; *Inorg. Chem.* **2001**, *40*, 2595.

Chapitre 5

(1) Zink, J.I.; Kim Shin, K.-S.; *Adv. Photochem.*; Volman, D. H., Hammond, G.S. and Neckers, D.C.; John Wiley: New York, **1991**; *16*, p 119.

(2) Brunold, T.; Güdel, H.U.; dans Inorganic Electronic Structure and Spectroscopy; Solomon, E.I. et Lever, A.B.P.; John Wiley: New York, **1999**, p 259.

(3) Bussière, G.; Reber, C.; *J. Am. Chem. Soc.* **1998**, *120*, 6306.

(4) Triest, M.; Bussière, G.; Bélisle, H.; Reber, C.; *J. Chem. Ed*. **2000**, *77*, 670, http://jchemed.chem.wisc.edu/JCEWWW/Articles/index.html

(5) Savoie, C.; Reber, C.; *J. Am. Chem. Soc.* **2000**, *122*, 844.

(6) Åkesson, R.; Pettersson, L.G.M.; Sandström, M.; Wahlgren, U.; *J. Am. Chem. Soc.* **1994**, *116*, 8691.

(7) Oetliker, U.; Riley, M.J.; Güdel, H.U.; *J. Lumin.* **1995**, *63*, 63.

(8) Oetliker, U.; Riley, M.J.; May, P.S.; Güdel, H.U.; *J. Lumin.* **1992**, *53*, 553.

(9) Oetliker, U.; Reber, C.; *Phys. Chem. Comm.* **1999**, article 13.

(10) Hehlen, M.; Güdel, H.U.; *J. Chem. Phys.* **1992**, *98*, 1768.

(11) May, P.S.; Güdel, H.U.; *Chem. Phys.* Lett. **1989**, *164*, 612.

(12) May, P.S.; Güdel, H.U.; *J. Lumin.* **1990**, *47*, 19.

(13) McClure, D.S.; *Sol. Stat. Phys.* **1959**, *8-9*, 1.

(14) Hitchman, M.A.; McDonald, R.G.; Smith, P.W.; Stranger, R.; *J. Chem. Soc., Dalton Trans.* **1988**, 1393.

(15) Tregenna-Piggott, P.W.L.; Best, S.P.; Güdel, H.U.; Weihe, H.; Wilson, C.C.; *J. Sol. State Chem.* **1999**, *145*, 460.

(16) Solomon, E.I.; Ballhausen, C.J.; *Mol. Phys.* **1975**, *29*, 279.

(17) Johnson, D.A.; Nelson, P.G.; *Inorg. Chem.* **1999**, *38*, 4949.

(18) Grimes, N.W.; Kay, H.F.; Webb, M.W.; *Acta Crystallogr.* **1963**, *16*, 823.

(19) Liehr, A.D.; Ballhausen, C.J.; *Ann. Phys.* **1959**, *2*, 134.

(20) The following crystal field parameters were used: Dq = 910 cm^{-1}, B = 950 cm^{-1}, C/B = 4, λ = -270 cm^{-1}. The $^3T_{2g}$ energies calculated with these values are: 8872 cm^{-1} (E_g), 8995 cm^{-1} (T_{1g}), 9315 cm^{-1} (T_{2g}), 9451 cm^{-1} (A_{2g}).

(21) Wilson, R.B.; Solomon, E.I.; *Inorg. Chem.* **1978**, *17*, 1729.

(22) Güdel, H.U.; Snellgrove, T.R.; *Inorg. Chem.* **1978**, *17*, 1617.

(23) Bigoli, F.; Braibanti, A.; Tiripicchio, A.; Tiripicchio, C. *Acta Crystallogr.* **1971**, B*27*, 1427.

(24) Mizuno, J.; *J. Phys. Soc. Jpn.* **1961**, *16*, 1574.

(25) Beattie, J.K.; Best, S.P.; Skelton, B.W.; White, A.H.; *J. Chem. Soc., Dalton Trans.* **1981**, 2105.

(26) McCarthy, P.J.; Lauffenburger, J.C.; Schreiner, M.M.; Rohrer, D.C.; *Inorg. Chem.* **1981**, *20*, 1571.

(27) Roos, B.O.; Anderson, K.; Fülscher, M.P.; Serrano-Andres, L.; Pierloot, K.; Merchan, M.; Molina, V.; *J. Mol. Struct.* (*Theochem*) **1996**, *388*, 257.

(28) Roos, B. O.; Anderson, K.; *Chem. Phys. Lett.* **1995**, *245*, 215.

(29) Pierloot, K.; Dumez, B.; Widmark, P.O.; Roos, B.O.; *Theor. Chim. Acta.* **1995**, *90*, 87.

(30) Andersson, K.; Blomberg, M.R.A.; Fülscher, M.P.; Karlström, G.; Lindh, R.; Malmqvist, P.; Neogrády, P.; Olsen, J.; Roos, B.O.; Sadlej, A.J.; Schütz, M.; Seijo, L.; Serrano-Andrés, L.; Siegbahn, P.E.M.; Widmark, P.O.; MOLCAS; version 4.1; Lund University: Lund, Sweden, **1997**.

(31) König, E.; *Struct. Bond.* **1971**, *9*, 175.

(32) Figgis, B.N.; Introduction to Ligand Fields; John Wiley: New York, **1966**.

(33) Ballhausen, C.J.; Introduction to Ligand Field Theory; McGraw-Hill: New York, **1962**.

(34) Tanabe, Y.; Moriya, T.; Sugano, S.; *Phys. Rev. Lett.* **1965**, *15*, 1023.

(35) Talaga, D. S.; Zink, J. I.; *J. Phys. Chem.* **1996**, *100*, 8712-8721.

(36) Bellafrouh, K.; Daul, C.; Güdel, H.U.; Gilardoni, F.; Weber, J.; *Theor. Chim. Acta* **1995**, *91*, 215.

(37) Gilardoni, F.; Weber, J.; Bellafrouh, K.; Daul, C.; Güdel, H.U.; *J. Chem. Phys.* **1996**, *104*, 7624.

(38) Seijo, L.; Barandiarán, Z.; McClure, D. S.; *Int. J. Quant. Chem.* **2000**, *80*, 623.

(39) Ballhausen, C.J.; *Z. Phys. Chem.* **1958**, *17*, 246.

Chapitre 6

(1) Sutter, J.P.; Kahn, M.L.; Golhen, S.; Ouahab, L.; Kahn, O.; *Chem. Eur. J.* **1998**, *4*, 571.

(2) Lescop, C.; Luneau, D.; Belorizky, E.; Fries, P.; Guillot, M.; Rey, P.; *Inorg. Chem.* **1999**, *38*, 5472.

(3) Caneschi, A.; Dei, A.; Gatteschi, D.; Sorace, L.; Vostrikova, K.; *Angew. Chem.* **2000**, *112*, 252.

(4) Kahn, M.L.; Sutter, J.P.; Golhen, S.; Guionneau, P.; Ouahab, L.; Kahn, O.; Chasseau, D.; *J. Am. Chem. Soc.* **2000**, *122*, 3413.

(5) Fegy, K.; Luneau, D.; Ohm, T.; Paulsen, C.; Rey, P.; *Angew. Chem. Int. Ed. Engl.* **1998**, *37*, 1270.

(6) All three complexes were unambiguously authenticated based on the elemental analysis, crystal structure and powder X-ray diffraction. Anal. Found/Calcd for **1** ($C_{28}H_{34}N_{11}O_{13}La$): C, 38.36/38.60 H, 4.16/3.93 N, 17.29/17.68 La, 16.04/15.94. Anal. Found/Calcd for **2** ($C_{28}H_{34}N_{11}O_{13}Gd$): C, 37.32/37.79, H, 3.93/3.85, N, 16.98/17.31, Gd, 17.17/17.67. Anal. Found/Calcd for **3** ($C_{28}H_{34}N_{11}O_{13}Eu$): C, 37.76/38.00 H, 4.16/3.90 N, 16.93/17.40 Eu, 16.72/17.20.

(7) crystal data: BRUKER SMART CCD diffractometer equipped with a normal focus molybdenum-target X-ray tube. The data were processed through the SAINT reduction and SADABS absorption software packages and the structures were solved with the SHELXTL software[16]. **1**. $C_{28}H_{34}N_{11}O_{13}La$, MW = 871.57, dark-blue parallelipipedal, orthorhombic, space group $Pna2_1$ (no. 33), a=19.500(1) Å, b=13.0582(8) Å, c=14.5741(9) Å , Z=4, V=3711.1(4) $Å^3$, 22715 reflections measured, 8875 independent reflections (R_{int}=0.0609), R(F)=0.0331 ($I>2\sigma(I)$), $wR(F^2)$=0.1146 (all data). **2**. $C_{28}H_{34}N_{11}O_{13}Gd$, MW = 889.91, dark-blue parallelipipedal, orthorhombic, space group $Pna2_1$ (no. 33), a=19.183(1) Å, b=13.1600(7) Å, c=14.4107(7) Å , Z=4, V=3638.0(3) $Å^3$, 22941 reflections measured, 7728 independent reflections (R_{int}=0.0370), R(F)=0.0206 ($I>2\sigma(I)$), $wR(F^2)$=0.0625 (all data). **3**. $C_{28}H_{34}N_{11}O_{13}Eu$, MW =

884.62, Dark-blue parallelipipedal, orthorhombic, space group *Pna*2_1 (no. 33), a=19.210(1) Å, b=13.1447(7) Å, c=14.4200(7) Å , Z=4, V=3641.4(3) Å^3, 13092 reflections measured, 4769 independent reflections (R_{int}=0.0519), R(F)=0.0347 (I>2σ (I)), wR(F^2)=0.1048 (all data).

(8) Luminescence was excited with a 150 W Xe lamp filtered through a copper sulfate solution and a Schott BG 18 filter, leading to an excitation wavelength range from 300 nm to 400 nm. All samples were cooled in a helium gas-flow cryostat. The emitted light was dispersed by a 0.75m monochromator and detected by a cooled Hamamatsu R928 photomultiplier and a photon counting system. All spectra reported here are not corrected for system response. Absorption spectra were measured with a Cary 5E spectrometer.

(9) Davis, M.J.; Reber, C.; *Inorg. Chem.* **1995**, *34*, 4585.

(10) Adamo, C.; di Matteo, A.; Rey, P.; Barone, V.; *J. Phys. Chem.* A **1999**, *103*, 3481.

(11) Ullman, E.F.; Osiecki, J.H.; Boocock, D.G.B.; Darcy, R.; *J. Am. Chem. Soc.* **1972**, *94*, 7049.

(12) Karayannis, N.M.; Paleos, C.M.; Mikulski, C.M.; Pytlewski, L.L.; Blum, H.; Labes, M.M. *Inorg. Chim. Acta* **1973**, *7*, 74.

(13) Richardson, P.F.; Kreilick, R.W.; *J. Am. Chem. Soc.*, **1977**, *99*, 8183.

(14) Yoshida, T.; Suzuki, T.; Kanamori, K.; Kaizaki, S.; *Inorg. Chem.*, **1999**, *38*, 1059 and Corrigendum: *Inorg. Chem.* **1999**, *38*, 5926.

(15) Yoshida, T.; Kanamori, K.; Takamizawa, S.; Mori, W.; Kaizaki, S.; *Chem. Lett.* **1997**, 603.

(16) SAINT-Version 4.050; SHELXTL, Version 5.030; Bruker Analytical X-ray Instruments, Inc.: Madison, WI, 1998.

Chapitre 7

(1) Canham, L.T.; *Appl. Phys. Lett*. **1990**, *57*. 1046.

(2) Lehmann, V.; Gösele, U.; *Appl. Phys. Lett.* **1990**, *58*, 856.

(3) Dag, Ö.; Ozin, G.A.; Yang, H.; Reber, C.; Bussière, G.; *Adv. Mater.* **1999**, *11*, 474.

Chapitre 8

(1) Kettle, S.F.A.; Physical Inorganic Chemistry; University Science Books: Sausalito, **1996**, p. 175.

Remerciements

Je remercie mon directeur de recherche Christian Reber pour toutes les discussions palpitantes que nous avons eues sur la spectroscopie des complexes des métaux de transition. Je tiens a remercier aussi tout ceux avec qui j'ai travaillé dans ce groupe de recherche: Rémi Beaulac, Myriam Triest, Bruno Larue, Julie Landry-Hum, Jean Christophe Tremblay, Benoît Cardinal-David, Hugo Bélisle et Thierry Wamser.

Je tiens à remercier spécialement Dominique et Isabelle Luneau ainsi que Christophe Lescop pour nous avoir accueilli à Grenoble. Merci également pour cette collaboration scientifique intéressante au cours de laquelle j'ai appris énormément.